Probing Inflationary Physics with Gravitational Waves

Ameek Malhotra

A thesis in fulfilment of the requirements for the degree of

Doctor of Philosophy

School of Physics

Faculty of Science

The University of New South Wales

25 October 2023

ORIGINALITY STATEMENT

☑ I hereby declare that this submission is my own work and to the best of my knowledge it contains no materials previously published or written by another person, or substantial proportions of material which have been accepted for the award of any other degree or diploma at UNSW or any other educational institution, except where due acknowledgement is made in the thesis. Any contribution made to the research by others, with whom I have worked at UNSW or elsewhere, is explicitly acknowledged in the thesis. I also declare that the intellectual content of this thesis is the product of my own work, except to the extent that assistance from others in the project's design and conception or in style, presentation and linguistic expression is acknowledged.

COPYRIGHT STATEMENT

AUTHENTICITY STATEMENT

☑ I certify that the Library deposit digital copy is a direct equivalent of the final officially approved version of my thesis.

☑ The candidate has declared that **their thesis has publications - either published or submitted for publication - incorporated into it in lieu of a Chapter/s. Details of these publications are provided below.**.

Publication Details #1

Full Title:	Constraining primordial tensor features with the anisotropies of the cosmic microwave background
Authors:	Jan Hamann and Ameek Malhotra
Journal or Book Name:	Journal of Cosmology and Astroparticle Physics
Volume/Page Numbers:	JCAP 12 (2022) 015
Date Accepted/Published:	12 December 2022
Status:	published
The Candidate's Contribution to the Work:	JH and I came up with the idea for the paper. I was also responsible for the writing and performed all the numerical analysis with guidance from JH.
Location of the work in the thesis and/or how the work is incorporated in the thesis:	This paper is incorporated in lieu of chapter 6.

Publication Details #2

Full Title:	New universal property of cosmological gravitational wave anisotropies
Authors:	Ameek Malhotra, Ema Dimastrogiovanni, Guillem Domènech, Matteo Fasiello, and Gianmassimo Tasinato
Journal or Book Name:	PHYSICAL REVIEW D
Volume/Page Numbers:	Phys. Rev. D 107, 103502
Date Accepted/Published:	4 May 2023
Status:	published
The Candidate's Contribution to the Work:	I derived the main result of the paper, performed all the numerical calculations, generated all but one of the figures and wrote the bulk of the text.
Location of the work in the thesis and/or how the work is incorporated in the thesis:	The results of this publication are presented in section 4.2 and 4.4 of chapter 4.

Publication Details #3

Full Title:	Enhancing gravitational wave anisotropies with peaked scalar sources
Authors:	Ema Dimastrogiovanni, Matteo Fasiello, Ameek Malhotra and Gianmassimo Tasinato
Journal or Book Name:	Journal of Cosmology and Astroparticle Physics
Volume/Page Numbers:	JCAP 01 (2023) 018
Date Accepted/Published:	13 January 2023
Status:	published
The Candidate's Contribution to the Work:	I performed all the numerical and analytic calculations and contributed to a major part of the writing.
Location of the work in the thesis and/or how the work is incorporated in the thesis:	The results of this paper are described in section 4.2 and 4.3 of chapter 4.

Publication Details #4

Full Title:	Testing the early universe with anisotropies of the gravitational wave background
Authors:	Ema Dimastrogiovanni, Matteo Fasiello, Ameek Malhotra, P. Daniel Meerburg and Giorgio Orlando
Journal or Book Name:	Journal of Cosmology and Astroparticle Physics
Volume/Page Numbers:	JCAP 02 (2022) 040
Date Accepted/Published:	28 February 2022
Status:	published
The Candidate's Contribution to the Work:	I performed all the calculations and forecasts described in sections 2 and 3 and the parameter space analysis and forecasts described in section 4 of the of the paper. Sections 2 and 3 were written entirely by me and I also contributed to the writing in section 4.
Location of the work in the thesis and/or how the work is incorporated in the thesis:	The results of this paper are described in chapter 5.

Publication Details #5

Full Title:	Cross-correlations as a Diagnostic Tool for Primordial Gravitational Waves
Authors:	Ameek Malhotra, Ema Dimastrogiovanni, Matteo Fasiello and Maresuke Shiraishi
Journal or Book Name:	Journal of Cosmology and Astroparticle Physics
Volume/Page Numbers:	JCAP 03 (2021) 088
Date Accepted/Published:	26 March 2021
Status:	published
The Candidate's Contribution to the Work:	I performed all the numeric and most of the analytic calculations and contributed to the bulk of the writing.
Location of the work in the thesis and/or how the work is incorporated in the thesis:	The results of this paper are described in chapter 5.

Candidate's Declaration

I confirm that where I have used a publication in lieu of a chapter, the listed publication(s) above meet(s) the requirements to be included in the thesis. I also declare that I have complied with the Thesis Examination Procedure.

Abstract

Cosmological observables beyond the two-point function of density perturbations may hold the key to answering fundamental questions about inflation. One such observable is the inflationary gravitational wave (GW) background, expected to arise in all models of inflation. A detection of this GW background may reveal to us the energy scale of inflation and even point us towards the fields and interactions present during the inflationary epoch. In this thesis, I explore the GW signatures of inflationary models beyond the simple single-field scenarios, focusing on their anisotropies, non-Gaussianity and spectral shape.

For the anisotropies, I first study GW backgrounds with a sharply peaked spectral shapes, which can arise in inflationary scenarios involving primordial black hole formation and discuss the implications of this spectral shape for the detection of the anisotropies. I then derive general results for cosmological gravitational wave background anisotropies arising from adiabatic initial conditions. I also discuss the impact of isocurvature initial conditions through the representative example of the curvaton mechanism and show how GW anisotropies and their cross-correlations with the CMB provide an alternative handle on the curvaton dynamics.

On the subject on non-Gaussianity, I show how a sizeable squeezed limit tensor bispectrum can generate large GW anisotropies. Although the direct measurement of tensor non-Gaussianity is not possible at interferometer scales, this method still provides an indirect way to observe tensor non-Gaussianity with interferometers. I then discuss the prospects of doing "cosmological collider physics" with such GW anisotropies, showing that the correlators of these anisotropies are particularly sensitive to the spin of additional fields that source the GW.

Finally, I turn to the GW spectral shape, focusing on large scale observations through the temperature and polarisation anisotropies of the CMB. Using current CMB data, I test for GW signatures of axion-gauge field models which typically produce a bump like spectral shape and demonstrate the detectability of such signatures with future experiments such as LiteBIRD and CMB-S4.

Acknowledgements

First of all, I would like to thank my supervisor Ema Dimastrogiovanni for giving me the opportunity to work on this exciting topic and for her constant support and guidance throughout my PhD. Thank you for encouragement and invaluable feedback during this journey, I feel incredibly lucky to have had you as my supervisor.

I am grateful to Susan Coppersmith for making sure that my candidature went smoothly, allowing me to fully focus on my research. I would also like to thank the faculty in the Particle Physics and Cosmology group: Yvonne Wong, Michael Schmidt and Jan Hamann, for all the useful discussions and assistance and for creating such a wonderful atmosphere in the department. My candidature at UNSW has been supported by the University International Postgraduate Award.

During my PhD it was also a great pleasure to work with and learn from the following people: Matteo Fasiello, Jan Hamann, Gianmassimo Tasinato, Guillem Domènech, Giorgio Orlando, Maresuke Shiraishi and Daan Meerburg. Thank you very much for the fruitful collaborations that led to the results presented in this thesis. A special thank you to Matteo Fasiello for his tremendous help during my stay at IFT-Madrid.

Thank you to all my friends and colleagues in the Physics department: Adam, Gabriela, Giovanni, Julius, Tobias and Yuqi, and my friends outside the department: Abhinav, Alejandro, Ave, Derek, Emily and Mattia, for making this an extremely enjoyable experience.

Finally, I would like to thank my family for the endless love and support they have given me throughout all these years.

Publications and Presentations

List of Publications

The original work presented in this thesis is based on publications listed below. For the papers in which I was not the sole primary author, the contributions of my co-authors are also provided.

[1] **A. Malhotra**, E. Dimastrogiovanni, M. Fasiello and M. Shiraishi, "*Cross-correlations as a Diagnostic Tool for Primordial Gravitational Waves,*" JCAP **03** (2021), 088 [arXiv:2012.03498]. The results of this paper are described in chapter 5.

[2] E. Dimastrogiovanni, M. Fasiello, **A. Malhotra**, P. D. Meerburg and G. Orlando, "*Testing the early universe with anisotropies of the gravitational wave background,*" JCAP **02** (2022), 040 [arXiv:2109.03077].

ED and MF came up with the idea of the paper. I performed all the calculations and forecasts for the model independent part described in sections 5.2.1 and 5.2.3 and the parameter space analysis and forecasts for the model-specific part, described in section 5.3.1. GO, ED and MF were responsible for the calculation of the mode functions and the squeezed limit tensor bispectra. Section 5.2.3 was written predominantly by me and everyone contributed to the writing in the rest of the paper. The results of this paper are described in chapter 5.

[3] E. Dimastrogiovanni, M. Fasiello, **A. Malhotra** and G. Tasinato, "*Enhancing gravitational wave anisotropies with peaked scalar sources,*" JCAP **01** (2023), 018, [arXiv:2205.05644].

ED, MF and GT were responsible for the idea of the paper. I performed all the numerical calculations and the forecasts and everyone contributed to the writing. The results of this paper are described in chapter 4.

[4] J. Hamann and **A. Malhotra**, "*Constraining primordial tensor features with the anisotropies of the cosmic microwave background,*" JCAP **12** (2022), 015, [arXiv:2209.00827].

JH and I came up with the idea for the paper. I was responsible for the writing and performed the MCMC and Fisher analysis with guidance from JH. This paper is incorporated in lieu of chapter 6.

[5] **A. Malhotra**, E. Dimastrogiovanni, G. Domènech, M. Fasiello and G. Tasinato,"*A new universal property of cosmological gravitational wave anisotropies,*",

Phys. Rev. D 107 (2023) 103502, [arXiv:2212.10316]. The results of this paper are described in chapter 4.

List of Presentations

The results obtained in the publications [1–5] have also been presented in the following conferences and workshops,

Oral presentations:

- ICG Portsmouth Theoretical Cosmology Seminar, "*Gravitational wave anisotropies as a probe of the early universe*" [9th March 2022] (50 min)
- Cosmology journal club, Van Swinderen Institute for Particle Physics and Gravity, University of Groningen, "*Probing the early universe with gravitational waves*" [25 October 2022] (50 min)
- Majorana-Raychaudhuri Seminar Series, "*Probing the early universe with gravitational waves*" [25 November 2022] (45 min)
- Sixth Sydney CPPC meeting, "*Probing the early universe with stochastic gravitational wave backgrounds*" [26 July 2023], (25 min)
- Cosmology from Home 2023, "*Cosmological gravitational wave anisotropies from adiabatic and isocurvature perturbations*" [6 July 2023] (15 min)
- Third EuCAPT Annual Symposium, 2023, "*A new universal property of cosmological gravitational wave anisotropies*" [2 Jun 2023] (5 min)
- Dark Side of the Universe 2022, Sydney, "*Constraining primordial tensor features with the anisotropies of the Cosmic Microwave Background*" [6 December 2022] (15 min)
- A Cosmic Window to Fundamental Physics: Primordial Non-Gaussianity and Beyond, IFT Madrid, "*Gravitational wave anisotropies as a probe of primordial non-Gaussianity*" [23 September 2022] (15 min)
- 14th International LISA Symposium 2022, *"Gravitational wave anisotropies as a probe of the inflationary particle content"* [20 July 2022] (15 min)
- 23rd International Conference on General Relativity and Gravitation, Beijing, "*Gravitational wave anisotropies as probe of the inflationary particle content*" [7 July 2022] (15 min)
- Cosmology from Home 2022, "*Gravitational wave anisotropies as probe of the inflationary particle content*" [5 July 2022] (15 min)
- 4th Sydney CPPC meeting, "*Searching for primordial tensor modes across small and large scales*" [27 June 2022] (20 min)
- Gravity: Current challenges in black hole physics and cosmology, YITP Kyoto, "*Gravitational wave anisotropies as probe of the inflationary particle content*" [24 June 2022] (15 min)

- ACAMAR meeting on Astroparticle Physics 2022, "*Gravitational wave anisotropies as probe of the inflationary particle content*" [24 June 2022] (15 min)

Poster presentations

- Gravitational Wave Orchestra 2022, UCLouvain, "*Constraining primordial tensor features with the anisotropies of the Cosmic Microwave Background*" and "*Gravitational wave anisotropies as probe of the inflationary particle content*" [8-9 September 2022]

Contents

List of Figures

List of Tables

Abbreviations

AGWB	Astrophysical Gravitational Wave Background
BBN	Big Bang Nucleosynthesis
BBO	Big Bang Observer
CGWB	Cosmological Gravitational Wave Background
CMB	Cosmic Microwave Background
EFT	Effective Field Theory
ET	Einstein Telescope
EW	Electroweak
GR	General Relativity
GW	Gravitational Waves
IR	Infrared
LIGO	Laser Interferometer Gravitational-Wave Observatory
LISA	Laser Interferometer Space Antenna
PT	Phase transition
PTA	Pulsar Timing Array
QCD	Quantum Chromodynamics
QFT	Quantum Field Theory
SGWB	Stochastic Gravitational Wave Background
SIGW	Scalar Induced Gravitatioanal Waves
UV	Ultraviolet
vev	Vacuum Expectation Value

Units and Conventions

We use natural units with $\hbar = c = k_B = 1$. For the space-time metric, we adopt the mostly positive metric signature $(-,+,+,+)$ so that the Minkowski space metric reads,

$$\eta_{\mu\nu} = \mathrm{diag}(-,+,+,+).$$

Four-vectors are denoted as x^μ, p^μ where the Greek indices run from $\mu = 0$ to 3. We denote three-vectors using bold font, e.g. $\boldsymbol{x}$, and use Latin letters for spatial indices e.g. x^i with i running from 1 to 3. The Einstein summation convention is adopted throughout.

Our Fourier transform convention is,

$$f(\boldsymbol{x}) = \int \frac{d^3x}{(2\pi)^3}\, \tilde{f}(\boldsymbol{k}) e^{i\boldsymbol{k}\cdot\boldsymbol{x}}\,, \qquad \tilde{f}(\boldsymbol{k}) = \int d^3k\, f(\boldsymbol{x}) e^{-i\boldsymbol{k}\cdot\boldsymbol{x}}.$$

Some commonly used units and conversions are also listed below,

$1\,\mathrm{Mpc} = 3.08 \times 10^{22}\,\mathrm{m}$,
$H_0 = 100h\,\mathrm{km\,sec^{-1}\,Mpc^{-1}} = 2.86h \times 10^{-4}\,\mathrm{Mpc^{-1}}$,
$T_{\mathrm{CMB}} = 2.73\,K = 2.3 \times 10^{-12}\,\mathrm{GeV}$,
$m_{\mathrm{Pl}} = \sqrt{\dfrac{\hbar c}{G_N}} = 1.22 \times 10^{19}\,\mathrm{GeV}$,
$M_{\mathrm{Pl}} = \dfrac{m_{\mathrm{Pl}}}{\sqrt{8\pi}} = 2.44 \times 10^{18}\,\mathrm{GeV}$,
$\dfrac{k}{\mathrm{Mpc^{-1}}} = 6.46 \times 10^{14} \dfrac{f}{\mathrm{Hz}}$.

Chapter 1

Introduction

1.1 The Standard Model of Cosmology

Cosmology, the study of the origins and evolution of the universe, has fascinated us from time immemorial. The modern era of cosmology can be thought to have begun in the early 20^{th} century with development of the theory of General Relativity and the discovery of expansion of the universe. Space-time was no longer the static background in which events occurred, but itself now dynamical, bending and warping to the will of the matter and energy contained within it. Since then, field of cosmology has made enormous progress and achieved significant milestones such as the observation of the cosmic microwave background (CMB), the realisation that universe contained more matter than could be seen and the theory of Big Bang Nucleosynthesis (BBN). In the past few decades, the discovery of the accelerated expansion of the universe [6, 7] and the precision measurement of the CMB and its anisotropies by COBE [8, 9], WMAP [10] and the *Planck* satellite [11], have completely revolutionised our understanding of the universe.

Altogether, this has culminated in a remarkably simple cosmological model – our universe appears to be homogeneous and isotropic on large scales ($\gtrsim 100\,\text{Mpc}$) [12, 13], its spatial geometry is flat [14, 15], and it is expanding at an accelerating rate. It can be described by a handful of parameters representing the present day energy densities of its primary constituents, *baryonic matter*, *dark matter* and *dark energy* $\{\Omega_\text{b}, \Omega_\text{c}, \Omega_\Lambda\}$, and two parameters $\{A_\text{s}, n_\text{s}\}$ describing small initial deviations from ho-

mogeneity and isotropy, believed to be generated during an early period of accelerated expansion known as *inflation*. General Relativity provides the underlying theoretical framework for this model, known as the ΛCDM (Lambda Cold Dark Matter) model of modern cosmology.[1] It has been tremendously successful in explaining a host of cosmological observations, ranging from the abundances of light elements, temperature and polarisation anisotropies of the CMB, the formation of galaxies and the distribution of Large Scale Structure (LSS) to the late time accelerated expansion.

Despite the success and apparent simplicity of ΛCDM, it is well understood that the model is not yet complete. Each parameter of the ΛCDM model is inextricably linked to a major open question of modern cosmology:

- $\mathbf{\Omega_c}$: What is the fundamental nature of dark matter?
- $\mathbf{\Omega_\Lambda}$: What is the fundamental nature of dark energy and is it truly a cosmological constant?
- $\mathbf{\Omega_b}$: How did the matter anti-matter asymmetry of the universe arise?
- $\mathbf{A_s}, \mathbf{n_s}$: What is the physics of inflation and the origin of the primordial perturbations?

Recent observations also hint towards the fact that ΛCDM might need updating, with disagreement between values of cosmological parameters such as H_0 and S_8 inferred from late and early-time observations [16, 17].

Several theoretical and experimental endeavours are currently underway, aimed at unravelling these mysteries and providing new insights into the laws that govern our universe. The answer to these questions will likely involve physics beyond the Standard Model of Particle Physics or even require us to move beyond General Relativity as our preferred theory of gravity. It is a great time to be a cosmologist, with the field poised to make transformative discoveries in the future. Within this exciting landscape, this thesis sets out on a modest but nevertheless important goal of understanding certain aspects of *cosmic inflation*, our most compelling explanation of the origin of the primordial perturbations.

[1] The ΛCDM model is sometimes also referred to as the Standard Model or the Concordance model of cosmology. Furthermore, in addition to the parameters mentioned above, the model also consists of an astrophysical parameter τ, which represents the optical depth to reionization.

1.2 The Inflationary Paradigm

Inflation refers to a period of accelerated, near-exponential expansion in the early universe and is currently the most widely accepted theory of how the primordial perturbations originate. Historically,[2] inflation was introduced in 1981 by Alan Guth [20] for a different reason, namely to provide a solution to the horizon and flatness problems of the 'hot big bang' model, which represented the dominant cosmological paradigm at that time. Soon afterwards, it was realised that inflation provides a natural mechanism to produce the primordial perturbations [21–29], by stretching microscopic quantum fluctuations to cosmological scales through the accelerated expansion.

In its simplest incarnation, inflation is driven by the nearly constant potential energy of a single scalar field, dubbed the *inflaton*. As the inflaton field slowly rolls down its potential, it also experiences quantum fluctuations which get stretched out to cosmological scales by the rapid expansion. Eventually the inflaton rolls towards the minimum of its potential and inflation ends. The inflaton then decays into the Standard Model particles in a process known as *reheating*, leading to a hot thermal universe. The initial scalar field fluctuations thus source the density fluctuations that later seed the anisotropies of the CMB and the large scale structure (LSS). This minimal model, called *single-field slow-roll* (SFSR) inflation, predicts a nearly scale-invariant and Gaussian spectrum of density perturbations arising from adiabatic initial conditions. Remarkably, the predictions of this model are in excellent agreement with observations, with the strongest evidence for inflation coming from the precision measurements of the CMB temperature and polarisation anisotropies (Figure 1.1).

Inflationary models also predict the existence of primordial gravitational waves (PGW), arising from quantum fluctuations of the tensor degrees of freedom of the space-time metric [30–33]. In SFSR models, the PGW spectum is nearly scale invariant and Gaussian with an amplitude which is in one-to-one correspondence with the energy scale of inflation. Such PGW would in fact be a signature of *linearised quantum gravity* and detecting them would provide further strong evidence that inflation did occur. Currently, CMB observations have allowed us to precisely measure the primordial scalar power parameters $\{A_{\rm s}, n_{\rm s}\}$, and put upper limits on the amplitude of PGW [15, 34, 35]. Numerous single field models/potentials have been pro-

[2] The early history of the development of inflationary theory can be found in [18, 19].

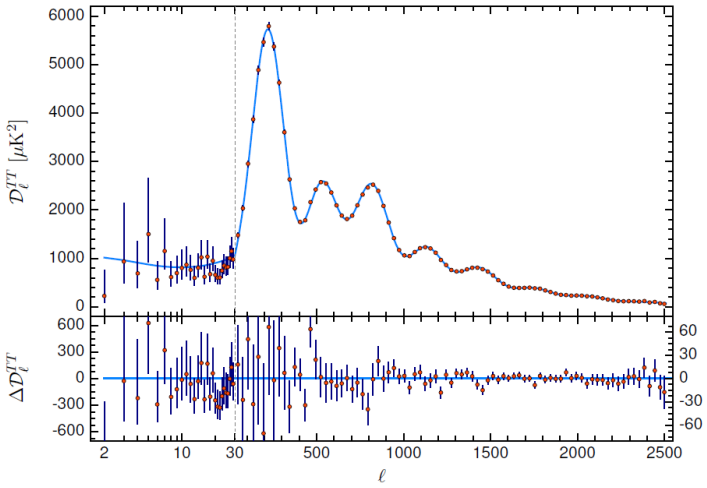

Figure 1.1: The angular power spectrum of the CMB temperature anisotropies: best-fit from ΛCDM (blue) vs observed (red) [15].

posed (see [36] for an overview), with some such as Starobinsky [21, 37, 38] and Higgs inflation [39] providing an excellent fit to the data while others such as Natural inflation [40] and inflation with monomial potentials [27] are disfavoured or ruled out [41]. In the future, the improved sensitivity of next generation CMB experiments such as the BICEP Array [42], Simons Observatory [43], CMB-S4 [44] and LiteBIRD [45], will allow us to put further constraints on inflationary models or even detect PGW, which will have significant implications for our understanding of inflation.

Inflation: single-field or multi-field?

Although the inflationary paradigm has been quite successful, the micro-physical description of inflation, i.e., its field content and interactions, still eludes us. Single field inflation, which agrees well with current observations and is appealing due to its simplicity, remains difficult to reconcile with more fundamental high energy theories such as string theory. These theories generally predict a rather rich inflationary environment, with several fields and non-negligible interactions amongst them, markedly different from the single field description [46]. The *swampland* program, which attempts to study the properties of low energy theories which can be consistently embedded in theories of quantum gravity, also indicates that conventional single-field slow-roll models could possibly be in the *swampland*, i.e. they do not possess a UV completion allowed by quantum gravity [47, 48]. It is possible that multi-field inflation might evade such conjectures [49].

Another issue is the sensitivity of the inflationary potential to Planck scale physics, resulting in the well known η-problem of inflation. For successful resolution of the horizon problem, inflation must provide at least 50-60 e-folds of accelerated expansion. This requires that the inflaton potential be extremely flat which is quantified in terms of the smallness of the inflationary slow roll parameters $\epsilon_V, \eta_V \ll 1$ (defined in eq. (2.64)). If we embed slow-roll inflation in an Effective Field Theory (EFT) framework, one must include in the effective Lagrangian *all* possible operators compatible with the symmetries of the theory. Integrating out the effects of high energy physics above a certain cut-off Λ gives rise to operators of the form,

$$\mathcal{L}_{\text{eff}} \supset \frac{\mathcal{O}_n}{\Lambda^{4-n}} \tag{1.1}$$

where n is the dimension of the operator. Identifying the cutoff scale with the Planck scale and focusing on the dimension-6 operator $\mathcal{O}_6 = c\,\mathcal{O}_4\,\phi^2$ leads to an $\mathcal{O}(1)$ correction of the parameter η_V and ends inflation too quickly, assuming the coupling c is $\mathcal{O}(1)$ and that the dimension-4 operator has a vacuum expectation value $\langle \mathcal{O}_4 \rangle \sim V$. Additionally, radiative corrections also drive the inflaton mass to the cut-off scale, also leading to large corrections to the η_V parameter (see [46, 50] for a review of the η-problem). A possible solution is to posit a shift symmetry, i.e., letting the inflaton be a pseudo-Nambu-Goldstone boson such as an axion, to forbid such corrections. The simplest model of inflation with an axion, *Natural inflation* [40], is already in tension with observational data. However, a shift symmetric coupling of the axion to additional fields, e.g. Abelian or non-Abelian gauge fields, can alleviate this tension and potentially make such setups viable again [51].

Inflationary signatures beyond SFSR: Gravitational Waves

The difficulties in realising single field inflation in a more fundamental high energy theory have naturally led to extensive interest in multi-field inflationary scenarios (e.g see [36, 46, 52–54] and references therein). The richer dynamics of multi-field inflation leads to a much more varied phenomenology in contrast to the single-field case. These models can reproduce the desirable predictions of SFSR inflation on CMB scales, while at the same time accommodate the possibility of distinct features in the primordial scalar [55, 56] and GW spectra [57–60], non-Gaussianity [61, 62] and even lead to the formation of primordial black holes [63, 64].

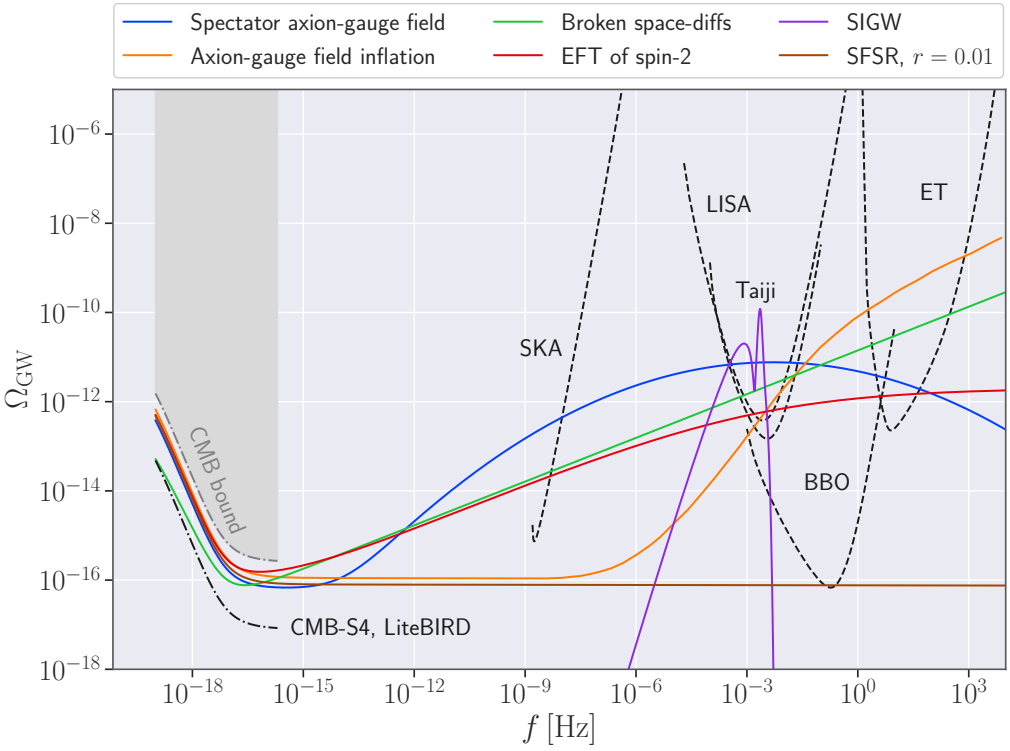

Figure 1.2: Gravitational waves from inflation: theoretical predictions, current bounds and future observational prospects. More details about the figure can be found in section 3.3.2.

This thesis focuses on the study of gravitational waves from inflationary scenarios beyond SFSR. Our goal is to explore the space of possible gravitational wave observables that can arise in these models and forecast their detectability with future experiments. Understanding these two aspects is important not only from a point of view of using GW observations to differentiate between single vs multi-field inflation, but also to discriminate among various models in case of a multi-field realisation.

In terms of detection, the B-mode polarisation of the CMB remains a potential avenue to detect PGW. Analysis of the correlation functions of the B-modes, such as $\langle BB \rangle$, $\langle BBB \rangle$ and mixed correlators such as $\langle TB \rangle$, $\langle EB \rangle$ etc. can be used to probe the spectral shape, non-Gaussianity and chirality of PGW.

The success of GW interferometers has also expanded the observational landscape of inflationary signatures to small scales. Indeed, several inflationary models beyond SFSR (see fig. 1.2) predict the existence of PGW with an amplitude sufficient to be detectable by next generation interferometers, Laser Interferometer Space Antenna (LISA) [65], Einstein Telescope (ET) [66] and Cosmic Explorer (CE) [67], to name a few. Direct detection with interferometers also opens up the possibility to map

the GW energy density across the sky and observe its anisotropies, in addition to its spectral shape, non-Gaussianity and chirality.

Pulsar timing arrays (PTAs) represent another intriguing possibility to detect GW on intermediate scales. Quite recently, several PTA collaborations have reported strong evidence for a stochastic background of GW, likely of astrophysical origin [68–71]. Irrespective of the origin of the background, it can still be used to constrain the parameter space of several cosmological mechanisms producing GW (e.g. inflation, phase transitions, cosmic strings) [72, 73], demonstrating the ability of small-scale GW experiments to probe the early universe. In the near future, the increasing number and sensitivity of CMB, PTA and interferometer experiments will bring within our reach an even larger number of inflationary models, making PGW an extremely promising tool for understanding inflationary physics.

1.3 Thesis Outline

The outline of the thesis is as follows. The thesis is divided into two parts and in Part I, I introduce the necessary background knowledge required for understanding the original results of the thesis. In chapter 2, I review the dynamics of homogenous and isotropic spacetimes, briefly present the ΛCDM model of cosmology and finally introduce the paradigm of cosmic inflation. Next, in chapter 3, I review the generation of quantum fluctuations during the inflationary epoch and the describe the connection between these inflationary fluctuations and cosmological observables such as the CMB and LSS.

The expert reader may skip directly to Part II, which represents the original work of this thesis. In chapter 4, I first review the anisotropies of stochastic gravitational wave backgrounds sourced by primordial perturbations using the line-of-sight formalism. As an application of this formalism, I use it to examine the frequency dependence of GW anisotropies arising in scenarios involving the production of primordial black holes, and study the implication of this frequency dependence on the detection prospects of these anisotropies with interferometers. Going back to the theoretical formalism, I derive the anisotropies sourced by primordial adiabatic and isocurvature perturbations, demonstrating along the way, how GW isocurvature can be generated through the example of the curvaton mechanism.

In chapter 5, I illustrate how gravitational wave anisotropies are sensitive to squeezed limit primordial non-Gaussianity and how information about the masses and spins of additional inflationary particles (*'cosmological collider physics'*) could be extracted from the detection of these anisotropies and their cross-correlation with the CMB. Chapter 6 studies the detectability of GW produced in inflationary models involving axions and gauge fields, using the temperature and polarisation anisotropies of the CMB. In the same chapter, I also forecast the precision with which such GW signals may be measured with the next generation of CMB experiments. The conclusions of this thesis are presented in Chapter 7.

Part I

Preliminaries

Chapter 2

Homogeneous and Isotropic Cosmology

Introduction

In this chapter, I begin by reviewing the dynamics of our homogeneous and isotropic universe, describe the known and unknown components that contribute to its energy content and finally conclude with a discussion of the most important stages in its evolution. The presentation in this chapter draws largely from the textbooks by Mukhanov [74], Dodelson and Schmidt [75], and the lecture notes by Baumann [76].

2.1 FLRW metric

Modern cosmology rests on the *cosmological principle*, which states that the universe is homogeneous and isotropic, when averaged over large enough length scales. Observational evidence from the CMB and LSS supports the validity of this principle on length scales $L \gtrsim 100\,\mathrm{Mpc}$. Thus, as a first approximation we can safely assume our universe to be spatially homogeneous and isotropic. To describe our universe and gravitational effects within it, we turn to the theory of General Relativity in which the geometrical properties of spacetime are encoded in the metric tensor $g_{\mu\nu}$. Under

the assumptions of homogeneity and isotropy, the metric takes the form,

$$\boxed{ds^2 \equiv g_{\mu\nu}dx^\mu dx^\nu = -dt^2 + a^2(t)\left[d\chi^2 + S_k^2(\chi)(d\theta^2 + \sin^2\theta d\phi^2)\right]}. \tag{2.1}$$

Here, the x^i are called *comoving coordinates*, t is the *cosmic time* and the scale factor a is an arbitrary function of t and is independent of the spatial position. The metric in this form is called the Friedman-Lemâitre-Robertson-Walker (FLRW) metric and describes a uniformly expanding, homogeneous and isotropic universe. There exist three distinct possibilities for term $S_k(\chi)$ which determines the spatial curvature of the universe,

$$S_k(\chi) = \begin{cases} \sinh\chi, & k < 0 \\ \chi, & k = 0 \\ \sin\chi, & k > 0 \end{cases}. \tag{2.2}$$

These correspond to a negatively curved universe ($k < 0$), flat universe ($k = 0$) and positively curved universe ($k > 0$). The space with $k = 1$ is finite in extent but without a boundary, since it is equivalent to the 3-sphere $\mathbb{S}^3$. The $k = 0, -1$ cases correspond to 3D Euclidean space and a hyperboloid embedded in 4D Lorentzian space respectively and thus represent universes of infinite extent.

Inflationary cosmology predicts the spatial curvature to be extremely small (section 2.6.1) and current observations do not indicate any preference for non-zero spatial curvature [15]. Therefore, in what follows we will restrict ourselves to the case of the spatially flat universe with $k = 0$,

$$ds^2 = -dt^2 + a^2(t)\delta_{ij}dx^i dx^j. \tag{2.3}$$

Physical distances within the expanding universe are given by,

$$D_{\text{phys}} = a(t)\Delta\boldsymbol{x} \tag{2.4}$$

where $\Delta\boldsymbol{x}$ denotes the spatial coordinate separation. Thus, we see that the physical distances change with time, even if the coordinate separation remains fixed,

$$\dot{D}_{\text{phys}} = \underbrace{H(t)D_{\text{phys}}}_{\text{Hubble flow}} + v_{\text{pec}}. \tag{2.5}$$

Here

$$H(t) = \frac{\dot{a}}{a}, \quad v_{\text{pec}} = a\frac{d\mathbf{x}}{dt}. \tag{2.6}$$

The quantity $H(t)$ is called the *Hubble parameter*. The first term on the R.H.S of eq. (2.5) represents the Hubble expansion law which states that objects further away from us appear to be receding away at a faster rate compared to objects closer to us. The second term is called the *peculiar velocity* and accounts for motion in the comoving coordinates.

2.2 Kinematics

What are the trajectories followed by freely falling test particles in the FLRW universe? Under the action of purely gravitational forces, freely falling particles travel along *geodesics* which are curves that extremise the the proper time $\Delta s = \int ds$, between two spacetime events.

2.2.1 Geodesics

The geodesic equation is given by,

$$\boxed{\frac{d^2x^\mu}{d\lambda^2} + \Gamma^\mu_{\alpha\beta}\frac{dx^\alpha}{d\lambda}\frac{dx^\beta}{d\lambda} = 0} \tag{2.7}$$

where λ is a parameter along the geodesic and $\Gamma^\mu_{\alpha\beta}$ denote the Christoffel symbols which are defined in terms of the metric $g_{\mu\nu}$ as,

$$\Gamma^\mu_{\alpha\beta} \equiv \frac{1}{2}g^{\mu\nu}\left[\frac{\partial g_{\alpha\nu}}{\partial x^\beta} + \frac{\partial g_{\beta\nu}}{\partial x^\alpha} - \frac{\partial g_{\alpha\beta}}{\partial x^\nu}\right]. \tag{2.8}$$

Note that by definition, the Christoffel sybmols are symmetric in the lower indices since $g_{\mu\nu}$ is also symmetric. For the FLRW metric, the only non-zero Christoffel symbols are,

$$\Gamma^0_{ij} = \dot{a}a\delta_{ij} \quad \text{and} \quad \Gamma^i_{0j} = \Gamma^i_{j0} = H\delta_{ij} \tag{2.9}$$

The 4-momentum $P = (E, \vec{P})$ of the particle along the geodesic can be written as,

$$P^\mu = \frac{dx^\mu}{d\lambda}. \tag{2.10}$$

In terms of P^μ the geodesic equation takes the form,

$$\frac{dP^\mu}{d\lambda} + \Gamma^\mu_{\alpha\beta}P^\alpha P^\beta = 0. \tag{2.11}$$

The parameter λ can be eliminated by noticing that,

$$\frac{d}{d\lambda} = \frac{dx^0}{d\lambda}\frac{d}{dx^0} = E\frac{d}{dt}. \tag{2.12}$$

Now, the $\mu = 0$ component of the geodesic equation becomes,

$$E\frac{dE}{dt} = -\Gamma^0_{ij}P^iP^j = -\dot{a}a\delta_{ij}P^iP^j. \tag{2.13}$$

Finally, defining the magnitude of the physical momentum

$$p^2 \equiv g_{ij}P^iP^j. \tag{2.14}$$

and using $g_{\mu\nu}P^\mu P^\nu = m^2$ we obtain

$$\frac{dp}{dt} + Hp = 0. \tag{2.15}$$

Thus, the physical momentum of all particles (massive or massless) decreases with the expansion of the universe,

$$\boxed{p \propto a^{-1}.} \tag{2.16}$$

For massless particles one has $E = p$ and we see that their energy also decays with the expansion.

Light propagation and Null Geodesics

The trajectories of photons are studied most conveniently by introducing the a new time coordinate known as the *conformal time* η,

$$d\eta \equiv \frac{dt}{a}. \tag{2.17}$$

The metric in the new coordinates looks particularly simple,

$$ds^2 = a^2(t)\left[-d\eta^2 + \delta_{ij}dx^idx^j\right], \tag{2.18}$$

and is equivalent to the Minkowski metric up to an overall conformal factor. Let us rewrite this metric in polar coordinates,

$$ds^2 = a^2(t)\left[-d\eta^2 + dr^2 + r^2(d\theta^2 + \sin^2\theta d\phi^2)\right]. \tag{2.19}$$

Since photons travel along null geodesics $ds^2 = 0$, if we consider light propagation in the radial direction we find that the photon paths are defined by,

$$\boxed{d\eta^2 = dr^2 \implies r = \pm\eta + \text{const.},} \tag{2.20}$$

corresponding to straight lines at 45° in these η–r coordinates.

2.2.2 Redshift

The expansion of the universe leads to a redshift of light emitted from distant objects. Consider a signal emitted from a far away galaxy at conformal time η_e with duration $\delta\eta$. We observe it at conformal time η_o and measure its duration to be $\eta_o + \delta\eta$.

The corresponding physical time intervals are,

$$\delta t_e = a(\eta_e)\delta\eta, \quad \delta t_o = a(\eta_o)\delta\eta$$

We thus realise that for a wave with period δt_e and frequency at emission is $f_e = 1/\delta t_e$, the observed frequency is $f_o = 1/\delta t_o$

$$\boxed{\frac{f_e}{f_o} = \frac{a_o}{a_e} = \frac{1}{a_e} \equiv 1 + z\,.} \tag{2.21}$$

Here, z is called the *redshift parameter* and we have set the scale factor at the time of observation to be $a_o = 1$.

We see that the wavelength of the observed photons increases with the expansion of universe as $\lambda \propto a$. Equivalently, the frequency/energy of photons decreases as $E \propto a^{-1}$, a result that we also derived in the previous section via the geodesic equation.

2.2.3 Distances

In a cosmological setting, defining distances requires careful considerations as multiple notions of distances can exist, each being useful depending on the particular context. We start by defining two natural distances – the *comoving distance* and the *physical distance*. The comoving distance is simply the coordinate separation between two fixed points on the comoving grid while the physical distance takes into account the expansion of the universe. If a source emits a signal at t_e and is observed today at time t_0, its comoving distance is calculated as,

$$d = \eta_0 - \eta_e = \int_{t_e}^{t_0} \frac{dt}{a(t)} = \int_{z_e}^{z_0} \frac{dz}{H(z)}. \tag{2.22}$$

The corresponding physical distance is then given by

$$d_{\text{phys}}(t) = a(t)d. \tag{2.23}$$

It happens quite often that these two distances are not the most useful ones from the point of view of observations. In fact, the comoving and physical distances turn out to be unobservable on cosmological scales. Two additional definitions of observationally relevant distances are reviewed below.

Luminosity distance

Consider a light source at a distance d in static Euclidean space. The relation between the source luminosity and the observed flux at the distance d is given by,

$$F = \frac{L}{4\pi d^2}. \tag{2.24}$$

The generalisation of this distance to expanding spacetimes is known as the luminosity distance. The static space formula needs modification for three reasons, namely the area of a sphere drawn around the source and passing through the observer position scales as $a^2(t_0)d^2$ rather than d^2, the rate of photon arrival is reduced by a factor $1/(1+z)$ and finally the energy of photons is again lower by $1/(1+z)$ where z is the redshift parameter of the source. Altogether, the observed flux is given by

$$F = \frac{L}{4\pi a^2(t_0) d^2 (1+z)^2} \equiv \frac{L}{4\pi d_L^2}, \tag{2.25}$$

where d_L is the luminosity distance and is related to the comoving distance d as,

$$d_L = d(1+z). \tag{2.26}$$

Angular diameter distance

The angular diameter distance d_A relates the observed angular size of an object $\Delta\theta$ to its physical size D

$$d_A \equiv \frac{D}{\Delta\theta}. \tag{2.27}$$

The physical size can be written as,

$$D = a(t_e) d\Delta\theta = \frac{d\Delta\theta}{1+z}, \tag{2.28}$$

and thus,

$$d_A = \frac{d}{1+z} = \frac{d_L}{(1+z)^2}. \tag{2.29}$$

2.3 Dynamics

The Einstein equation,

$$\boxed{G_{\mu\nu} \equiv R_{\mu\nu} - \frac{1}{2} g_{\mu\nu} R = 8\pi G T_{\mu\nu}\,,} \tag{2.30}$$

dictates the dynamics of our universe. It relates the spacetime curvature, encoded in $G_{\mu\nu}$, to the matter-energy content of the universe. The requirements of homogeneity and isotropy constrain the stress-energy tensor $T_{\mu\nu}$ to be that of a perfect fluid[1],

$$T_{\mu\nu} = (\rho + P) U_\mu U_\nu + P g_{\mu\nu} \tag{2.31}$$

where ρ and P denote the energy density and pressure of the fluid and $U_{\mu\nu}$ is the 4-velocity of the observer. A comoving observer $U^\mu = (1, 0, 0, 0)$, will observe this stress-energy tensor to be diagonal,

$$T^\mu{}_\nu = g^{\mu\alpha} T_{\alpha\nu} = \mathrm{diag}(-\rho, P, P, P). \tag{2.32}$$

The fluid stress-energy tensor also obeys a continuity equation for the energy density, which can be derived from the first law of thermodynamics $dE + PdV = 0$. Since $V \propto a^3$ and $E = \rho V$, this takes the form

$$d\rho = -3(\rho + P) d \ln a, \tag{2.33}$$

or equivalently,

$$\boxed{\dot{\rho} + 3H(\rho + P) = 0.} \tag{2.34}$$

Alternatively, this follows from the $\nu = 0$ component of the general relativistic conservation equation $\nabla_\mu T^\mu{}_\nu = 0$.

The rate of dilution of the energy density with the expansion of the universe depends crucially on the relation between the pressure and the energy density. In the next section, we will specify this relation for the known constituents of the universe.

2.3.1 The cosmic inventory

Several different components contribute to the energy budget of the universe. To describe these contributions, it is convenient to introduce the density parameters Ω_i,

[1] Fluids which do not conduct heat and have zero viscosity are known as perfect fluids. They can be completely characterised in terms of their rest frame energy density ρ and pressure P.

defined as,

$$\Omega_i \equiv \frac{\rho_i}{\rho_{\rm cr}}, \quad \rho_{\rm cr} \equiv \frac{3H_0^2}{8\pi G}. \tag{2.35}$$

Here, H_0 is the present day value of the Hubble parameter and $\rho_{\rm cr}$ is the *critical energy density* needed to close the universe. For a flat ($k = 0$) universe, $\rho_{\rm cr}$ is the same as the total energy density $\rho = \sum_i \rho_i$, $\rho > \rho_{\rm cr}$ leads to a a closed universe and $\rho < \rho_{\rm cr}$ leads to an open universe. It is also customary to write $H_0 = 100h\,\mathrm{km/s/Mpc}$ and work with the combination $\Omega_i h^2$, due to the uncertainty in determination of H_0 and also since many observations constrain this combination rather than H_0 and Ω_i separately.

Now we look at the relative contributions of the different constituents of the universe to the total energy density, focusing on the components that enter into the ΛCDM model of modern cosmology – *(i)* Matter *(ii)* Radiation and *(iii)* Dark energy.

Matter

The term matter refers to any component whose pressure is negligible compared to its energy density, $|P| \ll \rho$. Matter can thus be represented by an equation of state parameter $w_m = 0$ with energy density decaying as,

$$\rho_m \propto a^{-3} \tag{2.36}$$

- **Baryons**

  Baryonic matter encompasses all ordinary matter. As a matter of convention, this term also includes all known non-baryonic particles of the Standard Model e.g. electrons. Observations of the CMB by *Planck* constrain the baryon density parameter to be $\Omega_{\rm b}h^2 = 0.02237 \pm 0.00015$ [15].

- **Dark matter**

  A variety of cosomological observations also provide strong evidence for the presence of non-baryonic matter [77] which does not couple (or couples extremely weakly) to electromagnetism. Its density parameter has been inferred to be $\Omega_{\rm c}h^2 = 0.1200 \pm 0.0012$ [15], making up about 80% of the total matter content of the universe. Although several candidates for dark matter exist, the fundamental nature of dark matter remains unknown.

Radiation

Species which are relativistic have an equation of state $w_r = 1/3$, implying that their energy density decays as

$$\rho_r \propto a^{-4} \tag{2.37}$$

This can be understood as the dilution of the number density ($n \propto a^{-3}$, same as matter) and the redshifting of the individual particle energy $E \propto a^{-1}$.

- **Photons**

  The total radiation energy density is dominated by the CMB photons, which have been observed to have a near perfect black-body spectrum with present day temperature $T = 2.72548 \pm 0.00057$ K [78] and hence $\Omega_\gamma h^2 = 2.44 \times 10^{-5}$. Since photons are massless, they always remain relativistic. The expansion of the universe preserves the black-body distribution of the photons and the distribution temperature redshifts as $T \propto a^{-1}$.

- **Neutrinos**

  Much like the CMB, one also expects the existence of a primordial neutrino background. Unlike photons however, neutrinos are not massless and at least two of the neutrino species must be non-relativistic today. These background neutrinos have not yet been directly observed yet but there is strong indirect evidence of their existence from CMB/BBN. The current constraints on the effective number of relativistic species after e^+e^- annihilation read $N_{\text{eff}} = 2.92^{+0.36}_{-0.37}$ [15], entirely consistent with the Standard Model of particle physics expectation of $N_{\text{eff}} = 3.0440 \pm 0.0002$ [79] . The present neutrino density parameter is expected to be $\Omega_\nu h^2 = \sum_i m_i/(94\,\text{eV})$, where the sum is over the three neutrino species.

In addition to the above mentioned components, it is possible that the universe is permeated by a background of relic gravitational radiation. These have also not been detected yet and their energy density[2] is constrained to be $\Omega_{\text{GW}} < 1.2 \times 10^{-6} h^{-2}$ from CMB and BBN observations [80].

[2]This bound is applicable to the total energy density in GW, not the usual frequency dependent spectral energy density $\Omega_{\text{GW}}(f)$. Furthermore, the BBN/CMB bound only concerns GW produced before BBN/last scattering.

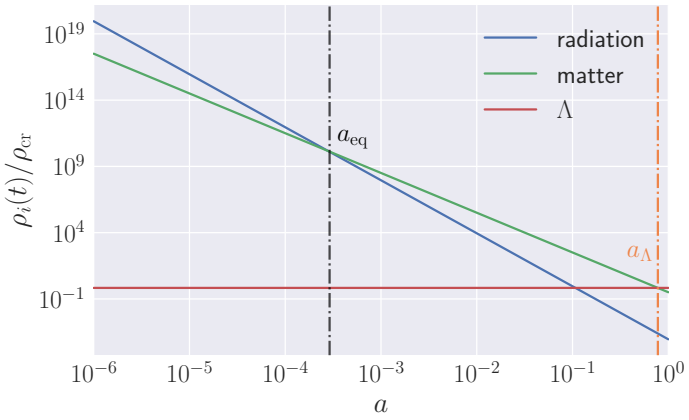

Figure 2.1: Evolution of the energy density for matter, radiation and the cosmological constant Λ. The black and orange lines denote the time of matter-radiation and matter-Λ equality respectively.

Dark Energy

The above mentioned components only account for about 30% of the total energy density of the universe. The late-time accelerated expansion of the universe requires the presence of a mysterious *dark energy* component with $w_{de} < -1/3$ (see eq. (2.43)), which no matter or radiation source can have. In general, its energy density could be time-dependent but current observations indicate a strong preference for a dark energy equation of state $w_{de} \simeq -1$ [15]. In this case the energy density of dark energy remains constant with the expansion,

$$\rho_{de} \propto a^0. \tag{2.38}$$

The simplest candidate for this is the cosmological constant term Λ. The fundamental nature of dark energy remains one of the most important unsolved mysteries of modern cosmology [81, 82].

The time evolution of the energy densities of radiation, matter and Λ is depicted in Figure 2.1 and the relative energy densities of the different components are shown in Figure 2.2. As we go back in time the energy density of matter and radiation increases while that of Λ remains constant. We also see that at very early times, the energy density of the universe was completely dominated by that of radiation. Today, about 70% of the total energy density is made up by the cosmological constant while dark matter and baryonic matter combined account for the remaining 30%. Spatial curvature, if at all present today, makes up only a small fraction $|\Omega_K| < 0.01$ of the total energy budget [15]. Its energy density scales as $\rho_K \propto a^{-2}$ so it is subdominant

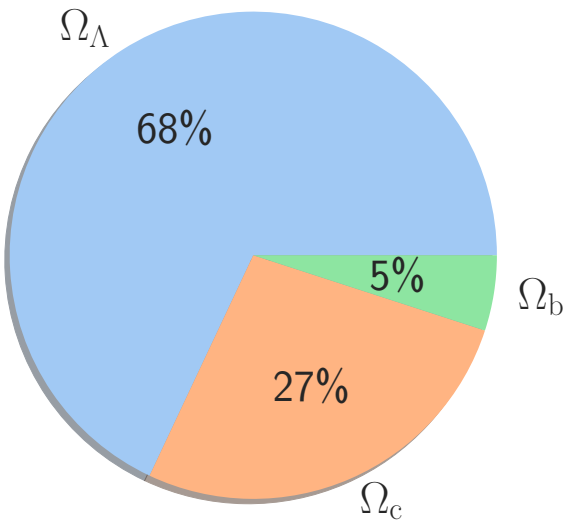

Figure 2.2: The fraction of the total energy density in the different components of the cosmic inventory. The energy density in photons, neutrinos and gravitational waves is much smaller than the other components and is not shown here.

at earlier times compared to matter and radiation.

2.3.2 Friedmann equations

Using the Einstein equations, we can now relate these matter-energy sources to the expansion rate of the universe,

$$H^2 = \frac{8\pi G}{3} \sum_i \rho_i, \tag{2.39}$$

where the sum is over all the components contributing the to energy budget of the universe. Using the definition of the density parameters Ω_i (2.35), one can rewrite the above equation as,

$$H^2 = H_0^2 \sum \Omega_i \, a(t)^{-3(1+w_i)}. \tag{2.40}$$

A second equation concerns the acceleration of the expansion rate,

$$\frac{\ddot{a}}{a} = -\frac{4\pi G}{3}(\rho + 3P). \tag{2.41}$$

Together, equations (2.39) and (2.41) constitute the *Friedmann equations*[3], and describe the evolution of the expansion rate of our FLRW universe. The behaviour of

[3]The second Friedmann equation is not an independent equation and can be derived from the first equation and the continuity equation (2.34).

the scale factor as a function of time for different scenarios is given below,

$$a(t) \propto \begin{cases} \exp(Ht), & w = -1, \\ t^{2/3}, & w = 0, \\ t^{1/2}, & w = 1/3. \end{cases} \tag{2.42}$$

It is also clear from the Friedmann equations that the present day accelerated expansion of our universe requires that

$$\rho + 3P < 0 \Longleftrightarrow w < -1/3. \tag{2.43}$$

Hence, the presence of dark energy component is necessary since matter and radiation necessarily have $w \geq 0$.

2.4 A Brief Thermal History of the Universe

Having studied the geometrical and dynamical properties of our universe, we now focus on its thermal history. The discussion here will be kept at a qualitative level and the reader is referred to refs. [74, 83] for a more detailed treatment.

The thermal history of the universe depends crucially on the interactions between the different particles that are present, characterised by the interaction rate Γ. If this rate is larger than the expansion rate H, the interactions between particles occur on a much shorter time scale $1/\Gamma$ compared to the timescale of expansion $1/H$. The interacting particles are then said to be in a state of *local thermal equilibrium* with each other and share the same temperature T. At very early times, our universe was extremely hot and dense making interactions between different particles extremely efficient. In fact, at temperatures above a few hundred GeV, all the Standard Model particles are ultra-relativistic and their interactions are strong enough for them to be in local thermal equilibrium. This initial hot, dense state consisting of a 'soup' of elementary particles is where the story of the hot big bang model begins.

As the universe expands, it cools down ($T \propto a^{-1}$) and the number density of elementary particles also decreases. The QCD phase transition occurs around $T \sim 150$ GeV, afterwards quarks and gluons no longer exist as free states but become confined within baryons and mesons. At $T \sim 100$ GeV, electroweak symmetry is broken and the gauge

bosons acquire mass. The production of dark matter and the baryon asymmetry of the universe is also expected to take place around such early times, but these are not so well understood compared to the known Standard Model processes.

Several important events occur around MeV scales. First, neutrinos decouple from the rest of the thermal plasma at $T \sim 1$ MeV as weak interactions become inefficient. These decoupled neutrinos then propagate freely throughout the universe and retain their distribution at the time of coupling. Shortly after neutrino decoupling, the temperature of the universe falls below the mass of electron and positron ($T \sim 0.5$ MeV) and these now begin to annihilate. Since neutrinos are already decoupled at this state, this process only injects energy into the photon bath, raising its temperature compared to that of neutrinos by roughly a factor $(11/4)^{1/3}$.

Big bang nucleosynthesis begins around $T \sim 0.1$ MeV, free protons and neutrons combine to form light elements such as hydrogen, helium and lithium with the out of equilibrium thermodynamics of these reactions playing an important role. Calculations of the abundances of light elements have turned out to be in excellent agreement with observations and lend strong support to the hot big bang model. As the universe cools down further, the energy density in relativistic particles falls below that of matter. This happens around $T \sim 1$ eV and is known as the epoch of matter radiation equality.

Protons and electrons combine around $T \sim 0.1$ eV, forming neutral hydrogen in a process known as recombination. Around the same time, Thomson scattering of photons becomes inefficient due to the sharp decrease in the free electron density. Photons now decouple and free stream throughout the universe and this is referred to the epoch of last scattering. Closer to the present day, gravitational instabilities become significant leading to the formation of galaxies and clusters from small initial inhomogeneities in the matter distribution. These free-streaming photons are observed today as the CMB, having a spectrum consistent with that of a black-body and having a present day temperature $T \simeq 0.23\,\text{meV}$.

2.5 Shortcomings of the Hot Big Bang model

The picture of cosmology described in the previous section, starting from a hot thermal state is sufficient to explain several cosmological observations, if one imposes certain initial conditions. However, the question of why the universe started with this particular set of initial conditions, cannot be answered satisfactorily within the framework of this model. These are typically stated as the horizon and the flatness problems of hot big bang cosmology. To understand these, we need to first introduce a quantity essential for studying causality in an expanding universe, the *particle horizon.*

Particle horizon

The particle horizon χ_p is the boundary of our past light cone. Since we can only receive signals from points within our past light cone, the particle horizon sets the size of the region which is causally connected to us.

$$\chi_p(\eta) = \eta - \eta_i = \int_{t_i}^{t} \frac{d\tilde{t}}{a(\tilde{t})} = \int_{a_i}^{a} \frac{d\tilde{a}}{\tilde{a}\dot{\tilde{a}}} = \int_{\ln a_i}^{\ln a} \frac{d \ln \tilde{a}}{\tilde{a} H(\tilde{a})} \tag{2.44}$$

In terms of the redshift parameter z, this is

$$\chi_p = \int_{z_i}^{z} \frac{dz}{H(z)}. \tag{2.45}$$

Whether or not the event and particle horizons are finite depends on the exact form of $a(t)$ and hence, the matter-energy content of the universe. In a universe dominated by a component with equation of state $w > -1/3$, the scale factor and the Hubble parameter evolve with time as

$$a \propto t^{\frac{2}{3(1+w)}}, \quad H \propto t^{-1}. \tag{2.46}$$

The quantity aH decreases with time in a universe with $w > -1/3$. With the initial singularity $a_i = 0$, this tells us that the particle horizon at a given time t is finite

$$\chi_p(t) \propto a(t)^{1+3w}. \tag{2.47}$$

Analogously, one can define the event horizon χ_e, which sets the boundary of the region which can receive signals from us in the future.

$$\chi_e = \eta_f - \eta_0 = \int_{t_0}^{t_f} \frac{dt}{a(t)} \tag{2.48}$$

where η_f denotes the denotes the maximum conformal time, i.e., the final moment of time which may or may not be finite, depending on the behaviour of $a(t)$.

2.5.1 Horizon Problem

The finite size of the particle horizon implies that the near uniformity of the CMB cannot be explained within the hot big bang model. In fact, a causally connected region at the time of photon last scattering subtends an angle of about 1.2° on the sky. This can be calculated as follows,

$$\chi_{p,\mathrm{lss}} = \int_{z_i \to \infty}^{z_{\mathrm{lss}} \simeq 1100} \frac{dz}{Hz}. \tag{2.49}$$

The angular size of the particle horizon on the sky can be estimated using,

$$\theta = \frac{\chi_{p,\mathrm{lss}}}{d_{\mathrm{lss}}} \simeq 1.2^\circ, \tag{2.50}$$

where d^{lss} is the present day comoving distance to the last scattering surface. Therefore, regions separated by an angle $\theta \gtrsim 2^\circ$ would never have had time to thermalise previously and one would expect them to have significantly different temperatures. However, the CMB on these and even larger angular scales is nearly uniform with small temperature fluctuations $\delta T/T \sim 10^{-5}$. This is quite hard to explain if these regions had never been causally connected in the past.

2.5.2 Flatness Problem

The second major issue is the observed flatness of the universe. We can understand this by first writing the Friedmann equation in the presence of curvature k,

$$H^2 = \frac{\rho}{3M_{\mathrm{Pl}}^2} - \frac{k}{a}. \tag{2.51}$$

This can be re-written as,

$$1 - \Omega = -\frac{k}{(aH)^2} \tag{2.52}$$

In this form, we realise that as long as $(aH)^{-1}$ increases with time, the spatially flat universe is not a dynamical attractor. Small perturbations of the density parameter around $\Omega = 1$ show that $k = 0$ is an unstable solution. The present day value $\Omega \approx 1$ requires an extremely small value of the initial curvature and thus, *extreme* fine-tuning of the initial conditions.

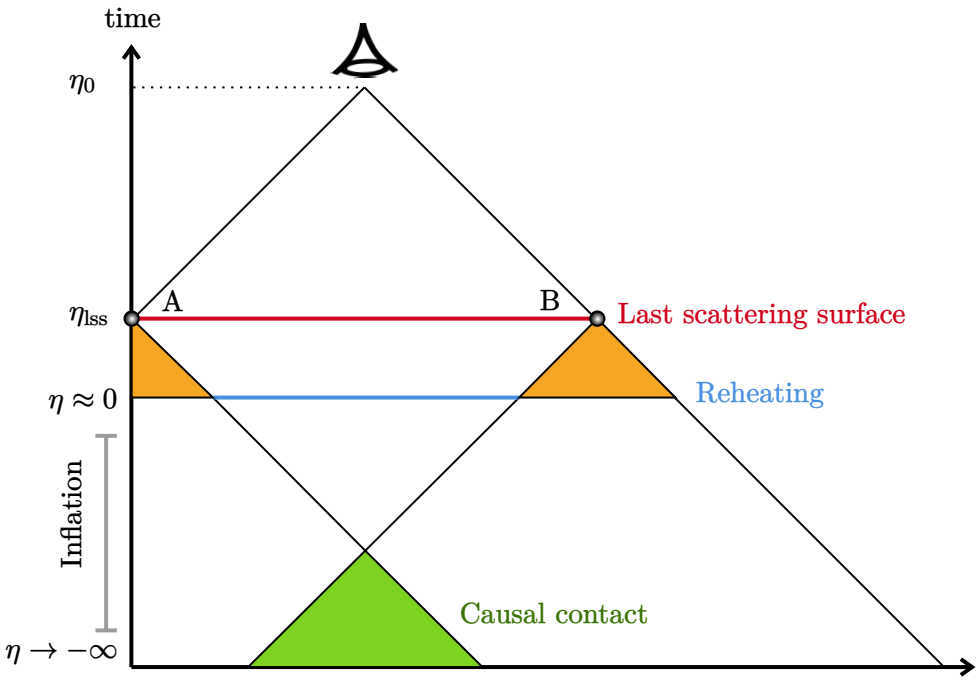

Figure 2.3: A present day observer sees two widely separated points A and B at the last scattering surface to be at nearly the same temperature. Within the hot big bang model, these points could never have been in causal contact in the past. The introduction of the inflationary epoch pushes the initial singularity of the hot big bang $\eta = 0$, to $\eta = -\infty$, thereby allowing the past light cones of A and B to intersect. Figure adapted from [76].

2.6 Inflation: homogeneous and isotropic dynamics

The inflationary scenario postulates that the early universe ($t \sim 10^{-34}\,s$) went through a period of accelerated, near exponential expansion before the hot big bang era [20, 27, 84–86]. In addition to providing a solution to the shortcomings of hot big bang cosmology [20], inflation also provides a natural origin for the primordial fluctuations that seed the CMB anisotropies and large-scale structure [21–29]. This section provides an overview of the homogeneous and isotropic dynamics of inflation, starting with inflationary solution to the aforementioned horizon and flatness problems of big bang cosmology.

2.6.1 Solution to the horizon and flatness problems

Notice that for $w < -1/3$, the expansion of the universe is accelerating (see (2.41)). Equivalently, the the quantity $(aH)^{-1}$ is increasing with time, suggesting that this may provide a common solution to the horizon and flatness problems. In fact, a

period of expansion *before* the hot big bang phase with

$$\boxed{\frac{d}{dt}(aH)^{-1} < 0,} \tag{2.53}$$

naturally solves both of these issues. For $w < -1/3$ the size of the comoving particle horizon diverges, meaning that CMB photons coming from different directions were causally connected in the past (see Figure 2.3), explaining the near uniformity of the observed CMB temperature[4]. Similarly, when $(aH)^{-1}$ decreases with time, the effects of initial non-zero curvature also get diluted, as can be seen from (2.52). $\Omega = 1$, which is an unstable fixed point of the hot big bang phase now becomes an attractor during the inflationary phase. Roughly speaking, one requires that the scale factor grow about 50–60 e-folds, i.e. by a factor e^{50-60}, during this period to solve both the horizon and flatness problems.

2.6.2 Single-field slow-roll Inflation

In the simplest scenarios, inflation is driven by a single scalar field, called the inflaton, whose classical background evolution drives the accelerated expansion. The action for a minimally coupled scalar field ϕ with canonical kinetic terms can be written as,

$$S^{(\phi)} = \int d^4x \sqrt{-g} \left[\frac{M_{\rm Pl}^2}{2} R - \frac{1}{2} g^{\mu\nu} \partial_\mu \phi \partial_\nu \phi - V(\phi) \right] \tag{2.54}$$

where R is the Ricci scalar and $V(\phi)$ the potential energy of the scalar field. Under the assumptions of homogeneity and isotropy, the evolution of the the scalar field is governed by the following equation,

$$\ddot{\phi} + 3H\dot{\phi} + V'(\phi) = 0, \tag{2.55}$$

which is simply the Klein-Gordon equation in an expanding universe.

The stress energy tensor of the scalar field is,

$$\boxed{T_{\mu\nu}^{(\phi)} \equiv -\frac{2}{\sqrt{-g}} \frac{\delta S^{(\phi)}}{\delta g_{\mu\nu}} = \partial_\mu \phi \partial_\nu \phi - \frac{1}{2} g_{\mu\nu} \left[\partial^\alpha \phi \partial_\alpha \phi + V(\phi) \right]}. \tag{2.56}$$

Assuming a homogeneous field profile, the stress energy tensor takes the form of a perfect fluid (eq. (2.31)) with

$$\rho = \frac{1}{2}\dot{\phi}^2 + V(\phi), \quad P = \frac{1}{2}\dot{\phi}^2 - V(\phi). \tag{2.57}$$

[4] In fact, inflation also explains why there exist correlations in the temperature fluctuations over scales larger than the particle horizon at last scattering. The exact mechanism of how these fluctuations are generated during inflation will be discussed in chapter 3.

The resulting equation of state parameter is,

$$w = \frac{\dot{\phi}^2 + 2V(\phi)}{\dot{\phi}^2 - 2V(\phi)} \tag{2.58}$$

and we see that inflation can occur for $\dot{\phi}^2 \ll 2V(\phi)$ since that implies $w < -1/3$, required for the accelerated expansion.

The background evolution during inflation is commonly characterised by the Hubble 'slow-roll' parameters ϵ and η, defined as

$$\epsilon \equiv -\frac{\dot{H}}{H^2} = \frac{3}{2}\left(1 + \frac{P}{\rho}\right), \quad \eta \equiv \frac{\dot{\epsilon}}{\epsilon H} \tag{2.59}$$

For a sufficient number of e-folds of accelerated expansion to take place one requires that these slow-roll parameters stay small $\epsilon, \eta \ll 1$. Thus the Hubble parameter during inflation remains nearly constant, except towards the end of inflation when the slow-roll parameters may become large. The Hubble parameter during inflation is related to the scalar field profile using the Friedmann equation,

$$H^2 = \frac{1}{3M_{\rm Pl}^2}\left[\frac{1}{2}\dot{\phi}^2 + V(\phi)\right] \tag{2.60}$$

For the slow-roll conditions to hold we require,

$$\epsilon = \frac{\dot{\phi}^2}{2M_{\rm Pl}^2 H^2} \ll 1 \tag{2.61}$$

to be satisfied for a long period of time. This means that the acceleration of the field must also be small for which we define the parameter

$$\delta \equiv -\frac{\ddot{\phi}}{H\dot{\phi}}\,. \tag{2.62}$$

The smallness of the second slow-roll parameter $\eta = 2(\epsilon - \delta)$ is then enforced by $\epsilon, |\delta| \ll 1$. Under the slow-roll approximation we get the following set of equations,

$$3H\dot{\phi} + V'(\phi) = 0, \quad H^2 \approx \frac{V(\phi)}{3M_{\rm Pl}^2}. \tag{2.63}$$

Thus, in the simplest models inflation is driven entirely by the near constant potential energy of the scalar field and the scale factor evolves grows almost exponentially with time[5].

[5]The universe having $\dot{H} = 0$ is known as the *de-Sitter* universe with the scale factor growing as $a(t) = a(t_0)e^{H(t-t_0)}$.

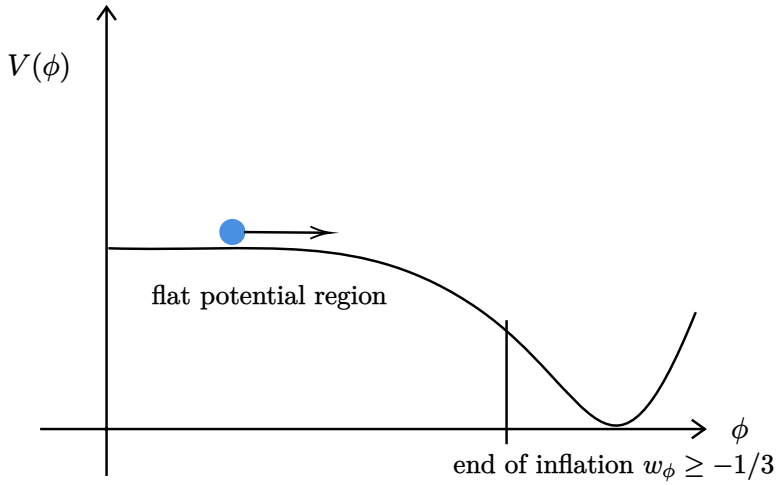

Figure 2.4: Inflation occurs in the flat region of the potential.

The flatness of the potential during inflation can be quantified in terms of the potential slow-roll parameters,

$$\epsilon_V \equiv \frac{M_{\rm Pl}^2}{2}\left(\frac{V'}{V}\right)^2 \ll 1, \quad |\eta_V| \equiv M_{\rm Pl}^2\frac{|V''|}{V} \ll 1. \tag{2.64}$$

The potential slow-roll parameters are related to the previously introduced Hubble slow-roll parameters η, ϵ as,

$$\epsilon_V \approx \epsilon, \quad \eta_V \approx 2\epsilon - \frac{\eta}{2} \tag{2.65}$$

Thus, slow-roll inflation occurs for any generic potential which is sufficiently flat. As the inflaton field rolls down its potential, it eventually leaves the flat region of the potential and inflation ends.

2.6.3 Reheating

Reheating refers to the post-inflationary era in which the matter and radiation components of the universe are generated, typically from the decay of the inflaton. The decay products then eventually scatter and thermalise, leading to a radiation dominated universe. I provide here a brief qualitative description of how reheating may occur. The interested reader may refer to [87–90] for a more comprehensive treatment of the reheating process.

After inflation ends, the inflaton field oscillates coherently around the minimum of

its potential $\phi_{\min}$. We can Taylor expand the potential around the minima as,

$$V(\phi) = \frac{1}{2} m^2 (\phi - \phi_{\min})^2 + \dots . \tag{2.66}$$

During this oscillatory phase, the inflaton field behaves like pressureless matter (averaged over several periods of oscillation) and dominates the energy density of the universe.

We now introduce a coupling between the inflaton and a scalar field χ, which is a surrogate for the known particles of the Standard Model. Let Γ be the decay rate of the inflaton into χ. Then the equation of motion of the inflaton becomes

$$\ddot{\phi} + 3H\dot{\phi} + \Gamma\dot{\phi} + m^2\phi = 0. \tag{2.67}$$

As H decreases with time after inflation, the interaction term takes over and reheating is said to be completed when $\Gamma = H$. The temperature when this happens is called the reheating temperature $T_{\rm rh}$ and can be estimated, given a form for the coupling between the inflaton and χ.

The simple description above ignores additional non-perturbative effects that can play a crucial role in the reheating process. An important example is the fact that the inflaton oscillations back-react on the evolution of χ and can exponentially enhance the production of χ through resonance effects.

$$\ddot{\chi}_k + 3H\dot{\chi}_k + \left(\frac{k^2}{a^2} + f(\phi) \right) \chi_k = 0. \tag{2.68}$$

Here, f is a function of ϕ determined by the coupling between ϕ and χ. These resonance effects can dominate in the initial phase of reheating which is why this phase is sometimes called *preheating*. Eventually, preheating becomes inefficient and the perturbative effects described above may take over.

Chapter 3

Primordial perturbations from Inflation

Introduction

We now we turn to the study of the fluctuations of the inflaton field $\delta\phi(\boldsymbol{x}, t)$, and how they relate to cosmological observables such as the CMB and LSS. The content in this chapter is adapted largely from the lecture notes by Baumann [91] and Riotto [92].

3.1 Quantum fluctuations in de-Sitter space

As a warm-up exercise, let us begin with a simple example and study the fluctuations of a minimally coupled massless scalar field σ (not the inflaton) during inflation described by the action of (2.54). For simplicity, we neglect the the back-reaction of the field on the background[1]. Splitting the field into a homogeneous part and a fluctuation we can write $\sigma(\mathbf{x}, t) = \bar{\sigma}(t) + \delta\sigma(\mathbf{x}, t)$. The evolution equation for the homogeneous part is the same as (2.55), while for the fluctuations it is

$$\delta\ddot{\sigma}_{\boldsymbol{k}} + 3H\delta\dot{\sigma}_{\boldsymbol{k}} + \frac{k^2}{a^2}\delta\sigma_{\boldsymbol{k}} = 0. \tag{3.1}$$

Here, we have used the following convention for the Fourier transform,

$$f(\boldsymbol{x}, t) = \int \frac{d^3x}{(2\pi)^3} f_{\boldsymbol{k}}(\eta) e^{i\boldsymbol{k}\cdot\boldsymbol{x}}. \tag{3.2}$$

[1] We will need to take this into account when we study the fluctuations of the inflaton field ϕ.

Next, we define $u = a\delta\sigma$ and switch to conformal time η to obtain[2],

$$u_{\mathbf{k}}'' + \underbrace{\left(k^2 - \frac{a''}{a}\right)}_{\text{time dep. } \omega(\eta)} u_{\mathbf{k}} = 0. \tag{3.3}$$

This is the equation of motion of a harmonic oscillator with a time dependent frequency $\omega(\eta) = k^2 - a''/a$ and can also be obtained from the following kind of action

$$S = \frac{1}{2}\int d\eta\, d^3\mathbf{x}\, \left[\frac{1}{2}(u')^2 - (\partial_i u)^2 + \frac{a''}{a}u^2\right]. \tag{3.4}$$

It is instructive to study the sub-Hubble ($k \ll aH$) and super-Hubble ($k \gg aH$) limits of equation (3.3). Assuming an exactly de-Sitter spacetime where $a(\eta) = -1/(H\eta)$, we obtain an oscillatory behaviour for the short wavelength modes

$$u_{\mathbf{k}}'' + k^2 u_{\mathbf{k}} = 0 \implies u_{\mathbf{k}} \propto \exp\{\pm i\mathbf{k}\cdot\mathbf{x}\}. \tag{3.5}$$

For the long wavelength modes we obtain a growing and decaying mode solution

$$u_{\mathbf{k}}'' = \frac{a''}{a}u_{\mathbf{k}} \implies u_{\mathbf{k}} \propto a, a^{-2}. \tag{3.6}$$

Focusing only on the growing mode solution, this implies that the original field fluctuation $\delta\sigma = u/a$ freezes on super-Hubble scales.

A general solution of (3.3) can be written as

$$u_{\mathbf{k}} = a_{\mathbf{k}}^{-} u_k(\eta) + a_{-\mathbf{k}}^{+} u_k^*(\eta) \tag{3.7}$$

with $u_k(\eta)$ and $u_k^*(\eta)$ being two linearly independent solutions and $a_{\mathbf{k}}^{-}$, $a_{\mathbf{k}}^{+}$ being some constants. It will later turn out that these represent the creation and annihilation operators, respectively. The Wronskian of the mode functions is independent of time and can be taken to be

$$W[u_k u_k^*] = u_k' u_k^* - u_k u_k^{*\prime} = -i, \tag{3.8}$$

since we can always rescale the mode functions $u_k \to \lambda u_k$.

Quantisation of these perturbations requires that we promote the field u and its canonically conjugate momentum $\pi = \delta\mathcal{L}/\delta u' = u'$ to quantum operators $\hat{u}$ and $\hat{\pi}$ with the standard commutation relation,

$$[\hat{u}(\eta,\mathbf{x}), \hat{\pi}(\eta,\mathbf{y})] = i\delta(\mathbf{x}-\mathbf{y}), \quad [\hat{u}(\eta,\mathbf{x}), \hat{u}(\eta,\mathbf{y})] = [\hat{\pi}(\eta,\mathbf{x}), \hat{\pi}(\eta,\mathbf{y})] = 0. \tag{3.9}$$

[2] Eq. (3.3), when applied to the inflaton field fluctuations, leads to the famous *Mukhanov-Sasaki* equation of inflationary cosmology, e.g. see [91].

The constants $a_{\mathbf{k}}^{\pm}$ now become operators $\hat{a}_{\boldsymbol{k}}^{\pm}$ such that the field operator $\hat{u}$ can be written as

$$\hat{u}(\eta, \mathbf{x}) = \int \frac{d^3k}{(2\pi)^3} \left[\hat{a}_{\mathbf{k}}^{-} u_k(\eta) e^{i\mathbf{k}\cdot\mathbf{x}} + \hat{a}_{\mathbf{k}}^{+} u_k(\eta) e^{-i\mathbf{k}\cdot\mathbf{x}}\right]. \tag{3.10}$$

The commutation relation (3.9) and our normalisation of the Wronskian now ensures that

$$\left[\hat{a}_{\mathbf{k}}^{-}, \hat{a}_{\mathbf{k}'}^{+}\right] = \delta(\mathbf{k} - \mathbf{k}') \quad \text{and} \quad \left[\hat{a}_{\mathbf{k}}^{-}, \hat{a}_{\mathbf{k}'}^{-}\right] = \left[\hat{a}_{\mathbf{k}}^{+}, \hat{a}_{\mathbf{k}'}^{-}\right] = 0. \tag{3.11}$$

Thus, the operators $\hat{a}_{\mathbf{k}}^{\pm}$ can be thought of as the usual creation and annihilation operators with

$$\hat{a}_{\mathbf{k}}^{-}|0\rangle = 0, \quad \hat{a}_{\mathbf{k}}^{+}|0\rangle = |\mathbf{k}\rangle. \tag{3.12}$$

We can then proceed to create general quantum states through repeated actions of the creation and annihilation operators.

3.1.1 Choice of vacuum

The vacuum state in our theory has not yet been uniquely defined. To do this, we need to find a set of mode functions that minimises the expectation value of the Hamiltonian. In general time dependent space-times, this is not so simple since the minimum energy state can itself depend on the time at which it is defined, in this case due to the time dependent frequency $\omega(\eta)$. One can still find a vacuum state that minimises the energy at a given time t_0, i.e. an *instantaneous* vacuum state but this is not guaranteed to be the minimum energy state at a later time t_1. For (quasi)de-Sitter space-times, we can observe that at very early times all the k-modes of interest were sub-Hubble,

$$\frac{k}{aH} \ll 1 \text{ for } |k\eta| \ll 1. \tag{3.13}$$

They have time independent frequencies $\omega = k^2 - 2/\eta^2 \to k^2$ and do not feel the effects of the expansion. Thus, the Minkowski vacuum state can be chosen as the initial state for the fluctuations in de-Sitter spacetimes,

$$\boxed{\lim_{k\eta\to-\infty} u_k(\eta) = \frac{1}{\sqrt{2k}} e^{-ik\eta}} \tag{3.14}$$

This choice of vacuum state is called the *Bunch-Davies* vacuum.

The vacuum state in the far past:
When a given k-mode is sufficiently sub-horizon ($|k\eta| \ll 1$), the equation of motion can be written as,

$$u_k'' + k^2 u_k = 0, \tag{3.15}$$

the same as that of a simple harmonic oscillator in flat space. Each mode has an energy $E_k = |u_k|' + k^2|u_k|^2$. Writing $u_k = r_k e^{id_k}$ gives,

$$E_k = r_k'^2 + r_k^2 d_k'^2 + k^2 r_k, \quad r_k^2 d_k'^2 = -\frac{1}{2}. \tag{3.16}$$

This is minimised with $r_k'^2 = 0$, $r_k = 1/\sqrt{2k}$. We integrate to obtain $d_k = -k\eta$ up to an irrelevant phase factor and finally arrive at,

$$\lim_{k\eta \to -\infty} u_k(\eta) = \frac{1}{\sqrt{2k}} e^{-ik\eta}, \tag{3.17}$$

as the minimum energy state in the far past.

3.1.2 Power spectrum

Coming back to (3.3), we can write a general solution as,

$$u_k(\eta) = A\frac{e^{-ik\eta}}{\sqrt{2k}}\left(1 - \frac{i}{k\eta}\right) + B\frac{e^{ik\eta}}{\sqrt{2k}}\left(1 + \frac{i}{k\eta}\right). \tag{3.18}$$

Imposing the Bunch-Davies vacuum sets $A = 1$, $B = 0$, thus the required mode function is

$$u_k(\eta) = \frac{e^{-ik\eta}}{\sqrt{2k}}\left(1 - \frac{i}{k\eta}\right). \tag{3.19}$$

Finally, the power spectrum is defined as vacuum expectation value (vev) of the two-point function,

$$\langle 0|u_{\mathbf{k}} u_{\mathbf{k}'}|0\rangle = (2\pi)^3 \delta(\mathbf{k} + \mathbf{k}')|u_{\mathbf{k}}|^2 \tag{3.20}$$

In position space we have

$$\langle 0|u(\mathbf{x}, t)^2|0\rangle = \int \frac{d^3k}{(2\pi)^3}|u_{\mathbf{k}}|^2 \equiv \int d\ln k\, \mathcal{P}_u(k). \tag{3.21}$$

Now, recalling that the field fluctuations $\delta\sigma$ were frozen on super-Hubble scales, we can evaluate the power spectrum $\mathcal{P}_{\delta\sigma}(k)$ at Hubble crossing to get,

$$\boxed{\mathcal{P}_{\delta\sigma}(k) = \frac{\mathcal{P}_u(k)}{a^2}\bigg|_{k=aH} = \left(\frac{H}{2\pi}\right)^2\bigg|_{k=aH}}. \tag{3.22}$$

Thus, the spectrum of fluctuations is scale invariant if the spacetime is exactly de-Sitter.

3.1.3 General field fluctuations in quasi de-Sitter

Let us build upon the previous result by first adding a mass term for the field fluctuations. In the presence of a mass term, (3.1) becomes

$$u_{\mathbf{k}}'' + [k^2 + M^2(\eta)]u_{\mathbf{k}} = 0 \tag{3.23}$$

where $M^2(\eta) = (m^2 - 2H^2)a^2(\eta)$. We can rewrite this equation in the form,

$$u_{\mathbf{k}}'' + \left[k^2 - \frac{1}{\eta^2}\left(\nu^2 - \frac{1}{4}\right)\right] u_{\mathbf{k}} = 0, \quad \nu^2 = \frac{9}{4} - \frac{m^2}{H^2} \tag{3.24}$$

For real values of ν_σ and imposing the Bunch-Davies vacuum condition, the solution is

$$u_{\mathbf{k}} = \frac{\sqrt{\pi}}{2} e^{i(\nu+1/2)\frac{\pi}{2}} \sqrt{-\eta}\, H_\nu^{(1)}(-k\eta), \tag{3.25}$$

where $H_\nu^{(1)}$ is the Hankel function of the first kind. In terms of $\delta\sigma$, we have on super-Hubble scales,

$$|\delta\sigma_{\mathbf{k}}| \simeq \frac{H}{\sqrt{2k^3}} \left(\frac{k}{aH}\right)^{\frac{3}{2}-\nu} \tag{3.26}$$

In this case, the fluctuations are not constant and have a small time-dependence on super-Hubble scales due to the mass term.

Finally, we consider the case of inflationary backgrounds where the spacetime is not exactly de-Sitter but has small deviations from it, quantified by the slow-roll parameters of (2.59) which we assume to be small. At first order in the slow-roll parameters, the relation between the scale factor and the conformal time is given by

$$a = -\frac{1}{H\eta}(1+\epsilon), \quad \frac{a''}{a} = \frac{1}{\eta^2}(2+3\epsilon). \tag{3.27}$$

We can now solve (3.23) using these relations to find,

$$\boxed{\mathcal{P}_{\delta\sigma} = \left(\frac{H_*}{2\pi^2}\right)^2 \left(\frac{k}{k_*}\right)^{3-2\nu}} \tag{3.28}$$

where $\nu = 3/2 - \epsilon + m^2/H^2$ for $\epsilon, m^2/H^2 \ll 1$, k_* is a reference scale and H_* is the Hubble parameter evaluated at the time the reference scale crosses the horizon.

3.2 Perturbations from inflation

Let us now calculate the inflaton field perturbations, taking the example of a single field slow-roll model with action,

$$S = \int d^4x \sqrt{-g} \left[\frac{R}{2} - \frac{1}{2} g^{\mu\nu} \partial_\mu \phi \partial_\nu \phi - V(\phi) \right]. \tag{3.29}$$

where ϕ is the inflaton field. We split the inflaton field into a homogeneous part $\bar{\phi}(t)$ and perturbations $\delta\phi(\boldsymbol{x}, t)$. Here, one cannot proceed as in the previous section to compute the perturbation spectrum. Since the inflaton dominates the energy budget of the universe, its field fluctuations induce fluctuations in the stress-energy tensor $T_{\mu\nu}$ and consequently perturbations of the metric tensor $g_{\mu\nu}$. The metric fluctuations then back-react on the inflaton evolution through the perturbed Klein-Gordon equation – in short, these fluctuations cannot be treated independently of each other. Let us now take a look at these metric perturbations in more detail.

3.2.1 Metric Perturbations

The most general perturbations to the FLRW metric can be written as

$$ds^2 = a^2(\tau) \left[-(1+2A) d\eta^2 + 2B_i dx^i d\tau + (\delta_{ij} + h_{ij}) dx^i dx^j \right]. \tag{3.30}$$

Here, A, B_i and h_{ij} are some unknown functions of both space and time, to be determined by solving the Einstein equations. We split the metric into the homoegenous FLRW metric with perturbations on top

$$g_{\mu\nu} = \underbrace{\bar{g}_{\mu\nu}}_{\text{FLRW}} + \delta g_{\mu\nu}, \qquad |\delta g_{\mu\nu}| \ll |\bar{g}_{\mu\nu}| \tag{3.31}$$

Working to linear order in the perturbations, the inverse metric and its perturbations are given by

$$g^{\mu\nu} = \bar{g}^{\mu\nu} + \delta g^{\mu\nu}, \quad \delta g^{\mu\nu} = -\bar{g}^{\mu\alpha} \bar{g}^{\nu\beta} \delta g_{\alpha\beta}. \tag{3.32}$$

SVT decomposition

The metric perturbations can be decomposed into three independent kinds of fluctuations based on their transformation properties under rotations – scalars, vectors

and tensors (SVT). Scalars correspond to density perturbations, vectors to vorticity and tensors correspond to gravitational waves.

A general vector field can be decomposed into the gradient of a scalar and a divergence-less vector

$$B^i = \partial^i B + \bar{B}^i, \tag{3.33}$$

with $\partial^i \bar{B}_i = 0$. Along similar lines, a general rank-2 symmetric tensor can be split into the following

$$h_{ij} = \underbrace{2C\delta_{ij} + 2\partial_i\partial_j E - \frac{2}{3}\delta_{ij}\nabla^2 E}_{\text{scalar}} + \underbrace{\partial_{(i}\bar{E}_{j)}}_{\text{vector}} + \underbrace{2\bar{E}_{ij}}_{\text{tensor}}, \tag{3.34}$$

where $\partial^i \bar{E}_i = \partial^i \bar{E}_{ij} = \bar{E}^i_i = 0$. The significance of this decomposition can be understood from the fact that scalars, vectors and tensors do not mix with each other at linear order, thus we can solve for one kind of perturbation without needing to worry about the other two [93, 94].

Gauge Issues

Consider a general transformation of coordinates,

$$x^\mu \to \tilde{x}^\mu = x^\mu - \xi^\mu, \quad \xi^0 = T \text{ and } \xi^i = \partial_i L + \bar{L}^i \tag{3.35}$$

where $\partial_i \bar{L}_i = 0$ and the metric in the new coordinates now denoted as $\tilde{g}_{\mu\nu}$. The perturbations in the transformed metric can be calculated using

$$ds^2 = g_{\mu\nu}dx^\mu dx^\nu = \tilde{g}_{\mu\nu}d\tilde{x}^\mu d\tilde{x}^\nu \tag{3.36}$$

so

$$g_{\alpha\beta}(x^\mu) = \frac{d\tilde{x}^\mu}{dx^\alpha}\frac{d\tilde{x}^\nu}{dx^\beta}\tilde{g}_{\mu\nu}(\tilde{x}^\mu) \tag{3.37}$$

As an example for the transformation $A \to \tilde{A}$, we find

$$g_{00} \approx \left(\frac{d\tilde{x}^0}{dx^0}\right)^2 \tilde{g}_{00} \tag{3.38}$$

So for the metric in (3.30), one finds

$$\begin{aligned} a^2(\tau)(1+2A) &= (1-2T')a^2(\tau - T)(1+2\tilde{A}) \\ &= a^2(\tau)(1-2T'-2\mathcal{H}T)(1+2\tilde{A}), \end{aligned} \tag{3.39}$$

such that

$$\begin{aligned}\tilde{A} &= A + T' + \mathcal{H}T,\\ \tilde{B}_i &= B_i - \partial_i T + L_i',\\ \tilde{h}_{ij} &= h_{ij} + 2\mathcal{H}T\delta_{ij} + \partial_i\xi_j + \partial_j\xi_i.\end{aligned} \tag{3.40}$$

Note that the quantity $\mathcal{H} = a'/a = aH$ is the conformal Hubble parameter. In terms of the SVT decomposition introduced earlier, the transformations can be written as,

$$\begin{aligned}&A \to A + T' + \mathcal{H}T, \quad B \to B + T - L', \quad \bar{B}_i \to \bar{B}_i + \bar{L}_i\\ &C \to C + \mathcal{H}T + \frac{1}{3}\nabla^2 L, \quad E \to E + L, \quad E_i \to E_i + L_i,\\ &E_{ij} \to E_{ij}.\end{aligned} \tag{3.41}$$

The tensor perturbation E_{ij} is manifestly gauge invariant. At first glance, it would appear that the metric $g_{\mu\nu}$ contains 10 degrees of freedom. However, the gauge freedom of GR means that not all of these degrees of freedom are physical. The coordinate transformations parameterised by $(T, L, \bar{L}_i)$ allow us to eliminate 4 out of 10 of the metric perturbations, leaving us with 6 degrees of freedom – 2 scalars, 2 vectors and 2 tensors. One can see this for instance, by defining gauge invariant variables through linear combinations of the previously defined quantities,

$$\Phi_B \equiv A + \mathcal{H}(B - E') + (B - E')', \quad \bar{\Psi}_i \equiv \bar{E}_i' - \bar{B}_i, \tag{3.42}$$

$$\Psi_B \equiv -C - \mathcal{H}(B - E') + \frac{1}{3}\nabla^2 E, \quad \bar{E}_{ij}. \tag{3.43}$$

The potentials Φ_B and Ψ_B here are the famous *Bardeen potentials* [95].

Gauge invariant quantities can be regarded as truly physical perturbations because they cannot be removed by arbitrary gauge transformations. However, assigning a clear physical meaning to these gauge-invariant quantities may not always be possible and one may need to resort to fixing the gauge to relate these perturbations with observable quantities. In what follows we shall only consider the case of scalar and tensor perturbations, since these are the ones most relevant for inflation. Vector perturbations decay in the absence of a source, thus their effects are rapidly washed out by the inflationary expansion and can be ignored [94].

Newtonian gauge

The Newtonian or longitudinal gauge is defined by the conditions,

$$B = E = 0. \tag{3.44}$$

In this gauge, we have

$$\Phi_B = A, \quad \Psi_B = -C. \tag{3.45}$$

The gauge gets its name from the fact that evolution equations for the metric perturbations in this gauge are most similar to their Newtonian counterparts.

Spatially flat gauge

The spatially flat gauge or the flat slicing gauge is defined by turning off the scalar perturbations in the spatial part of the metric,

$$C = E = 0. \tag{3.46}$$

This gauge will turn out to be quite convenient for the purpose of calculating the inflaton field fluctuations in section 3.2.3.

Comoving gauge

Another commonly used gauge choice is the comoving gauge, defined by requiring the momentum flux of the perturbed stress energy tensor to vanish,

$$\delta T^0{}_i = 0. \tag{3.47}$$

For a scalar field, this is obtained by expanding the scalar field stress energy tensor (2.56), to linear order in the perturbations

$$\delta T^0{}_i = -\frac{\bar{\phi}'}{a^2}\partial_i \delta\phi. \tag{3.48}$$

Thus the comoving gauge condition reads,

$$\delta\phi = 0. \tag{3.49}$$

An extensive review of cosmological perturbation theory can be found in [93, 94].

3.2.2 The curvature perturbation

An important quantity for the study of inflationary perturbations is the comoving curvature perturbation $\mathcal{R}$, which represents the curvature perturbation in the comoving gauge. The curvature perturbation C in a generic gauge is related to the 3-curvature of the spatial hypersurfaces as,

$${}^{(3)}R = -\frac{4}{a^2}\nabla^2 C \tag{3.50}$$

Thus, one can define the gauge invariant curvature perturbation $\mathcal{R}$ as

$$\boxed{\mathcal{R} = -C + \mathcal{H}\frac{\delta\phi}{\phi'}, \quad \mathcal{R} = -C|_{\text{comoving}}}. \tag{3.51}$$

The comoving curvature perturbation has a remarkable property – it remains constant on super-Hubble scales ($k \gg \mathcal{H}$) as long as the perturbations are *adiabatic* [96, 97].

Another useful quantity that one sometimes encounters in the literature is the curvature perturbation in uniform density gauge,

$$\zeta = -C + \mathcal{H}\frac{\delta\rho}{\rho'}. \tag{3.52}$$

This quantity is also gauge invariant and represents the curvature perturbation in the uniform density gauge. On super-Hubble scales, $\zeta \approx \mathcal{R}$ and thus the two variables can be used interchangeably [92].

Adiabatic and Isocurvature perturbations:
In a universe with multiple matter components or fields, two types of perturbations may arise. The first type, *adiabatic* perturbations, refer to perturbations that correspond to common, local time shifts along the background solution, e.g.

$$\delta\rho_i(\boldsymbol{x}, \eta) = \bar{\rho}_i(\eta + \delta\eta(\boldsymbol{x})) - \bar{\rho}_i(\eta). \tag{3.53}$$

The time shift $\delta\eta(\boldsymbol{x})$ is common to all components i. As a consequence of this, one can write

$$\delta\eta = \frac{\delta\rho_i}{\bar{\rho}_i'}, \quad \forall\, i. \tag{3.54}$$

Equivalently, this implies

$$\frac{\delta\rho_i}{1+w_i} = \frac{\delta\rho_j}{1+w_j} \tag{3.55}$$

for all i, j. The perturbations generated during SFSR inflation are always of an adiabatic nature.

On the other hand, models with multiple fields can excite perturbations *orthogonal* to the inflationary background trajectory in field space [94, 98]. This implies that the relative overdensities of the different components are not fixed as in (3.55). These *isocurvature* perturbations are defined as,

$$S_{ij} \equiv 3\mathcal{H}\left(\frac{\delta\rho_i}{\rho_i'} - \frac{\delta\rho_j}{\rho_j'}\right) = 3(\zeta_i - \zeta_j), \tag{3.56}$$

and are gauge invariant by definition.

3.2.3 Curvature power spectrum

To compute the power spectrum of the curvature perturbation, we will switch to the spatially flat gauge $C = 0$. The advantage of using this gauge is that by setting the perturbations δg_{ij} to zero, we need only work with the inflaton fluctuations whose evolution equation is essentially the same as that of a massless field in quasi-de Sitter spacetime[3],

$$\delta\ddot{\phi} + 3H\delta\dot{\phi} + \frac{k^2}{a^2}\delta\phi = 0. \tag{3.57}$$

By evaluating the power spectrum of the inflaton fluctuations at horizon crossing, we can obtain the curvature power spectrum using,

$$\mathcal{R} = \mathcal{H}\frac{\delta\phi}{\phi'}\bigg|_{\text{flat}} \implies \mathcal{P}_{\mathcal{R}}(k) = \left(\frac{\mathcal{H}}{\phi'}\right)^2 \mathcal{P}_{\delta\phi_{\text{flat}}}(k). \tag{3.58}$$

Using the results from section 3.1, we finally obtain

$$\boxed{\mathcal{P}_{\mathcal{R}}(k) = \frac{1}{8\pi^2\epsilon}\left(\frac{H}{M_{\text{Pl}}}\right)^2\bigg|_{k=aH} \equiv A_{\text{s}}\left(\frac{k}{k_*}\right)^{n_{\text{s}}-1}}, \tag{3.59}$$

where A_{s} and n_{s} represent the amplitude and spectral index of the curvature power spectrum and k_* is a reference scale at which the inflationary quantities H, ϵ, η are evaluated,

$$A_{\text{s}} = \frac{1}{8\pi^2\epsilon_*}\left(\frac{H_*}{M_{\text{Pl}}}\right)^2, \quad n_{\text{s}} - 1 \equiv \frac{d\ln\mathcal{P}_{\mathcal{R}}}{d\ln k} = -2\epsilon_* - \eta_* = 2\eta_V - 6\epsilon_V. \tag{3.60}$$

The parameter n_{s} is known as the spectral tilt and measures the deviation from perfect de-Sitter geometry during inflation. During the slow-roll phase, the scale/time dependence of n_{s} can be neglected since $\epsilon' \sim \eta' \sim \mathcal{O}(\epsilon, \eta)^2$.

3.2.4 Gravitational Waves

The case of gravitational waves is now quite straightforward to analyse. Expanding the Einstein-Hilbert action to second order in h_{ij}, we obtain

$$S_{h(2)} = \frac{M_{\text{Pl}}^2}{8}\int d\eta\, d^3x\, a^2\left[(h_{ij})^2 - (\partial_m h_{ij})^2\right]. \tag{3.61}$$

[3]More precisely, this is true up to subdominant slow roll corrections which give a small effective mass ($m \propto \eta_V \ll 1$) to the inflaton field [99, 100]. In general, these corrections may not remain small towards the end of inflation which is why it is convenient to switch to the curvature perturbation $\mathcal{R}$ at the time of Hubble crossing.

Fourier expanding h_{ij} as

$$h_{ij}(t,\mathbf{x}) = \int \frac{d^3k}{(2\pi)^3} \sum_\lambda \epsilon_{ij}^\lambda(k) h_\mathbf{k}(\eta) e^{i\mathbf{k}\cdot\mathbf{x}}, \quad k_i\epsilon_\lambda^{ij} = 0 \text{ and } \epsilon_{ij}^\lambda \epsilon_{ij}^{\lambda'} = 2\delta_{\lambda\lambda'} \tag{3.62}$$

and defining the canonically normalised field

$$v_\mathbf{k} \equiv \frac{aM_{\rm Pl} h_\mathbf{k}}{2}, \tag{3.63}$$

we obtain

$$S_{h(2)} = \frac{1}{2}\sum_\lambda \int d\eta\, d^3k \left[(v_\mathbf{k}^\lambda)^2 - \left(k^2 - \frac{a''}{a}\right)(v_\mathbf{k}^\lambda)^2 \right]. \tag{3.64}$$

This gives us essentially two copies of the scalar field action (3.1) that we have seen previously. Thus, the tensor power spectrum can be written as

$$\mathcal{P}_T(k) = 2\mathcal{P}_h(k) = \left.\frac{2H^2}{\pi^2 M_{\rm Pl}^2}\right|_{k=aH} \tag{3.65}$$

Equivalently, one can write

$$\boxed{\mathcal{P}_T(k) = \frac{2H_*^2}{\pi^2 M_{\rm Pl}^2}\left(\frac{k}{k_*}\right)^{n_{\rm t}} \equiv A_{\rm t}\left(\frac{k}{k_*}\right)^{n_{\rm t}}}, \tag{3.66}$$

where $n_{\rm t} \simeq -2\epsilon_*$ is the tensor tilt and $A_{\rm t}$ the amplitude of the tensor power spectrum.

As can be seen from (3.65), the amplitude of the tensor power spectrum depends only on the the value of the Hubble parameter during inflation. Thus, a detection of primordial tensor modes allows us to directly probe the energy scale of inflation, within single field slow-roll (SFSR) models. SFSR models also predict a slightly red tilted spectrum $n_{\rm t} < 0$ with the tensor tilt related to the tensor-scalar ratio,

$$\boxed{r = \frac{A_{\rm t}}{A_{\rm s}} = 16\epsilon = -8n_{\rm t}.} \tag{3.67}$$

This is known as the *tensor consistency* relation of SFSR inflation.[4]

The tensor-scalar ratio can also be related to the field excursion during inflation [101],

$$\frac{\Delta\phi}{M_{\rm Pl}} = \mathcal{O}(1)\sqrt{\frac{r}{0.01}}. \tag{3.68}$$

Here, $\Delta\phi$ is the difference in field values between the time the CMB scales exited the horizon and the end of inflation. The above relation, known as the *Lyth bound*, tells us that $r \gtrsim 0.01$ requires the inflaton field to traverse super-Planckian distances during inflation. Obtaining such large field excursions is known to be quite challenging in theories of quantum gravity [46].

[4] Models of inflation which are single field, but with non-canonical kinetic terms, non-minimal couplings to gravity and more generally, the EFT of single-field inflation, may not necessarily obey this one-to-one relation, see [58] for a review.

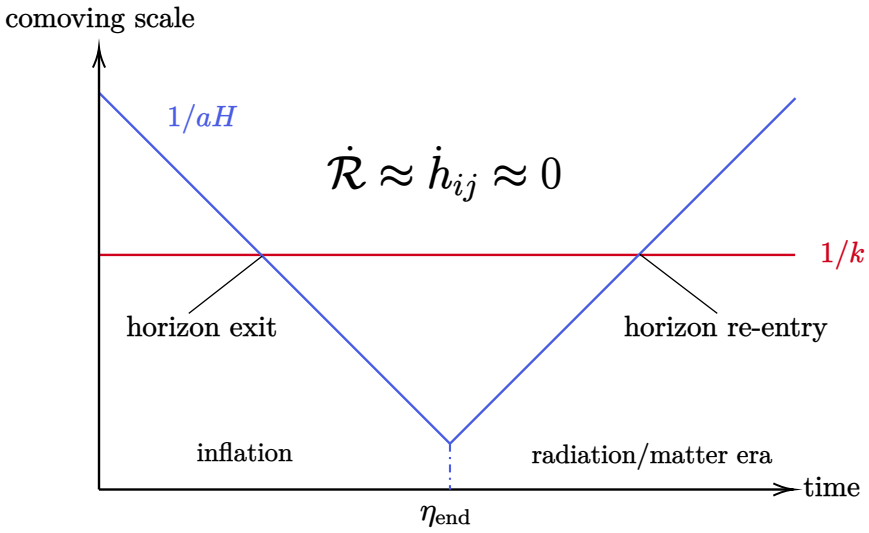

Figure 3.1: Generation of perturbations during inflation, their super-horizon conservation and subsequent horizon re-entry during the radiation and matter dominated eras.

3.3 From Inflation to Observations

During inflation all modes are stretched to super-Hubble scales and the constancy of $\mathcal{R}$ allows us to relate the curvature perturbation generated during inflation to the large scale density fluctuations observed today. Essentially, $\mathcal{R}_{\mathbf{k}}$ (and also $h_{\boldsymbol{k}}$) remains constant after the mode k becomes super-Hubble during inflation. After inflation ends, the universe reheats into a radiation dominated phase and the comoving Hubble radius $(aH)^{-1}$ starts increasing. Eventually the mode 're-enters' the horizon ($k = aH$) during radiation or matter domination as illustrated in Figure 3.1. This sets the initial conditions for the perturbations of the matter and radiation components that constitute the universe.

Observed quantities such as the CMB anisotropies or the inhomogeneities in the distribution of large scale structure can be written in terms of the primordial perturbation as

$$O_{\boldsymbol{k}}(\eta) = T_k(\eta)\mathcal{R}_k^{\rm prim}. \tag{3.69}$$

Here T_k denotes the transfer function that accounts for the post-inflationary evolution of the perturbations.

In what follows I briefly describe the CMB anisotropies and discuss how their observations provide us the strongest evidence for inflation. An exhaustive treatment of CMB anisotropies can be found in the textbook by Durrer [102].

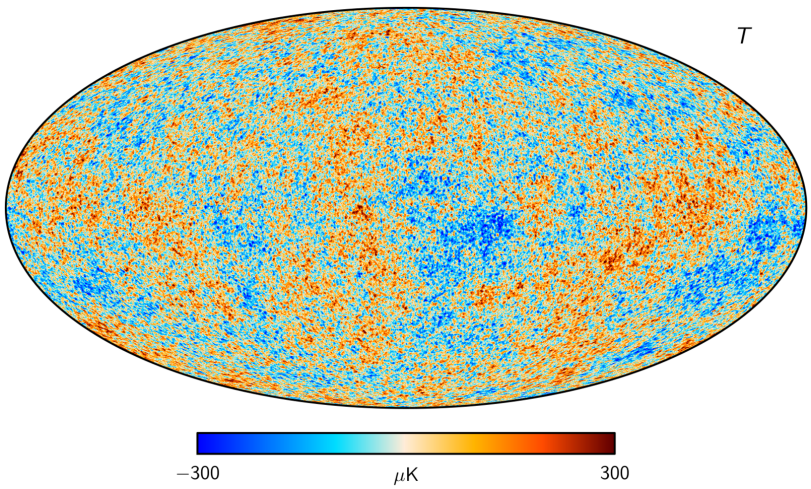

Figure 3.2: Map of temperature anisotropies from *Planck* [103].

3.3.1 CMB anisotropies

In Figure 3.2, we show a map of the CMB temperature anisotropies as observed the *Planck* [103]. The CMB temperature is seen to be nearly uniform across the sky with small fluctuations having a typical magnitude $\Delta T/T \sim 10^{-5}$. This temperature anisotropy, being a function of the sky direction $\hat{n}$, can be expanded in spherical harmonics as,

$$\Theta(\hat{n}) \equiv \frac{\Delta T}{T}(\hat{n}) = \sum_{\ell m} a_{\ell m} Y_{\ell m}(\hat{n}). \tag{3.70}$$

The $a_{\ell m}$ are the multipole moments

$$a_{\ell m} = \int d^2\hat{n}\, Y^*_{\ell m}(\hat{n})\Theta(\hat{n}), \tag{3.71}$$

and can be combined into the rotationally invariant angular power spectra

$$C_\ell = \frac{1}{2\ell+1}\sum_m \langle a_{\ell m} a^*_{\ell m}\rangle, \quad \text{or} \quad \langle a_{\ell m} a^*_{\ell' m'}\rangle = \delta_{\ell\ell'}\delta_{mm'}C_\ell, \tag{3.72}$$

assuming statistical isotropy of the background. The angular power spectrum is an extremely useful quantity as it allows us to compress the millions of pixels carrying information about the temperature anisotropies into a much smaller set of numbers. For Gaussian random fields, this compression is completely *loss-less* since the power spectrum contains all the information about the statistical properties of the fields [104]. Furthermore, since inflation predicts only the statistical properties of the primordial perturbations and not the actual values of the perturbations themselves, the angular power spectrum is the ideal quantity to work with. The $a_{\ell m}$ and C_ℓ can be written

in terms of $\mathcal{R}$[5] as

$$\frac{a_{\ell m}}{4\pi(-i)^\ell} = \int \frac{d^3k}{(2\pi)^3}\, \Delta_\ell^T(k)\mathcal{R}_{\boldsymbol{k}} Y_{\ell m}(\hat{\boldsymbol{k}}), \quad C_\ell = \frac{2}{\pi^2}\int k^2 dk\, \mathcal{P}_\mathcal{R}(k)(\Delta_\ell^T)^2(k). \tag{3.73}$$

The harmonic transfer function Δ_ℓ^T accounts for several different effects – namely the gravitational redshift, coupled oscillations of the photon-baryon fluid and diffusion damping effects on small angular scales. The formalism for CMB polarisation is more mathematically involved, since polarisation is described by a spin-2 field on the sphere rather than a scalar function and the corresponding transfer functions are more complicated. The analytic expressions for the transfer functions can be found in [105–108]. Typically, these are calculated numerically using Boltzmann codes such as `CLASS` [109, 110] or `CAMB` [111].

The primordial fluctuations that source the CMB anisotropies are observed to be nearly scale invariant with a slight red tilt, Gaussian and adiabatic. The CMB fluctuations are correlated on scales much larger than the causal horizon at recombination and were generated with coherent phases[6], as evidenced by the acoustic peaks in the angular power spectrum of the CMB anisotropies. *All of these observations* are elegantly predicted by the simplest models of inflation. The primordial power spectrum amplitude and the tilt have been inferred to be [15],

$$\boxed{\ln\left(10^{10}A_\mathrm{s}\right) = 3.044 \pm 0.014, \quad n_\mathrm{s} = 0.9649 \pm 0.0042}\,, \tag{3.74}$$

assuming the base ΛCDM model with no evidence for the running (scale dependence) of the spectral index. The results quoted above are at 68% CL and obtained from the *Planck* TT,TE,EE+lowE+lensing datasets [15].

B-mode polarisation

The linear polarisation of the CMB can be specified in terms of two fields E and B, which represent the '*gradient*' and '*curl*' modes of the polarisation field (Figure 3.3). While tensors generate both E and B-modes [107, 108], scalar perturbations *cannot* generate B-mode polarisation at linear order [113]. This implies that the detection of

[5] One can also write similar expression for the temperature anisotropies from tensors. This contribution is much smaller than the one from scalars (since $r \ll 1$) and we shall study it further in chapter 6.

[6] In other words, SFSR inflation excites the cosine mode of perturbations, i.e. the perturbations start off as $\dot{\mathcal{R}}_k = 0$ on super-horizon scales and interfere coherently at recombination, producing the characteristic peaks and troughs in the $\langle TT\rangle$, $\langle EE\rangle$ and $\langle TE\rangle$ spectra [112].

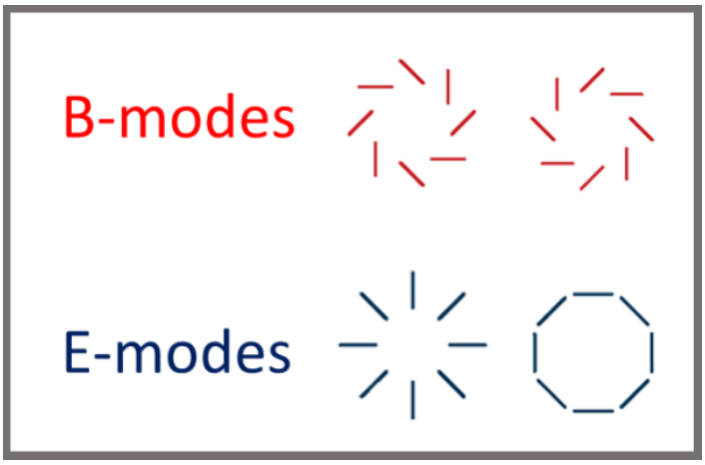

Figure 3.3: For a given point on the sky, B-modes appear to 'curl' around that point whereas E-modes lie either parallel or perpendicular to the radial direction. Image credit: APS/Michael Schirber.

a *primordial* B-mode polarisation would provide proof of the existence of inflationary tensor perturbations, and give us access to the energy scale of inflation B-mode polarisation has not been detected so far and measurements from the CMB temperature and polarisation have been able to place an upper bound on r, obtaining [35, 114]

$$r_{0.002} < 0.032, \ (95\% \text{ C.L.}) \tag{3.75}$$

assuming the tensor consistency relation holds. The next generation of CMB experiments such as the BICEP Array [42], Simons Observatory [43], LiteBIRD [45] and CMB-S4 [115] will be sensitive to values of $r \gtrsim 0.001$, allowing for either a detection or further constraints on inflationary models. So far, the non-detection of r, along with the constraints on n_s has already ruled several inflationary models, as depicted in the inflationary 'zoo' plot in figure Figure 3.4. The Starobinsky (R^2) model of inflation [37, 38], is currently in excellent agreement with the data and intriguingly, its prediction of $r \gtrsim 0.002$ will be within the reach of LiteBIRD and CMB-S4. Other models of inflation such as the ones with monomial potentials ϕ^p [27], and natural inflation [40] are strongly disfavoured by the data.

Deviations from the tensor consistency relation can also occur when one goes beyond the slow roll scenarios or considers models with multiple fields, alternative symmetry breaking patterns (see ref. [58, 59] for a review). Future CMB experiments will also be able to test for these deviations from SFSR scenarios and an example of this is studied in Chapter 6.

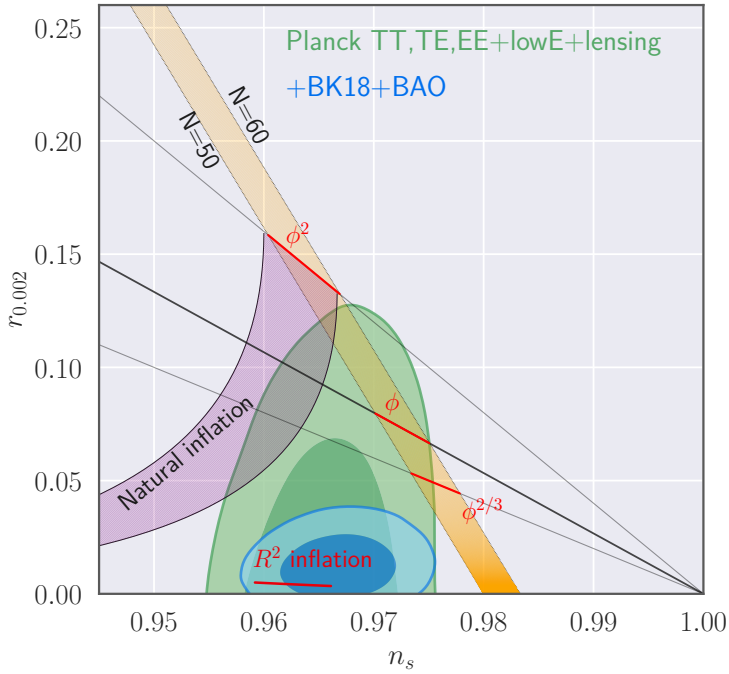

Figure 3.4: Predictions of selected inflationary models assuming between 50-60 e-folds vs 68% and 95% contours from *Planck*, BAO and BICEP in the $n_s - r$ plane. The data for the figure is obtained from [35, 41].

3.3.2 GW at interferometer scales

The present day spectral energy density of gravitational waves, denoted by $\Omega_{\rm GW}$, is typically used to describe the sensitivities of interferometer experiments. This quantity is defined as [116],

$$\boxed{\Omega_{\rm GW}(k,\eta)_0) \equiv \frac{1}{\rho_{\rm cr}}\frac{d\rho_{\rm GW}}{d\ln k} = \frac{\mathcal{P}_T(k)}{12H_0^2}\left[T'(k,\eta_0)\right]^2}\,, \tag{3.76}$$

where $\rho_{\rm cr}$ is the critical energy density (2.35). The transfer function $T(k,\eta)$ accounts for the time evolution of the primordial tensor perturbation [117], i.e.

$$h_k(\eta) = T(k,\eta)\, h_k^{\rm prim}. \tag{3.77}$$

Taking into account the current constraints on r and extrapolating the SFSR tensor spectrum to interferometer scales, we see that the GW amplitude is going to be too small to be detectable in future experiments, with the possible exception of the proposed Big Bang Observer (BBO) [118] (fig. 3.5). On the other hand, several models of inflation beyond the SFSR paradigm do predict sizeable GW signals at small scales, which may be observable with next generation experiments (see Figure 3.5). Possible scenarios include the following:

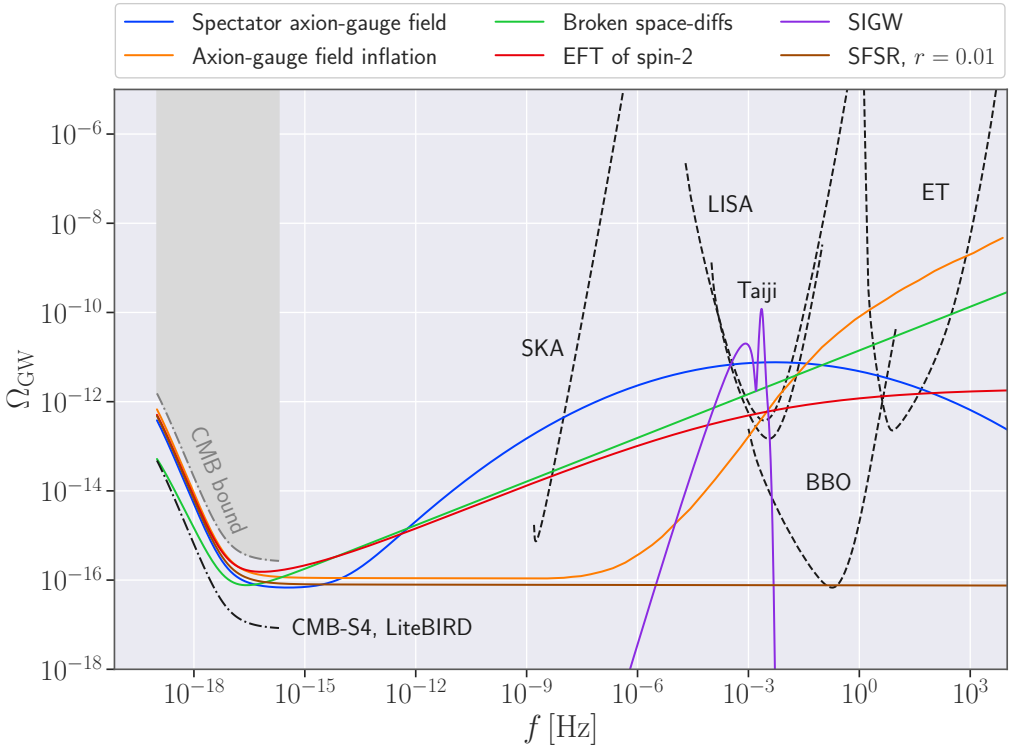

Figure 3.5: GW from inflation — the future observational landscape.

- Gravitational waves sourced by additional fields [119–134] (e.g. axion gauge fields [125, 126] or an additional spin-2 field [127–129]), or due to enhanced second order curvature perturbations on small scales [135–138].

$$h_{ij}'' + 2\mathcal{H}h_{ij}' + k^2 h_{ij} = 16\pi G a^2 \Pi_{ij}^{TT} \tag{3.78}$$

Here, Π_{ij}^{TT} is the transverse-traceless part of the anisotropic stress. GW in the latter scenario are sometimes called scalar-induced GW (SIGW) and may be accompanied by primordial black hole formation, due to the enhancement of the small scale curvature perturbation [63, 64].

- Inflationary models with alternative symmetry breaking patterns[7] can lead to a non-zero mass for the tensor modes and consequently a blue tilted tensor spectrum [140–147],

$$\mathcal{P}_t(k) = A_{\rm t}\left(\frac{k}{k_p}\right)^{n_{\rm t}}, \quad n_{\rm t} \approx \frac{2}{3}\frac{m_h^2}{H^2}. \tag{3.79}$$

The tensor mass in such cases is related to the (small) symmetry breaking parameters of the theory.

[7] In contrast, standard single field inflation can be thought of as a theory of weakly broken time translations, with the small symmetry breaking parameter ϵ [139].

- A non-slow roll phase to enhance the would-be decaying mode [148, 149],

$$\ddot{h}_{ij} + 3f(t)H\dot{h}_{ij} + \frac{k^2}{a^2}h_{ij} = 0. \tag{3.80}$$

Inteferometeric observations will also open up the possibility to map the SGWB intensity across the sky, much like the CMB and its anisotropies. The physics of SGWB anisotropies and their detection prospects are studied in Chapters 4 and 5.

3.4 Primordial non-Gaussianity

Non-Gaussianities, i.e., correlations beyond the 2-point function encode the interactions of the inflaton and allow us to probe the inflationary action beyond the free field limit [150–158]. The additional information provided by non-Gaussianity can also help to distinguish inflationary models from each other, beyond what can be done using the power spectra alone.

The primary diagnostic of non-Gaussianity is the bispectrum[8] $B_{\mathcal{R}}$, defined as the 3-point function in Fourier space [62],

$$\boxed{\langle \mathcal{R}_{\boldsymbol{k}_1}\mathcal{R}_{\boldsymbol{k}_2}\mathcal{R}_{\boldsymbol{k}_3}\rangle = (2\pi)^3\delta(\boldsymbol{k}_1+\boldsymbol{k}_2+\boldsymbol{k}_3)B_{\mathcal{R}}(\boldsymbol{k}_1,\boldsymbol{k}_2,\boldsymbol{k}_3)} \tag{3.81}$$

The delta function enforces momentum conservation and arises due to the translation invariance of the background. Rotational invariance of the background further implies that the bispectrum is independent of the orientation of the triangle formed by the $\boldsymbol{k}_i$.

3.4.1 Amplitude and shapes of non-Gaussianity

For scale-invariant perturbations[9], it is customary to write the the bispectrum in the following manner,

$$B_{\mathcal{R}}(k_1,k_2,k_3) = \frac{18}{5}f_{\rm NL}\frac{S(x_2,x_3)}{(k_1k_2k_3)^2}\mathcal{P}_{\mathcal{R}}^2. \tag{3.82}$$

[8] At next order in the perturbations lies the trispectrum [159–165], which refers to the 4-point function in Fourier space.

[9] Although we only focus on scale invariant examples here, the running of the bispectrum i.e. its dependence on $K = k_1 + k_2 + k_3$ can also be important [62].

The amplitude of non-Gaussianity $f_{\rm NL}$ is defined as,

$$f_{\rm NL}(k) \equiv \frac{5}{18}\frac{B_{\mathcal{R}}(k,k,k)}{\mathcal{P}_{\mathcal{R}}^2}. \tag{3.83}$$

On the other hand, the shape S of the bispectrum describes its dependence on the momentum ratios $x_2 = k_2/k_1$ and $x_3 = k_3/k_1$ and is normalised as $S(1,1) = 1$. Some of the typical shapes of the bispectrum generated during inflation are described below:

Local shape

This shape gets its name from a local parametrisation of non-Gaussianity in real space,

$$\zeta(x) = \zeta_g(\boldsymbol{x}) + \frac{3}{5}f_{\rm NL}\left[\zeta_g(\boldsymbol{x})^2 - \langle\zeta_g^2\rangle\right], \tag{3.84}$$

with ζ_g a Gaussian field. In Fourier space, the local bispectrum reads,

$$B_{\mathcal{R}}(\boldsymbol{k}_1,\boldsymbol{k}_2,\boldsymbol{k}_3) = \frac{6}{5}f_{\rm NL}\frac{A_{\mathcal{R}}^2}{(k_1k_2k_3)^3}\left(\frac{k_1^2}{k_2k_3} + 2 \text{ perms.}\right). \tag{3.85}$$

The shape function in this case is

$$S_{\rm loc} = \frac{1}{3}\left(\frac{k_1^2}{k_2k_3} + 2 \text{ perms.}\right). \tag{3.86}$$

Let us order the momenta as $k_1 \leq k_2 \leq k_3$, without loss of generality. We now see that the local shape is peaked for *squeezed* triangles with $k_1 \ll k_2 \sim k_3$.

Equilateral shape

The equilateral shape bispectrum is peaked for equilateral triangles $k_1 = k_2 = k_3$ and can be described by the following template

$$S_{\rm eq} = \left(\frac{k_1}{k_2} + 5 \text{ perms.}\right) - \left(\frac{k_1^2}{k_2k_3} + 2 \text{ perms.}\right) - 2. \tag{3.87}$$

This type of non-Gaussianity is typically generated by higher derivative interactions which are suppressed when any of the modes are outside the horizon, but are sizeable when all the modes are the size of the horizon scale.

Orthogonal shape

The orthogonal shape is defined phenomenologically as a shape that has minimal overlap with the local and equilateral shapes,

$$S_{\rm ortho} = -3.84\left(\frac{k_1^2}{k_2 k_3} + 2 \text{ perms.}\right) + 3.94\left(\frac{k_1}{k_2} + 5 \text{ perms.}\right) - 11.10. \tag{3.88}$$

The overlap is checked by computing the cosine $\mathcal{C}(S_1, S_2)$ between two different shapes S_1 and S_2 through,

$$\mathcal{C}(S_1, S_2) = \frac{S_1 \cdot S_2}{\sqrt{(S_1 \cdot S_1)\,(S_2 \cdot S_2)}}, \quad S_1 \cdot S_2 = \int S_1(x_2, x_3) S_2(x_2, x_3) dx_2 dx_3. \tag{3.89}$$

Here we defined $x_2 = k_2/k_1$ and $x_3 = k_3/k_1$.

In general, the level of non-Gaussianity within vanilla SFSR inflation,[10] whether in the local or equilateral shape, is expected to be quite small with $f_{\rm NL} < 1$ [150–153]. On the other hand, single field models beyond the vanilla scenario, models with multiple fields or models with alternative symmetry breaking patterns provide a way to generate larger levels of non-Gaussianity, see e.g. [140–146, 156–158, 166–182]. The subject of non-Gaussianity from inflationary models is reviewed in further detail in [61, 62].

3.4.2 In-In formalism

Let us now review how to calculate the bispectrum and other higher order correlation functions in an inflationary background using the *in-in* formalism [183–189], which is an application of quantum field theory to time dependent backgrounds.

Our goal is to calculate the expectation value of a general operator $Q = \delta\phi_1 \delta\phi_2 \ldots$, which may be a product of several different field perturbations, at a *given time* t, usually taken to be the end of inflation,

$$\langle Q(t) \rangle \equiv \langle \Omega | Q(t) | \Omega \rangle. \tag{3.90}$$

Here Ω denotes the vacuum of the interacting theory at some point t_i in the far past. This is in contrast to the standard *in-out* formalism of particle physics used to calculate transition amplitudes for a given state in the far past to evolve to a

[10] This refers to simplest class of SFSR models with the inflaton field minimally coupled to gravity, having canonical kinetic terms and starting from Bunch-Davies initial conditions.

different state in the far future. However, in cosmological space-times one cannot define asymptotic free states in the far future since gravitational interactions will always be present, even if all other interactions are switched off.

The *in-in* computation strategy can be summarised as follows. We split our Hamiltonian into a classical background, a quadratic kinematic part H_0 and interactions $H_{\rm int}$. Working in the interaction picture, we evolve the fields $Q(t)$ back to t_i, using the quadratic Hamiltonian H_0 and then treat the interactions as a perturbative series in $H_{\rm int}$.

At the end (see Appendix A for the full derivation), we arrive at the following result

$$\boxed{\langle Q(t)\rangle = \langle 0|\bar{T}e^{i\int_{-\infty-}^{t} H_{\rm int}(t')dt'}Q(t)Te^{i\int_{-\infty+}^{t} H_{\rm int}(t')dt'}|0\rangle}, \tag{3.91}$$

where $\bar{T}$ represents anti time-ordering and the $-\infty^{\pm} = -\infty(1 \mp i\epsilon)$. Here, both Q and $H_{\rm int}$ are evaluated in terms of the *interaction picture fields*. The tree level effects of the interaction are encapsulated in the expansion of the above expression to first order in $H_{\rm int}$, giving us

$$\langle Q(t)\rangle_{\rm tree} = -i\int_{-\infty}^{t} dt'\langle 0|[Q(t), H_{\rm int}(t')]|0\rangle. \tag{3.92}$$

Using this formalism, one may then calculate the non-Gaussianity associated with a given model of inflation.

3.4.3 Single field consistency relation

For SFSR inflation with canonical kinetic terms and Bunch-Davies initial conditions, Maldacena used the *in-in* formalism to show that the the 3-point function in the squeezed limit takes the following form [151],

$$\boxed{\lim_{k_1\ll k_2,k_3}\langle \mathcal{R}_{\boldsymbol{k}_1}\mathcal{R}_{\boldsymbol{k}_2}\mathcal{R}_{\boldsymbol{k}_3}\rangle = (2\pi)^3\delta^3(\boldsymbol{k_1}+\boldsymbol{k_2}+\boldsymbol{k_3})(1-n_{\rm s})P_\zeta(k_1)P_\zeta(k_3)}\,. \tag{3.93}$$

Here, $n_{\rm s}$ is the scalar spectral index. This result has been shown to be valid for *all* single-field models [190–192] and is known as the *consistency relation* of single field inflation.[11] In general, the consistency relations of single-field inflation relate the soft limits ($k \to 0$ for one of the momenta) of N point correlation functions to symmetry transformations of $N-1$ point correlation functions of the hard-momentum

[11] Not to be confused with the tensor consistency relation of eq. (3.67).

modes [160–162, 193–200]. Similar relations also apply to the case of multiple soft limits.

The consistency relation eq. (3.93) corresponds to the fact that when the inflaton is the only dynamical field, the effect of a long wavelength mode can simply be reabsorbed into a rescaling of the coordinates. Since de-Sitter correlation functions are scale invariant due to the scale invariance of the background, this contribution is non-zero only to the extent of the deviation of the background from a pure de-Sitter geometry, quantified by $(1 - n_s)$. In addition, it has been shown the consistency relation part of the squeezed bispectrum is not observable. It is a *gauge artifact* and the physical effects of the squeezed bispectrum in cosmological observables are highly suppressed, appearing at $\mathcal{O}(k_1^2/k_3^2)$ [201–206].[12]

Thus, a detection of large non-Gaussianity in the squeezed limit would be highly suggestive of a multi-field realisation of inflation. Observably large squeezed limit non-Gaussianity may typically be generated if the consistency relations are violated, which is possible in models with additional fields [127, 171, 208–213], non-Bunch Davies initial states [178, 214–219] and alternative symmetry breaking patterns [140–145], to name a few.[13]

3.4.4 Cosmological collider physics

Additional fields during inflation can leave distinctive signatures in the squeezed limit non-Gaussianity, allowing us to probe their mass, spin and interactions during inflation [208, 227–234]. For this reason inflation has sometimes been referred to as a *cosmological collider* and the corresponding primordial non-Gaussianity as a particle detector. As an example, the contribution to the curvature bispectrum from an additional field σ (Figure 3.6) has the following characteristics [229, 233]:

- Angular dependence arising from the spin s of σ

$$\lim_{k_1 \ll k_2 \sim k_3} \langle \mathcal{R}_{\boldsymbol{k}_1} \mathcal{R}_{\boldsymbol{k}_2} \mathcal{R}_{\boldsymbol{k}_3} \rangle \propto P_s(\hat{\boldsymbol{k}}_1 \cdot \hat{\boldsymbol{k}}_2), \tag{3.94}$$

  where P_s denotes the Legendre polynomial of degree s.

[12] However, see ref. [207] for a different take on this matter.

[13] A non-attractor period in single-field inflation may lead to a violation of Maldacena's consistency relation [220–225], but the size of observable squeezed limit non-Gaussianity is still expected to be extremely small [226].

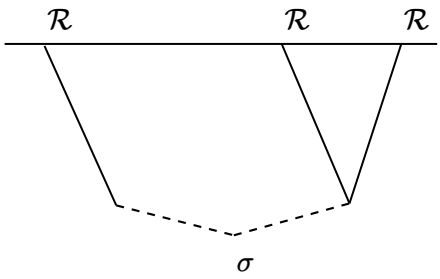

Figure 3.6: Cosmological collider example — inflationary correlation functions arising from the exchange of an additional field σ.

- A non-analytic scaling and oscillatory behaviour in the squeezed limit

$$\lim_{k_1 \ll k_2 \sim k_3} \langle \mathcal{R}_{\boldsymbol{k}_1} \mathcal{R}_{\boldsymbol{k}_2} \mathcal{R}_{\boldsymbol{k}_3} \rangle \propto \frac{1}{k_1^3 k_2^3} \left(\frac{k_1}{k_2} \right)^{3/2} \cos \left[\frac{m_\sigma}{H} \ln \left(\frac{k_1}{k_2} \right) + \alpha \right], \tag{3.95}$$

  for $m_\sigma^2/H^2 > (s - 1/2)^2$ and with α a phase factor.

Thus, we see that the squeezed bispectrum carries information about the masses and spins of additional fields during inflation. We will revisit the subject of non-Gaussianity in Chapter 5 where we shall study the ability of GW interferometers to probe primordial tensor non-Gaussianity and observe certain cosmological collider signatures.

Currently, primordial non-Gaussianity remains undetected with the most stringent bounds on scalar non-Gaussianity coming from the *Planck* 2018 data. The obtained constraints are $f_{\rm NL}^{\rm local} = -0.9 \pm 5.1$, $f_{\rm NL}^{\rm equil} = -26 \pm 47$, and $f_{\rm NL}^{\rm ortho} = 38 \pm 24$ at 68% CL [235]. Reaching experimental thresholds where the single field nature of inflation can actually be tested ($\sigma_{f_{\rm NL}} \sim 1$) is an important target for future CMB and LSS probes [236].

Part II

Original work

Chapter 4

Gravitational wave anisotropies: theory and applications

This chapter presents the results of the following articles:

- E. Dimastrogiovanni, M. Fasiello, **A. Malhotra** and G. Tasinato, *"Enhancing gravitational wave anisotropies with peaked scalar sources,"*, JCAP **01** (2023), 018, [arXiv: 2205.05644] (appears as [4]).
- **A. Malhotra**, E. Dimastrogiovanni, G. Domènech, M. Fasiello and G. Tasinato, *"A new universal property of cosmological gravitational wave anisotropies,"* [arXiv: 2212.10316] (appears as [5]).

4.1 Introduction

The detection of stochastic gravitational wave backgrounds (SGWB) has long been an important goal for gravitational wave astronomy. Several PTA collaborations have recently reported strong evidence for a stochastic gravitational wave background, representing a major triumph for the field [68–71]. Although the inferred properties of the signal appear to be compatible with an astrophysical background arising from a large number of supermassive black hole binaries in their inspiral phase, a possible cosmological origin cannot yet be discounted [72, 73]. Cosmological backgrounds may be produced during high-energy processes in the early universe — inflation, phase tran-

sitions, cosmic strings and primordial black holes, to name a few (see [59] for a review of possible mechanisms). The discovery potential of such cosmological backgrounds is immense, especially in light of the fact that the universe is transparent to gravitational waves below the Planck scale, meaning that the detection of these backgrounds may provide us a pristine snapshot of the early universe. Future experiments such as ET [66], CE [67] (1–10^3 Hz) and space-based experiments including LISA [65], Taiji [237] (10^{-4}–10^{-1} Hz), are also well poised to observe such cosmological backgrounds and are all expected to begin operations around 2035.

The possibility of detection with interferometers as well as PTAs provides us with an opportunity to the measure the direction dependence of the SGWB [238–252]. In general cosmological backgrounds are expected to be predominantly isotropic with a small level of anisotropies ($\sim 10^{-4}$ relative to the monopole) arising from the fact that GW propagate in a perturbed universe [253–256]. The specific SGWB production mechanism can also imprint an anisotropic component which can be much larger depending on the model under consideration. Thus, these anisotropies carry precious information about the primordial perturbations, complementary to the CMB anisotropies, and also the SGWB production mechanism.

Astrophysical backgrounds are also expected to be anisotropic, with the anisotropies reflecting the inhomogeneous distribution of large scale structure [257–274]. As a result they are strongly correlated with observables such as galaxy clustering, weak lensing etc. [258, 259, 266, 269, 270, 274]. Techniques to separate the monopoles of astrophysical and cosmological SGWB, based on their different frequency/time dependence, have been proposed in [275–284]. Developing a comprehensive understanding of the different properties of cosmological and astrophysical background anisotropies w.r.t their frequency and multipole dependence, and cross-correlations with CMB/LSS, will be essential to also separating the different anisotropic components in the SGWB map. Component separation techniques, which have proved to be successful in the CMB case [103], may then be applied to the SGWB too, as shown recently in [285].

Recent works have studied the anisotropies of cosmological backgrounds and their effectiveness in probing the early universe, focusing on phase transitions [286, 287, 287–290], non-Gaussianity [1, 2, 291–296], cosmic strings [297–300], preheating [301, 302], $\Delta N_{\rm eff}$ [303], and various other pre-recombination scenarios [304]. Their cross-

correlations with the CMB temperature and polarisation anisotropies have been investigated in [304–306] using numerical methods. A comprehensive review of these scenarios was also carried out in [246].

To analyse these anisotropies, we first need a theoretical framework. This is provided by the line-of-sight (los) formalism, which was recently applied to gravitational waves in [254–256]. This extremely powerful formalism allows for a description of the SGWB anisotropies in a manner similar to those of the CMB [75, 307], with the SGWB anisotropies also feeling the familiar Sachs-Wolfe (SW) and an integrated Sachs-Wolfe (ISW) effect. Another contribution arises from the model dependent initial condition term, which represents the SGWB density perturbation at the time of production.

This chapter focuses on the physics of these gravitational wave anisotropies, starting with a review of the los formalism in section 4.2. In the same section I then discuss some aspects of the GW initial conditions for the case of adiabatic primordial perturbations and draw a connection between the los results of [254–256] and the approach of [253], as first presented in [4, 5].

Section 4.3 is based entirely on [4]. Here, I study the anisotropies of cosmological SGWB induced via second order effects of the primordial curvature perturbation [135–138]. Even though scalar and tensor perturbations are decoupled from each other at linear order, at second order this is no longer true as the sub-horizon primordial scalar perturbations source gravitational waves through their anisotropic stress. Significant interest in such scalar induced gravitational waves (SIGW) stems from their strong connection to the physics of primordial black holes (PBH), which are a candidate for dark matter [308, 309]. The formation of PBH typically involves the enhancement of the scalar perturbation on small scales [64], inevitably accompanied by SIGW which may peak at frequencies relevant for LISA or ET, depending on the PBH mass. Through the representative example of a log-normal, we demonstrate how a sharply peaked curvature power spectrum imparts a distinctive frequency dependence to the SIGW and its anisotropies. We then discuss the implications of the frequency dependence for the anisotropy detection.

Section 4.4 presents the results of [5] where we go back to the topic of GW initial conditions for both adiabatic and isocurvature primordial perturbations. In the adiabatic case we prove that the GW anisotropies are completely insensitive to the

equation of state (eos) of the universe before BBN, leading to a completely universal result for the anisotropies of *all* early universe SGWB. Indeed, there exist several well-motivated early universe scenarios which lead to a departure from the standard radiation dominated (RD) universe (ref. [310] provides a review of such scenarios). In brief, the possibilities include a period of early matter domination due to the coherent oscillations of a scalar field [311], a period of kinetic energy domination ('kination') in quintessential inflation [312–316] or even a kination phase inside the RD epoch [317].

Our results demonstrate that for anisotropies sourced by adiabatic perturbations, the effects of a non-standard expansion history can only be observed at the level of the SGWB frequency spectrum [318–339]. Deviation from the above-mentioned universal result would then hint towards the presence of non-adiabatic sources of perturbations in the early universe.[1] We then provide an example of this through the curvaton mechanism [340–342] and derive the angular power spectrum of the SGWB anisotropies for some representative curvaton scenarios, emphasising the differences w.r.t the adiabatic case.

4.2 Line of sight formalism – a review

Following [254–256], we adopt the Newtonian gauge as the starting point for the line-of-sight formalism,

$$ds^2 = a^2(\eta)\left[-(1+2\Phi)d\eta^2 + (1-2\Psi)d\boldsymbol{x}^2\right], \tag{4.1}$$

with $a(\eta)$ the scale factor in conformal time, and Φ, Ψ the gravitational potentials (same as the Bardeen potentials of eq. (3.42) in this gauge). We describe the SGWB by its distribution function $f(x^\mu, p^\mu)$, with x^μ the position and p^μ the GW momentum[2]. The total energy density of GW is given by an integral over the GW momenta,

$$\rho_{\rm GW} = \int d^3p\, p f(p). \tag{4.2}$$

As is customary, we work not with $\rho_{\rm GW}$ but with the GW spectral energy density

[1] A similar point was first raised in ref. [253].

[2] The geometric optics approach to GW propagation forms the backbone of the line-of-sight formalism. This approach allows us to study the propagation of short-wavelength GWs in a background that varies over length scales much larger than the GW wavelength [343–345].

parameter $\Omega_{\rm GW}(q)$, defined as [116]

$$\Omega_{\rm GW} = \frac{1}{\rho_{\rm cr}} \frac{d\rho_{\rm GW}}{d\ln q} \,, \tag{4.3}$$

where $q = |p|a$ is the comoving momentum of the gravitons and ρ_{cr} the critical energy density of the universe. GW are massless, thus they propagate along the null geodesics of the perturbed space-time. Let λ be the affine parameter along the geodesic, then the distribution function along the geodesic evolves according to the *Liouville* equation [254–256],

$$\frac{df}{d\lambda} = C[f(\lambda)] + I[f(\lambda)], \tag{4.4}$$

where C and I are the collision and injection terms. GW collisions can be safely neglected at energies below the Planck scale, owing to the weakness of the gravitational interaction. As for the injection term, this can be understood as the initial condition of the GW distribution, for SGWB of cosmological origin [255, 256].

Then, one can show that the distribution function obeys the following *Boltzmann*-type equation [254–256],

$$\frac{\partial f}{\partial \eta} + \frac{\partial f}{\partial x^i} n^i + q \frac{\partial f}{\partial q} \left[\frac{\partial \Psi}{\partial \eta} - \frac{\partial \Phi}{\partial x^i} n^i \right] = 0, \tag{4.5}$$

where we have kept terms up to first order in the scalar perturbations. The derivation closely follows the similar one performed for the CMB anisotropies e.g. see [75]. The contribution from large-scale tensors can also be calculated [255], but similarly to the CMB, this is smaller than the scalar one by roughly a factor $r \ll 1$.

We now split the distribution function into a homogeneous part and a perturbation Γ as follows,

$$f(\boldsymbol{q}, \boldsymbol{x}) \equiv \bar{f}(q) - \Gamma(\eta, \boldsymbol{x}, q, \hat{n}) \frac{d\bar{f}}{d\ln q} \,. \tag{4.6}$$

The homogeneous part obeys,

$$\frac{\partial \bar{f}}{\partial \eta} = 0, \tag{4.7}$$

and simply tells us that that the GW momentum redshifts as $|p| \propto 1/a$ and the number density $n \propto \int d^3p\, f(q)$ decays as $1/a^3$. This is completely consistent with what we already saw in section 2.3.1 for relativistic particles. The homogeneous part of the energy density can be related to the zeroth order distribution function as,

$$\overline{\Omega}_{\rm GW}(q) = \frac{4\pi}{\rho_{\rm cr}} \left(\frac{q}{a_0} \right)^4 \bar{f}(q). \tag{4.8}$$

One can introduce a spatial dependence to this quantity as,

$$\Omega_{\rm GW}(q,\boldsymbol{x}) \equiv \frac{1}{4\pi}\int d^2\hat{n}\,\omega_{\rm GW}(\hat{n},\boldsymbol{x},q)\,, \tag{4.9}$$

where

$$\omega_{\rm GW}(\hat{n},\boldsymbol{x},q) \equiv \frac{q^4}{a^4\rho_{\rm cr}} f(\hat{n},\boldsymbol{x},q)\,. \tag{4.10}$$

The SGWB anisotropy $\delta_{\rm GW}$ observed today is [255, 256],

$$\begin{aligned}\delta_{\rm GW} &\equiv \frac{\omega_{\rm GW}(\hat{n},\boldsymbol{x},q)-\overline{\Omega}_{\rm GW}(q)}{\overline{\Omega}_{\rm GW}(q)}\\ &= \left[4-\frac{\partial\ln\overline{\Omega}_{\rm GW}(q)}{\partial\ln q}\right]\Gamma(\eta_0,\hat{n},\boldsymbol{x},q)\\ &= [4-n_\Omega]\Gamma, \qquad n_\Omega = \frac{\partial\ln\overline{\Omega}_{\rm GW}(q)}{\partial\ln q}.\end{aligned} \tag{4.11}$$

Moving on to the perturbation Γ, we find in Fourier space a CMB-like equation[3],

$$\Gamma' + ik\mu\Gamma = \Psi' - ik\mu\Phi, \quad \mu \equiv \hat{k}\cdot\hat{n}, \tag{4.12}$$

with solution [255, 256],

$$\boxed{\begin{aligned}\Gamma(\eta_0,k,q,\hat{n}) = \int_{\eta_i}^{\eta_0} d\eta\,\{&\delta(\eta-\eta_i)[\Phi(k,\eta)+\Gamma_{\rm I}]\\ &+\Phi'(k,\eta)+\Psi'(k,\eta)\}\,e^{-ik\mu(\eta_0-\eta)}\,,\end{aligned}} \tag{4.13}$$

where η_0 denotes the conformal time at present and $\hat{n}\equiv\hat{p}$ is the direction of the GW momentum. The initial perturbation to the distribution is denoted by $\Gamma_{\rm I}\equiv\Gamma(\eta_i,k,q)$ and $\delta(\eta-\eta_i)$ represents the Dirac-delta in conformal time, with η_i the time when the GW are produced (or re-enter the horizon). For GW detectable at PTA or interferometer scales, this corresponds to an initial time deep within the epoch of radiation domination.

The quantity Γ can be expanded in spherical harmonics

$$\Gamma(\hat{n}) = \sum_{\ell m}\Gamma_{\ell m}Y_{\ell m}(\hat{n}). \tag{4.14}$$

The spherical harmonic coefficients $\Gamma_{\ell m}$ can be obtained by inverting eq. (4.14)

$$\Gamma_{\ell m} = 4\pi(-i)^\ell\int\frac{d^3\vec{k}}{(2\pi)^3}Y^*_{\ell m}(\hat{k})T^{\rm GW}_\ell(k), \tag{4.15}$$

[3] In the CMB case, the perturbation Γ would correspond to the fractional temperature perturbation, i.e. $\Gamma=\Delta T/T$ [75, 255].

where the function $T_\ell^{\rm GW}(k)$ combines the initial condition, the Sachs-Wolfe (SW), and the Integrated Sachs-Wolfe (ISW) terms [255, 256], completely analogous to the CMB case,

$$T_\ell^{\rm GW}(k) = \int_{\eta_i}^{\eta_0} d\eta \, \{\delta(\eta-\eta_i)[\Phi(k,\eta)+\Gamma_{\rm I}] + \Phi'(k,\eta)+\Psi'(k,\eta)\} \, j_\ell[k(\eta_0-\eta)] \, . \tag{4.16}$$

Here, j_ℓ is the spherical Bessel function which arises from the expansion of plane waves in terms of spherical waves using the identity,

$$e^{-i\boldsymbol{k}\cdot\boldsymbol{x}} = 4\pi \sum_\ell \sum_{m=-\ell}^{\ell} (-i)^\ell j_\ell(kx) Y_{\ell m}(\hat{k}) Y^*_{\ell m}(\hat{x}). \tag{4.17}$$

We can now calculate the correlators of Γ, defined as,

$$\langle \Gamma_{\ell m} \Gamma_{\ell' m'} \rangle \equiv C_\ell^\Gamma \delta_{\ell\ell'} \delta_{mm'} \, , \tag{4.18}$$

where we assumed the statistical isotropy of the background.

Appendix B.1 relates this line-of-sight derivation, performed in the Newtonian gauge, to the uniform density gauge calculation of [253].

4.2.1 Initial condition term

In general, the initial condition $\Gamma_{\rm I}$ is model-dependent. Its physical meaning can be understood as the perturbation to the GW distribution function at the time of emission which can be related to the initial GW density perturbation. In analogy with the CMB case [346], we write,

$$\begin{aligned} \rho_{\rm GW}(\boldsymbol{x}) &= \int d^3p \, p \bar{f}(q) \left[1 - \frac{\partial \ln \bar{f}}{\partial \ln q} \Gamma(\eta_i, \boldsymbol{x}, q, \hat{n})\right] \\ &= \frac{4\pi}{a^4} \int dq \, \bar{f}(q) q^3 - \frac{1}{a^4} \int dq \frac{\partial \bar{f}}{\partial q} q^4 \int d^2\hat{n} \, \Gamma_{\rm I}, \end{aligned} \tag{4.19}$$

Writing $\delta\rho_{\rm GW} \equiv \rho_{\rm GW} - \bar{\rho}_{\rm GW}$ and integrating by parts[4] on the R.H.S we find [4],

$$\begin{aligned} \bar{\rho}_{\rm GW} + \delta\rho_{\rm GW} &= \frac{4\pi}{a^4} \int dq \, \bar{f}(q) q^3 \left(1 + 4 \int \frac{d^2\hat{n}}{4\pi} \Gamma_{\rm I}\right) \\ \implies \frac{\delta\rho_{\rm GW}}{\bar{\rho}_{\rm GW}} &= 4 \int \frac{d^2\hat{n}}{4\pi} \Gamma_{\rm I} \equiv 4\Gamma_{\rm I}^{(0)}. \end{aligned} \tag{4.20}$$

[4] Note that here we have assumed that $\Gamma_{\rm I}$ is q-independent, just like the CMB. For the scenarios we shall consider in this chapter, this assumption will indeed hold true. However, there do exist scenarios where this q-dependence can be present with the specific form of the dependence related to the SGWB production mechanism (see [255, 256] for an example).

where $4\Gamma_{\rm I}^{(0)}$ denotes the monopole of $\Gamma_{\rm I}$ and is the GW counterpart of the CMB quantity Θ_0, which describes the monopole of the temperature fluctuation at recombination [75]. Since the large scale perturbations that will source $\Gamma_{\rm I}$ are super-Hubble at the initial time, higher order multipoles can safely be neglected and we shall identify $\Gamma_{\rm I}^{(0)} \equiv \Gamma_{\rm I}$. For instance, the velocity perturbation is $v_i \propto (k/\mathcal{H})\Phi$, thus is negligible on superhorizon scales.

4.2.2 Adiabatic initial conditions

We now calculate $\Gamma_{\rm I}$ for adiabatic initial conditions,[5] set during the radiation dominated epoch. Using the fact that the radiation density contrast during this epoch is given by [346] (we have neglected the anisotropic stress and set $\Phi = \Psi$),

$$\frac{\delta\rho_r}{\bar{\rho}_r} = -2\Phi, \tag{4.21}$$

and by the condition of adiabaticity we find [4]

$$\frac{\delta\rho_{\rm GW}}{\bar{\rho}_{\rm GW}} = \frac{\delta\rho_r}{\bar{\rho}_r} = -2\Phi \implies \Gamma_{\rm I} = \frac{1}{4}\frac{\delta\rho_{\rm GW}}{\bar{\rho}_{\rm GW}} = -\frac{1}{2}\Phi. \tag{4.22}$$

All quantities are understood to be evaluated at the initial time η_i. More generally, in case the initial time corresponds to an epoch where the dominant component ρ has an equation of state w, we obtain [5]

$$\boxed{\frac{\delta\rho_{\rm GW}}{(1+w_{\rm GW})\rho_{\rm GW}} = \frac{\delta\rho}{\rho(1+w)} \implies \frac{\delta\rho_{\rm GW}}{\rho_{\rm GW}} = -\frac{8\Phi}{3(1+w)}}. \tag{4.23}$$

Here, we used $\delta\rho/\rho = -2\Phi$ and $w_{\rm GW} = 1/3$. An alternative derivation of these results is also presented in appendix B.2.

Collecting together the results of the previous section, the quantity $T_\ell^{\rm GW}$ defined in eq. (4.16) for adiabatic initial conditions is,

$$\boxed{T_\ell^{\rm GW}(k) = \underbrace{\frac{1}{2}\Phi(k,\eta_i) j_\ell[k(\eta_0-\eta_i)]}_{\rm SW} + \underbrace{\int_{\eta_i}^{\eta_0} d\eta\ \left(\Phi'(k,\eta)+\Psi'(k,\eta)\right)\ j_\ell[k(\eta_0-\eta)]}_{\rm ISW}}, \tag{4.24}$$

with the initial time η_i taken to be during radiation domination ($w = 1/3$). Note that in this case we have combined the SW and initial condition term since they are completely correlated.

[5] Adiabatic initial conditions may arise if the GW are sourced by a field which is also responsible for generating the primordial curvature perturbation. As an example, if GW are sourced directly by the dynamics of the inflaton and if the inflaton then reheats the universe, the GW initial conditions would be adiabatic.

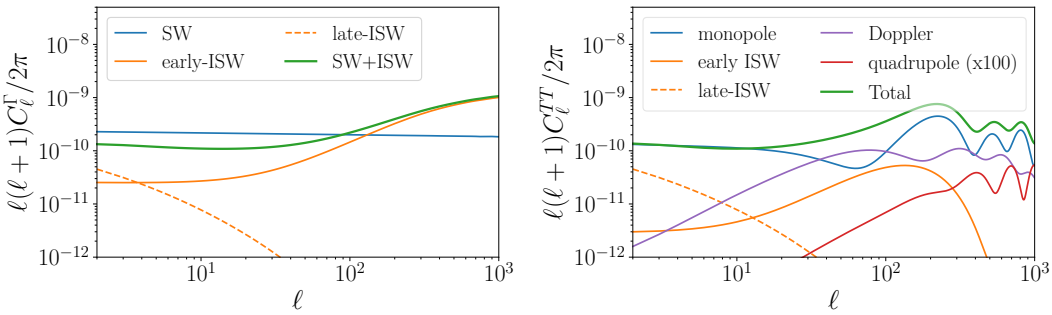

Figure 4.1: GW anisotropies and a comparison with the CMB temperature anisotropies. The relative contributions of the different terms are also shown. The anisotropies are calculated using `CAMB` [111], assuming the best-fit values for the ΛCDM cosmological parameters [15].

In fig. 4.1 we plot the GW anisotropies for adiabatic initial conditions. The fact that the initial time η_i for GW is well before recombination results in striking differences with the CMB. The large-scale modes of interest are all super-Hubble at the initial time leading to negligible Doppler and quadrupolar anisotropies (not shown in the figure). There are no acoustic peaks and the ISW effect is also larger in the GW case, especially at higher-ℓ due to the much earlier initial time [303, 306]. The early-ISW makes the difference here, whereas the late-ISW, which arises from the decay of the potentials in a Λ-dominated universe, is the same for both GW and CMB anisotropies.

These GW anisotropies are also correlated with those of the CMB, both being sourced by the primordial scalar perturbations. The resulting cross-correlation is defined as,

$$\langle \Gamma_{\ell m} \Delta^{\mathrm{T(E)}}_{\ell' m'} \rangle \equiv C_\ell^{\Gamma\,\mathrm{T(E)}} \delta_{\ell\ell'} \delta_{mm'} \tag{4.25}$$

where $\Delta^{\mathrm{T(E)}}_{\ell m}$ denotes the spherical harmonic coefficients of the CMB temperature or E-mode polarisation anisotropies. A detailed numerical study of the SGWB anisotropies and their cross-correlation with the CMB has been performed in refs. [303–306]. Further aspects related to the initial conditions, including the case of isocurvature fluctuations will be discussed in section 4.4.

4.3 Application: anisotropies for peaked GW spectra

We now apply the formalism of Sec. 4.2 to calculate the propagation anisotropy spectrum associated to SIGW [135–137]. The results shown here are based on Section 3 of [4].

We are interested in scenarios having an enhanced curvature power spectrum on small scales with a sharply peaked spectral shape. Taking a phenomenological approach to the shape, we parametrize it around the peak wavenumber k_* by a log-normal, i.e. we take

$$\boxed{\mathcal{P}_\mathcal{R}(k)|_{k\gg k_{\rm CMB}} = \frac{A_\mathcal{R}}{\sqrt{2\pi}\Delta}\exp\left[-\frac{\ln^2(k/k_*)}{2\Delta^2}\right].} \tag{4.26}$$

The parameter Δ is the width of the log-normal and $A_\mathcal{R}$ its amplitude.[6] Our choice of the log-normal shape for the power spectrum is motivated by the fact that it can serve as a useful proxy for a peaked spectrum. Such a spectrum can be realised in several inflationary models which also produce PBH, see [347] and references therein.

4.3.1 Scalar induced GW background and its anisotropies

The observed GW energy density today arising from a log-normal scalar power spectrum is given by [347],

$$\Omega_{\rm GW}(k,\eta_0)h^2 \simeq 1.6\times10^{-5}\left(\frac{g_{*s}(\eta_k)}{106.75}\right)^{-1/3}\left(\frac{\Omega_{r,0}h^2}{4.1\times10^{-5}}\right)\Omega_{\rm GW,r}(k). \tag{4.27}$$

Here $g_{*s}(\eta_k)$ is the effective entropy degrees of freedom and $\Omega_{\rm GW,r}$ denotes the GW energy density at the epoch of matter-radiation equality,

$$\Omega_{\rm GW,r}(k) = 3\int_0^\infty dv\int_{|1-v|}^{1+v} du\frac{\mathcal{T}(u,v)}{u^2v^2}\mathcal{P}_\mathcal{R}(vk)\mathcal{P}_\mathcal{R}(uk)\,, \tag{4.28}$$

with the function $\mathcal{T}(u,v)$ a complicated transfer function defined in Eq.(10) of [347]. We recall the definition of the SGWB anisotropies,

$$\delta_{\rm GW}(k,\hat{n}) = [4-n_\Omega(k)]\,\Gamma(k,\hat{n}), \quad n_\Omega(k)\equiv\partial\ln\overline{\Omega}_{\rm GW}/\partial\ln k\,, \tag{4.29}$$

where Γ was defined in Eq. (4.6). The propagation anisotropies that we consider in this section are frequency independent, i.e. $\Gamma(k,\hat{n}) = \Gamma(\hat{n})$ [255]. We do not include

[6] The Dirac-delta power spectrum $\mathcal{P}_\mathcal{R} = A_\mathcal{R}\delta(\ln(k/k_*))$ is recovered in the limit $\Delta\to0$.

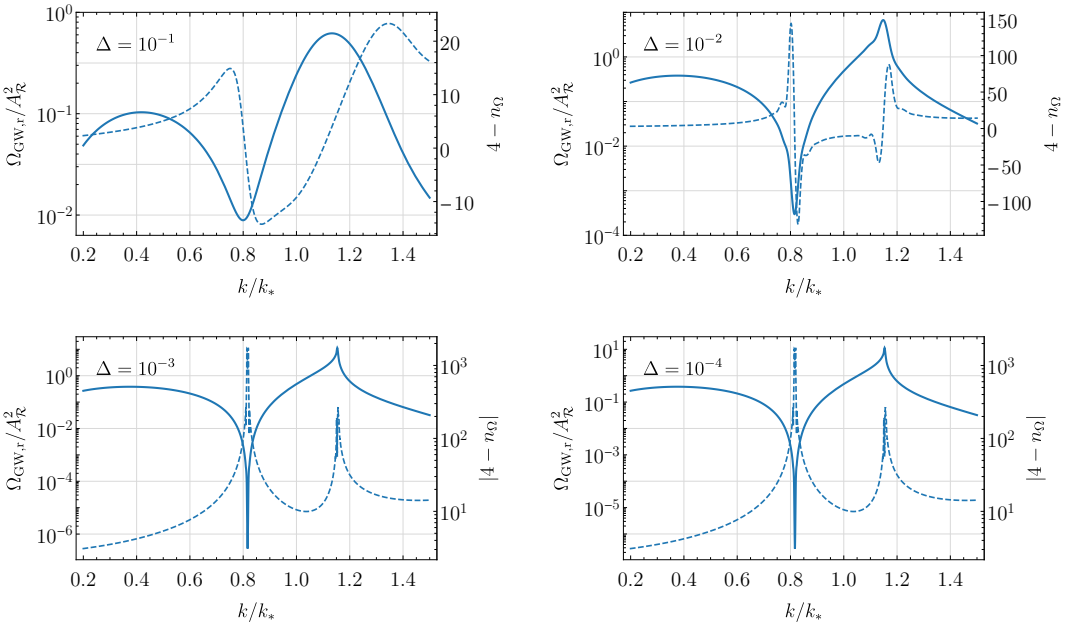

Figure 4.2: The dashed curves show the spectral tilt factor $4 - n_\Omega$, the solid curves show the GW amplitude $\Omega_{\mathrm{GW,r}}/A_{\mathcal{R}}^2$.

other possible sources of anisotropies that could be present, e.g. anisotropies arising from primordial non-Gaussianity due to a squeezed $\langle\zeta^3\rangle$ bispectrum [291, 296].

From (4.29), we can see that a sharply peaked spectrum ($|n_\Omega(k)| \gg 1$) leads to an enhancement of C_ℓ^{GW} relative to C_ℓ^Γ (see Eqs. 4.36) by a factor $\sim \mathcal{O}(10\text{–}1000)$ at certain frequencies. In Fig. 4.2, we plot the quantities $\Omega_{\mathrm{GW,r}}/A_{\mathcal{R}}^2$ and the spectral tilt factor n_Ω for representative choices of the log-normal width Δ.

Frequency profile of the SIGW:
One can understand features in the frequency shape of the SIGW at a qualitative level using the example of a Dirac-delta curvature power spectrum, peaked at a wavenumber k_*. In this case, the resulting SIGW peaks at $k/k_\star = \sqrt{4/3}$, and has a pronounced dip at $k/k_\star = \sqrt{2/3}$, where the SIGW spectrum goes exactly to zero for a Dirac-delta curvature spectrum. The presence of these features is explained by interference and resonant effects in the scalar modes sourcing these GW [136–138, 348]. For a curvature power spectrum that is narrow but not a Dirac-delta these features are smoothed out, leading to the results we see in Fig. 4.2.

4.3.1.1 Inflationary models with peaked spectra

There exist several inflationary models capable of producing such narrow peaks in the GW spectrum. These include models with modified gravity [349], multiple fields [350–355], parametric resonance [356–360], particle production [361] or models with non-standard kinetic terms [148, 149], all of which can produce the narrow spectra corresponding to $\Delta \sim 10^{-2}$. On the other hand, in single-field models with an ultra slow-roll phase, the growth rate of the curvature power spectrum is bounded from above (see e.g. [362–365]), thereby restricting the steepness of the induced GW spectrum and the enhancement of n_Ω. In fact, these single-field scenarios generally lead to the $\Delta = 10^{-1}$ (or larger) case of Fig. 4.2.

4.3.1.2 Other sources of peaked GW spectra

Apart from inflation, other cosmological sources such as phase transitions cosmic strings [366], can also produce peaked GW spectra. However, the enhancement from the tilt is not as large as the SIGW case. As an example, we consider the sound wave contribution for SGWB produced from cosmological phase transitions. It has a steeper spectral shape compared to the other modes of GW production during phase transitions with [367]

$$S(k, k_*) = \left(\frac{k}{k_*}\right)^3 \left(\frac{7}{4 + 3(k/k_*)^2}\right)^{7/2}, \tag{4.30}$$

and

$$\Omega_{\rm GW}(k) = \Omega_{\rm GW}(k_*) S(k, k_*)\,, \tag{4.31}$$

where $\Omega_{\rm GW}(k_*)$ is the GW amplitude at the peak wavenumber k_*. From Eq. (4.30) we can easily see that the factor $(4 - n_\Omega(k))$ is only $\mathcal{O}(1)$ in this case.

4.3.2 LISA GW-PBH scenario

We now study a representative example in which the peak of the curvature power spectrum is at scales 10^{-4} Hz $\leq f \leq 10^{-1}$ Hz such that the corresponding SIGW may be detectable by LISA. The frequency and comoving wavenumber are related by

$$\frac{k}{\rm Mpc^{-1}} \simeq 6.5 \times 10^{14} \frac{f}{\rm Hz}\,. \tag{4.32}$$

Δ	10^{-2}
f_*	$5 \times 10^{-3}\,\mathrm{Hz}$
k_*	$3 \times 10^{12}\,\mathrm{Mpc}^{-1}$
$A_{\mathcal{R}}$	7.5×10^{-3}

Table 4.1: Parameter choice for the LISA GW scenario.

We plot the induced GW spectrum in the left panel of Fig. 4.3 for the parameter choice of table 4.1. To avoid numerical artifacts arising due to the sharply peaked spectrum, we have also smoothed the $\Omega_{\rm GW}$ spectrum using the peak width as the smoothing scale,

$$\widetilde{\Omega}_{\rm GW}(f) = \frac{1}{2\Delta}\int_{fe^{-\Delta}}^{fe^{\Delta}} \Omega_{\rm GW}(f')\, d\ln f' \,. \tag{4.33}$$

with $\widetilde{\Omega}_{\rm GW}$ the smoothed spectrum.

The enhancement of the curvature power spectrum is the most commonly invoked mechanism to generate large density perturbations capable of collapsing into PBH. We have ensured that the scenario considered here is allowed by current constraints on the PBH abundance. The PBH mass at formation is related to the comoving scale k re-entering the horizon (during the radiation era). This relation can be estimated as [63, 368],

$$M_{\rm PBH} \simeq 30 M_\odot \left(\frac{\gamma}{0.2}\right)\left(\frac{g_*}{10.75}\right)^{-1/6}\left(\frac{2.9\times 10^5 \mathrm{Mpc}^{-1}}{k}\right)^2 . \tag{4.34}$$

If we consider peak frequencies/wavenumbers in the LISA band, this leads to PBH with masses in the range $M_{\rm PBH} \sim \mathcal{O}(10^{-15} - 10^{-12}) M_\odot$ (a comprehensive analysis of the LISA PBH-GW scenario is presented in [369, 370]).

We plot the corresponding PBH abundance in the right panel of Fig. 4.3, with the same choice of parameters as table 4.1. Along with the abundance, we also show the corresponding constraints[7], for which we use the tool provided in [399]. Our calculation of the PBH mass function follows the method of ref. [400], using a simple Press-Schechter approach and also accounting for critical collapse[8]. The PBH mass

[7] Strictly speaking, the constraints shown in Fig. 4.3 are valid only for an exactly monochromatic mass function. For extended mass functions the constraints need to be calculated in a different manner [398].

[8] Ref [401] presents a detailed comparison of different methodologies for calculating the PBH abundances and mass distributions.

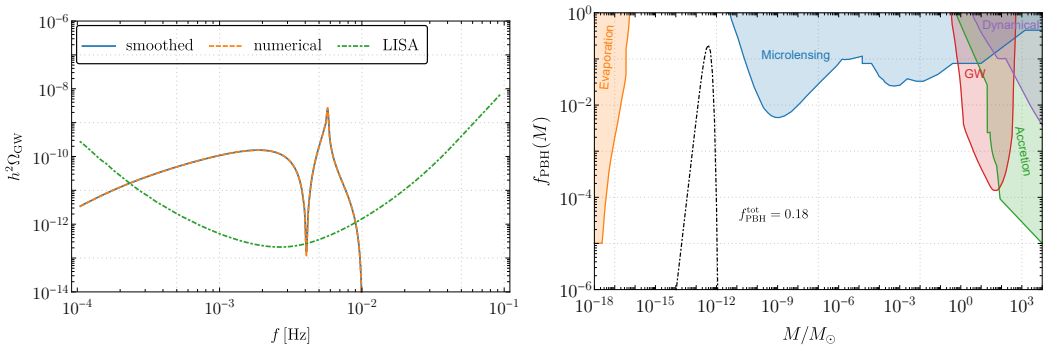

Figure 4.3: Left - The induced GW spectrum at LISA scales for the parameter choice given in table 4.1 and the smoothed spectrum defined in Eq. (4.33). The green dashed curve shows power-law integrated sensitivity curve for LISA [371] (see [372] for the updated sensitivity curves due to the impact of foregrounds and resolvable binaries). Right - The PBH abundance for the same values of the parameters plotted along with the constraints from microlensing [373–379], accretion [380–383], GW [384], evaporation [385–395] and dynamical constraints [396, 397].

function $f_{\rm PBH}(M)$, plotted in Fig. 4.3 is defined as,

$$\frac{\Omega_{\rm PBH}}{\Omega_{\rm DM}} = \int f_{\rm PBH}(M)\, d\ln M\,, \tag{4.35}$$

where the L.H.S. denotes the total fraction of the dark matter density constituted by PBH.

4.3.2.1 Angular power spectrum of GW anisotropies

Let us now calculate the angular power spectrum of the GW anisotropies for the LISA GW scenario. The quantity relevant for GW detectors is the anisotropy in the energy density $C_\ell^{\rm GW}$ whose angular power spectrum is defined as

$$\boxed{C_\ell^{\rm GW}(k) = (4 - n_\Omega(k))^2\, C_\ell^\Gamma}\,, \tag{4.36}$$

with n_Ω given by Eq. (4.29) and C_ℓ^Γ defined in Eq. (4.18). We recall here that Γ (Eq. (4.24)), and consequently C_ℓ^Γ, are frequency independent. The left panel of Fig. 4.4 shows the auto-correlation of the GW anisotropies and their cross-correlation with CMB temperature and E-mode polarisation anisotropies, defined in Eq. (4.25). We use `CAMB` [111] to calculate the T and E transfer functions. The right panel shows the frequency dependence of $C_\ell^{\rm GW}$ (for $\ell = 2$) for the LISA GW scenario and for a flat spectrum of GW for comparison. For simplicity, we have only considered the SW contribution for GW anisotropies, Eq. (4.24) since this dominates on large angular

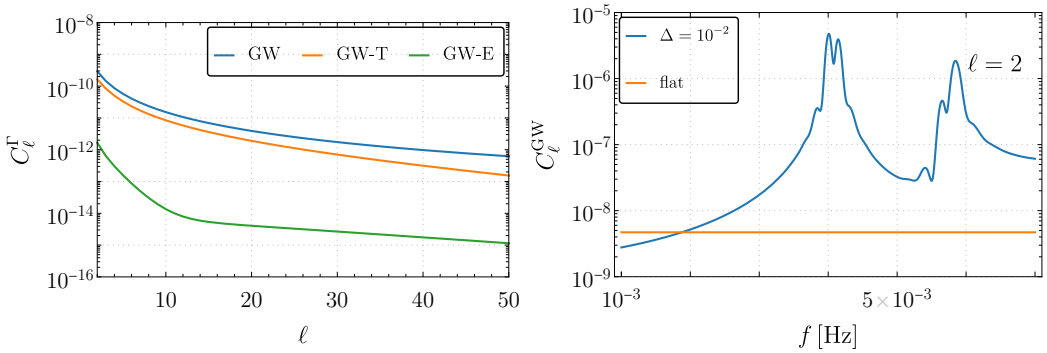

Figure 4.4: Left - Angular power spectrum of the GW anisotropies and their cross-correlation with CMB-T, E. Right - Frequency dependence of the angular power spectrum, for $\ell = 2$, for the LISA model of table 4.1 (blue line) and for a flat spectrum (orange line) plotted in a frequency range where LISA has the highest sensitivity.

scales and can also be estimated analytically [303].[9] It is worth pointing out here that the frequency dependence of the anisotropies ($C_\ell^{\rm GW}$) arises for SGWB spectral shapes different from power-laws. The latter have $n_\Omega =$ constant.

4.3.2.2 SNR of the anisotropies

We now turn to the detectability of these anisotropies and show that the enhancement of anisotropies for a peaked spectrum makes them easier to detect compared to the case of a standard power-law spectrum.[10] To perform this comparison, we consider a flat power-law spectrum $n_\Omega = 0$ whose amplitude is such that the resulting SNR of the monopole is the same in the LISA range. Since the results for a power law with a small spectral tilt $n_\Omega \sim \mathcal{O}(1)$ turn out to be quite similar, we do not present them separately. We limit our analysis to the first few multipoles since in general GW detectors are limited by their angular resolution $\ell_{\rm max} \sim 15$ [240, 243, 403–405], making these large angular scales the most relevant ones from the point of view of detection.

We plot the signal to noise ratio (SNR) for the individual multipoles in Fig. 4.5. Our results demonstrate that the anisotropy is easier to detect in case of a peaked spectrum as compared to a flat spectrum. We see that the $\ell = 2$ multipole, although the detectable with the LISA-Taiji network for the peaked spectra, is not detectable

[9] The inclusion of the ISW will not change our conclusions since the same factor $4 - n_\Omega$ multiplies this contribution as well.

[10] Ref. [402] also studied a related phenomenon in the context of kinematic anisotropies.

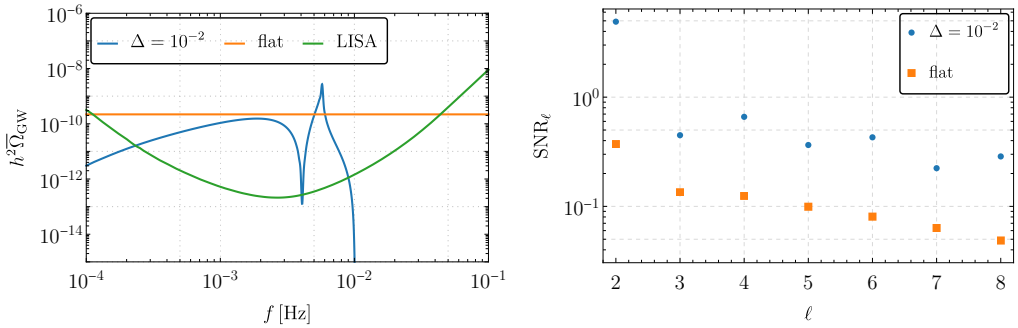

Figure 4.5: Left - $\Omega_{\rm GW}(f)$ plotted for the two spectra. Right - SNR of the individual multipoles with $T_{\rm obs} = 3$ years for observation with the LISA-Taiji network.

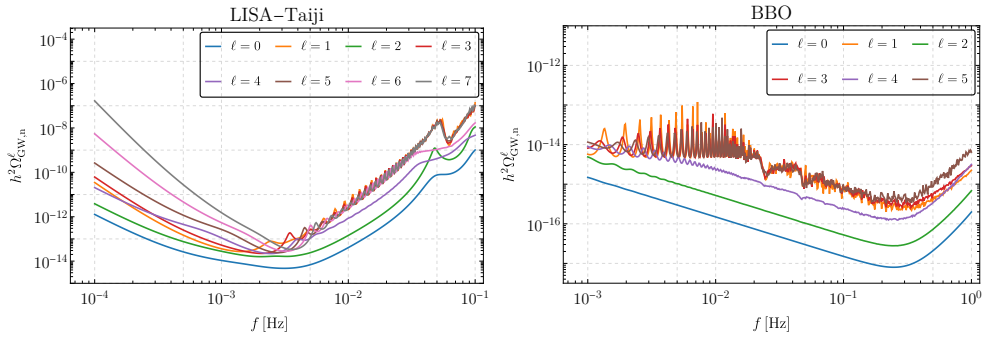

Figure 4.6: Sensitivity of LISA-Taiji and BBO to the different multipoles of the SGWB as a function of frequency. The time of observation is taken to be 3 years for both plots.

for the flat spectra. The SNR of the individual multipoles is defined as [246]

$$\mathrm{SNR}_\ell^2 = \int df\, C_\ell^{\rm GW}(f) \left(\frac{\Omega_{\rm GW}(f)}{\Omega^\ell_{{\rm GW},n}(f)} \right)^2 , \tag{4.37}$$

The quantity $\Omega^\ell_{{\rm GW},n}(f)$ represents the effective angular sensitivity of the detector network to the $\ell-$th multipole and is defined in eq. (C.15). Fig. 4.6 presents a plot this for the LISA-Taiji [406] and for the BBO configuration with 4 constellations [118]. More details about the calculation of $\Omega^\ell_{{\rm GW},n}(f)$ and the detector network specifications can be found in appendix C.

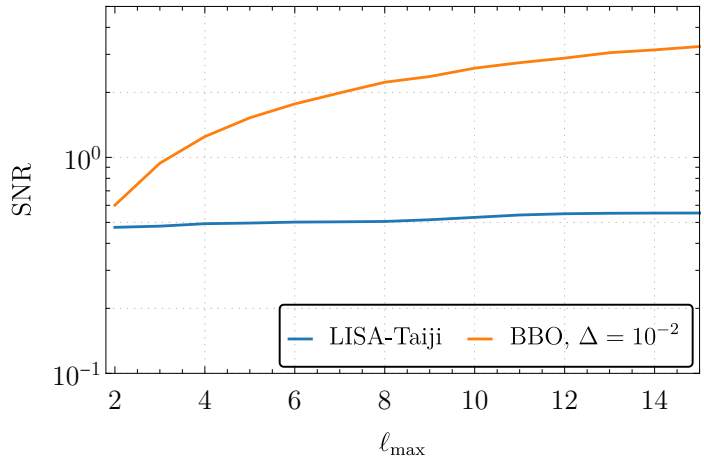

Figure 4.7: SNR of the cross-correlation between the GW anisotropies and the CMB-T, E mode anisotropies.

SNR of the cross-correlation

The SNR of the cross-correlation with the CMB-T, E anisotropies is defined as[11]

$$\mathrm{SNR}^2 = \sum_{\ell=2}^{\ell_{\rm max}} \sum_{\mathrm{X=T,E}} (2\ell+1) \frac{\left(C^{\mathrm{X}\Gamma}\right)^2}{\left(C^{\mathrm{X}\Gamma}\right)^2 + \left(C_\ell^\Gamma + N_\ell^\Gamma\right) C_\ell^{\mathrm{X}}} \,, \tag{4.38}$$

where the quantity N_ℓ^Γ is (for $\ell > 0$)

$$N_\ell^\Gamma \equiv \left[\int df \frac{(4 - n_\Omega(f))^2 \overline{\Omega}_{\rm GW}(f)^2}{\Omega^\ell_{\rm GW,n}(f)^2} \right]^{-1} . \tag{4.39}$$

We plot the SNR with which LISA-Taiji and BBO will detect the cross-correlation in Fig. 4.7 as a function of $\ell_{\rm max}$. In the example considered here, the cross-correlation will be detectable by a BBO (or equivalent sensitivity detector) but not with LISA-Taiji. The contribution from the GW-T cross-correlation dominates the total cross-correlation SNR while the the contribution of GW-E is negligible.

[11] In general, incomplete sky coverage will lead to correlations between nearby ℓ and degrade the sensitivity to the individual multipoles. To estimate the cross-correlation, as in ref. [305], we have assumed for simplicity full sky GW and CMB maps, which makes our estimate an optimistic one. The SNR would be reduced by a factor $\sqrt{f_{\rm sky}} < 1$ in a more realistic case [407, 408].

4.4 Initial conditions revisited

The results presented here are based on sections 3 and 4 of [5].

4.4.1 Universal relation for adiabatic initial conditions

In this section, we study the case of a non-standard early cosmological history and its impact on the GW anisotropies through the initial condition term $\Gamma_{\rm I}$ (see (4.23)). In this scenario, we have a post-inflationary universe whose energy density is dominated by a component with $w_0 \neq 1/3$, in contrast to the standard RD phase. It is known that the spectral shape of GW generated or re-entering the horizon during this phase is significantly affected by the non-standard equation of state [58, 317, 324, 332, 335]. We now investigate the effect on the anisotropies and show explicitly that the SGWB anisotropies are *completely unaffected* by an early non-standard phase, assuming the initial conditions are adiabatic. As we shall see next, this result can be physically understood as arising from the conservation of the curvature perturbation on super-horizon scales.

Our starting point is (4.16) for which we notice that the Newtonian gauge potential Φ is related to the uniform density gauge curvature perturbation by [92],

$$\Phi = -\frac{3(1+w)}{(5+3w)}\zeta\,, \qquad \zeta \equiv -\Psi - \mathcal{H}\frac{\delta\rho}{\rho'}\,. \tag{4.40}$$

Here, $\delta\rho$ denotes the perturbation in the total energy density. In case there are multiple components, one can define the individual curvature perturbation for each component

$$\zeta_i = -\Psi + \mathcal{H}\frac{\delta\rho_i}{\rho_i'}. \tag{4.41}$$

The adiabatic condition implies $\zeta = \zeta_i$.

The initial value of Φ appearing in (4.16) is then related to the non-standard eos through (4.40). Once the universe transitions into the radiation dominated epoch, the potential again changes according to the same equation. As shown in section 4.2.2, the initial condition term for a general w assuming adiabaticity is given by,

$$\Gamma_{\rm I} = -\frac{2\Phi}{3(1+w)} \;=\; \frac{2\,\zeta}{5+3w}\,, \tag{4.42}$$

where we also used Eq. (4.40). Collecting the results obtained so far, and applying them to (4.16) we find,

$$T_\ell^{\rm GW}(k) = \int_{\eta_i}^{\eta_0} d\eta \, \{\Phi(\eta)[1-(2/3(1+w_0))]\delta(\eta-\eta_i) + \Phi'(k,\eta) + \Psi'(k,\eta)\} \, j_\ell[k(\eta_0-\eta)] \, . \tag{4.43}$$

We split the the R.H.S of the above equation in two parts,

$$T_\ell^{\rm GW}(k) = \underbrace{\int_{\eta_i}^{\eta_r} \ldots}_{\rm (I)} + \underbrace{\int_{\eta_r}^{\eta_0} \ldots}_{\rm (II)} \, . \tag{4.44}$$

Here, η_r denotes the conformal time at the transition to the standard RD era and the dots represent the terms in the integrand of (4.44). The term (II) on the R.H.S is common to all scenarios and has no dependence on the initial equation of state. It represents the ISW effect associated to the standard ΛCDM universe and we calculate it using `CAMB` [111] assuming the *Planck* bestfit values for the ΛCDM parameters [15].

Let us now focus on term (I). Notice that we will always have $k\eta \ll 1$ for the large scale modes of interest here.[12] This in fact represents the condition for the mode k to be super-horizon and is always satisfied during the non-standard phase which happens before radiation domination. For instance, assuming a transition redshift of $z \sim 10^8$ (around the time of BBN), we find $\eta_r \sim 10^{-4}$. As a result of this, in the arguments of the spherical Bessel functions appearing in the term (I) we can always approximate $k(\eta_0-\eta) \simeq k\eta_0$ (see also fig. 4.8). Consequently, we find

$$\begin{aligned} T_\ell^{{\rm GW}(I)}(k) \approx \, & (\Phi(\eta_i) + \Gamma_{\rm I}(\eta_i) \\ & + [\Phi(k,\eta) + \Psi(k,\eta)]_i^f \,) j_\ell[k\eta_0] \\ & + \mathcal{O}(\eta_r/\eta_0) \, . \end{aligned} \tag{4.45}$$

This holds even if there are intermediate phases between the two eras. Now, substituting the values of Φ, Γ in terms of w_0, the above equation reads,

$$\begin{aligned} \frac{T_\ell^{{\rm GW}(1)}(k)}{j_\ell[k\eta_0]} \approx & \, \Gamma_{\rm I}(w_0) - \Psi(w_0) \\ & + \Phi(1/3) + \Psi(1/3) \, . \end{aligned} \tag{4.46}$$

[12] These are essentially the same as the large scale modes relevant for the CMB, $10^{-4}\,{\rm Mpc}^{-1} \lesssim k \lesssim 0.1\,{\rm Mpc}^{-1}$.

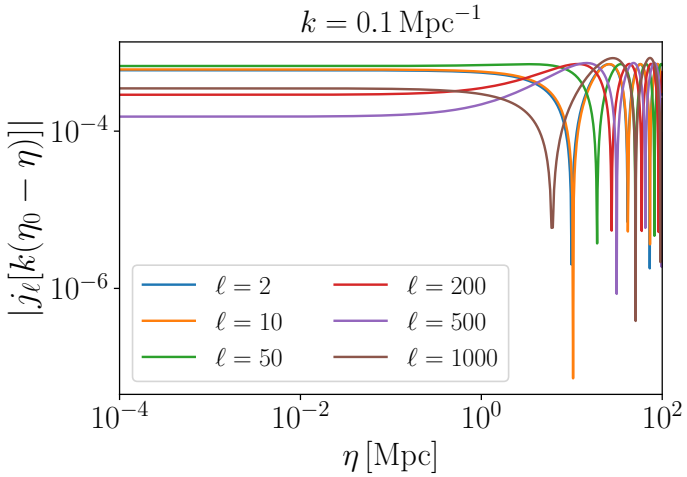

Figure 4.8: A graphical demonstration of the validity of the approximation involving the spherical Bessel functions, as used in Eqs. (4.45) and (4.46). We selected $k = 0.1\,\mathrm{Mpc}^{-1}$ as an example. For a given k, the Bessels are essentially constant as long as $k\eta \ll 1$, roughly corresponding to the duration over which the mode k remains super-Hubble.

The first two terms taken together, represent the definition of the curvature perturbation for gravitational waves. i.e.

$$\Gamma_{\rm I} - \Psi = -\Psi + \frac{1}{4}\frac{\delta\rho_{\rm GW}}{\rho_{\rm GW}} \equiv \zeta_{\rm GW}\,. \tag{4.47}$$

Since by adiabaticity $\zeta = \zeta_{\rm GW}$ and the curvature perturbation is conserved on super-horizon scales, we realise that (4.46) is independent of the initial equation of state w_0. This can be checked explicitly,

$$\Gamma_{\rm I}(w_0) - \Psi(w_0) = -\Phi\left[1 + \frac{2}{3+3w_0}\right] = \zeta, \tag{4.48}$$

assuming no anisotropic stress at these early times so that $\Phi = \Psi$. Using the fact that $\Phi(1/3) = -2\zeta/3$, we conclude that

$$\frac{T_\ell^{\rm GW(1)}(k)}{j_\ell[k(\eta_0)]} = -\frac{4}{3}\zeta + \zeta = -\frac{1}{3}\zeta, \tag{4.49}$$

Altogether, we can write the quantity $T_\ell^{\rm GW}$ as,

$$\boxed{T_\ell^{\rm GW} = -\frac{1}{3}\zeta\, j_\ell[k\eta_0] + \int_{\eta_r}^{\eta_0} d\eta\,[\Phi(k,\eta)' + \Psi(k,\eta)']j_\ell[k(\eta_0 - \eta)]}\,, \tag{4.50}$$

completely independent of the initial non-standard phase of expansion.

The approximation involving the spherical Bessel functions that we utilised in Eqs. (4.45) and (4.46) can also be understood physically. The integral along the GW geodesic accounts for the (temporal and spatial) variation of the potential along the line-of-sight.

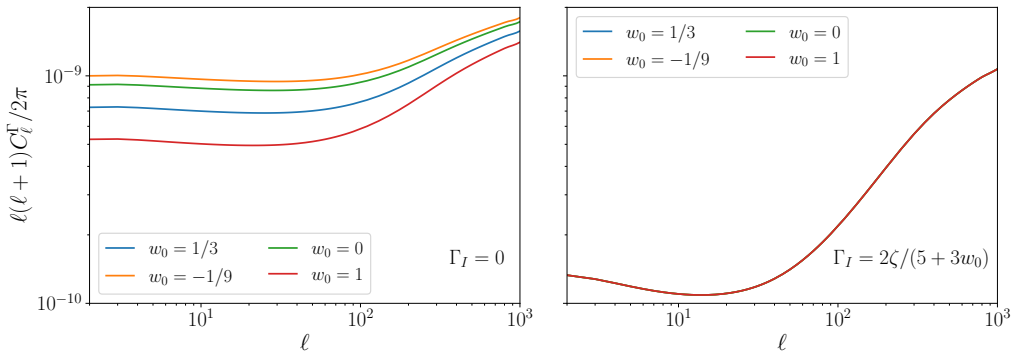

Figure 4.9: The upper plot shows the effect of varying w_0 on the SGWB anisotropies without including the initial condition term. The lower plot includes the contribution from the initial condition contribution $\Gamma_{\rm I}$.

Crucially, for a fast and early transition to RD, GW cover an infinitesimal comoving distance with $k\Delta\eta \ll 1$. This implies small potential gradients ($\sim k\Delta\eta \times \Phi$), which can be neglected. Equivalently, in Fourier space it means that the arguments of the Bessel functions in the first integral of Eq. (4.44) can be taken to be constant.

The result is valid for GW produced "early-enough", when all the large-scale modes of interest are still super-Hubble. Adiabaticity then implies the conservation of the curvature perturbation, unaffected by any changes in the equation of state. The fact that the non-standard phase must take place early in the cosmological evolution is not so stringent an assumption, since we know that the universe must be radiation dominated already by the time of BBN. This process itself happens quite early ($z \sim 10^8$, $T \sim 100\,\text{keV}$).[13] What matters here is the equation of state when long wavelength mode re-enters the horizon: as long as the early phase does not change that, the anisotropy spectrum remains unaffected. In the case of GW anisotropies, the the relevant modes re-enter the horizon towards the end of radiation domination or during matter domination.

Our result also emphasises the importance of the initial condition term $\Gamma_{\rm I}$, without it one may end up with a spurious dependence on the initial equation of state (see Fig. 4.9). We also briefly comment regarding the initial time η_i in Eq. (4.50), which in general corresponds to the time when the GW are produced/emitted (see the discussion in section 4.2). For the CMB case, this corresponds to the time of photon decoupling since that is when the CMB photons start propagating freely. Our deriva-

[13] Additionally, there exist lower bounds of $\mathcal{O}$(MeV) on the reheating temperature, obtained using constraints from BBN [409–411].

tion here shows that for a given long wavelength mode k, η_i can also be set to be the time when the mode re-enters the horizon and ζ_k starts evolving. For adiabatic initial conditions, both choices lead to the same result.[14] One point of difference from the CMB anisotropies is that although changes in the expansion history at the epoch of photon decoupling would affect the CMB anisotropies (especially on intermediate and small angular scales), GW anisotropies remain impervious to changes in the initial equation of state.

Implications

This result has implications for early universe scenarios involving only Standard Model Physics. We know that during the QCD phase transition ($T \sim 100$ MeV), the background equation of state changes with significant implications for primordial black hole formation [400, 412, 413] as well for the SGWB, see e.g. [414, 415]. Even though the QCD phase transition affects the SGWB spectral shape, our results show that it does not affect the anisotropies. Thus, the SGWB anisotropies cannot provide any independent information about this phase transition.

Another implication of this result is that SGWB anisotropies cannot be used to break degeneracies among different models that may produce the same frequency profile of $\Omega_{\rm GW}$. We provide an example of this below, showing the different production mechanisms that may produce a peaked broken power-law shape. These include SGWB from first order phase transitions [416], kination [317], cosmic domain walls [417] and SIGW. In fact, due to the absence of constraints on the shape of the small scale curvature power spectrum, one can have different power law indices on either side of the peak and replicate the SGWB from other mechanisms using SIGW.

SIGW have an approximately broken power-law shape with a peak in two cases: (a) the curvature power spectrum is a broken power-law and (b) the eos at early times is negative [330, 335, 418, 419]. We work here only with case (a) since it suffices to demonstrate our point regarding the degeneracy in the spectral shape. In this case,

[14] The choice of η_i does matter for the SGWB-CMB cross-correlation, since the difference between η_i for GW and SGWB becomes relevant (see e.g. section 5.2.2 or [305, 306]).

if the primordial curvature power spectrum around the peak k_{pk} is,

$$P_\zeta \propto \begin{cases} \left(\dfrac{k}{k_{pk}}\right)^{n_{IR}} & (k \ll k_{pk}) \\ \left(\dfrac{k}{k_{pk}}\right)^{-n_{UV}} & (k \gg k_{pk}) \end{cases} \tag{4.51}$$

Then the corresponding SIGW spectrum is roughly [138, 419]

$$\Omega_{\rm GW} \propto \begin{cases} \left(\dfrac{k}{k_{pk}}\right)^{n_{IR}^{ind}} & (k \ll k_{pk}) \\ \left(\dfrac{k}{k_{pk}}\right)^{-n_{UV}^{ind}} & (k \gg k_{pk}) \end{cases} \tag{4.52}$$

where

$$n_{IR}^{ind} = \begin{cases} 2n_{IR} - 2b & (n_{IR} < 3/2) \\ 3 - 2|b| & (n_{IR} > 3/2) \end{cases} \tag{4.53}$$

and

$$n_{UV}^{ind} = \begin{cases} 2n_{UV} + 2b & (n_{UV} < 4(2)) \\ 4(2) + n_{UV} + 2b & (n_{IR} > 4(2)) \end{cases} \tag{4.54}$$

We have defined here

$$b = \frac{1 - 3w}{1 + 3w}\,. \tag{4.55}$$

In Eq. (4.54), the numbers in parenthesis represent the scenario $c_s^2 \sim 1$ [419]. At the boundaries of the inequalities and for the case of $n_{IR} > 3/2$ and $w = 1/3$, logarithmic corrections appear which we can safely neglect here.

It is clear that for different values of the parameters b, c_s, n_{IR} and n_{UV}, we can obtain different UV and IR scalings of $\Omega_{\rm GW}$ (i.e. n_{UV}^{ind} and n_{IR}^{ind}), allowing us to replicate the SGWB shape produced by the other mechanisms mentioned previously. Thus, the spectral shape and the anisotropies (under adiabatic initial conditions) cannot be used to unambiguously determine the origin of the SGWB. To do so, one would need independent constraints, e.g. on the amplitude of curvature power spectrum to avoid PBH overproduction, or other non-GW constraints.

4.4.2 Isocurvature initial conditions

Having derived a robust prediction for the GW anisotropies in the adiabatic case, we now explore the potential consequences of dropping the assumption of adiabaticity and allowing for the presence of isocurvature perturbations. In contrast to the

previous section, here we do not intend to explore the consequences of non-standard equations of state for isocurvature perturbations, but rather we wish to investigate the general implications of isocurvature initial conditions and see how they differ w.r.t the adiabatic scenario.

We begin by reviewing the definition of GW isocurvature perturbations and consider isocurvature initial conditions set during the radiation era. The GW isocurvature component w.r.t the Standard Model radiation bath is defined as [287]

$$S_{\mathrm{GW},r} = 3(\zeta_{\mathrm{GW}} - \zeta_r), \quad \zeta_x = -\Psi - \mathcal{H}\frac{\delta\rho_x}{\rho_x'}, \tag{4.56}$$

where $x = \{\mathrm{GW}, r\}$. This gives us [287]

$$\Gamma_{\mathrm{I}} = \zeta_{\mathrm{GW}} + \Psi = \zeta_r + \frac{1}{3}S_{\mathrm{GW},r} - \frac{2}{3}\zeta\,, \tag{4.57}$$

where we used the RD relation $\Psi = -2\zeta/3$. We now relate ζ_r with the total curvature perturbation ζ, assuming that we only have radiation and the GW background,

$$\zeta = -\Psi - \mathcal{H}\frac{\delta\rho}{\rho'} = \zeta_r + \frac{1}{3}f_{\mathrm{GW}}S_{\mathrm{GW},r}\,. \tag{4.58}$$

Introducing the quantity,

$$f_{\mathrm{GW}} = \frac{(1+w_{\mathrm{GW}})\rho_{\mathrm{GW}}}{\sum_x (1+w_x)\rho_x}. \tag{4.59}$$

with w_x the equation of state parameter of the component x, we obtain [287]

$$\Gamma_{\mathrm{I}} = \frac{1}{4}\frac{\delta\rho_{\mathrm{GW}}}{\rho_{\mathrm{GW}}} = \frac{\zeta}{3} + \frac{1}{3}(1 - f_{\mathrm{GW}})S_{\mathrm{GW},r}. \tag{4.60}$$

These isocurvature perturbations also affect the CMB anisotropies in a manner given by $\Theta_I = \zeta/3 - f_{\mathrm{GW}}S_{\mathrm{GW,r}}/3$, where Θ_I are the initial temperature fluctuations. However, their effects on the CMB anisotropies are suppressed by a factor $f_{\mathrm{GW}} \ll 1$ w.r.t the GW anisotropies [287].

Eq. (4.60) can also be extended to scenarios where the background is dominated by a component with arbitrary equation of state w_0. Since we always have $f_{\mathrm{GW}} \ll 1$, such that $\zeta \approx \zeta_x$, using Eq. (4.40) we now define the GW isocurvature as

$$\Gamma_{\mathrm{I}} \simeq \frac{2\zeta_x}{5+3w_0} + \frac{1}{3}S_{\mathrm{GW},x}, \quad S_{\mathrm{GW},x} = 3(\zeta_{\mathrm{GW}} - \zeta_x). \tag{4.61}$$

which generalises Eq. (4.60).

We now study an early-universe scenario capable of generating GW isocurvature perturbations and analyse its consequences for the angular power spectrum of the

GW anisotropies. In refs. [287, 290] phase transitions during RD were invoked to produce GW isocurvature perturbations. Our analysis will be based on a different scenario, known as the *curvaton mechanism*.

4.4.2.1 Curvaton scenario

The curvaton model [340–342, 420] postulates the presence of a spectator field χ which remains sub-dominant during the inflationary dynamics. The field χ remains massless during inflation and has a non-vanishing vev χ_*. Curvaton fluctuations generated during inflation, denoted as $\delta\chi$ are initially of an isocurvature nature. As the universe expands further, inflation ends after which at some point the curvaton mass overcomes the Hubble friction. The curvaton then oscillates coherently around the minimum of its potential, its energy density decays just like that of pressure-less matter and it comes to dominate the energy density of the universe. Eventually the curvaton decays to the Standard Model particles and the universe begins its radiation dominated phase.

Within the curvaton scenario, we foresee two possible mechanisms for generating GW isocurvature perturbations. These are:

(i) The curvature perturbation arises from the curvaton itself, as in the original curvaton scenario through the isocurvature-to-adiabatic conversion of the primordial perturbations which happens after the decay of the curvaton into the Standard Model particles. In this case, GW are not a decay product of the curvaton but are instead generated during inflation or another pre-curvaton domination phase. As a result, the initial isocurvature perturbation survives only in the density perturbation of the GW.

(ii) The curvaton itself sources GW on small scales, e.g. [421]. GW anisotropies then inherit the curvaton fluctuations on large cosmological scales. The other difference with case (i) arises from the fact that we assume the curvaton energy density to remain subdominant throughout, with negligible contribution to the total curvature perturbation (otherwise there would be no GW isocurvature!). This physics of the isocurvature perturbations in this scenario is similar to other set-ups that have been analysed recently e.g. those involving phase transitions [290] or the effects of dark radiation [422].

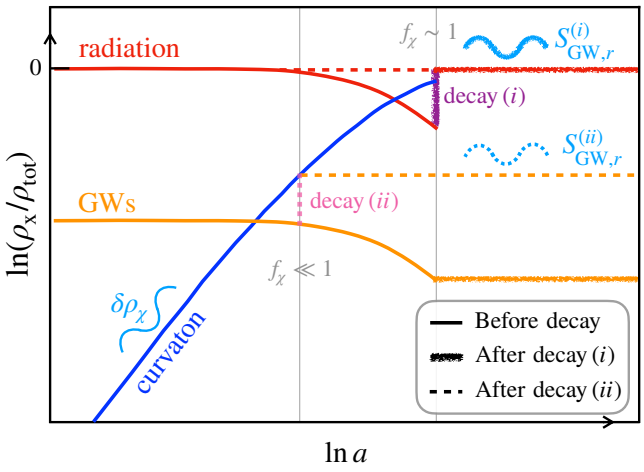

Figure 4.10: Illustration of the curvaton mechanism and its implications for initial GWB isocurvature fluctuations. We show the logarithm of energy density of a given fluid (standard radiation r, GWs and the curvaton χ) normalised to the total energy density as a function of e-folds or $\ln a$. Note that we assume $w_\chi = 0$ and we take arbitrary initial background densities for illustrative purposes. At some point, the curvaton decays either to standard radiation (case (i)) or to GWs (case (ii)). The fraction of the curvaton at the time of decay for (i) is $f_\chi \sim 1$ while for (ii) is $f_\chi \ll 1$. Then the initial isocurvature fluctuations due to the curvaton are either transferred to standard radiation in case (i) or to GWs in case (ii). Due to the asymmetric decay of the curvaton, there remains an isocurvature component between radiation and GWs, labelled $S_{\mathrm{GW},r}$.

We now examine these two scenarios in more detail, starting with some general results and the description of our set-up, common to both scenarios. The post-inflationary universe is characterised by three components $\{r, \chi, \mathrm{GW}\}$, i.e. radiation, curvaton and GW. The radiation component ρ_r dominates the energy density of the universe after inflation.[15] The curvaton component, ρ_χ decays at some point after inflation and the final component ρ_{GW} always remains subdominant. The individual curvaton perturbations are defined as in (4.41) and the isocurvature component between two fluids i and j is given by,

$$S_{ij} = 3(\zeta_i - \zeta_j)\,. \tag{4.62}$$

The quantities ζ_i, S_{ij} are gauge-invariant and we choose to evalaute them in the spatially flat gauge ($\Psi = 0$). For the initial curvaton perturbation we find,

$$\zeta_{\chi,\mathrm{ini}} = \frac{1}{3(1+w_\chi)} \left(\frac{\delta\rho_\chi}{\rho_\chi}\right)_* . \tag{4.63}$$

The * signifies that the quantities are evaluated at horizon crossing during inflation. To keep things as general as possible we do not yet fix the curvaton equation of state

[15] A more general approach would allow for an arbitrary equation of state after inflation but would not significantly change our findings.

parameter w_χ.[16] The decay product of the inflaton is assumed to be radiation so that $\zeta_{r,\rm ini}$ is the same as the inflaton curvature perturbation.

All the components here obey their individual energy conservation equations and do not have any non-adiabatic pressure. Thus, the individual curvature perturbations are conserved throughout [423, 424], except at the moment the curvaton decays. In order to obtain analytic results for the SGWB anisotropies, we make the simplifying assumption of instantaneous curvaton decay and denote ζ before and after the decay as $\zeta^b_{\rm dec}$ and $\zeta^a_{\rm dec}$. In the uniform density gauge ($\sum_x \delta\rho_x = 0$), we have

$$\delta\rho_x/\rho_x = 3(1+w_x)(\zeta_x - \zeta) \tag{4.64}$$

Thus, we can write

$$\begin{aligned}\zeta^b_{\rm dec} = f^b_\chi \zeta_{\chi,\rm ini} + f^b_{\rm GW}\zeta_{\rm GW,ini} \\ + (1 - f^b_\chi - f^b_{\rm GW})\,\zeta_{r,\rm ini}\,,\end{aligned} \tag{4.65}$$

where the f_i are defined as in (4.59). The fractions $f^a_{\rm GW}$ and $f^b_{\rm GW}$ can be different and depend upon the end products of the curvaton decay. In what follows, we shall assume $f^b_{\rm GW} \ll 1$ and no initial isocurvature between GW and radiation i.e. $\zeta_{r,\rm ini} = \zeta_{\rm GW,ini}$ (unless otherwise stated). After the decay, the curvature perturbation reads,

$$\zeta^a_{\rm dec} = f^a_{\rm GW}\zeta^a_{\rm GW,dec} + (1 - f^a_{\rm GW})\,\zeta^a_{r,\rm dec}\,. \tag{4.66}$$

The remnant isocurvature after the decay depends on what the curvaton decays into which is different for cases (i) and (ii). We now study these cases in more detail.

Curvaton case (i)

Here, the curvaton decays completely into radiation implying

$$\zeta^a_{\rm r,dec} \approx \zeta^a_{\rm dec} \approx \zeta^b_{\rm dec}\,, \tag{4.67}$$

in the limit of instantaneous decay. Consequently, the final isocurvature perturbation is

$$\begin{aligned}S^a_{\rm GW,r|dec} &\equiv 3(\zeta^a_{\rm GW,dec} - \zeta^a_{\rm r,dec}) \\ &\approx 3(\zeta_{\rm GW,ini} - \zeta^b_{\rm dec}) \approx f^b_\chi S_{\rm GW,\chi|ini}\,.\end{aligned} \tag{4.68}$$

[16] Note that in general $\delta\rho_\chi$ depends on χ through the form of the potential, e.g. for $V = m^2\chi^2$ we have $\delta\rho_\chi/\rho_\chi = 2\delta\chi/\chi_*$.

To arrive at this result, we used Eq. (4.65) and the fact that $\zeta_{r,\rm ini} = \zeta_{\rm GW,ini}$. The resulting isocurvature is related to the initial isocurvature $S_{{\rm GW},\chi|\rm ini}$ multiplied by a factor f_χ, which denotes the fraction of the energy density of radiation that is contributed by the curvaton decay.

One can understand the consequences of this scenario further, by taking a simple example in which the initial conditions are such that $\zeta_{\chi,\rm ini} \gg \zeta_{r,\rm ini} = \zeta_{\rm GW,ini}$. When the curvaton decays to radiation we will then have,

$$\zeta^a_{r,\rm dec} \simeq f^b_\chi \zeta_{\chi,\rm ini}\,. \tag{4.69}$$

In this simple example, it is the curvaton which sources the curvature perturbation ζ^a_r. Since ζ^a_r is the source of the CMB anisotropies, its amplitude and also that of $f^b_\chi \zeta_{\chi,\rm ini}$ is fixed. This perturbation is related to the initial curvaton density fluctuation in the spatially flat gauge through Eq. (4.63). In principle there is a dependence on the curvaton equation of state, but as we see from Eq. (4.63), observations are only sensitive to the combination $f_\chi(1+3w_\chi)^{-1}\delta\rho_\chi/\rho_\chi$.

Now, we apply these results to small-scale GW re-entering the horizon during radiation domination. Using Eq. (4.60) and $f_{\rm GW} \ll 1$, we obtain

$$\begin{aligned}\Gamma_{\rm I} &\simeq \frac{1}{3}\zeta^a_{r,\rm dec} + \frac{1}{3}S^a_{{\rm GW},r} = \frac{1}{3}\zeta^a_{r,\rm dec} + \frac{1}{3}f^b_\chi S_{{\rm GW}\chi,\rm ini} \\ &\simeq -\frac{2}{3}f^b_\chi \zeta_{\chi,\rm ini} = -\frac{2}{3}\zeta^a_{r,\rm dec}\,.\end{aligned} \tag{4.70}$$

We can see that in this case, the initial condition term differs from the adiabatic result of Eq. (4.42) which for radiation domination reads $\Gamma_{I,\rm ad} = \zeta/3$. The total anisotropy is now given by ,

$$\boxed{T^{\rm GW}_\ell = -\frac{4}{3}\zeta^a_{r,\rm dec}\, j_\ell[k\eta_0] + \int_{\eta_r}^{\eta_0}[\Phi(k,\eta)' + \Psi(k,\eta)']j_\ell[k(\eta_0-\eta)]}\,, \tag{4.71}$$

where we used Eq. (4.16) with the isocurvature initial conditions of Eq. (4.70).

Notice that in this case, the first term on the R.H.S of Eq. (4.71) is 4 times the adiabatic result. Since the first term dominates on large angular scales, this will lead to roughly a 16 times enhancement of the anisotropies (in terms of C^Γ_ℓ), compared to the adiabatic case. The SGWB map also exhibits strong correlations with the CMB anisotropies, both being derived from the initial fluctuations of χ. This cross-correlation is given by (4.25) and is approximately 4 times larger compared to the adiabatic result. A detection of such a cross-correlation would strongly hint towards this simple curvaton scenario.

Curvaton case (ii)

In case (ii), the only source of GW is the curvaton, which itself remains subdominant throughout the cosmic evolution. Taking the extreme example of the entire energy density of the curvaton decaying into GW, we have $\rho^a_{\rm GW} = \rho^b_{\rm GW} + \rho^b_\chi$ and $\delta\rho^a_{\rm GW} = \delta\rho^b_{\rm GW} + \delta\rho^b_\chi$ such that

$$\begin{aligned} S^{a,(ii)}_{\rm GWr,dec} &= 3(\zeta^a_{\rm GW,dec} - \zeta^a_{r,\rm dec}) \\ &= 3\frac{\rho^b_\chi + \rho^b_r + \rho^b_{\rm GW}}{\rho^b_\chi + \rho^b_{\rm GW}}\Big[f^b_\chi\zeta_{\chi,\rm ini} \\ &+ f^b_{\rm GW}\zeta_{\rm GW,ini} - (f^b_\chi + f^b_{\rm GW})\zeta_{r,\rm ini}\Big]\,. \end{aligned} \tag{4.72}$$

If instead we assumed that only a fraction of the curvaton energy density decayed into GW, i.e. $\rho^a_{\rm GW} = \rho^b_{\rm GW} + \sigma\rho^b_\chi$, we would have

$$\begin{aligned} S^a_{\rm GWr,dec} &= 3(\zeta^a_{\rm GW,dec} - \zeta^a_{r,\rm dec}) \\ &= 3\frac{(\rho^b_\chi + \rho^b_r + \rho^b_{\rm GW})^2}{(\rho^b_{\rm GW} + \sigma\rho^b_\chi)(\rho^b_{\rm r} + (1-\sigma)\rho^b_\chi)} \\ &\times \Big[(\sigma\omega^b_r - (1-\sigma)\omega^b_{\rm GW})f^b_\chi\zeta_{\chi,\rm ini} \\ &+ (\omega^b_r + \frac{1+w_\chi}{1+w_r}(1-\sigma)\omega^b_\chi)f^b_{\rm GW}\zeta_{\rm GW,ini} \\ &- (\omega^b_{\rm GW} + \frac{1+w_\chi}{1+w_r}\sigma\omega^b_\chi)f^b_{\rm r}\zeta_{r,\rm ini}\Big]\,. \end{aligned} \tag{4.73}$$

The quantity ω is defined as,

$$\omega_x \equiv \frac{\rho_x}{\rho_\chi + \rho_r + \rho_{\rm GW}}\Big|_{\rm dec}\,. \tag{4.74}$$

Reassuringly, we recover case (i) in the limit $\sigma \to 0$ and case (ii) when $\sigma \to 1$.

Another assumption we make is that $\zeta_{\chi,\rm ini} \gg \zeta_{r,\rm ini}$, but $f^b_\chi\zeta_{\chi,\rm ini} \ll \zeta_{r,\rm ini}$. This example suffices to qualitatively understand the predictions of case (ii). Using these assumptions we find for the GW isocurvature,

$$\begin{aligned} S^{a,(ii)}_{{\rm GW},r|\rm dec} &\equiv 3(\zeta^a_{\rm GW,dec} - \zeta^a_{r,\rm dec}) \approx 3(\zeta^a_{\rm GW,dec} - \zeta^b_{r,\rm dec}) \\ &\approx 3\frac{(1+w_\chi)}{(1+w_r)}\zeta_{\chi,\rm ini}\,, \end{aligned} \tag{4.75}$$

Here we assumed that $\zeta^a_{\rm dec} = \zeta^b_{\rm dec} \ll \zeta_{\chi,\rm ini}$ and used the spatially flat gauge result

stated below,

$$\zeta^a_{\rm GW,dec} = \zeta^a_{\rm dec} + \frac{1}{3(1+w_r)}\frac{\delta\rho^a_{\rm GW}}{\rho^a_{\rm GW}} \approx \frac{1}{3(1+w_r)}\frac{\delta\rho^b_\chi}{\rho^b_\chi} \approx \frac{(1+w_\chi)}{(1+w_r)}\zeta_{\chi,\rm ini}\,. \tag{4.76}$$

The GW isocurvature in this case is derived entirely from the large initial curvaton fluctuations. The energy density of the curvaton remains subdominant and does not contribute appreciably to the total curvature perturbation, ensuring that CMB constraints on isocurvature perturbations remain satisfied.

The resulting GW anisotropy can now be written as,

$$\boxed{T^{\rm GW}_\ell \approx \left[\frac{(1+w_\chi)}{(1+w_r)}\zeta_{\chi,\rm ini} - \frac{1}{3}\zeta^a_{r,\rm dec}\right] j_\ell[k\eta_0] + \int_{\eta_r}^{\eta_0}[\Phi'(k,\eta)+\Psi'(k,\eta)]j_\ell[k(\eta_0-\eta)]\,,} \tag{4.77}$$

where we used that $f^b_\chi\zeta_{\chi,\rm ini} \ll \zeta_{r,\rm ini}$. The CMB anisotropies here are sourced entirely by ζ_r and one can accommodate large isocurvature perturbations, i.e. $\zeta_{\chi,\rm ini} \gg \zeta^a_{r,\rm dec}$, for $f^b_\chi \ll 1$, so that their impact on the CMB is negligible. The CMB-GW cross-correlation here is also smaller compared to that of case (i).[17]

We see that large GW isocurvature i.e. large $\zeta_{\chi,\rm ini}$, requires $f^b_\chi \ll 1$. Importantly, this can lead to large non-Gaussianities, as already pointed out for the standard curvaton mechanism [424]. This happens because the decrease of f^b_χ requires a decrease of the curvaton vev χ_* (assuming a fixed curvaton mass). Thus, higher order terms in $\delta\chi/\chi$ become more and more relevant. Interestingly, similar non-Gaussianity can result in scenarios that share features with the curvaton case (ii), i.e. whenever GW are sourced by a subdominant field having large isocurvature, e.g. see [290].

Curvaton summary plot

Fig. 4.11 shows a plot of the quantity C^Γ_ℓ, for cases (i) and (ii)(Eqs. (4.71) and (4.77) respectively). It can be seen that the isocurvature perturbations lead to a noticeable deviation from the adiabatic result shown in Fig. 4.9 with an enhancement due to the larger isocurvature component. In case (ii), the amplitude and scale

[17] One can obtain a larger CMB-GW cross correlation for $f^b_\chi \ll 1$ if we assume $\zeta^b_\chi \ll \zeta^b_r$ instead. The resulting isocurvature is now $S_{{\rm GW},r} \approx -9(1+w_\chi)\zeta_r/4$ with SGWB anisotropies larger by roughly a factor 3 compared to those of the CMB for $w_\chi = 0$.

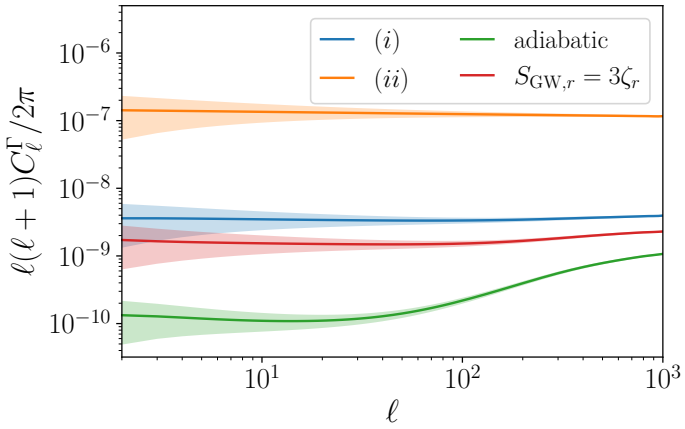

Figure 4.11: The angular power spectrum of the SGWB anisotropies for cases (i) and (ii). For case (i) the isocurvature amplitude is fixed (see Eq. (4.71)). For case (ii) we have chosen $|\zeta_\chi| = 10|\zeta_r|$ and $w_\chi = 0$. The adiabatic prediction and a scenario with the sign of $S_{\mathrm{GW},r}$ opposite to that of case (i) are also shown for comparison. The quantity ζ_r is determined by the CMB amplitude $\mathcal{P}_{\zeta_r} = 2.09 \times 10^{-9}$ and the spectral tilt $n_s = 0.9649$. The shaded regions denote the cosmic variance limited error bars [104].

dependence of ζ_χ is fixed, leading to a flat spectrum throughout. For case (ii) we have assumed an enhanced but flat spectrum of curvaton fluctuations, but in general this is not constrained and features in the spectral shape of $\mathcal{P}_{\zeta_\chi}(k)$ can lead to interesting signatures in the ℓ-dependence of C_ℓ^Γ (see [290] for an example). Finally, we have also shown in the same plot a scenario with $S_{\mathrm{GW},r} = 3\zeta_r$, equal in magnitude but having a sign opposite that of case (i). This leads to a contribution which is anti-correlated with the rest of the GW anisotropy terms, leading to slightly smaller amplitude on large angular scales and also an anti-correlation of the CMB and GW maps. It may be possible to realise such an isocurvature component, which needs to already be anti-correlated with the initial adiabatic perturbations, in two-field models of inflation [425–427]. This requires further study which we leave for future work.

4.5 Summary

GW backgrounds can be produced by numerous early universe mechanisms such as inflation, phase transitions, cosmic strings and even PBH. The backgrounds are expected to have a small anisotropy resembling that of the CMB, as a consequence of GW propagation in an inhomogeneous universe. Additional anisotropies may arise due to inhomogeneities in the production mechanism and can be highly model inde-

pendent. A detailed characterisation of the anisotropies is essential to distinguishing cosmological and astrophysical GW backgrounds and may also help in determining the precise origin of a given cosmological background. In this chapter we have studied two aspects of these anisotropies, namely their frequency dependence and the role played by the GW initial conditions.

We first reviewed reviewed the line-of-sight formalism for GW anisotropies and then derived the initial conditions for the anisotropies, assuming adiabatic primordial perturbations. Then, in section 4.3 we applied the los formalism to analyse the propagation anisotropies of SGWB induced at second order in the primordial curvature perturbation. We showed that the if the curvature power spectrum happens to peak at certain scales, as is common in scenarios associated to PBH formation, the SGWB anisotropies around those scales may be enhanced by factor $\mathcal{O}(10-100)$ compared to the anisotropies in the case of a power law $\Omega_{\rm GW}$ spectrum with $n_\Omega \sim \mathcal{O}(1)$. The enhancement can also make the anisotropies easier to detect and we illustrated this through a representative scenario of SGWB at mHz scales, relevant for next generation detectors such as LISA and Taiji and even futuristic ones like BBO/DECIGO.

Section 4.4 dealt with additional aspects related to the initial conditions of the SGWB anisotropies for both adiabatic and isocurvature initial conditions. We first studied the dependence of the SGWB anisotropies on the initial (pre-BBN) equation of state and found that under the assumption of adiabaticity, the anisotropies turn out to be completely insensitive to the early universe eos. Physically, we understood this result as a consequence of the curvature perturbation on super-horizon scales, and saw that the anisotropies are affected by the equation of state *when* the curvature perturbation re-enters the horizon, but not before.

We then looked at the generation of isocurvature GW perturbations through the example of the curvaton mechanism. We found a roughly four-fold larger anisotropy amplitude in the simplest curvaton scenario of case (i) while case (ii) turned out to be more model-dependent. The CMB-GW cross-correlation in case (i) also provides an additional handle on the curvaton scenario, complementary to CMB constraints on non-Gaussianity and isocurvature. The generation of anisotropies in case (ii) as well as the possibility of anti-correlated GW and CMB maps requires a model-specific analysis and we plan to return to this topic in the near future.

Chapter 5

Primordial tensor non-Gaussianity at interferometer scales

This chapter presents the results of the following articles:

- **A. Malhotra**, E. Dimastrogiovanni, M. Fasiello, M. Shiraishi, "*Cross-correlations as a Diagnostic Tool for Primordial Gravitational Waves*", JCAP **03**, 088 (2021), [arxiv: 2012.03498] (appears as [1])
- E. Dimastrogiovanni, M. Fasiello, **A. Malhotra**, P. D. Meerburg and G. Orlando, "*Testing the Early Universe with Anisotropies of the Gravitational Wave Background*", JCAP **02**, 040 (2022), [arxiv: 2109.03077] (appears as [2])

5.1 Introduction

Having studied the anisotropies of gravitational wave backgrounds, we now look at their non-Gaussianity. Such higher order correlations ($n > 2$) of the primordial perturbations serves as an effective probe of the inflationary action, beyond the free field limit. In addition to scalar non-Gaussianity (section 3.4), inflationary models may also generate non-Gaussianity in the tensor sector. On CMB scales, this is

searched for in the auto and cross-bispectra involving the B-mode polarisation[1] e.g. $\langle BBB\rangle$, $\langle BTT\rangle$ etc. (see [429] for a review). Tensor non-Gaussianity may also leave imprints in the correlation functions involving the tracers of large scale-structure (so called "fossil effects") e.g. see [430–432].

In this chapter we focus on much smaller scales and analyse the detectability of tensor non-Gaussianity at interferometer scales. References [369, 370, 433, 434] have brought into question the feasibility of directly measuring the primordial bispectrum at interferometers through the 3-point function of the GW strain $\langle h^3\rangle$. The observed 3-point function at interferometers is highly suppressed as a consequence of propagation effects through large scale structure — incoming GW from different directions get phase shifted by *different* amounts which destroys the phase coherence of the inflationary GW. This renders not just the bispectrum, but also any odd n-point function of the strain h, completely unobservable [369, 370, 434]. The suppression occurs for all GW modes which re-enter the horizon during radiation domination and are relevant for interferometer/PTA scales.

A possible workaround is to consider specific momentum configurations which are not subject to such suppression. The ultra-squeezed limit is in one such configuration[2], with the long-wavelength mode being around the size of the present day cosmological horizon and the short wavelength modes taken to be at interferometer scales. The effect of the long-wavelength mode (which can either be a scalar or a tensor) is to induce a large scale modulation in the GW energy density contained within the short modes, leading to anisotropies in the GW background [292]. Thus, GW anisotropies provide an indirect probe of tensor non-Gaussianity in the squeezed limit. From a phenomenological point of view, the importance of the squeezed limit cannot be understated since it knows about the spin and mass of additional fields present during inflation (section 3.4). In the case of tensor non-Gaussianity, this implies the squeezed limit can provide us a handle on the fields sourcing GW, beyond what we can learn from the power spectrum alone.

This chapter is organised as follows. In section 5.2, I first describe the link between GW anisotropies and squeezed limit non-Gaussianity by deriving the result-

[1] Cross-correlations of μ-type spectral distortions with CMB anisotropies are also sensitive to primordial tensor non-Gaussianity [428].

[2] Another exception is the folded configuration, where the 3 momenta are aligned [435].

ing anisotropy and its cross-correlation with the CMB, extending to more general cases the results of [293]. I then provide model independent forecasts for the detection prospects of the non-linear parameter $f_{\rm NL}$ associated to squeezed tensor non-Gaussianity, assuming a detection of such anisotropies by interferometers. To complete the analysis and show that such scenarios can indeed by realised in nature, in section 5.3.1 I provide examples of inflationary models that can produce sufficiently large non-Gaussianity and consequently observable GW anisotropies which are larger than the propagation anisotropies discussed in the previous chapter. Section 5.4 provides a summary of the chapter.

5.2 GW anisotropies from tensor non-Gaussianity

As we already saw in chapter 4, cosmological gravitational wave backgrounds can have anisotropies arising from propagation or due to inhomogeneities in the production mechanism. Anisotropies arising as a consequence of primordial non-Gaussianity fall into the latter category and from here onward we shall refer to them as *intrinsic* anisotropies. We can understand the generation of these intrinsic anisotropies as follows. Let us consider primordial bispectra of the form $\langle h_{\boldsymbol{k}_1} h_{\boldsymbol{k}_2} X_{\boldsymbol{q}}\rangle$ where $X_{\boldsymbol{q}}$ can be a long-wavelength scalar or tensor perturbation at CMB scales and $h_{\boldsymbol{k}_{1,2}}$ are the short-wavelength tensor modes taken to be at interferometer scales. We work in the squeezed limit such that $q \to 0$ and $k_1 \simeq k_2$.[3] It is known that the existence of this coupling between the long and short wavelength modes leads to a modulation of the short mode power spectrum given by [292, 430–432, 436, 437],

$$\mathcal{P}_h^{\rm mod}(\boldsymbol{k},\boldsymbol{x}) = \sum_\lambda \mathcal{P}_h^\lambda(k)\left[1+\int_{q\ll k}\frac{d^3q}{(2\pi)^3}\, e^{i\boldsymbol{q}\cdot\boldsymbol{x}} F_{\rm NL}^{\lambda,{\rm tts}}(\boldsymbol{k},\boldsymbol{q})\zeta(\boldsymbol{q})\right], \tag{5.1}$$

in the case of $X=\zeta$. A formal derivation of this expression via the in-in formalism can be found in [294].

[3] Note that here we are specifically interested in the part of the squeezed bispectrum that violates the single-field consistency relations. Otherwise, when consistency relations are preserved, the physical effects of the squeezed bispectrum are highly suppressed (see section 3.4.3). These consistency relations are indeed violated in the models that we consider in section 5.3. For instance, in the spin-2 model this can be seen due to the presence of certain cubic order coefficients which appear in the bispectra but are absent in the tree level power spectra [127].

The non-linear parameter $F_{\rm NL}^{\lambda,\rm tts}$ is defined as,

$$F_{\rm NL}^{\lambda,\rm tts}(\boldsymbol{k},\boldsymbol{q}) = \frac{B^{\lambda}_{\rm tts}(\boldsymbol{k}-\boldsymbol{q}/2,-\boldsymbol{k}-\boldsymbol{q}/2,\boldsymbol{q})}{P_\zeta(q)P_h^\lambda(k)}, \quad \langle h^\lambda_{\boldsymbol{k}_1} h^{\lambda'}_{\boldsymbol{k}_2}\zeta_{\boldsymbol{k}_3\to 0}\rangle' = \delta^{\lambda\lambda'}B^\lambda_{\rm tts}(\boldsymbol{k}_1,\boldsymbol{k}_2,\boldsymbol{k}_3)\,. \tag{5.2}$$

The prime here is used to denote the fact that we have omitted the momentum conserving factor $(2\pi)^3\,\delta^{(3)}(\boldsymbol{k}_1+\boldsymbol{k}_2+\boldsymbol{k}_3)$ from the corresponding 3-point function. Before moving on to the case of the long-wavelength tensor mode ($X = h$), it is worth understanding what eq. (5.1) here actually represents. The quantity $\mathcal{P}_h(\boldsymbol{k},\boldsymbol{x})$ has the standard 'homogeneous' part, denoted by $\mathcal{P}_h(k)$ and a second part which is non-zero only in the presence of this long-short mode coupling. The $\boldsymbol{x}$-dependence, arising from the latter term should be understood as the power spectrum being evaluated in a volume which has linear dimension $L \ll 1/q$ and is centered around the point $\boldsymbol{x}$. As a consequence of this modulation, the GW energy density, which itself is proportional to the tensor power spectrum, varies across large-scales. The energy density in a given region thus depends upon the realisation of the long-wavelength mode within that region.[4] The results are applicable whenever there is a large hierarchy of scales between the long and short-wavelength modes.

Consequently, we can generalise the quantity $\Omega_{\rm GW}$ (defined in eq. (3.76)) to have an isotropic and anisotropic component [293] with

$$\overline{\Omega}_{\rm GW}(k,\eta_0) = \frac{k^2}{12a_0^2H_0^2}\mathcal{T}^2(k,\eta_0)\mathcal{P}_h(k,\eta_{\rm in})\,, \tag{5.3}$$

and

$$\boxed{\delta^{\rm tts}_{\rm GW}(k,\hat{n}) = \int_{q\ll k}\frac{d^3q}{(2\pi)^3}\,e^{-id\hat{n}\cdot\boldsymbol{q}}F^{\rm tts}_{\rm NL}(\boldsymbol{k},\boldsymbol{q})\zeta(\vec{q})}\,. \tag{5.4}$$

Here $\mathcal{T}(k,\eta_0)$ is the tensor transfer function (3.77), η_0 is the present-day conformal time, $\hat{n} = \boldsymbol{k}/k$ and $\mathbf{d} = -d\hat{n}$ with $d = \eta_0 - \eta_{\rm i}$ representing the conformal time elapsed between the horizon re-entry of the mode k to the present.

Note that here we have discarded the polarisation dependence of the bispectra and hence written $F_{\rm NL}^{\lambda,\rm tts} \equiv F_{\rm NL}^{\rm tts}$. In principle it is indeed possible to have a polarisation dependent bispectrum, i.e. $F_{\rm NL}^{\lambda_1,\rm tts} \neq F_{\rm NL}^{\lambda_2,\rm tts}$, however the models we shall consider in this chapter will not exhibit such a dependence.

[4] Refs. [291, 296] study a related phenomena in the context of the $\langle\zeta^3\rangle$ bispectrum. The modulation by the long mode can also lead to polarisation anisotropies of the GW background, as shown in [295].

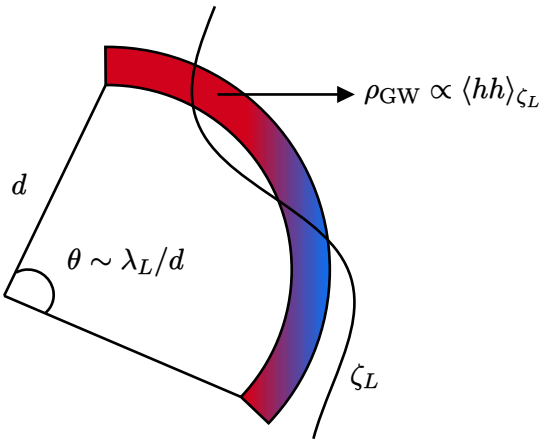

Figure 5.1: A schematic illustration of anisotropies generated from squeezed non-Gaussianity.

The case of the long-wavelength tensor can also be analysed similarly. In this case the modulated power spectrum reads [292]

$$\mathcal{P}_h^{\rm mod}(\boldsymbol{k},\boldsymbol{x}) = \mathcal{P}_h(k)\left[1+\int_{q\ll k}\frac{d^3q}{(2\pi)^3}\,e^{i\boldsymbol{q}\cdot\boldsymbol{x}}F_{\rm NL}^{\rm ttt}(\boldsymbol{k},\boldsymbol{q})\sum_\lambda h^\lambda(\boldsymbol{q})\epsilon_{ij}^\lambda(\hat{q})\hat{n}^i\hat{n}^j\right], \tag{5.5}$$

where we have again ignored polarisation dependence in $F_{\rm NL}^{\rm ttt}$,

$$F_{\rm NL}^{\rm ttt}(\boldsymbol{k},\boldsymbol{q}) = \frac{B_{\rm ttt}(\boldsymbol{k}-\boldsymbol{q}/2,-\boldsymbol{k}+\boldsymbol{q}/2,\boldsymbol{q})}{P_h(q)P_h(k)}\,. \tag{5.6}$$

$B_{\rm ttt}(\boldsymbol{k}_1,\boldsymbol{k}_2,\boldsymbol{k}_3)$ here is the squeezed-limit primordial bispectrum defined as

$$\langle h_{\boldsymbol{k}_1}^{\lambda_1}h_{\boldsymbol{k}_2}^{\lambda_1}h_{\boldsymbol{k}_3\to 0}^{\lambda_3}\rangle' = -\delta^{\lambda_2\lambda_3}\,\epsilon_{ij}^{\lambda_3}(k_3)\,k_2^ik_1^j\,B_{\rm ttt}(\boldsymbol{k}_1,\boldsymbol{k}_2,\boldsymbol{k}_3)\,. \tag{5.7}$$

As a result, the anisotropies are now given by

$$\boxed{\delta_{\rm ttt}^{\rm GW}(k,\hat{n}) = -\int_{q\ll k}\frac{d^3q}{(2\pi)^3}\,e^{-id\hat{n}\cdot\boldsymbol{q}}F_{\rm NL}^{\rm ttt}(\boldsymbol{k},\boldsymbol{q})\sum_\lambda h^\lambda(\boldsymbol{q})\epsilon_{ij}^s(\hat{q})\hat{n}^i\hat{n}^j}\,. \tag{5.8}$$

From the expressions in eqs. (5.4) and (5.8), we can estimate the typical magnitude of these anisotropies to be,

$$\begin{aligned}\delta_{\rm tts}^{\rm GW} &\sim F_{\rm NL}^{\rm tts}\sqrt{A_{\rm s}}\\ \delta_{\rm ttt}^{\rm GW} &\sim F_{\rm NL}^{\rm ttt}\sqrt{rA_{\rm s}}\,.\end{aligned} \tag{5.9}$$

We can recall from chapter 4 that the propagation anisotropies have magnitude $\delta_{\rm prop}^{\rm GW}\sim\sqrt{A_{\rm s}}$, thus for $F_{\rm NL}\gg 1$ the intrinsic anisotropies can be much larger than the ones from propagation for the inflationary GW. We now evaluate these explicitly, for both the scalar and tensor case.

Relation to line-of-sight approach:

The above results, combined with eq. (4.11) tell us that we can incorporate the intrinsic anisotropy as an initial condition term in the line-of-sight formalism. For the anisotropies from the TTS bispectrum, this reads

$$\left[4 - \frac{\partial \ln \overline{\Omega}_{\rm GW}(k)}{\partial \ln k}\right] \Gamma_I(\eta_{\rm in}, \boldsymbol{q}, k, \hat{n}) = F^{\rm tts}_{\rm NL}(\boldsymbol{q}, \boldsymbol{k}) \zeta(\eta_{\rm in}, \vec{q}) \,, \tag{5.10}$$

and similarly for the TTT bispectrum.

5.2.1 Angular power spectra

In this section we calculate the angular power spectrum of the intrinsic anisotropies defined as

$$\langle \delta^{\rm GW}_{\ell m} \delta^{\rm GW *}_{\ell' m'} \rangle \equiv \delta_{\ell \ell'} \delta_{m m'} C^{\rm GW}_{\ell} \,, \tag{5.11}$$

under the assumption of statistical isotropy of the background.

Here, $\delta^{\rm GW}_{\ell m}$ denote the coefficients of the spherical harmonic expansion of $\delta^{\rm GW}$

$$\delta^{\rm GW}_{\ell m} = \int d^2\hat{n}\, \delta^{\rm GW}(\hat{n}) Y^*_{\ell m}(\hat{n}) \,. \tag{5.12}$$

To obtain analytical estimates and understand the behaviour of the angular power spectra, we make two simplifying assumptions: *(i)* a scale-invariant spectrum for the large scale perturbations, i.e $\mathcal{P}_\zeta = A_{\rm s}$ and $\mathcal{P}_h = r A_{\rm s}$ and *(ii)* scale-invariant $F^{\rm tts}_{\rm NL}$, $F^{\rm ttt}_{\rm NL}$. For brevity's sake, we only state the final expressions and highlight the important characteristics of the angular power spectra. The full derivations of the relevant expressions can be found in appendix D where we also discuss how to calculate the intrinsic anisotropies in a statistically anisotropic background.

5.2.1.1 Anisotropies from $\langle hh\zeta \rangle$ bispectrum

For this case we shall consider two possibilities. The first and the simplest one is when there is no dependence of the bispectrum on the angle between $\boldsymbol{q}$ and $\boldsymbol{k}$ in eq. (5.4).[5] The second one is where the bispectrum has a quadrupolar angular dependence in

[5] This kind of angular depence can arise in SFSR inflation [151], even though the signal is extremely small, and also in supersolid inflation in the regime where GW are sourced by second order scalars [146, 294].

$\hat{q}\cdot\hat{k}$, arising in inflationary models of the type considered in [127, 140, 141] which we shall also describe in sections 5.3.1 and 5.3.2.

Monopolar TTS

Let us begin with the case of no angular dependence in the TTS bispectra, i.e. we can write

$$F_{\rm NL}^{\rm tts}(\boldsymbol{k},\boldsymbol{q}) = \tilde{F}_{\rm NL}^{\rm tts}\,. \tag{5.13}$$

The anisotropies for a bispectrum of this form were already calculated in ref [293] with the result,

$$C_\ell^{\rm GW,tts} = \frac{2}{\pi}\int_{q\ll k} q^2 dq\, j_\ell(qd)^2 \tilde{F}_{\rm NL}^{\rm tts}(q,k)^2 P_\zeta(q)\,. \tag{5.14}$$

The integration over q leads to,

$$\boxed{C_\ell^{\rm GW,tts} \simeq \left(\tilde{F}_{\rm NL}^{\rm tts}\right)^2 \frac{2\pi A_S}{\ell(\ell+1)}}\,. \tag{5.15}$$

In fact, the ℓ-dependence of these anisotropies is exactly the same as that of the SW term in the propagation anisotropies of the CMB [75] and GW [255, 256].

Quadrupolar TTS

In the case where the bispectrum has a quadrupolar angular dependence in $\hat{q}\cdot\hat{k}$, we parameterise $F_{\rm NL}^{\rm tts}$ as

$$F_{\rm NL}^{\rm tts}(\boldsymbol{k},\boldsymbol{q}) = \tilde{F}_{\rm NL}^{\rm tts}(q,k)\left[\frac{4\pi}{5}\sum_M Y_{2M}(\hat{k})Y_{2M}^*(\hat{q})\right] = \tilde{F}_{\rm NL}^{\rm tts}\,\mathcal{P}_2(\hat{q}\cdot\hat{k})\,, \tag{5.16}$$

where $\mathcal{P}_2$ is the second Legendre polynomial. This leads to (see appendix D),

$$C_\ell^{\rm GW,tts} = 16\pi^2\sum_{L_1,L_2} i^{L_1-L_2} h^2_{\ell L_1 2} h^2_{\ell L_2 2}\frac{H_{L_1L_2}}{(2\ell+1)^2}, \tag{5.17}$$

where

$$h_{\ell_1\ell_2\ell_3} \equiv \sqrt{\frac{(2\ell_1+1)(2\ell_2+1)(2\ell_3+1)}{4\pi}}\begin{pmatrix}\ell_1 & \ell_2 & \ell_3\\ 0 & 0 & 0\end{pmatrix}, \tag{5.18}$$

and

$$H_{L_1L_2} \equiv \frac{2}{25\pi}\int_{q\ll k} q^2 dq\, j_{L_1}(qd) j_{L_2}(qd)\tilde{F}_{\rm NL}^{\rm tts}(k,q)^2 P_\zeta(q)\,. \tag{5.19}$$

We can further simplify this assuming scale invariance and using the identity (D.18) to obtain (for $\ell > 2$)

$$\boxed{C_\ell^{\rm GW,tts} \simeq \frac{2\pi}{5}\frac{(\tilde{F}_{\rm NL}^{\rm tts})^2 A_S}{(\ell-2)(\ell+3)}}\,. \tag{5.20}$$

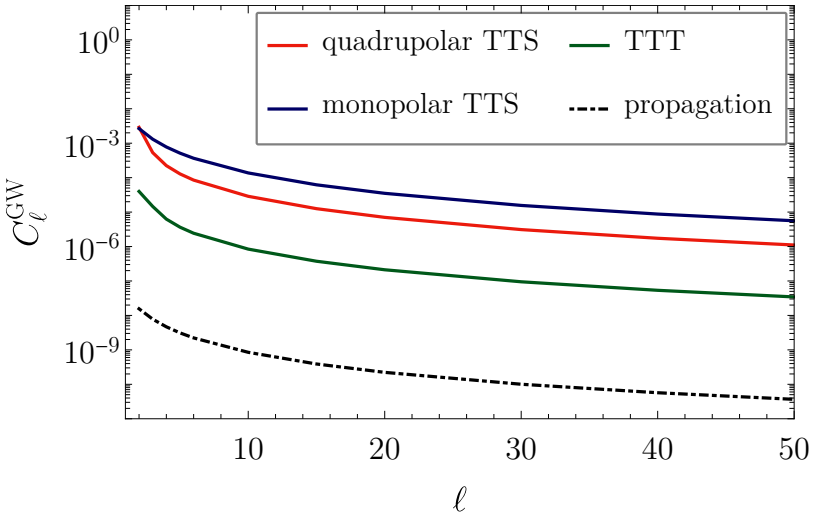

Figure 5.2: The auto-correlation of the SGWB anisotropies as a function of ℓ plotted for $|\tilde{F}^{\rm tts}_{\rm NL}| = |F^{\rm ttt}_{\rm NL}| = 10^3$ and the tensor-scalar ratio $r = 0.05$.[6]

5.2.1.2 Anisotropies from $\langle hhh \rangle$ bispectrum

In this case we find for the corresponding correlator (see appendix D)

$$C_\ell^{\rm GW,ttt} = \frac{(\ell-1)\ell(\ell+1)(\ell+2)}{2\pi} \sum_{s=\pm 2} \int_{q\ll k} q^2 dq\, F^{\rm ttt}_{\rm NL}(k,q)^2 P_h^s(q) \frac{j_\ell(qd)^2}{(qd)^4} \,. \tag{5.21}$$

Assuming scale independent $F^{\rm ttt}_{\rm NL}$ and a scale invariant $P_h = (2\pi^2/q^3) r A_S$, this becomes

$$\boxed{C_\ell^{\rm GW,ttt} \simeq \frac{4\pi\,(F^{\rm ttt}_{\rm NL})^2\, r A_S}{15(\ell-2)(\ell+3)}} \,, \tag{5.22}$$

where we have used eq. (D.25).

5.2.1.3 Summary plot

The resulting anisotropies are plotted in fig. 5.2 taking $|\tilde{F}^{\rm tts}_{\rm NL}| = |F^{\rm ttt}_{\rm NL}| = 10^3$ and $r = 0.05$. The figure validates our estimate for the magnitude of the anisotropies in eq. (5.9), for $|F_{\rm NL}| \gg 1$, the intrinsic anisotropies are much larger than the propagation anisotropies, roughly by a factor $(\tilde{F}^{\rm tts}_{\rm NL})^2$ in the TTS case and $r(F^{\rm ttt}_{\rm NL})^2$ in the TTT case.

[6] Note that this value of r is now excluded by CMB data with the current upper limit being $r < 0.032$ at 95% CL [35, 114]. This will not significantly affect our analysis in section 5.3.1, as long as $rF^{\rm ttt}_{\rm NL} \gg 1$ still holds true.

5.2.2 CMB-GW cross-correlation

The intrinsic anisotropies, arising from the modulation of the small-scale tensor power spectrum by the long-wavelength perturbations, are correlated with the CMB anisotropies as well. We now calculate this correlation and discuss how the correlation depends on the angular structure of $F_{\rm NL}$. Once again, for analytic estimates we shall make the assumption of scale invariance throughout and only consider the SW term of the CMB anisotropy.

SGWB anisotropies also have a non-zero correlation with the E-mode polarisation anisotropies of the CMB. However, this has been found to be smaller than the GW-T cross-correlation by at least one order of magnitude [304]. We also recall this from section 4.3, where we saw that the GW-E cross-correlation provided a negligible contribution to the total GW-CMB cross-correlation. Finally, since the B-modes are parity-odd, the cross-correlation with CMB B-mode polarisation will be non-zero only when there is parity violation. The same happens in the CMB case where $\langle TB\rangle = 0$ if parity is preserved [438].

5.2.2.1 Anisotropies from $\langle hh\zeta\rangle$ bispectrum

Monopolar TTS

The monopolar case was first analysed in [293] with the result,

$$C_\ell^{\rm GW-T} = \frac{4\pi}{5}\tilde{F}_{\rm NL}^{\rm tts} A_S \int_{q\ll k} \frac{dq}{q}\, j_\ell(qd) j_\ell(q r_{\rm lss})\,. \tag{5.23}$$

where $r_{\rm lss}$ is the distance to the last scattering surface. As a first approximation, we can set $d \approx r_{\rm lss}$ to get

$$C_\ell^{\rm GW-T} \simeq \frac{4\pi}{5}\tilde{F}_{\rm NL}^{\rm tts} \frac{A_S}{2\ell(\ell+1)}\,. \tag{5.24}$$

If we do not make the above approximation and keep $d \neq r_{\rm lss}$ we find

$$\boxed{C_\ell^{\rm GW-T} = \frac{\pi^{3/2}}{5}\tilde{F}_{\rm NL}^{\rm tts} A_S \left(\frac{r_{\rm lss}}{d}\right)^\ell \frac{\Gamma(\ell)}{\Gamma(\ell+\frac{3}{2})}\, {}_2F_1\left(-\frac{1}{2}, \ell; \ell+\frac{3}{2}; \frac{r_{\rm lss}^2}{d^2}\right)}\,. \tag{5.25}$$

in terms of the Gamma functions and the Hypergeometric function ${}_2F_1$ (see appendix D). The cross-correlation scales with ℓ in the same manner as the cross-correlation of the SW term of the GW propagation anisotropies with the CMB SW term, which is not surprising given that they share the same ℓ-dependence.

An interesting feature of this cross-correlation is that it decays strongly with ℓ as a consequence of the factor $(r_{\rm lss}/d)^\ell$.[7] This suppression results from the fact that GW 'last scattered' much earlier than the CMB ($r_{\rm lss}/d < 1$) which leads to the anisotropies becoming uncorrelated on smaller angular scales (large ℓ). Since $d \approx r_{\rm lss}$, the approximate result of eq. (5.24) does work well for small ℓ but not for $\ell \gtrsim 20$ (see Figure 5.3). Numerically, we find the following scaling with ℓ

$$C_\ell^{\rm GW-T,tts} \propto \left(\frac{r_{\rm lss}}{d}\right)^\ell \frac{1}{\ell^2}\,. \tag{5.26}$$

Quadrupolar TTS

In this case we find,

$$C_\ell^{\rm GW-T,tts} = 4\pi \sum_L i^{L-\ell} h^2_{2L\ell} \frac{G_{L\ell}}{2\ell+1}\,, \tag{5.27}$$

where

$$G_{\ell_1\ell_2} = \frac{2}{25\pi}\int_{q\ll k} q^2 dq\, j_{\ell_1}(qd) j_{\ell_2}(q r_{\rm lss}) \tilde{F}^{\rm tts}_{\rm NL}(k,q) P_\zeta(q). \tag{5.28}$$

and the sum is over $L = \ell-2, \ell, \ell+2$. This above expression can be analytically estimated to be (appendix D)

$$\boxed{C_\ell^{\rm GW-T,tts} = \frac{\pi^{3/2}\tilde{F}^{\rm tts}_{\rm NL} A_S}{20}\left(\frac{r_{\rm lss}}{d}\right)^\ell \left(\frac{r_{\rm lss}}{d}-1\right)\left(\frac{r_{\rm lss}}{d}+1\right)\Delta F_\ell}\,, \tag{5.29}$$

where ΔF_ℓ is given by eq. (D.37).

Numerically, we obtain the following scaling with ℓ for the quadrupolar case,

$$C_\ell^{\rm GW-T,tts} \propto \left(\frac{r_{\rm lss}}{d}\right)^\ell \frac{1}{\ell^{1/2}}\,. \tag{5.30}$$

In addition to the expected $(r_{\rm lss}/d)^\ell$ that we saw previously, we also notice that when $d \to r_{\rm lss}$, the cross-correlation drops to zero. Physically, this is explained by the fact that the GW source term is locally a quadrupole while the CMB SW is a monopole. If the sources are located at the same point ($d = r_{\rm lss}$), the cross-correlation will be exactly zero due to the orthogonality of the Legendre polynomials $\mathcal{P}_\ell(\hat{k}\cdot\hat{q})$ and $\mathcal{P}_{\ell'}(\hat{k}\cdot\hat{q})$ for $\ell \neq \ell'$.

The results of this section indicate that the cross-correlation for the quadrupolar TTS will be smaller than the monopolar TTS. This will have significant consequences

[7] This has also been pointed out in ref. [293] and in ref. [305] for the propagation anisotropies.

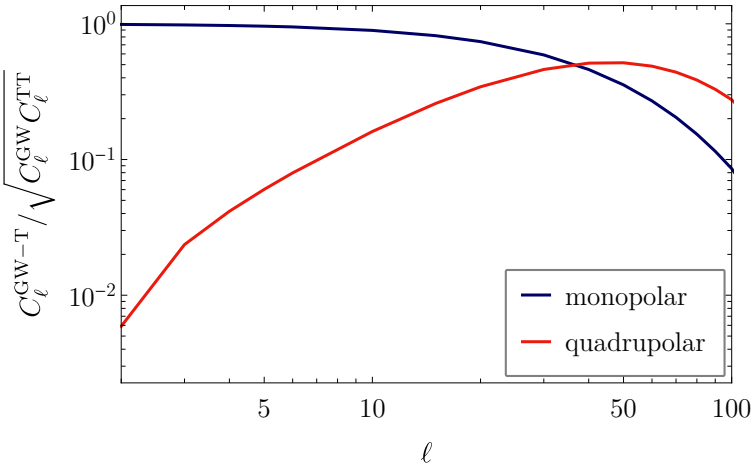

Figure 5.3: The ratio $C_\ell^{\mathrm{GW-T}}/\sqrt{C_\ell^{\mathrm{GW}}C_\ell^{\mathrm{TT}}}$ plotted for the monopolar and the quadrupolar TTS cross-correlation. The corresponding ratio for the induced anisotropies follows the same curve as the one for the monopolar TTS.

for cross-correlation-based constraints on tensor non-Gaussianity through the GW anisotropies. In the cosmic variance limit, the relative error in the estimates of the individual $C_\ell^{\mathrm{GW-T}}$ are given by (e.g. see [439]),

$$\delta C_\ell^{\mathrm{GW-T}} \propto \left[\frac{C_\ell^{\mathrm{TT}}C_\ell^{\mathrm{GW}}}{(2\ell+1)(C_\ell^{\mathrm{GW-T}})^2}\right]^{1/2} . \tag{5.31}$$

This ratio is shown in Fig. 5.3 for the monopolar and the quadrupolar cross-correlations. For the low-ℓ range[8] $(C_\ell^{\mathrm{GW-T}})^2 \simeq C_\ell^{\mathrm{GW}}C_\ell^{\mathrm{TT}}$ for the monopolar TTS. On the other hand we have $(C_\ell^{\mathrm{GW-T}})^2 \ll C_\ell^{\mathrm{GW}}C_\ell^{\mathrm{TT}}$ for the quadrupolar TTS. As a consequence, we can expect cross-correlations to have more constraining power in the case of the monopolar TTS which shall be confirmed when perform our forecasts in section 5.2.3.

Anisotropies from $\langle hhh\rangle$ bispectrum

The final cross-correlation that we study is that of the intrinsic anisotropies from the TTT bispectrum with the CMB temperature anisotropies sourced by large scale tensor perturbations. The latter can be written as [441],

$$\delta^{\mathrm{T}}(\hat{n}) = -\frac{1}{2}\sum_{s=\pm 2}\int d\eta\,\frac{d^3q}{(2\pi)^3}\frac{\partial h_{\boldsymbol{q}}^s}{\partial\eta}\epsilon_{ij}^s(\hat{q})\hat{n}^i\hat{n}^j e^{-i\chi(\eta)\hat{n}\cdot\boldsymbol{q}} , \tag{5.32}$$

[8] The higher-ℓ range turns out to be not so relevant for current and near-future observations, due to the limited angular resolution of current and future planned interferometers. Estimates indicate that this will be limited to $\ell_{\mathrm{max}} \sim 10-15$ [243, 403–405, 440].

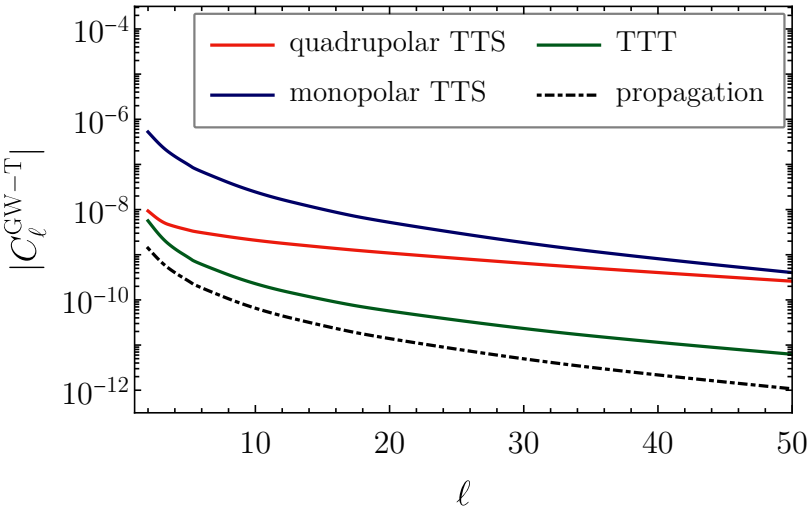

Figure 5.4: The cross-correlation of the SGWB anisotropies as a function of ℓ plotted for $|\tilde{F}_{\rm NL}^{\rm tts}| = |F_{\rm NL}^{\rm ttt}| = 10^3$ and a tensor-to-scalar ratio $r = 0.05$.

The resulting cross-correlation is (see appendix D)

$$C_\ell^{\mathrm{GW-T,ttt}} = \frac{(\ell-1)\ell(\ell+1)(\ell+2)}{4\pi} \sum_{s=\pm 2} \int_{q\ll k} q^2 dq\, F_{\rm NL}^{ttt}(\boldsymbol{k},\boldsymbol{q}) P_h^s(q) \frac{j_\ell(qd)}{(qd)^2} \times \int d\eta\, \frac{\partial \mathcal{T}(k,\eta)}{\partial \eta} \frac{j_\ell(q\chi(\eta))}{(q\chi(\eta))^2}\,. \tag{5.33}$$

To evaluate this, we limit ourselves to large-scale modes which re-enter the horizon after matter domination ($k \geq k_{\rm eq}$). Their post-horizon re-entry evolution can be written in terms of the tensor transfer function as [442],

$$\mathcal{T}_h(k,\eta) = \frac{3 j_1(k,\eta)}{k\eta}\,. \tag{5.34}$$

This gives

$$C_\ell^{\mathrm{GW-T,ttt}} \simeq \frac{(\ell-1)\ell(\ell+1)(\ell+2)}{4\pi} \sum_{s=\pm 2} \int_{1/\eta_0}^{k_{\rm eq}} q^2 dq\, F_{\rm NL}^{\rm ttt}(\boldsymbol{k},\boldsymbol{q}) P_h^s(q) \frac{j_\ell(qd)}{(qd)^2} \times \int_{\eta_{\rm rec}}^{\eta_0} d\eta\, \frac{\partial \mathcal{T}(k,\eta)}{\partial \eta} \frac{j_\ell(q\chi(\eta))}{(q\chi(\eta))^2}\,. \tag{5.35}$$

which we evaluate numerically.

The different cross-correlations are plotted in fig. 5.4 with the same parameter choices as fig. 5.2.

5.2.3 Model independent forecasts

In this section we use the Fisher matrix formalism to present forecasts for the expected error in measuring $F_{\rm NL}$ with GW interferometers. We focus only on $F_{\rm NL}^{\rm tts}$ here and

analyse the case of $F_{\rm NL}^{\rm ttt}$ separately in section 5.3.1.

The Fisher matrix is given by [443],

$$F_{ij} = \sum_{XY} \sum_{\ell=\ell_{\rm min}}^{\ell_{\rm max}} \frac{\partial C_\ell^X}{\partial \theta_i} \left(\mathscr{C}_\ell^{XY}\right)^{-1} \frac{\partial C_\ell^Y}{\partial \theta_j}\,, \tag{5.36}$$

where $X, Y = \{\rm TT, GW, GW\text{-}T\}$ and $\vec{\theta_i}$ is the vector representing the parameters being measured. The matrix $\mathscr{C}_\ell$ is defined as,

$$\mathscr{C}_\ell = \frac{2}{2\ell+1} \begin{bmatrix} (C_\ell^{\rm TT})^2 & (C_\ell^{\rm GW-T})^2 & C_\ell^{\rm TT} C_\ell^{\rm GW-T} \\ (C_\ell^{\rm GW-T})^2 & (C_\ell^{\rm GW})^2 & C_\ell^{\rm GW} C_\ell^{\rm GW-T} \\ C_\ell^{\rm TT} C_\ell^{\rm GW-T} & C_\ell^{\rm GW} C_\ell^{\rm GW-T} & \frac{1}{2}(C_\ell^{\rm GW-T})^2 + \frac{1}{2} C_\ell^{\rm TT} C_\ell^{\rm GW} \end{bmatrix}, \tag{5.37}$$

with,

$$\begin{aligned} C_\ell^{\rm TT} &\simeq \frac{2\pi A_S}{25\ell(\ell+1)}, \\ C_\ell^{\rm GW} &= C_\ell^{\rm GW,tts} + C_\ell^{\rm GW,prop} + N_\ell^{\rm GW}, \\ C_\ell^{\rm GW-T} &= C_\ell^{\rm GW-T,tts} + C_\ell^{\rm GW-T,prop}. \end{aligned} \tag{5.38}$$

The $N_\ell^{\rm GW}$ represent the noise angular power spectra of the detector network being used for the measurement. For our forecasts, we make use of the expected sensitivities of ET-CE, LISA-Taiji, BBO and SKA and plot the $N_\ell^{\rm GW}$ for these in fig. 5.5. The calculation of the noise spectra and the detector configurations used are described further in appendix C.

Finally, the quantity $\Delta\theta_i = \sqrt{(F^{-1})_{ii}}$ then represents the minimum expected error in the measurement of the parameter θ_i. In fig. 5.6 we plot the expected relative error, defined as

$$\delta \tilde{F}_{\rm NL}^{\rm tts} \equiv \Delta \tilde{F}_{\rm NL}^{\rm tts} / \tilde{F}_{\rm NL}^{\rm tts}\,, \tag{5.39}$$

taking a scale independent $\tilde{F}_{\rm NL}^{\rm tts} = 10^3$ and for different values of $\Omega_{\rm GW}$,[9] which we also take to be scale-independent in each case. We remind the reader that we have defined

$$F_{\rm NL}^{\rm tts}(\boldsymbol{k}, \boldsymbol{q}) = \tilde{F}_{\rm NL}^{\rm tts}\, \mathcal{P}_\ell(\hat{q}\cdot\hat{k})\,. \tag{5.40}$$

[9] The effects of the parameters $\tilde{F}_{\rm NL}^{\rm tts}$ and $\bar{\Omega}_{\rm GW}$ are nearly degenerate, since observations are sensitive to the combination $\bar{\Omega}_{\rm GW} \times \tilde{F}_{\rm NL}^{\rm tts}$.

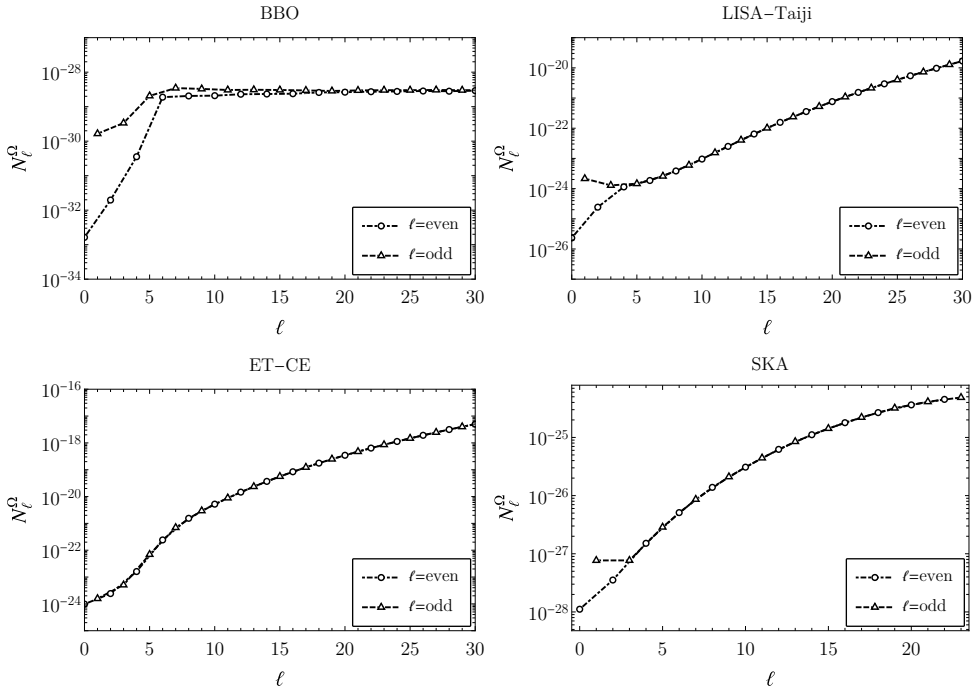

Figure 5.5: N_ℓ^Ω plotted for BBO, LISA-Taiji, ET-CE and SKA at $f_{\rm ref}^{\rm BBO} = 0.1$ Hz, $f_{\rm ref}^{\rm LISA-Taiji} = 0.01$ Hz, $f_{\rm ref}^{\rm ET-CE} = 63$ Hz and $f_{\rm ref}^{\rm SKA} = 1\,{\rm year}^{-1}$ Hz. The quantity $N_\ell^{\rm GW}$ is defined as $N_\ell^{\rm GW} \equiv N_\ell^\Omega/\bar{\Omega}_{\rm GW}^2$.

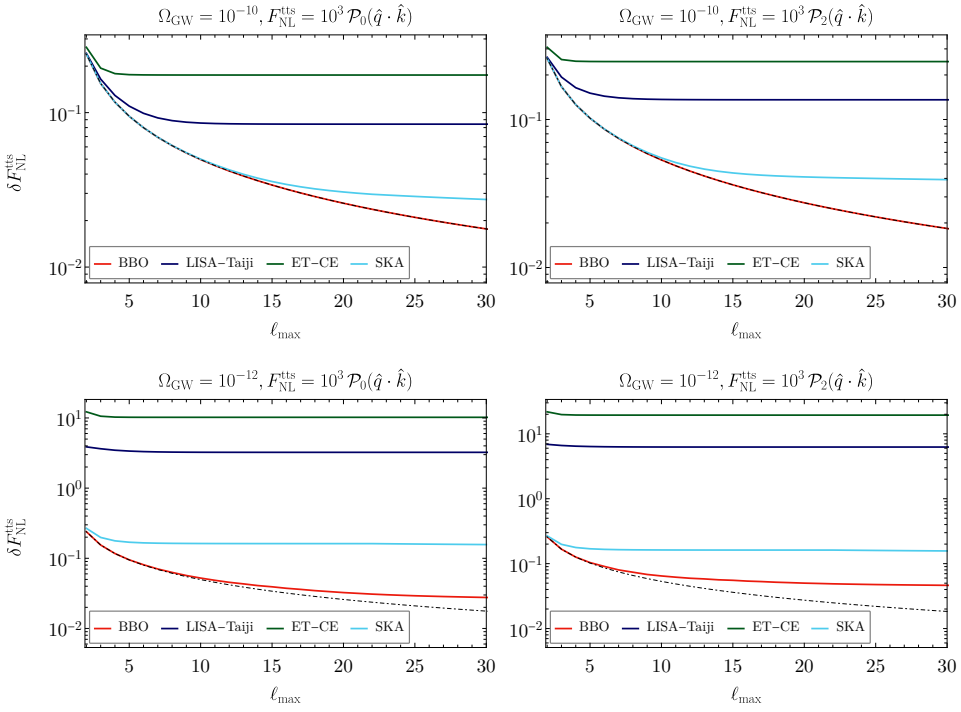

Figure 5.6: The relative error in the measurement of $\tilde{F}_{\rm NL}^{\rm tts}$ as a function of $\ell_{\rm max}$ for BBO, SKA, LISA-Taiji and ET-CE. The dashed curves show the errors for an idealised, cosmic variance limited measurement.

We see from the figure that with larger $\Omega_{\rm GW} = 10^{-10}$ we can achieve a smaller relative error $\delta\tilde{F}^{\rm tts}_{\rm NL}$. For instance, we obtain $\delta\tilde{F}^{\rm tts}_{\rm NL} \simeq 10^{-2}$ with BBO for both the monopolar and the quadrupolar $F^{\rm tts}_{\rm NL}$ and a slightly increased error with SKA. The lower overall as well as angular sensitivity of the ET-CE and LISA-Taiji networks means that the relative error turns out to be larger, of the order 10^{-1} and saturates within the first few multipoles $\ell_{\rm max} \sim 10$. In fact, 3G detectors like LISA-Taiji and ET-CE are unlikely to provide any constraints on the anisotropies for a monopole amplitude $\Omega_{\rm GW} \lesssim 10^{-10}$. For $\Omega_{\rm GW} = 10^{-12}$, we find that only BBO and SKA are able to detect $F^{\rm tts}_{\rm NL}$, reaching a relative error $\delta\tilde{F}^{\rm tts}_{\rm NL} \sim 10^{-1}$. In fact, for both values of $\Omega_{\rm GW}$ BBO is almost cosmic variance limited, especially for the monopolar TTS. Finally, as expected from the arguments of the previous section, the error is smaller in the case of the monopolar TTS as compared to the quadrupolar one.

Astrophysical foregrounds

The forecasts of the previous section assumed only the presence of cosmological backgrounds in the total SGWB. However, gravitational wave backgrounds of astrophysical origin, arising from the superposition of signals from numerous unresolved mergers are also expected to be present and contribute to the anisotropies [257–274]. Techniques to separate the astrophysical and cosmological background monopoles using their different properties — frequency range, spectral shape, time dependence — have been proposed in [275–284].

Astrophysical anisotropies trace the distribution of large-scale structure and are strongly correlated with observables such as galaxy clustering and weak-lensing [258, 259, 266, 269, 270, 274]. The cross-correlation of astrophysical anisotropies with those of the CMB has also been studied recently in [305]. The results of ref. [305] suggest that cosmological background anisotropies have a stronger correlation with the CMB, compared to astrophysical ones. This fact may be exploited to detect cosmological background anisotropies in the presence of astrophysical backgrounds.

To test the effectiveness of this idea, we compute the signal to noise ratio of the cross-correlation of the CMB anisotropies with the intrinsic GW anisotropies studied in this chapter, in the presence of an astrophysical GW background. We make the simplifying assumption of negligible astrophysical-CMB cross-correlation. The resulting SNR is

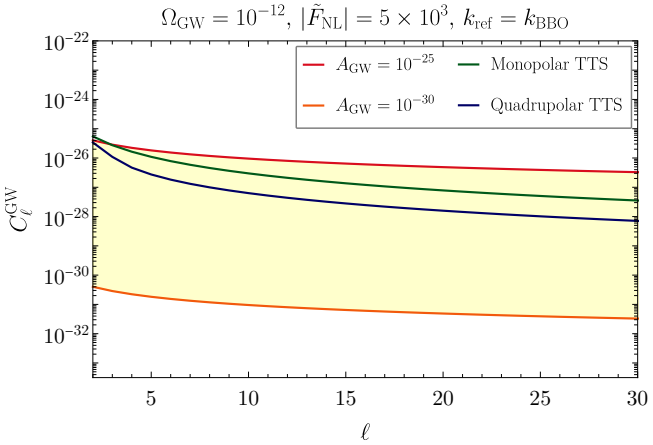

Figure 5.7: The $C_\ell^{\rm GW}$ for the astrophysical background (yellow shaded region) and for the CGWB with $\Omega_{\rm GW} = 10^{-12}, |\tilde{F}_{\rm NL}^{\rm tts}| = 5 \times 10^3$. We have assumed an astrophysical background of the form $(\ell+1/2)C_\ell = A_{\rm GWB}$. For comparison the $C_\ell^{\rm GW}$ of the CGWB have been rescaled as $C_\ell^{\rm GW} \to \overline{\Omega}_{\rm GW}^2 C_\ell^{\rm GW}$.

defined as

$$\text{SNR} = \left[\sum_{\ell_{\rm min}}^{\ell_{\rm max}} (2\ell+1) \frac{\left(C_\ell^{\rm GW-T,signal}\right)^2}{\left(C_\ell^{\rm GW-T,total}\right)^2 + C_\ell^{\rm GW,total} C_\ell^{\rm TT}}\right]^{1/2}, \tag{5.41}$$

where

$$\begin{aligned} C_\ell^{\rm GW-T,signal} &= C_\ell^{\rm GW-T,tts} \\ C_\ell^{\rm GW-T,total} &= C_\ell^{\rm GW-T,signal} + C_\ell^{\rm GW-T,prop}\,, \\ C_\ell^{\rm GW,total} &= C_\ell^{\rm GW,tts} + C_\ell^{\rm GW,prop} + C_\ell^{\rm GW,astro} + N_\ell^{\rm GW}\,. \end{aligned} \tag{5.42}$$

Based on the results of [259–261], we assume an astrophysical background of the type

$$(\ell + 1/2) C_\ell^{\rm GW,astro} \approx A_{\rm GWB}\,, \tag{5.43}$$

with $A_{\rm GWB} = \{10^{-25}, 10^{-30}\}$. The upper and lower limits correspond to the expected amplitude around $f = 63$ Hz and $f = 0.01$ Hz respectively [260, 261].[10] We plot the resulting SNR in fig. 5.8 where, once again, we find the SNR for the monopolar case to be greater than the quadrupolar one.

We also see that the intrinsic anisotropies can still be detected even assuming the upper limit for the astrophysical anistropies, even though in this case the astrophysical signal is larger than the intrinsic anisotropies $C_\ell^{\rm GW,tts}$ if $\Omega_{\rm GW} < 10^{-12}$ and $|\tilde{F}_{\rm NL}^{\rm tts}| < 5 \times 10^3$ (see Fig. 5.7). In the quadrupolar case, a similar magnitude for the SNR arises only when $A_{\rm GWB} \leq 10^{-27}$.

[10] Note that these C_ℓ are not defined relative to the monopole, in contrast to the C_ℓ of the primordial GW background.

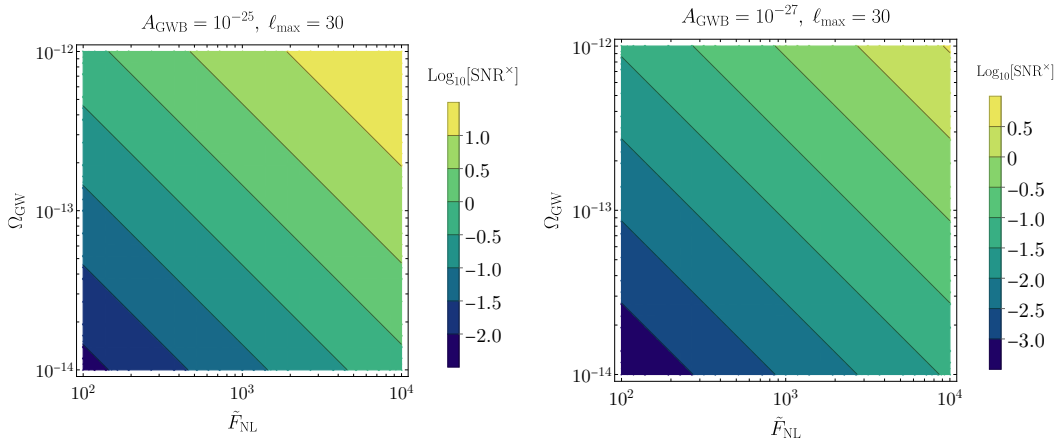

Figure 5.8: Left : SNR for the GW-CMB cross-correlation arising from the monopolar TTS bispectrum plotted as a function of $\Omega_{\rm GW}$ and $|\tilde{F}_{\rm NL}^{\rm tts}|$, taking $(\ell+1/2)C_\ell = A_{\rm GWB}$ for the astrophysical background. Right: SNR for the same cross-correlation but for the quadrupolar TTS bispectrum.

5.3 Inflationary models

We now discuss two specific models of inflation capable of generating the characteristic non-Gaussian signatures studied in this chapter. The first model is based on a the presence of an additional light (compared to H) spin-2 field present during inflation [127]. The second model, dubbed Solid inflation, features the breaking of space reparametrisation symmetry during inflation [140].

5.3.1 Spin-2 Model

The spin-2 model, first introduced in [127] and also studied in [128, 129], presents an effective field theory approach to the dynamics of the light spin-2 field σ_{ij}, which is taken to be non-minimally coupled to the inflaton.[11]

The model is described by the action

$$S = S_\pi + S_\sigma + S_{\rm int}\,, \tag{5.44}$$

where S_π denotes the slow-roll dynamics in the single-field EFT of inflation [139], S_σ is the free-field action for the spin-2 field and $S_{\rm int}$ containts quadratic and cubic order interaction terms between π and σ.[12] The interaction Lagrangian takes the

[11] Coupling σ_{ij} directly to the inflaton allows it to be light compared to the inflationary Hubble scale, thereby circumventing the *Higuchi* bound [444].

[12] As in ref. [127], we assume a negligible background value for the σ field.

form [127],

$$\begin{aligned}\mathcal{S}_{\rm int} = & \int d\eta\, d^3x\, a^4\Big[-\frac{g}{\sqrt{2\epsilon}H}a^{-2}\partial_i\partial_j\pi_c\sigma^{ij}+\frac{1}{2}a^{-1}g\,h'_{c,ij}\sigma^{ij}\Big] \\ & + \int d\eta\, d^3x\, a^4\Big[-\frac{g}{2\epsilon H^2 M_{\rm Pl}}a^{-2}(a^{-1}\partial_i\pi_c\partial_j\pi_c\sigma'^{ij} \\ & \qquad + 2H\partial_i\pi_c\partial_j\pi_c\sigma^{ij}) - \mu(\sigma_{ij})^3+\dots\Big]\,. \end{aligned} \tag{5.45}$$

Here, we defined the canonically normalised fields, $h_c \equiv hM_{\rm Pl}$, with h_{ij} the usual tensor perturbations of the metric and $\pi_c \equiv \sqrt{2\epsilon}HM_{\rm Pl}\,\pi$. The field π_c is linearly related to the curvature perturbation via $\zeta \simeq -H\pi$ [139]. The parameters g, μ are coupling constants and the dots in eq. (5.45) represent higher order interaction terms.

The spin-2 field can be expanded in terms of its helicity modes,

$$\sigma_{ij} = \sigma^{(0)}_{ij} + \sigma^{(1)}_{ij} + \sigma^{(2)}_{ij}\,. \tag{5.46}$$

We focus on the dynamics of helicity-0 and helicity-2 states, since the helicity-1 modes are washed away by the inflationary expansion (see chapter 3). The transverse and traceless modes, h_{ij} and $\sigma^{(2)}_{ij}$ can be expanded in the chiral basis,

$$h_{ij} = \int \frac{d^3k}{(2\pi)^3}e^{i\boldsymbol{k}\cdot\boldsymbol{x}}\sum_{\lambda=R/L}\epsilon^{\lambda}_{ij}(\hat{k})\,h^{\lambda}_{\boldsymbol{k}}(\eta)\,, \tag{5.47}$$

$$\sigma^{(2)}_{ij} = \int \frac{d^3k}{(2\pi)^3}e^{i\boldsymbol{k}\cdot\boldsymbol{x}}\sum_{\lambda=R/L}\epsilon^{\lambda}_{ij}(\hat{k})\,\sigma^{2,\lambda}_{\boldsymbol{k}}(\eta)\,, \tag{5.48}$$

where

$$\epsilon^{R/L}_{ij} = \frac{1}{2}\left(\epsilon^{+}_{ij} \pm i\epsilon^{\times}_{ij}\right)\,, \tag{5.49}$$

The polarisation tensors are normalised such that

$$\epsilon^{R/L}_{ij}(\hat{k})\cdot\epsilon^{L/R}_{ij}(\hat{k}) = 1\,, \tag{5.50}$$

$$\epsilon^{R/L}_{ij}(\hat{k})\cdot\epsilon^{R/L}_{ij}(\hat{k}) = 0\,, \tag{5.51}$$

$$\epsilon^{R/L*}_{ij}(\hat{k}) = \epsilon^{L/R}_{ij}(\hat{k}) = \epsilon^{R/L}_{ij}(-\hat{k})\,. \tag{5.52}$$

For the helicity-0 modes, we can write

$$\zeta = \int \frac{d^3k}{(2\pi)^3}e^{i\boldsymbol{k}\cdot\boldsymbol{x}}\zeta_{\boldsymbol{k}}(\eta)\,, \tag{5.53}$$

$$\sigma^{(0)}_{ij} = \int \frac{d^3k}{(2\pi)^3}e^{i\boldsymbol{k}\cdot\boldsymbol{x}}\epsilon^{0}_{ij}(\hat{k})\sigma^{0}_{\boldsymbol{k}}(\eta)\,, \tag{5.54}$$

where

$$\epsilon^{0}_{ij}(\hat{k}) = \sqrt{\frac{3}{2}}\left(\hat{k}_i\hat{k}_j - \frac{\delta_{ij}}{3}\right)\,, \quad \epsilon^{0}_{ij}(\hat{k})\cdot\epsilon^{0}_{ij}(\hat{k}) = 1\,. \tag{5.55}$$

Following the standard procedures (chapter 3), we obtain the mode functions of ζ and h,

$$u_{\mathbf{k}}^{\zeta}(\eta) = \frac{iH}{2M_{Pl}\sqrt{\epsilon k^3}}(1+ik\eta)e^{-ik\eta}\,, \tag{5.56}$$

$$u_{\mathbf{k}}^{h}(\eta) = \frac{2iH}{M_{Pl}\sqrt{2k^3}}(1+ik\eta)e^{-ik\eta}\,, \tag{5.57}$$

and for the σ_{ij} field,

$$u_{\mathbf{k}}^{\sigma^{(2)}}(\eta) = \sqrt{\frac{\pi}{2}}H(-\eta)^{3/2}\left(\frac{c_2(\eta)}{c_{2i}}\right)^{1/2}\mathcal{H}_{\nu}^{(1)}(-c_2(\eta)k\eta)\,, \tag{5.58}$$

$$u_{\mathbf{k}}^{\sigma^{(0)}}(\eta) = \sqrt{\frac{\pi}{2}}H(-\eta)^{3/2}\left(\frac{c_0(\eta)}{c_{0i}}\right)^{1/2}\mathcal{H}_{\nu}^{(1)}(-c_0(\eta)k\eta)\,. \tag{5.59}$$

The parameter $\nu = \sqrt{9/4-(m_\sigma^2/H^2)}$ is related to the mass of spin-2 field m_σ, $\mathcal{H}_\nu^{(1)}$ is the Hankel function of the first kind, and $c_{0/2}$ are the sound speeds of the helicity-$0/2$ components, with c_{0i} and c_{2i} the initial sound speeds. We have verified that these solutions for the mode functions[13] reproduce Bunch-Davies initial conditions at early times ($c_s k\eta \ll 1$) and reduce to those obtained in the $c_{0,2}=$ constant case for time-independent sound speeds considered in [127]. The individual sound speeds obey the following relation [127]

$$c_1^2 = \frac{1}{4}c_2^2 + \frac{3}{4}c_0^2\,, \tag{5.60}$$

We shall assume that the above relation remains valid for slowly varying sound speeds.

We have assumed slowly varying sound speeds with our parametrisation for the sound speed of the helicity mode-j being,

$$c_j(\eta) = c_j^i\left(\frac{\eta}{\eta_i}\right)^{s_j} + c_j^f\,. \tag{5.61}$$

The case of time dependent sound speeds for the spin-2 model was first considered in [129]. We have chosen to add an asymptotic value c_j^f on top of what was adopted in [129], which is convenient when it comes to imposing perturbativity bounds on the sound speeds ($c_j \gtrsim 10^{-3}$) [127].

In terms of calculating the relevant cosmological correlators, this choice is approximately equivalent to taking (see appendix D.3.1 for more details),

$$c_j(k) = c_j^i\left(\frac{k}{k_0}\right)^{-s_j} + c_j^f\,, \tag{5.62}$$

where $k_0 = a_0 H_0$ is a reference scale.

[13] The complete derivation of the mode in the case of a slowly varying sound speed can be found in [157] and our solutions for the mode-functions match in terms of canonically normalised fields. For cases where the time dependence of the sound speeds is significant, the solutions need to be obtained in a different manner (see e.g. [445]).

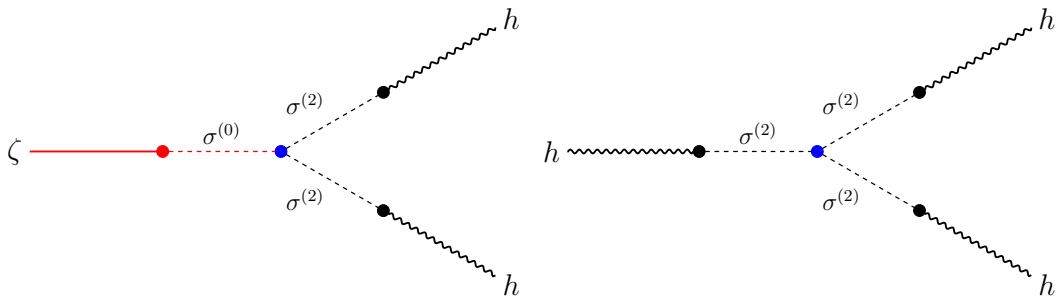

Figure 5.9: Leading σ-mediated contributions to $\langle hh\zeta\rangle$ and $\langle hhh\rangle$. Straight lines correspond to ζ, wiggly lines correspond to h, red (black) dashed lines correspond to $\sigma^{(0)}$ ($\sigma^{(2)}$) fields.

5.3.1.1 Tensor bispectra and power spectra

In terms of the helicity fields, the interaction vertices of interest for our analysis are the following

$$H_{\sigma^{(2)}h} = -\int d^3x\, \frac{g}{2} M_{Pl}\, a^3 h'_{ij}\sigma^{(2),ij}\,, \tag{5.63}$$

$$H_{(\sigma^{(2)})^3} = \int d^3x\, \mu\, a^4\, \sigma^{(2)}_{ij}\cdot\sigma^{(2)}_{jk}\cdot\sigma^{(2)}_{ki}\,, \tag{5.64}$$

$$H_{(\sigma^{(2)})^2\sigma^{(0)}} = \int d^3x\, 3\mu\, a^4\, \sigma^{(2)}_{ij}\cdot\sigma^{(2)}_{jk}\cdot\sigma^{(0)}_{ki}\,, \tag{5.65}$$

$$H_{\sigma^{(0)}\zeta} = -\int d^3x\, \frac{g}{H} M_{Pl}\, a^2 \partial_i\partial_j\zeta\, \sigma^{(0),ij}\,. \tag{5.66}$$

These lead to σ-mediated contributions to primordial correlators (Fig. 5.9), which we calculate using the *in-in* formalism [188]. The diagrams under consideration give contribution to the correlations that are leading and physical, i.e. they cannot be gauged away unlike the squeezed limit bispectrum in SFSR inflation [191, 201, 202]. Of particular interest to us are the three point functions $\langle hh\zeta\rangle$ and $\langle hhh\rangle$ and the tensor power spectrum $\langle hh\rangle$.

The full technical details related to the calculation of these correlators can be found in ref. [2]. I provide a summary of the computation strategy in appendix D and only report here the final results for the correlators.

The main σ-mediated diagram in the $\langle hhh\rangle$ bispectrum leads to

$$\langle h^{\lambda_1}_{k_1} h^{\lambda_2}_{k_2} h^{\lambda_3}_{k_3}\rangle = (2\pi)^3\delta^{(3)}(\vec{k}_1+\vec{k}_2+\vec{k}_3)\,\mathcal{A}^{\lambda_1\lambda_2\lambda_3} B_{\rm ttt}(k_1,k_2,k_3)\,, \tag{5.67}$$

where $B_{\rm ttt}(k_1,k_2,k_3)$ in the squeezed limit ($k_L=k_3\ll k_1\simeq k_2=k_S$) is given by

$$B_{\rm ttt}(k_S,k_S,k_L)=\frac{24\times 2^\nu\pi^2}{k_S^{9/2-\nu}k_L^{3/2+\nu}}\frac{\mu}{H}\left(\frac{g}{M_{\rm Pl}}\right)^3\left(\frac{c_2(k_S)}{c_{2i}}\right)^{5/2}\left(\frac{c_2(k_L)}{c_{2i}}\right)^{1/2}\mathcal{I}(c_2,\nu)\,, \tag{5.68}$$

and in the same limit we also have

$$\mathcal{A}^{\lambda_1\lambda_2\lambda_3}|_{\rm sq.}=-\frac{1}{2}\hat{k}_S^i\hat{k}_S^j\,\epsilon_{ij}^{\lambda_1}(\hat{k}_L)\times\begin{cases}1 & \text{if} \quad \lambda_1=\lambda_2\\ 0 & \text{if} \quad \lambda_1\neq\lambda_2\end{cases}\,. \tag{5.69}$$

The function $\mathcal{I}(c_2,\nu)$ can be well-fit by a power law, given by

$$\mathcal{I}(c_2,\nu)\simeq\frac{a(\nu)}{c_2(k_L)^\nu c_2(k_S)^{3\nu}}\,, \tag{5.70}$$

where a is a ν-dependent parameter (see table D.1 for a set of possible values). Similarly, for the σ-mediated contribution to $\langle hh\zeta\rangle$ we find [2]

$$\langle h^{\lambda_1}_{k_1}h^{\lambda_2}_{k_2}\zeta_{k_3}\rangle=(2\pi)^3\delta^{(3)}(\vec{k}_1+\vec{k}_2+\vec{k}_3)\,\mathcal{A}^{\lambda_1\lambda_2}B_{\rm tts}(k_1,k_2,k_3)\,. \tag{5.71}$$

In the squeezed limit we have $B_{\rm tts}(k_1,k_2,k_3)$

$$B_{\rm tts}(k_L,k_S,k_S)=-\frac{2\pi^2}{\epsilon}\frac{\mu}{H}\left(\frac{g}{M_{Pl}}\right)^3\frac{2^\nu}{k_S^{9/2-\nu}k_L^{3/2+\nu}}\left(\frac{c_2(k_S)}{c_{2i}}\right)^2\left(\frac{c_0(k_S)}{c_{0i}}\right)^{1/2}\left(\frac{c_0(k_L)}{c_{0i}}\right)^{1/2}$$
$$\times\,\mathcal{I}(c_0,c_2,\nu)\,, \tag{5.72}$$

and

$$\mathcal{A}^{\lambda_1\lambda_2}_{\rm sq.}=\frac{4\pi}{5}\sum_M Y_{2M}(\hat{k}_L)\,Y^*_{2M}(\hat{k}_S)\times\begin{cases}1 & \text{if} \quad \lambda_1=\lambda_2\\ 0 & \text{if} \quad \lambda_1\neq\lambda_2\end{cases}\,. \tag{5.73}$$

The function $\mathcal{I}(c_0,c_2,\nu)$ is fit by

$$\mathcal{I}(c_0,c_2,\nu)\simeq\frac{a(\nu)}{c_0(k_L)^\nu c_0(k_S)^\nu c_2(k_S)^{2\nu}}\,. \tag{5.74}$$

The scalar and tensor power spectra of this model are given by (see also [127, 128])

$$P_\zeta(k)=\frac{H^2}{4M_{Pl}^2\epsilon k^3}\left[1+\frac{\mathcal{C}_\zeta(\nu)}{\epsilon c_0^{2\nu}(k)}\left(\frac{c_0(k)}{c_{0i}}\right)\left(\frac{g}{H}\right)^2\right]\,, \tag{5.75}$$

$$P_h(k)=\frac{4H^2}{M_{Pl}^2k^3}\left[1+\frac{\mathcal{C}_\gamma(\nu)}{c_2^{2\nu}(k)}\left(\frac{c_2(k)}{c_{2i}}\right)\left(\frac{g}{H}\right)^2\right]\,. \tag{5.76}$$

The exact analytical form of $\mathcal{C}_\zeta(\nu)$ and $\mathcal{C}_\gamma(\nu)$ can be found in Ref. [127].

We are interested in scenarios where (i) the GW spectrum is sufficiently enhanced at small and intermediate scales to be observable, and (ii) we have large squeezed

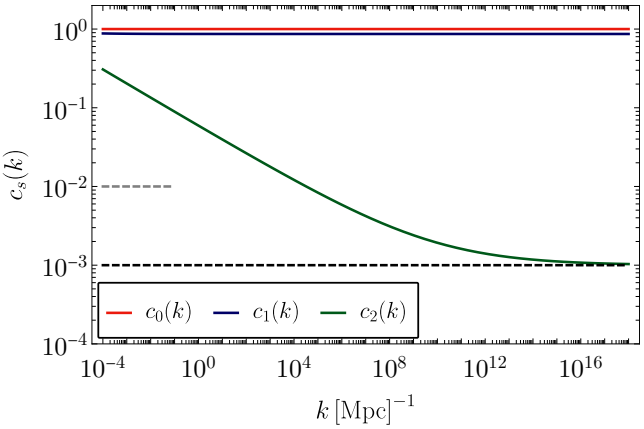

Figure 5.10: An example of scale-dependence of the sound speeds $c_s(k)$ taking $c_{2i} = 2.5 \times 10^{-1}$, $c_{2f} = 10^{-3}$, $s_2 = 1.8 \times 10^{-1}$, $c_{0i} = 1$, $s_0 = 0$. The black and grey dashed lines show the bounds from perturbativity and CMB non-Gaussianity respectively.

non-Gaussianity with $F_{\rm NL} \gg 1$ so as to have a detectable anisotropic component of $\Omega_{\rm GW}$. This is obtained in the $c_2 \ll 1$ regime, which keeping in mind the CMB constraints, suggest that the interesting region of parameter space is the one with c_0 nearly constant throughout and c_2 decreasing towards smaller scales in terms of the scale dependent sound speeds of eq. (5.62) (see fig. 5.10). Thus, we can approximate

$$P_\zeta(k_L) \simeq \frac{H^2}{4M_{Pl}^2 \epsilon k_L^3}\,, \quad P_h(k_L) \simeq \frac{4H^2}{M_{Pl}^2 k_L^3}\,, \tag{5.77}$$

$$P_h(k_S) \simeq \frac{4H^2}{M_{Pl}^2 k_S^3} \frac{\mathcal{C}_\gamma(\nu)}{c_2^{2\nu}(k_S)} \left(\frac{c_2(k_S)}{c_{2i}}\right) \left(\frac{g}{H}\right)^2\,, \tag{5.78}$$

where we have k_L at CMB scales and k_S corresponding to e.g. PTA or interferometer scales. The non-linear parameters as defined in Eqs. (5.6) and (5.16), can finally be obtained as

$$F_{\rm NL}^{\rm ttt}(k_S, k_L, \nu) = 3\,\pi^2\, 2^\nu \frac{a(\nu)}{C_\gamma(\nu)} \left(\frac{M_{Pl}}{H}\right) \left(\frac{c_2(k_S)^{\frac{3}{2}-\nu}}{c_2(k_L)^{\nu-\frac{1}{2}}\, c_{2i}^2}\right) \left(\frac{g}{H}\right) \left(\frac{\mu}{H}\right) \left(\frac{k_L}{k_S}\right)^{3/2-\nu}\,, \tag{5.79}$$

$$\tilde{F}_{\rm NL}^{\rm tts}(k_S, k_L, \nu) = -\,4\,\pi^2\, 2^\nu \frac{a(\nu)}{C_\gamma(\nu)} \left(\frac{M_{Pl}}{H}\right) \left(\frac{c_2(k_S)}{c_0(k_L)^{\nu-\frac{1}{2}} c_0(k_S)^{\nu-\frac{1}{2}}\, c_{2i}\, c_{0i}}\right) \left(\frac{g}{H}\right) \left(\frac{\mu}{H}\right) \left(\frac{k_L}{k_S}\right)^{\frac{3}{2}-\nu}\,. \tag{5.80}$$

The common $(k_L/k_S)^{3/2-\nu}$ scaling suggest that a small exponent (i.e. a light field) will provide large GW signatures that may be observable. Combining Eq. (5.79) with Eq. (5.80) we obtain

$$F_{\rm NL}^{\rm ttt}(k_S, k_L, \nu) = -\frac{3}{4} \left(\frac{c_{0i}}{c_{2i}}\right) \left(\frac{c_0(k_S) c_0(k_L)}{c_2(k_S) c_2(k_L)}\right)^{\nu-\frac{1}{2}} \tilde{F}_{\rm NL}^{\rm tts}(k_S, k_L, \nu)\,. \tag{5.81}$$

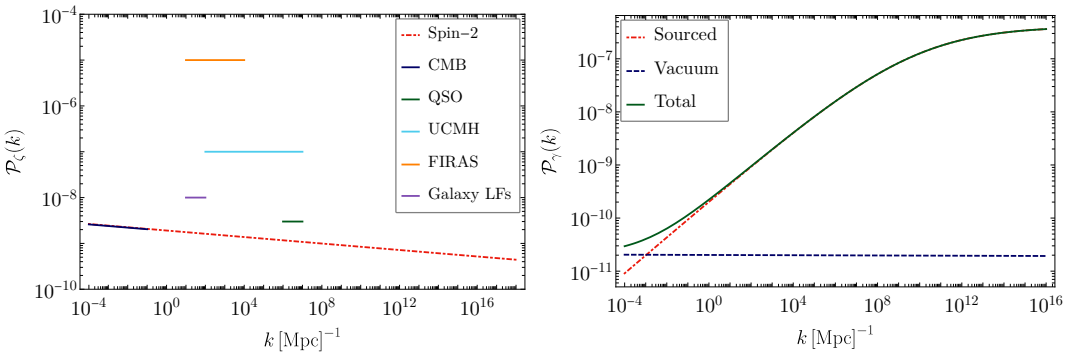

Figure 5.11: Left : The scalar power spectrum for the spin-2 model along with the measured power spectrum from CMB observations [41] and the constraints from various experiments (see [446–450] for the exact constraints). Right: The different contributions to the tensor power spectrum for the spin-2 model. The choice of parameters for both panels is $c_{2i} = 2.5 \times 10^{-1}$, $c_{2f} = 10^{-3}$, $s_2 = 1.8 \times 10^{-1}$, $c_{0i} = 1$, $s_0 = 0$, $g/H = 4 \times 10^{-3}, \nu = 1.45$.

This shows us that for $c_2 \ll c_0$ and a sufficiently light field, the TTT non-linear parameter will be enhanced with respect to the TTS one and can provide the dominant contribution to the GW anisotropies.

We plot the resulting scalar and tensor power spectra for this model in Fig. 5.11. We choose the parameter set $c_{2i} = 2.5 \times 10^{-1}$, $c_{2f} = 10^{-3}$, $s_2 = 1.8 \times 10^{-1}$, $c_{0i} = 1$, $s_0 = 0$, $g/H = 4 \times 10^{-3}, \nu = 1.45$, $H/M_{\rm pl} = 10^{-5}$ which is within the allowed range for this model, both in terms of theoretical consistency (gradient instabilities, perturbativity) [127, 128], and in terms of observational constraints on scalar and tensor perturbations from the CMB [41, 129, 451] (a more detailed discussion of these points can be found in [2]).

Finally, in Fig. 5.12, we plot the spectrum of $\Omega_{\rm GW}$ for different values of c_{2f}. For $c_{2f} = 10^{-3}$, we observe that the GW spectrum is well within the sensitivity range of next generation CMB experiments like CMB-S4 as well as SKA, Taiji and BBO.

5.3.1.2 Angular power spectra of GW anisotropies

Equipped with the results of section 5.2 and keeping the same choice of parameters as mentioned above, we calculate the angular power spectra of the GW anisotropies and plot them in fig. 5.13 at BBO frequency scales. As expected, both $C_\ell^{\rm GW}$ and $C_\ell^{\rm GW-T}$ turn out to be dominated by the TTT bispectrum, due to the smallness of the parameter c_2.

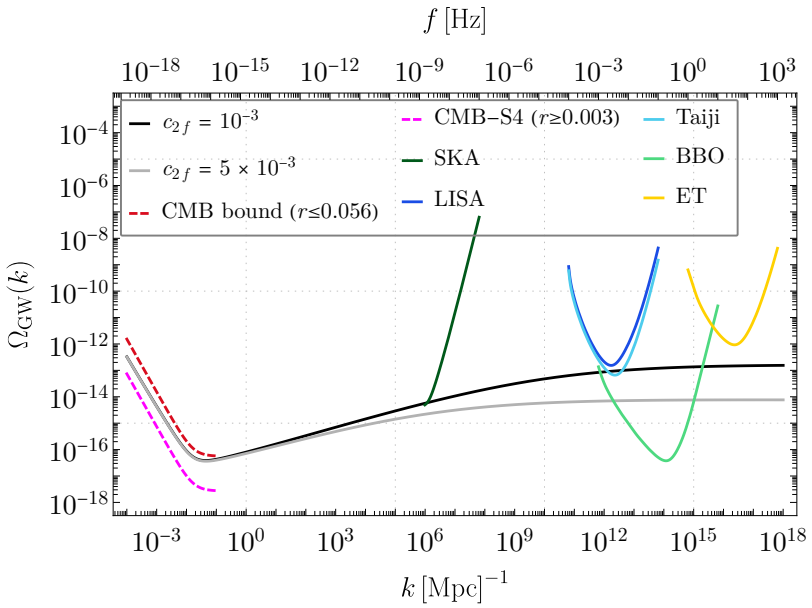

Figure 5.12: $\Omega_{\rm GW}(k)$ for different values of c_{2f} plotted alongside the power law sensitivity curves for SKA, LISA, Taiji, BBO and ET. We also plot the current bound from the CMB as well as the expected sensitivity of CMB-S4 [115].

As a consequence of the $(k_L/k_S)^{3/2-\nu}$ scale dependence, $C_\ell^{\rm GW,tts}$ is suppressed on large angular scales (compare to fig. 5.4). Although this can be a signature of the mass of the spin-2 field ($\nu = \sqrt{9/4 - m_\sigma^2/H^2}$), the TTS cross-correlation being much smaller than the TTT one makes this difficult to observe. The sign $C_\ell^{\rm GW-T,ttt} < 0$ can also be understood from the fact that tensor perturbations decay on sub-horizon scales, therefore $dh/d\eta < 0$. Thus, when $F_{\rm NL}^{\rm ttt} > 0$ we will have $C_\ell^{\rm GW-T,ttt} < 0$.

If we fix all parameters except μ/H and c_{2f} to the values considered previously (same

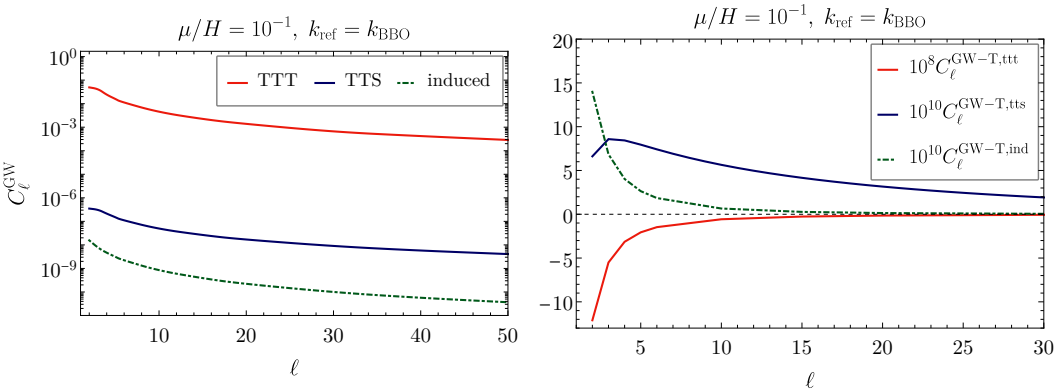

Figure 5.13: The different contributions to the auto-correlation $C_\ell^{\rm GW}$ and cross-correlation $C_\ell^{\rm GW-T}$ plotted for the spin-2 model. For comparison we also plot the induced anisotropies from propagation.

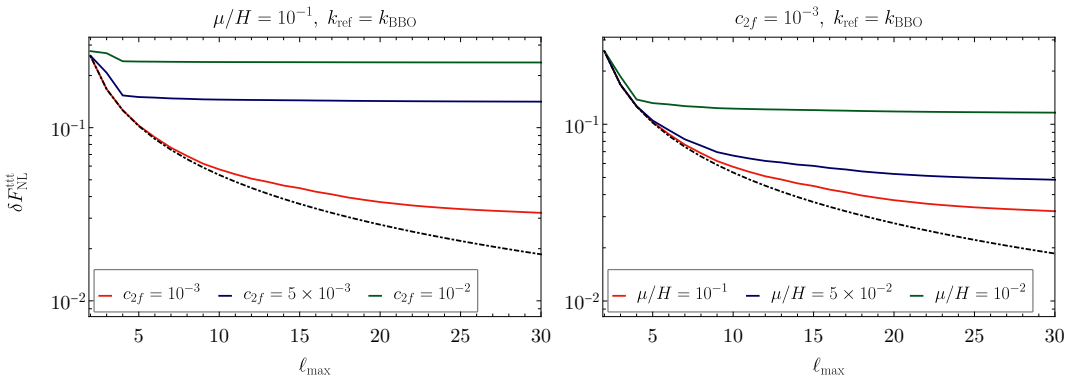

Figure 5.14: The relative error in the measurement of $F_{\rm NL}^{\rm ttt}$ as a function of $\ell_{\rm max}$ with BBO for different values of μ, c_{2f}. The dashed curves show the errors for an idealised, cosmic variance limited measurement.

as fig. 5.11), we can approximate

$$\begin{aligned}
\Omega_{\rm GW}(k_{\rm BBO}) &\simeq 1.3 \times 10^{-13} \left(\frac{c_{2f}}{10^{-3}}\right)^{-1.7}, \\
F_{\rm NL}^{\rm ttt}(k_{\rm BBO}, k_{\rm p}) &\simeq 1.2 \times 10^{6} \left(\frac{\mu}{H}\right), \\
\tilde{F}_{\rm NL}^{\rm tts}(k_{\rm BBO}, k_{\rm p}) &\simeq -3.5 \times 10^{2} \left(\frac{\mu}{H}\right),
\end{aligned} \tag{5.82}$$

in terms of μ/H and c_{2f}.[14] The angular power spectra inherit the scale dependence of the $F_{\rm NL}$, resulting in

$$\begin{aligned}
C_\ell^{\rm GW}(k_{\rm ref}) &\simeq C_\ell^{\rm GW}(k_{\rm BBO}) \times \left(\frac{k_{\rm BBO}}{k_{\rm ref}}\right)^{3-2\nu}, \\
C_\ell^{\rm GW-T}(k_{\rm ref}) &\simeq C_\ell^{\rm GW-T}(k_{\rm BBO}) \times \left(\frac{k_{\rm BBO}}{k_{\rm ref}}\right)^{3/2-\nu},
\end{aligned} \tag{5.83}$$

for the anisotropies arising from non-Gaussianity where $\nu = \sqrt{9/4 - m_\sigma^2/H^2}$ was related to the mass of the spin-2 field.

5.3.1.3 Projected constraints on $F_{\rm NL}$

We are now able to forecast the minimum expected error in the measurement of $F_{\rm NL}^{\rm ttt}$, knowing that the anisotropies from the TTT bispectrum are enhanced relative to those from the TTS one. We proceed in the same manner as section 5.2.3 and plot the relative error $\delta F_{\rm NL}^{\rm ttt} \equiv \Delta F_{\rm NL}^{\rm ttt}/F_{\rm NL}^{\rm ttt}$ in fig. 5.14 for different value of μ, c_{2f}. The corresponding $F_{\rm NL}^{\rm ttt}$ and $\Omega_{\rm GW}$ can be approximated at BBO scales using (5.82).

[14] Note that at these interferometer scales we have $c_2 \simeq c_{2f}$ (see fig. 5.10).

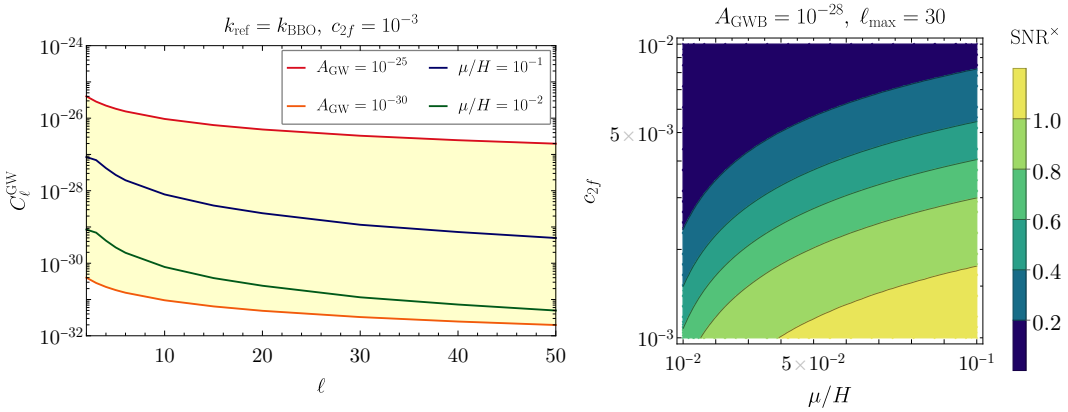

Figure 5.15: Left: The $C_\ell^{\rm GW}$ for the astrophysical background (yellow shaded region) and for the CGWB anisotropies in the spin-2 model for different values of μ/H taking $c_{2f} = 10^{-3}$. Right: Signal to noise of the total cross-correlation for the spin-2 model as a function of c_{2f}, μ/H.

We observe that for the parameter set $c_{2f} = 10^{-3}, \mu/H = 10^{-1}$, a relative precision of $\delta F_{\rm NL}^{\rm ttt} \sim 10^{-2}$ is achievable. This is similar to the cosmic variance limited error, expected due to the fact that in this case we have $C_\ell^{\rm GW,ttt} \gg N_\ell^{\rm GW}$. For values of μ, c_{2f} that lead to smaller $F_{\rm NL}^{\rm ttt}, \Omega_{\rm GW}$, the error saturates around $\ell_{\rm max} \sim 10$, which is consequence of the detector noise increasing rapidly after the first few multipoles (fig. 5.5).

SNR of the CMB-GW cross-correlation

As in section 5.2.3, we also provide here an estimate of the cross-correlation SNR assuming that an astrophysical background is also present. In this case the detectability of the cross-correlation is much lower, due to the fact that the tensor contribution to the CMB temperature anisotropies is much smaller (since $r \ll 1$). This implies that $C_\ell^{\rm GW-T,signal} \ll (C_\ell^{\rm GW,total} C_\ell^{\rm TT})^{1/2}$, leading to a signifanct reduction in the SNR compared to the TTS case considered in section 5.2.3.

$$\mathrm{SNR} \simeq \left[\sum_\ell (2\ell+1) \frac{\left(C_\ell^{\rm GW-T,signal}\right)^2}{C_\ell^{\rm GW,total} C_\ell^{\rm TT}} \right]^{1/2} . \tag{5.84}$$

5.3.2 Solid Inflation

The second inflationary model that we studied in [1], is Solid Inflation. In this model [140, 141], the inflationary expansion is driven by three scalar fields having

derivative couplings and particular symmetries that are similar to an effective field theory description of a homogeneous and isotropic solid [452]. The three fields ϕ_I here break space-reparametrization symmetry, i.e., they have space-dependent but time independent background configurations

$$\langle \phi^I \rangle = x^I \,, \tag{5.85}$$

where x are the comoving coordinates. Internal shift and rotational symmetries of the ϕ^I allow for the homogeneity and isotropy of the background space-time,

$$\phi^I \to \phi^I + a^I, \quad a^I = \text{const.}\,, \tag{5.86}$$

$$\phi^I \to O^I_J \phi^J, \quad O^I_J \in SO(3)\,. \tag{5.87}$$

Finally, allowing for an approximate internal dilation symmetry

$$\phi^I \to \lambda \phi^I\,. \tag{5.88}$$

ensures that (i) the EFT of the solid does not break down in an expanding background, and (ii) the solid can accommodate $\rho + p \ll \rho$ and thereby drive the accelerated expansion.

Bispectra and power spectra

The solid inflation tensor bispectra are given by [141]

$$\langle \zeta_{\boldsymbol{q}\to 0} h^\lambda_{\boldsymbol{k}} h^{\lambda'}_{-\boldsymbol{k}} \rangle' = \frac{16}{9}\frac{F_Y}{F}\mathcal{P}_\zeta(q)\mathcal{P}_h(k)\log\left(\frac{k}{aH}\right)\left(\epsilon^\lambda_{ij}\epsilon^{\lambda'}_{ij} - 3\hat{q}_i\epsilon^\lambda_{ij}\epsilon^{\lambda'}_{jk}\hat{q}_k\right)\,, \tag{5.89}$$

$$\langle h^\lambda_{\boldsymbol{q}\to 0} h^{\lambda'}_{\boldsymbol{k}} h^{\lambda''}_{-\boldsymbol{k}} \rangle' = \frac{8}{9}\frac{F_Y}{F}\mathcal{P}_h(q)\mathcal{P}_h(k)\log\left(\frac{k}{aH}\right)\epsilon^\lambda_{ij}\epsilon^{\lambda'}_{jk}\epsilon^{\lambda''}_{ki}\,. \tag{5.90}$$

Here, F_Y, F are model parameters with $F_Y/F < 1$.

Another important feature of this model is that that the tensor power spectrum is necessarily blue tilted [140]

$$\mathcal{P}_h(k) = A_T\left(\frac{k}{k_\mathrm{p}}\right)^{n_T}\,, \tag{5.91}$$

$$A_T \simeq \frac{H^2_\mathrm{p}}{\pi^2 M^2_\mathrm{Pl}}\left(\frac{\eta_\mathrm{p}}{\eta_e}\right)^{8c_T^2\epsilon/3}\,, \tag{5.92}$$

$$n_T \simeq 2\epsilon_p c_L^2\,. \tag{5.93}$$

The subscript 'p' denotes that these quantities are evaluated at the time when the pivot scale exits the horizon and η_e is the end of inflation. The quantities (c_T, c_L) are the tranverse and longitudinal sound speeds, related via $c_T^2 \simeq 3/4\,(1 + c_L^2 - 2\epsilon/3)$ [140].

We can see that in this model, since we have

$$\frac{F_{\rm NL}^{\rm ttt}}{F_{\rm NL}^{\rm tts}} = \frac{\mathcal{P}_h(q)}{2\mathcal{P}_\zeta(q)} = \frac{r}{2}, \tag{5.94}$$

it is the TTS bispectrum that will provide the leading contribution to the GW anisotropies (since $r \ll 1$). Thus, the forecasts performed in section 5.2.3 can be directly applied and I shall not repeat the same analysis for this model here. The specific forecasts as well as further details about the constraints on the parameter space of this model can also be found in [1].

5.4 Summary

In this chapter we have studied the anisotropies of inflationary gravitational wave backgrounds, induced to the presence of a non-trivial tensor bispectrum in the squeezed limit. These can be the *leading* source of the anisotropies, if the underlying tensor bispectrum is sufficiently large, i.e. $F_{\rm NL}^{\rm tts} \gg 1$ and/or $\sqrt{r}\,F_{\rm NL}^{\rm ttt} \gg 1$. Naturally, for these anisotropies to be useful as a probe of inflationary interactions, the isotropic background also needs to be enhanced to a level that can be detected at PTA/interferometer scales.

In the first part of this chapter, we took a phenomenological approach to these anisotropies and calculated their angular power spectra, providing analytical expressions wherever possible by means of some simplifying assumptions. We used this to study the detectability of such signals and highlighted the parameter space $(\Omega_{\rm GW}, F_{\rm NL})$ that will be within the reach of upcoming GW probes. The angular dependence of the mixed bispectra, which would hint to the presence of additional spinning fields during inflation, turned out to be especially important for GW-CMB cross-correlations. Our analysis showed that having a monopolar *vs* a quadrupolar angular dependence in the $\langle hh\zeta\rangle$ bispectrum can make a significant difference when it comes to the detectability of the cross-correlation. In general we estimate that signals with $\Omega_{\rm GW} \sim 10^{-10}, F_{\rm NL} \sim 10^3$ will be within the reach of 3G detectors such

as LISA, Taiji, ET and CE while futuristic detectors such as BBO may even reach $\Omega_{\rm GW} \sim 10^{-12}, F_{\rm NL} \sim 10^3$.

We have also accounted for the presence of the AGWB and its anisotropies, albeit in a fairly simplistic manner, by allowing the amplitude of its large scale (low-ℓ) angular power spectrum to vary between 10^{-30} and 10^{-25} (in the $10^{-2}\,{\rm Hz} \lesssim f \lesssim 100\,{\rm Hz}$ range). Our results show that cross-correlations with the CMB are likely to be the most important tool in this case to detect the primordial gravitational wave anisotropies. As more and more compact binary mergers and possibly even the AGWB are detected in the future, models of the AGWB anisotropies will become increasingly accurate and will lead to an even better understanding of the detectability of these primordial anisotropies.

In the second part of this chapter, we have shown through two representative examples, that there exist inflationary models which can indeed produce such GW signatures, namely large amplitudes of $\Omega_{\rm GW}, F_{\rm NL}$. In one of the models, we even find that the TTT bispectrum generates the leading contribution to the GW anisotropies, despite the fact that the corresponding angular power spectra $C_\ell^{\rm GW,ttt}$ is suppressed by a factor r w.r.t $C_\ell^{\rm GW,tts}$. For the same model, we demonstrated that a futuristic GW experiment with BBO-level sensitivity will be able to constrain $F_{\rm NL}^{\rm ttt}$ to the level of a few percent (for $F_{\rm NL}^{\rm ttt} \sim 10^4$).

Chapter 6

Constraining primordial tensor features with the anisotropies of the Cosmic Microwave Background

This chapter is an exact reproduction of the following article:

- J. Hamann and A. Malhotra, *"Constraining primordial tensor features with the anisotropies of the cosmic microwave background,"* JCAP **12** (2022), 015, [arXiv:2209.00827].

After having studied inflationary GW signatures at interferometer scales, we now turn to CMB scales and discuss the potential of future CMB experiments to constrain the PGW frequency spectrum. A detection of features in the PGW spectrum beyond a simple power law with a small red-tilt (as expected in SFSR) would provide us a powerful window into inflationary dynamics.

Abstract

It is commonly assumed that the stochastic background of gravitational waves on cosmological scales follows an almost scale-independent power spectrum, as generically

predicted by the inflationary paradigm. However, it is not inconceivable that the spectrum could have strongly scale-dependent features, generated, e.g., via transient dynamics of spectator axion-gauge fields during inflation. Using the temperature and polarisation maps from the *Planck* and BICEP/Keck datasets, we search for such features, taking the example of a log-normal bump in the primordial tensor spectrum at CMB scales. We do not find any evidence for the existence of bump-like tensor features at present, but demonstrate that future CMB experiments such as LiteBIRD and CMB-S4 will greatly improve our prospects of determining the amplitude, location and width of such a bump. We also highlight the role of delensing in constraining these features at angular scales $\ell \gtrsim 100$.

6.1 Introduction

The inflationary paradigm [20, 27, 84–86] is not only a compelling solution to the horizon and flatness problems of hot big bang cosmology, but also provides a means to naturally generate the seeds of the observed Cosmic Microwave Background (CMB) anisotropies and the Large Scale Structure (LSS) [21–24, 28] via quantum fluctuations. Cosmological observations are consistent with a power spectrum of scalar (density) fluctuations that is adiabatic, Gaussian and nearly (but not exactly) scale-invariant, in excellent agreement with the predictions of the simplest single field slow roll (SFSR) models [41]. Another universal prediction of inflation is the existence of a stochastic gravitational wave background produced during this epoch [30–33].

Although such primordial gravitational waves (PGW) have not yet been detected, their effects could show up in a wide variety of cosmological observables. Most notably, PGW contribute to both the temperature and polarisation anisotropies of the CMB [33, 105–108, 453–455], and this fact can be used to constrain their amplitude [35, 114, 456–460]. Indeed, the most stringent bounds on the amplitude of these PGW come from the CMB which constrains the tensor-scalar ratio to $r < 0.032$ [114] at 95% CL for a nearly scale-invariant power spectrum of tensor fluctuations, as expected in SFSR models.

Interferometric detection with next generation detectors like ET [66] and LISA [65] may also be a possibility, but only for inflationary models departing strongly from SFSR dynamics on direct detection scales [60, 461]. Additionally, PGW could also

be detected via Pulsar Timing arrays, through their imprints on large scale structure ('tensor fossils'), spectral distortions of the CMB, as well as through the gravitational lensing effects of PGW, see [58] for an overview.

The B-mode polarisation of the CMB remains the most promising avenue to detect these primordial tensor perturbations, keeping in the mind the projected sensitivities as well the foreground/noise sources affecting the various probes mentioned above. A detection of these primordial tensor perturbations would be extremely significant since their amplitude in SFSR models is directly related to the energy scale of inflation $V_{\rm inf} \simeq 3\pi^2 A_{\rm s} M_{\rm pl}^4 \, r/2$ [58] and would allow a precise reconstruction of the inflaton potential in the observable window [462–464]. Interestingly, certain well-motivated single field inflationary models are currently in excellent agreement with the CMB data [41], e.g. the Starobinsky model [37, 38, 465], and predict values of r within the reach of next generation of CMB experiments. For these reasons, it is easy to understand why the search for PGWs is an important science goal for future probes like the BICEP array [42], Simons Observatory [43], CMB-S4 [44] and LiteBIRD [45].

While a detection of PGW in itself would be extremely valuable, additional information on the production mechanism could be gleaned from measuring the shape of the GW spectrum. For PGW generated from vacuum fluctuations, the shape of the spectrum is a power law with spectral index related to the tensor-scalar ratio as $n_{\rm t} \simeq -r/8$. This 'tensor consistency relation' is valid for PGW arising from SFSR dynamics [466] and in the event of a B-mode detection, provides a way to confirm whether the observed PGW are arising from vacuum fluctuations or not. Unfortunately however, testing this relation appears out of reach with CMB data alone, even with the sensitivity of CMB-S4 [44] or LiteBIRD [130, 457]. On the other hand, large deviations from the consistency relation could still be observed with these experiments. Such deviations would signal a departure from SFSR dynamics at CMB scales which is possible in inflationary models with additional fields capable of sourcing PGW, e.g. [119, 123–126, 130, 132, 467–471].

In this paper we study one such example of a deviation from a power-law spectrum of tensor perturbations, namely a bump-like PGW feature at CMB scales. Such a feature is typical of GW sourced from spectator axion-gauge fields during inflation, leading to a strong scale-dependence. Parameterising the spectrum of these sourced PGW as a log-normal function, we present constraints on the amplitude, width and

location of the peak of the log-normal using temperature and polarisation data from the *Planck* and BICEP/Keck datasets and forecast the discovery potential of CMB-S4 and LiteBIRD for this scenario.

The paper is organised as follows: in Section 6.2 we describe the tensor power spectrum parameterisation and discuss possible inflationary models where such a spectrum may arise. We also describe the effects of such a tensor power spectrum shape on the CMB temperature and polarisation anisotropies. In Section 6.3 we present constraints on the model parameters from current data and forecast sensitivities of future CMB experiments. Finally, we conclude in Section 6.4.

6.2 Tensor modes from Inflation

In this section we first present the tensor power spectrum parameterisation used to describe the bump-like feature. We then discuss the effect of such a tensor spectrum shape on the CMB temperature and polarisation anisotropies and conclude this section with a discussion of inflationary models where one can expect such power spectrum shapes.

6.2.1 Log-normal spectrum

We parameterise the tensor power spectrum on CMB scales as a log-normal with

$$\mathcal{P}_{\rm t}(k) = r_{\rm pk} A_{\rm s} \exp\left[-\frac{\left(\ln\left(k/k_{\rm pk}\right)\right)^2}{2\sigma^2}\right]. \tag{6.1}$$

Here σ denotes the width of the log-normal, $k_{\rm pk}$ the location of the peak and $r_{\rm pk}$ the rescaled amplitude of the tensor power spectrum at the peak scale in terms of the scalar amplitude $A_{\rm s} = 2.09 \times 10^{-9}$ at the pivot scale $k_{\rm p} = 0.05\,{\rm Mpc}^{-1}$. When $\sigma \gg 1$, the power spectrum becomes degenerate with a flat spectrum on scales

$$-\sigma \lesssim \log k/k_{\rm pk} \lesssim \sigma. \tag{6.2}$$

For comparison, the power spectrum of tensor perturbations from vacuum fluctuations during inflation has the following form,

$$\mathcal{P}_{\rm t}^{\rm vac}(k) = r A_{\rm s} \left(\frac{k}{k_{\rm p}}\right)^{n_{\rm t}} \tag{6.3}$$

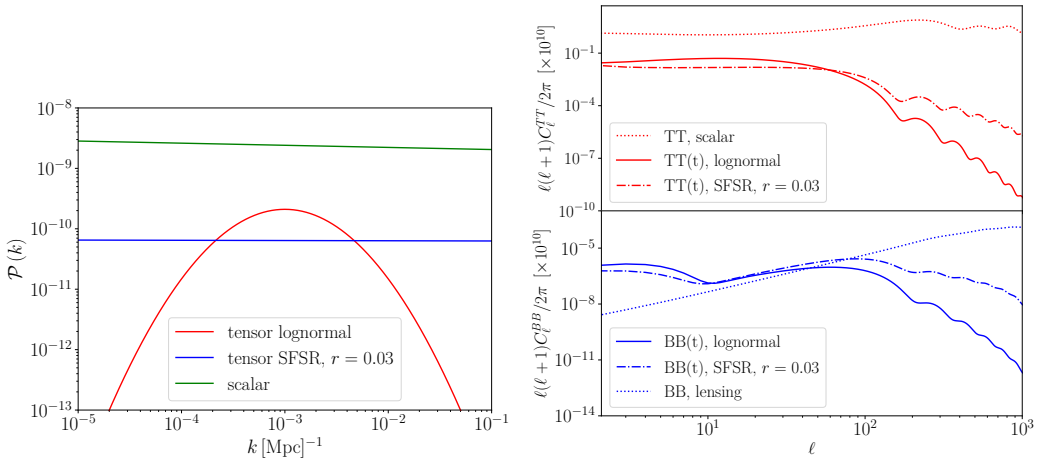

Figure 6.1: Left : Power spectra with tensor spectrum parameters $r_{\rm pk} = 0.1$, $\sigma = 1$ and $k_{\rm pk} = 10^{-3}$. Right: The temperature and B-mode anisotropies for the same value of the tensor power spectrum parameters.

where r denotes the vacuum tensor to scalar ratio and $n_{\rm t}$ the tensor spectral tilt. The two power spectra are plotted in the left panel of Figure 6.1 taking $r = 0.03$ and $n_{\rm t}$ given by the consistency relation for the SFSR spectrum and $r_{\rm pk} = 0.1$, $\sigma = 1$ and $k_{\rm pk} = 10^{-3}$ for the log-normal.

6.2.2 CMB anisotropies

Much like the scalar perturbations, tensors also contribute to the CMB anisotropies and this contribution can be expressed as

$$C_{\ell,{\rm t}}^{XY} = 4\pi \int d\ln k\, \mathcal{P}_{\rm t}(k)\, \Delta_{\ell,{\rm t}}^{X}(k) \Delta_{\ell,{\rm t}}^{Y}(k). \tag{6.4}$$

Here $X, Y = T, E, B$ and $\Delta_{\ell,{\rm t}}^{X}$ denotes the corresponding transfer function for the tensor source. The analytical expressions for these transfer functions can be found in [105–108], and they can be numerically computed using Boltzmann codes such as `CLASS` [110] or `CAMB` [111].

Physically, tensor modes generate a quadrupolar anisotropy in the radiation density field at last scattering and reionisation, and thus tensor perturbations lead to anisotropies in both temperature and polarisation of the CMB. Note that for non-chiral primordial tensor spectra, the correlations $\langle TB \rangle$ and $\langle EB \rangle$ vanish due to the fact that B-modes are parity-odd whereas T and E are not [438].

In general, the tensor contribution is relevant mainly on the largest angular scales since tensor modes decay rapidly on sub-horizon scales ($\ell \gtrsim 100$ at recombination).

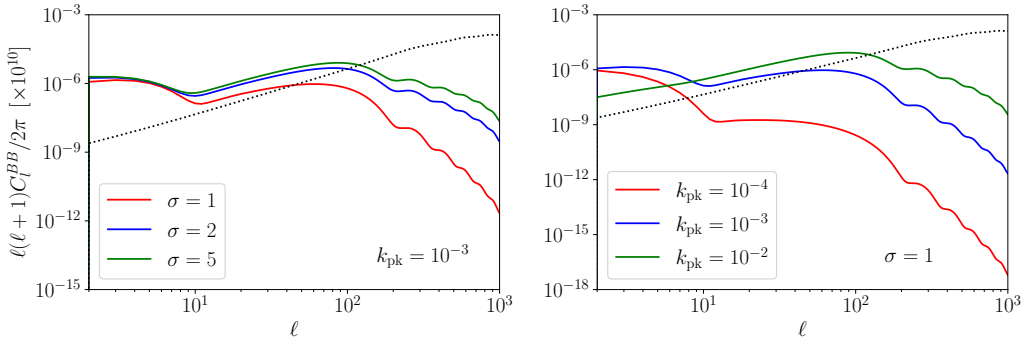

Figure 6.2: Effect of varying σ and $k_{\rm pk}$ on C_ℓ^{BB} taking $r_{\rm pk} = 0.1$. The black dotted lines show the B-modes from lensing.

For the temperature anisotropies, the tensor contribution is smaller than the scalar one by a factor of the tensor-scalar ratio r on these large scales. As for the B-mode polarisation, for $r \gtrsim 0.001$ this is dominated by the primordial tensor perturbations on these scales since scalars cannot source B-modes at linear order.

However, scalars do generate B-mode polarisation at second order via the lensing of the E-modes [113] and these lensing-induced B-modes dominate the primordial B-mode spectrum at smaller scales ($\ell \gtrsim 100$). In the B-mode polarisation angular power spectrum one can also see the reionization bump ($\ell \leq 10$) [107] and the recombination bump ($\ell \sim 80$) [472], corresponding to scales that re-enter the horizon at those times.

We plot the tensor contribution to the temperature and B-mode angular power spectra in the right panel of Figure 6.1. The difference between the SFSR prediction and the log-normal spectrum can also be understood from the same figure. The additional power on scales close to the peak scale $k = 10^{-3}$ leads to an enhancement of the temperature as well as the polarisation anisotropies on large angular scales. Away from the peak scales, the anistropy power spectrum in the log-normal case falls off rapidly relative to the SFSR one.

The effect of varying the log-normal parameters on the B-mode spectrum is illustrated in Figure 6.2. The location of the peak scale $k_{\rm pk}$ can be directly related to the angular scale at which the anisotropies are enhanced, whereas the peak width σ controls the range of scales around the peak where this happens. Roughly speaking, peaks at $k_{\rm pk} = 10^{-4}, 10^{-3}, 10^{-2}$ can be mapped to an enhancement of power centered around angular scales of $\ell \sim 2$, 10 and 100 respectively.

6.2.2.1 Inflationary Models

A peaked primordial tensor power spectrum is characteristic of transient phenomena occurring during inflation that source gravitational waves on scales of order the horizon size at that time. The prototypical examples of this type are inflationary models with a spectator sector involving an axion coupled to a gauge field [123–126, 130, 132, 469–471]. The spectator sector Lagrangian in this case can be written as

$$\mathcal{L}_{\rm spec} = -\frac{1}{2}(\partial\chi)^2 - U(\chi) - \frac{1}{4}F_{\mu\nu}F^{\mu\nu} + \frac{\lambda\chi}{f}F_{\mu\nu}\tilde{F}^{\mu\nu} \tag{6.5}$$

where χ represents the axion-like field, $U(\chi)$ is the axion potential, f the decay constant, $F_{\mu\nu}$ the field strength tensor of the gauge field and λ a coupling constant. The specific shape of the GW spectrum in such models arises from the fact that one of the gauge field helicities experiences a transient instability at horizon crossing and gets enhanced relative to the other. Thus, in general the GW spectrum sourced in these models is chiral, i.e. $\mathcal{P}_R \neq \mathcal{P}_L$. Although one can test for chirality through the observation of non-zero $\langle TE\rangle$ or $\langle EB\rangle$ cross-spectra [126, 438, 473], in our analysis we only concern ourselves with the overall shape and amplitude of the tensor power spectrum and neglect these parity violating correlations in obtaining the constraints in Section 6.3. In general the signal is much weaker in the cross-spectra than in the corresponding $\langle BB\rangle$ spectrum, making them harder to detect [126].

6.3 Constraints on model parameters

Constraints on the axion gauge-field model parameters of equation (6.5), specifically upper bounds on the effective coupling between the axion and the gauge field were also obtained in [471] for two different models of the axion potential $U(\chi)$. The analysis of [471] was carried out for fixed values of the peak width and location using the profile likelihood approach. However, our analysis cannot be directly compared with theirs since varying the effective coupling also affects the sourced scalar spectra whereas here we work at the level of the log-normal parameters which affects only the primordial tensor power spectrum through equation (6.1).

Parameter	range
$\boldsymbol{r_{\rm pk}}$	$[0, 1/5]$
$\boldsymbol{\sigma}$	$[1/10, 10]$
$\boldsymbol{\log_{10} k_{\rm pk}}$	$[-5, -1]$

Table 6.1: Prior ranges for the log-normal tensor power spectrum parameters.

6.3.1 Constraints from *Planck* + BK18

For the analysis of our model comprising the base ΛCDM parameters plus our additional tensor power spectrum parameters $\{r_{\rm pk}, k_{\rm pk}, \sigma\}$, we use the following data: Firstly, the *Planck* low-ℓ temperature+polarisation and high-ℓ $TTTEEE$ likelihood [474] and the *Planck* lensing likelihood [475]. We shall refer to this combination as *Planck* hereafter. Secondly, we also use the most recent BICEP/Keck data release (BK18 hereafter) which contains polarisation data in the multipole range $20 < \ell < 330$ obtained from the BICEP2, Keck Array and BICEP3 experiments [35].

We impose flat priors on the base ΛCDM parameters as well as flat priors on $r_{\rm pk}, \sigma$ and $\log_{10} k_{\rm pk}$ in the ranges shown in Table 6.1. The CMB power spectra are computed with `CAMB` [111] and the parameter space is explored using a Markov Chain Monte Carlo sampler [476, 477], through its interface with `Cobaya` [478]. The resulting chains are analysed with `GetDist` [479].

Note that we assume in our analysis that the scale-independent vacuum contribution to the tensor power spectrum has a much lower amplitude than the log-normal sourced one, so we do not include the variation of r and instead set it to zero. Current data do not indicate the presence of such vacuum tensor perturbations and for values of r much smaller than $r_{\rm pk}$ the constraints on $r_{\rm pk}$ will not be significantly affected. We will revisit this assumption when doing the Fisher forecasts in Section 6.3.2.

The joint posterior distributions for the scalar and tensor power spectrum parameters are shown in Figure 6.3 (for posterior contours of all 9 parameters we refer the reader to Figure E.1 in the Appendix). The tensor spectrum parameters are found to be mostly uncorrelated with the scalar spectrum ones. We also see that the strongest constraints on r come from the region $10^{-3} < k_{\rm pk} < 10^{-2}$ which is not surprising since features at these scales mainly affect anisotropies in the multipole range $20 \lesssim \ell \lesssim 300$, i.e., exactly the range covered by the BK18 B-mode data.

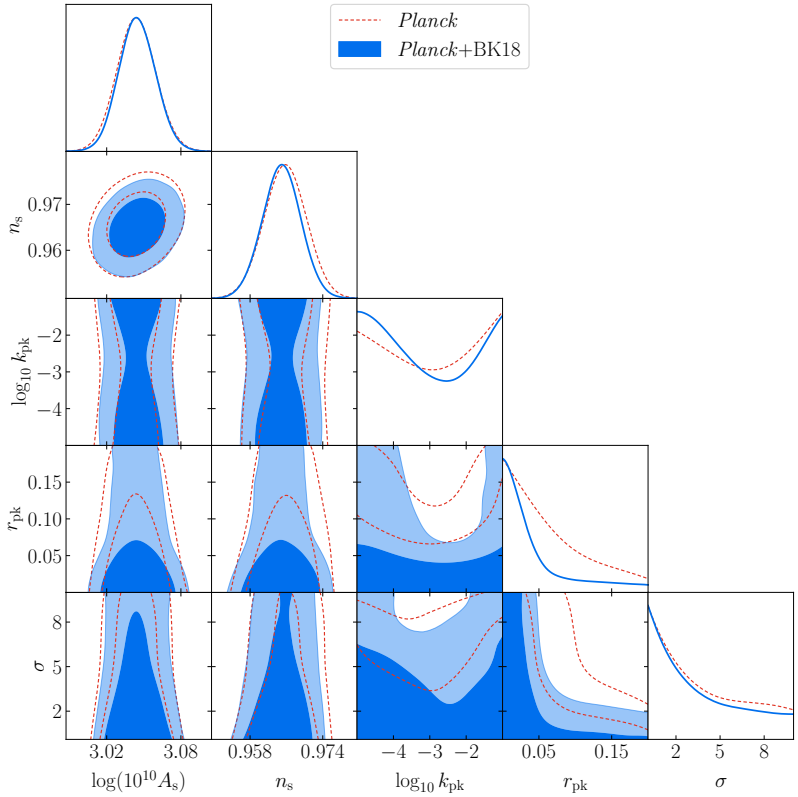

Figure 6.3: Marginalised 68% and 95% contours for the scalar and tensor power spectrum parameters. For comparison we also show the same contours obtained using only the *Planck* data, this mainly relaxes the constraints on $r_{\rm pk}$.

Parameter	68% limit
$\boldsymbol{\sigma}$	< 4.83
$\boldsymbol{r_{\rm pk}}$	< 0.0460

Table 6.2: Parameter limits for the tensor log-normal parameters from *Planck*+BK18 data. Note that these upper limits are prior dependent and may change considerably for different choices of the prior ranges for the three tensor power spectrum parameters.

For large σ the constraints on r reduce to the flat/power-law constraints, as expected. Figure 6.4 also shows that large values of $r \gtrsim 0.1$ are only allowed in the region $k_{\rm pk} \lesssim 10^{-4}$ or $k_{\rm pk} \gtrsim 10^{-2}$ and for $\sigma \lesssim 2$. The parameter limits are presented in Table 6.2. The best fit point is found to be $\{r_{\rm pk} = 0.04, \sigma = 0.43, k_{\rm pk} = 2 \times 10^{-2}\}$ with a $\Delta\chi^2$ relative to base ΛCDM of $\Delta\chi^2 = -0.22$. This result is fully compatible with the absence of tensor modes in the *Planck*+BK18 data.

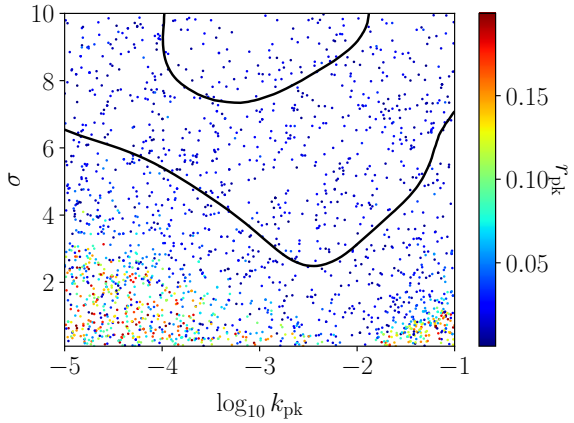

Figure 6.4: Distribution for the tensor power spectrum parameters using *Planck*+BK18 data.

6.3.2 Forecasts with LiteBIRD + CMB-S4

In this section we present forecasts of the ability of next generation CMB experiments to constrain the log-normal tensor parameters. We first take the example of LiteBIRD which is a proposed space-based CMB experiment led by JAXA with the goal of mapping the temperature and polarisation anisotropies of the CMB in the multipole range $2 \leq \ell \leq 200$ [45]. Thus, the reionization bump ($\ell \lesssim 10$) as well as the recombination bump ($\ell \sim 80$) will both be accessible to LiteBIRD. Note that a similar analysis of the detectability of such signals with LiteBIRD was also performed in Ref. [126], but only for values of σ in the range $2 \leq \sigma \leq 10$ and taking $k_{\rm pk} = 7 \times 10^{-5}$, $5 \times 10^{-3}{\rm Mpc}^{-1}$.

To estimate the constraining power of LiteBIRD, we perform a simple Fisher matrix forecast[1] to evaluate the detection prospects of the log-normal tensor spectrum. The Fisher matrix for the parameters $\vec{\theta} = (r_{\rm peak}, \sigma, k_{\rm pk})$ can be written as [480],

$$F_{ij} = f_{\rm sky} \sum_{\ell=2}^{\ell_{\rm max}} \frac{2\ell+1}{2} {\rm Tr}\left[\mathbf{C}_\ell^{-1} \frac{\partial \mathbf{C}_\ell}{\partial \theta_i} \mathbf{C}_\ell^{-1} \frac{\partial \mathbf{C}_\ell}{\partial \theta_j}\right], \tag{6.6}$$

with the marginalised 1σ error on the parameter θ_i given by

$$\sigma_i = \sqrt{(F^{-1})_{ii}}. \tag{6.7}$$

[1]The results presented in this paper are based on only varying the tensor parameters in the Fisher forecast. We checked that including the ΛCDM parameters does not significantly affect the estimates for the tensor parameters' expected uncertainties.

The matrix $\mathbf{C}_\ell$ is defined as,

$$\begin{pmatrix} C_\ell^{TT} + N_\ell^{TT} & C_\ell^{TE} & 0 \\ C_\ell^{TE} & C_\ell^{EE} + N_\ell^{EE} & 0 \\ 0 & 0 & C_\ell^{BB} + N_\ell^{BB} \end{pmatrix} \tag{6.8}$$

We also have

$$\frac{1}{N_\ell^{X,\mathrm{inst}}} = \sum_{\nu_i} \frac{1}{N_{\ell,\nu_i}^X} \tag{6.9}$$

where the instrument noise spectra at an observing frequency ν can be written as,

$$N_{\ell,\nu}^X = \Delta_\nu^X \exp\left[\ell(\ell+1)\frac{\theta_{\mathrm{FWHM}}^2}{8\log 2}\right] \tag{6.10}$$

with $X = TT, EE, BB$. We take $f_{\mathrm{sky}} = 0.65$, $\ell_{\mathrm{max}} = 200$ and adopt the LiteBIRD instrument noise specifications given in Eq. (3.1) of Ref. [481] for temperature. For the B-mode polarisation we also include foregrounds in addition to the instrument noise and then use the residual foregrounds plus post component separation noise as described in [130].[2] The lensing B-modes also act as a noise component in the search for the primordial signal and are included in the calculation of the Fisher matrices.

Much like the instrument noise, the presence of foregrounds and the lensing B-modes also hinders our ability to cleanly detect the primordial B-mode signal. Separating the contributions of these foregrounds and lensing B-modes is crucial for the detection of the inflationary gravitational wave background . Synchrotron and thermal dust emission from diffuse sources in the galaxy constitute the two main types of polarised foregrounds on large angular scales. Typically, one utilises the fact that the frequency dependence of these foregrounds is different from the CMB signal to separate their contributions to the observed polarisation and temperature maps [482]. Thus, having a large frequency coverage is vital to accurately constrain the primordial B-modes.

Removing the lensing contaminant instead requires high-resolution maps of the E-mode polarisation as well as the CMB lensing potential [483, 484] (or even the cosmic infrared background [485]). These are used to first estimate the lensing B-modes and then this estimate is used to delens the B-mode signal. The feasibility of this procedure in reducing the lensing B-mode power (and also in acoustic peak sharpening) has already been demonstrated with *Planck* [475] and will be greatly improved with next generation experiments like CMB-S4 [44, 115].

[2] The corresponding noise data were made available by the authors of Ref. [130] at https://github.com/pcampeti/SGWBProbe.

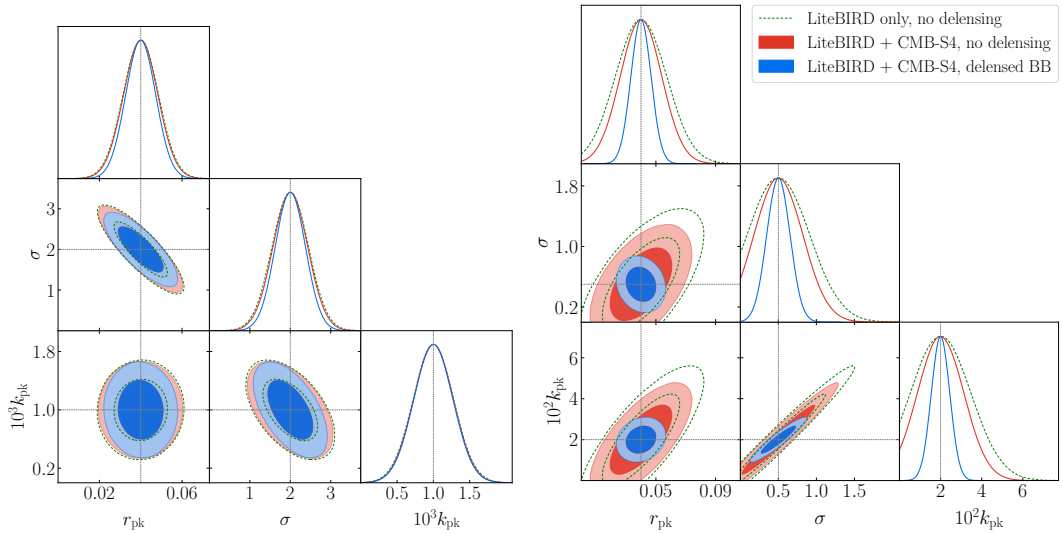

Figure 6.5: Fisher forecast for the tensor parameters assuming fiducial models with tensor features that have a chance of being detected by LiteBIRD and CMB-S4, taking $r_{\rm pk} = 0.05$, $\sigma = 2$, $k_{\rm pk} = 10^{-3}$ (left) and $r_{\rm pk} = 0.04$, $\sigma = 0.5$, $k_{\rm pk} = 2 \times 10^{-2}$ (right). The blue ellipses show the estimates in the case where the CMB-S4 data are delensed with $A_{\rm delens} = 0.8$.

In the left panel of Figure 6.5 we present the forecast for the parameter set $\{r_{\rm pk} = 0.04, \sigma = 2, k_{\rm pk} = 10^{-3}\}$. Although this parameter set is quite close to the upper limits from the *Planck*+BK18 data, it is useful to understand the constraining ability of LiteBIRD.

One can see that the tightest constraints can be achieved for $r_{\rm pk}$ whereas precise measurements of σ require a significant amount of delensing. This should be clear from the fact that to measure the width of the primordial spectrum accurately, we need to detect the primordial B-mode signal over a larger range of scales. However, significant delensing using CMB data is not possible with LiteBIRD alone since it requires information at small scales which are inaccessible to the experiment. This issue could however be overcome by using future external datasets such as those from CMB-S4.

In the right panel of Figure 6.5, we also present forecasts for the case of $\{r_{\rm pk} = 0.04, \sigma = 0.5, k_{\rm pk} = 2 \times 10^{-2}\}$, corresponding to a parameter set which produces features on scales $\ell \sim 100$. In this case, using LiteBIRD data alone, the constraints on $r_{\rm pk}$ are weaker since this corresponds to scales where the B-mode signal is lensing dominated. Significant delensing needs to be achieved to precisely constrain this scenario. For this purpose, we consider the possibility of delensing using the high-resolution capabilities of CMB-S4 [44, 115].

CMB-S4 forecasts for r typically assume $f_{\rm sky} = 0.03$ and we take the same value here for the Fisher forecasts of the lognormal parameters. This specific choice of $f_{\rm sky}$ arises from an optimisation procedure which takes into account delensing requirements, foreground mitigation and reproducibility of results across the sky [115]. We also take a delensing fraction $A_{\rm delens} = 0.8$ which represents an 80% reduction in the lensing B-mode power spectra. The analysis of [115] suggests that achieving this value is not entirely unrealistic. The CMB-S4 multipole range for the delensed B-mode data is taken to be $30 < \ell < 300$ and the instrument noise specifications are those corresponding to the 'SAT' configuration and are available at this link[3]. We do not take into account foreground residuals for CMB-S4 and assume that these have been perfectly subtracted from the data. In reality, imperfect subtraction will lead to the presence of foreground residuals which will again act as an additional noise towards the detection of the primordial signal but this will not degrade sensitivity to the tensor-scalar ratio by more than 10^{-3} [115], which is smaller than the B-mode amplitudes in our fiducial models. The resulting estimates for this setup are shown in the same figure. We can see that a significant increase in constraining power is obtained with the addition of CMB-S4 and a delensing level $A_{\rm delens} = 0.8$.

We conclude this section with two more examples. The left panel of Figure 6.6 presents forecasts assuming the presence of the vacuum contribution to the tensor power spectrum with $r = 0.03, 0.01$ which effectively acts as a 'noise' for the log-normal tensor spectrum detection. For the $r = 0.01$ scenario, the forecasts are not very different from the case of $r = 0$ which is expected since in this case the sourced tensor spectrum is much larger than the vacuum contribution on the relevant scales. As expected, for larger r, the sensitivity to the log-normal tensor spectrum parameters is slightly reduced. The right panel of the same figure shows how the degeneracy between the parameters r and $r_{\rm pk}$ increases as the peak width σ increases, which leads to significantly worse estimates of $r_{\rm pk}$. This is not unexpected, since for larger σ the lognormal spectrum starts to resemble a flat spectrum on the relevant scales.

Finally, the bottom panel presents a scenario with a smaller amplitude of the sourced tensors $r_{\rm pk} = 0.02$, $\sigma = 0.5$ and $k_{\rm pk} = 2 \times 10^{-2}$. In this case the signal is detectable only if a significant amount of delensing can be achieved. For this value of $r_{\rm pk}$, the B-mode signal is entirely lensing dominated on angular scales $\ell > 100$.

[3] https://cmb-s4.uchicago.edu/wiki/index.php/Delensing_sensitivity_-_updated_sensitivities,_beams,_TT_noise

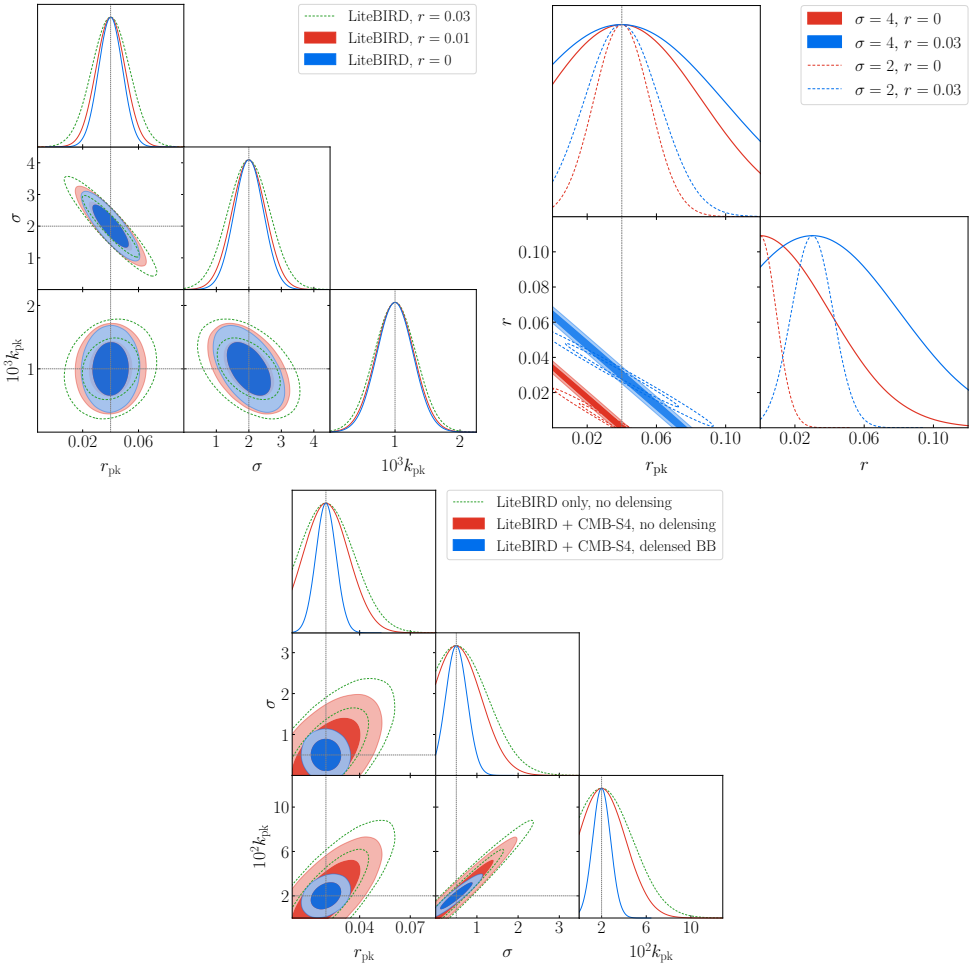

Figure 6.6: Left: Fisher forecast for the tensor parameters taking $r_{\rm pk} = 0.04$, $\sigma = 2$, $k_{\rm pk} = 10^{-3}$ for three different values of the vacuum tensor scalar ratio r. No delensing assumed for this case. Right: Forecasts for r-$r_{\rm pk}$ with σ and $k_{\rm pk}$ fixed to the same values as in the left panel. Bottom: $r_{\rm pk} = 0.02$, $\sigma = 0.5$, $k_{\rm pk} = 2 \times 10^{-2}$ assuming $A_{\rm delens} = 0.8$, $r = 0$ for this case.

6.4 Conclusions

In the event of a future B-mode detection associated to primordial tensor perturbations, the natural next step would be to understand the production mechanism behind these perturbations. This information is contained in the amplitude, shape, chirality and non-Gaussianity of the primordial tensor spectrum.

Our focus here has been on the shape of the tensor spectrum, taking the example of a bump-like feature typical of GW sourced by axion-gauge fields during inflation. This shape deviates sharply from the SFSR prediction which is bound by the tensor consistency relation to be a power law with a slightly red tilted spectrum.

Naturally, a detection of such a feature in the primordial tensor spectrum would hint to inflationary dynamics richer than those of SFSR and could be used to constrain the parameter space of such axion-gauge field models. On the other hand, even the non-detection of such a spectrum would be quite informative since that would strengthen our confidence in the SFSR model, especially given the difficulty in directly verifying the SFSR tensor consistency relation with future CMB probes.

In this paper, we first searched for the presence of such features using the temperature and polarisation anisotropy data from the *Planck* + BICEP/Keck experiments. While the current data do not provide any evidence for the presence of such features, they do place constraints on the tensor power spectrum parameters. In particular, strong constraints on the peak amplitude are obtained in the region $10^{-3} \lesssim k \lesssim 10^{-2}$ which is main sensitivity range of the BICEP/Keck B-mode data.

We also presented forecasts of the ability of two future CMB experiments, namely LiteBIRD and CMB-S4, to detect such features. LiteBIRD's unprecedented accuracy in measuring polarisation at large angular scales gives it an excellent sensitivity to the amplitude of such features and will improve upon current sensitivity by at least a factor of two. However, accurate measurements of the width will require a significant amount of delensing, which could be provided by high-resolution CMB experiments such as CMB-S4.

If primordial tensor power spectrum features were realised in Nature, their detection would represent a fascinating window into the earliest moments of the Universe, and help us get closer to a more complete understanding of the physics of inflation. With

the CMB experiments coming online in the next decade, we might just be able to take a peek.

Chapter 7

Conclusions

Four decades since its inception, inflation remains the leading paradigm to describe the physics of the early universe and has established itself as a cornerstone of ΛCDM cosmology. It provides a compelling solution to the shortcomings of the hot big bang model and naturally sets the initial conditions for the density perturbations of matter and radiation.

Despite these successes, the physics of inflation still remains a mystery to us. Observations of the CMB and LSS suggest a vanilla single field realisation, at least on the largest scales. Indeed, several observationally compatible single-field models exist, but none have yet emerged as the unequivocal choice to describe the physics of the inflationary era. There exist several embeddings of the inflationary mechanism in canditate theories of quantum gravity, e.g. string theory [46]. In this context however, multi-field realisations appear to be more likely to emerge compared to single-field ones.

Models beyond SFSR exhibit a much richer phenomenology compared to their single-field counterparts, they can break the inflationary consistency relations, generate large non-Gaussianity and produce observable GW signals on small scales. A detection of such signatures could definitively rule out all single-field models of inflation and may even point towards the specific multi-field realisation. Therefore, understanding the phenomenology of these models is essential for extracting crucial information about inflationary physics from observations.

This thesis has focused on gravitational wave signatures of multi-field models, with

particular attention paid to GW anisotropies and non-Gaussianity on interferometer scales, and the spectral shape on CMB scales. We started in chapters 2 and 3 with a brief introduction to the ΛCDM model and inflation, prioritising the main results and concepts necessary to understand the original work of this thesis.

In chapter 4, we studied the anisotropies of primordial gravitational wave backgrounds using the line-of-sight formalism, a standard tool originally developed to describe CMB anisotropies. As an application of this formalism, we computed the anisotropy spectrum associated to a GW background with a highly peaked spectral shape. Typically, such shapes arise in GW induced from sharply enhanced scalar perturbations on small scales, possible in several multi-field inflationary models and often invoked in scenarios involving the formation of primordial black holes. We found the spectral shape strongly affects the detectability of the anisotropies, leading to a strong enhancement and a non-trivial frequency dependence of the anisotropies in the case of a peaked spectral shape as opposed to a power-law background with $n_\Omega \sim \mathcal{O}(1)$. The frequency dependence of the anisotropies may prove to be an essential tool for the task of separating the anisotropies of different cosmological and astrophysical backgrounds in the SGWB map, similar to component separation methods used for the CMB.

The second part of chapter 4 explores the role of the initial condition term in the GW line-of-sight formalism with some representative applications. We first demonstrated that in the case of adiabatic initial conditions the anisotropies are insensitive to the presence of a non-standard equation of state before the standard radiation dominated era. We saw that physically, the result can be understood as a consequence of the conservation of the curvature perturbation ζ on super-horizon scales.

We then turned to the case of isocurvature initial conditions, generated through the curvaton mechanism in which the curvature perturbation is generated not by the inflaton, but by an additional light scalar field that dominates the energy budget of the universe after inflation. We found a four-fold enhancement of the GW anisotropies (w.r.t. the adiabatic case) in the simplest curvaton scenario. Understanding how large the GW isocurvature can be in a concrete realisation of the curvaton scenario, while keeping in mind the current constraints on isocurvature perturbations is a possibility worth looking into further. Another interesting direction of research would be to explore the cross-correlation of the GW anisotropies with those of the CMB for

different kinds of curvaton scenarios.

Chapter 5 is devoted to the generation of inflationary tensor non-Gaussianity and its detectability on interferometer scales. We showed that even though propagation effects forbid a direct detection of the tensor bispectrum ($\langle h^3 \rangle$) for most momentum configurations, the anisotropies of the energy density still retain information about squeezed limit tensor non-Gaussianity. These anisotropies and their cross-correlation with the CMB are sensitive to the mass, spin and couplings of the additional fields active during inflation. Importantly, we saw that models predicting enhanced GW signals at small scales can also accommodate large squeezed non-Gaussianity, with the resulting anisotropy a promising probe of the "cosmological collider". Exploring how such cosmological collider signals could also be extracted from the CMB temperature and polarisation anisotropies is a research direction that warrants further investigation and complements the work presented in this chapter.

The possibility of detecting large scale GW produced in axion-gauge field models of inflation, through their effects on the CMB anisotropies, was the subject of chapter 6. These models can violate the tensor consistency relation ($n_{\rm t} = -r/8$) of single-field inflation and typically predict a bump like GW spectral shape. We first derived constraints on the parameters describing the shape of this bump, using a combination of the *Planck* and the most recent BICEP/Keck datasets. We then presented forecasts of the precision with which LiteBIRD and CMB-S4 will be able to measure the spectral shape of the inflationary GW. In the future, it would also be important to explore the other types of GW features that inflationary models can generate and how well these experiments might be able to constrain them. Data analysis techniques that may be better suited for more complicated features (e.g. oscillatory) will also be worth exploring [486].

In summary, gravitational waves represent a missing piece of the inflationary puzzle and their detection has the potential to completely transform our picture of the primordial universe. The study of these gravitational waves carried out in this thesis serves as a contribution to a much broader effort, involving both theory and experiment, with the aim of developing a comprehensive understanding of inflation and the physical laws that govern the universe in its earliest stages. Hopefully, future cosmological observations will bring us closer to this ultimate goal.

Appendix A

In-In Formalism

In the Heisenberg picture, the time evolution of an operator O is derived from the full Hamiltonian H with

$$\frac{d}{dt}Q(t) = i[H, Q]. \tag{A.1}$$

The Hamiltonian is a functional of the fields and their conjugate momenta, defined as

$$H[\psi(t), \pi(t)] = \int d^3x\, \mathcal{H}[\psi(\boldsymbol{x}, t), \pi(\boldsymbol{x}, t)]. \tag{A.2}$$

We now split our fields ψ, π into a homogeneous background $\bar{\psi}(t), \bar{\pi}(t)$ and a space-time dependent perturbation $\delta\psi(\boldsymbol{x}, t), \delta\pi(\boldsymbol{x}, t)$. In our perturbative approach, the background fields are c-numbers and obey the classical equation of motion while the perturbations obey the usual commutation relations

$$[\delta\psi(\boldsymbol{x}, t), \delta\pi(\mathbf{y}, t)] = i\delta(\boldsymbol{x} - \mathbf{y}), \quad [\delta\psi(\boldsymbol{x}, t), \delta\psi(\mathbf{y}, t)] = [\delta\pi(\boldsymbol{x}, t), \delta\pi(\mathbf{y}, t)] = 0. \tag{A.3}$$

We expand the Hamiltonian around the classical solution

$$\begin{aligned} H[\psi(t), \pi(t)] = H[\bar{\psi}(t), \bar{\pi}(t)] &+ \int d^3x\, \frac{\delta\mathcal{H}}{\delta\psi}\bigg|_{\bar{\psi}, \bar{\pi}} \delta\psi(\boldsymbol{x}, t) + \int d^3x\, \frac{\delta\mathcal{H}}{\delta\pi}\bigg|_{\bar{\psi}, \bar{\pi}} \delta\pi(\boldsymbol{x}, t) \\ &+ \tilde{H}[\delta\psi(\boldsymbol{x}, t), \delta\pi(\boldsymbol{x}, t)], \end{aligned} \tag{A.4}$$

where the linear order terms vanish on the classical background solution and we collect in $\tilde{H}$ terms of quadratic or higher order in $\delta\psi(\boldsymbol{x}, t), \delta\pi(\boldsymbol{x}, t)$. The perturbations evolve according to

$$\frac{d}{dt}\delta\psi = i[\tilde{H}[\delta\psi(t), \delta\pi(t)], \delta\psi], \quad \frac{d}{dt}\delta\pi = i[\tilde{H}[\delta\psi(t), \delta\pi(t)], \delta\pi], \tag{A.5}$$

which has the solution

$$\delta\psi(t) = U^{-1}(t,t_0)\delta\psi(t_0)U(t,t_0), \quad \delta\pi(t) = U^{-1}(t,t_0)\delta\pi(t_0)U(t,t_0). \tag{A.6}$$

The unitary evolution operator U obeys,

$$\frac{d}{dt}U(t,t_0) = -i\tilde{H}(t_0)U(t,t_0), \quad U(t_0,t_0) = 1. \tag{A.7}$$

Unfortunately in this form the equations of motion become non-linear making it hard to obtain a solution. This necessitates a perturbative approach for which we further split $\tilde{H}$ into a quadratic kinematical part and interactions

$$\tilde{H} = H_0 + H_{\rm int}. \tag{A.8}$$

The leading time evolution of the perturbations now is governed by the their (free) quadratic Hamiltonian H_0 resulting in linear equations of motion. We label these *interaction picture* fields as $\delta\psi^I, \delta\pi^I$ with

$$\frac{d}{dt}\delta\psi^I = i[H_0[\delta\psi^I(t),\delta\pi^I(t)],\delta\psi^I], \quad \frac{d}{dt}\delta\pi^I = i[H_0[\delta\psi^I(t),\delta\pi^I(t)],\delta\pi^I], \tag{A.9}$$

and initial conditions

$$\delta\psi^I(\boldsymbol{x},t_0) = \delta\psi(\boldsymbol{x},t_0), \quad \delta\pi^I(\boldsymbol{x},t_0) = \delta\pi(\boldsymbol{x},t_0). \tag{A.10}$$

Notice that since H_0 generates their time evolution, the interaction picture fields are the same free fields we encountered when calculating the power spectrum in the previous sections. The interaction Hamiltonian $H_{\rm int}$ can then be used to compute the corrections to the correlation functions, perturbatively in $H_{\rm int}$. Notice that in (A.9), we can evaluate H_0 at any arbitrary time t. Taking this to be $t = t_0$, the solution to (A.9) is

$$\delta\psi^I(t) = U_0^{-1}(t,t_0)\delta\psi^I(t_0)U_0(t,t_0) \tag{A.11}$$

and similarly for $\delta\pi(t)$. Here

$$\frac{d}{dt}U_0(t,t_0) = -iH_0[\delta\psi(t_0),\delta\pi(t_0)]U_0(t,t_0), \quad U_0(t_0,t_0) = 1. \tag{A.12}$$

Now, we introduce $F(t,t_0) \equiv U_0^{-1}(t,t_0)U(t,t_0)$ as the evolution operator associated to $H_{\rm int}$, i.e.

$$\frac{d}{dt}F_0(t,t_0) = -iH_{\rm int}[\delta\psi^I(t),\delta\pi^I(t)]U_0(t,t_0), \quad F(t_0,t_0) = 1, \tag{A.13}$$

with the solution

$$F(t,t_0) = Te^{-\int_{t_0}^{t} H_{\rm int}(t')dt'}. \tag{A.14}$$

This allows us to write the expectation value of the operator $Q(t)$ as

$$\begin{aligned}
\langle Q(t)\rangle &= \langle\Omega|Q[\delta\psi(t),\delta\pi(t)]|\Omega\rangle \\
&= \langle\Omega|U^{-1}(t,t_0)Q[\delta\psi(t_0),\delta\pi(t_0)]U(t,t_0)|\Omega\rangle \\
&= \langle\Omega|F^{-1}(t,t_0)Q[\delta\psi^I(t_0),\delta\pi(t)]U(t,t)F(t,t_0)|\Omega\rangle \\
&= \langle\Omega|\left(\bar{T}e^{-i\int_{t_0}^{t} H_{\rm int}(t')dt'}\right)^{\dagger} Q[\delta\psi^I(t),\delta\pi^I(t)]Te^{-i\int_{t_0}^{t} H_{\rm int}(t')dt'}|\Omega\rangle
\end{aligned} \tag{A.15}$$

The final step is to relate the interaction vacuum $|\Omega\rangle$ to the vacuum of the free theory $|0\rangle$. Let $t_0 \to -\infty^+ \equiv -\infty(1+i\epsilon)$ in (A.15). This effectively turns off the interaction in the far past so that we can identify $|\Omega\rangle \to |0\rangle$. Thus, we finally arrive at the *in-in* master formula,

$$\boxed{\langle Q\rangle = \langle 0|\bar{T}e^{i\int_{-\infty^-}^{t} H_{\rm int}(t')dt'}Q(t)Te^{i\int_{-\infty^+}^{t} H_{\rm int}(t')dt'}|0\rangle}, \tag{A.16}$$

where $\bar{T}$ represents anti time-ordering and the $-\infty^- = -\infty(1-i\epsilon)$ limit arises from the complex conjugation.

Appendix B

GW anisotropies

B.1 Uniform density gauge calculation

To relate the Newtonian gauge results of section 4.2 with the calculation of [253], we provide here a simplified calculation of the anisotropies using the uniform density gauge. The starting point of the calculation of [253] is the metric in the uniform density gauge during matter domination. This is given by [487],

$$ds^2 = a^2(\eta)\left[-d\eta^2 + (1+2\zeta)\delta_{ij}dx^i dx^j - \frac{4}{5aH}\partial_i\zeta d\eta dx^i\right] . \tag{B.1}$$

We are now looking to solve the Boltzmann equation,

$$\frac{df}{d\eta} = \frac{\partial f}{\partial \eta} + \frac{\partial f}{\partial x^i}\frac{dx^i}{d\eta} + \frac{\partial f}{\partial q}\frac{dq}{d\eta} = 0, \tag{B.2}$$

in this gauge.

Let λ be the affine parameter along the graviton geodesic. The graviton 4-momentum is then $P^\mu = dx/d\lambda$. We can express this in terms of the physical momentum p defined as $p^2 \equiv g_{ij}P^iP^j$, and $\hat{n}$, the unit vector along the GW direction. To this end, we first write $P^i = C\hat{n}$, where C can be determined in terms of p as,

$$\begin{aligned} p^2 = g_{ij}P^iP^j &= a^2(1+2\zeta)C^2\delta_{ij}n^in^j \\ \implies C &= \frac{p}{a}(1-\zeta)\,. \end{aligned} \tag{B.3}$$

Next, using $g_{\mu\nu}P^\mu P^\nu = 0$ we find,

$$P^0 = \frac{p}{a}\left(1 - \frac{2}{5aH}\partial_i\zeta n^i\right) . \tag{B.4}$$

We can now write the graviton 4-momentum P^μ in terms of the magnitude of the physical momentum p and the direction of propagation $\hat{n}$ as

$$P^\mu = \frac{p}{a}\left(1 - \frac{2}{5aH}\partial_i\zeta n^i, (1-\zeta)\hat{n}\right) . \tag{B.5}$$

To solve the Boltzmann equation (B.2) we need to calculate $dq/d\eta$ with $q = |\vec{p}|a$. Using Eqs. (B.3) and (B.4) one finds $P_0 = -q$. Thus, it only remains to solve the geodesic equation for P_0. This equation is given by [74],

$$\frac{dP_0}{d\lambda} = \frac{1}{2}\partial_0 g_{\alpha\beta}P^\alpha P^\beta . \tag{B.6}$$

Using the fact that $d/d\lambda = P^0 d/d\eta$ one can re-write the above equation as

$$P^0\frac{dP_0}{d\eta} = \frac{1}{2}\partial_0 g_{\alpha\beta}P^\alpha P^\beta . \tag{B.7}$$

To simplify things further, we can work with the re-scaled metric without the scale factor which we denote by $\tilde{g}_{\mu\nu}$, i.e. $g_{\mu\nu} = a^2\tilde{g}_{\mu\nu}$. The null geodesics remain the same; the affine parameters and the tangent vectors in the rescaled metric, on the other hand, are respectively given by $d\tilde{\lambda} = a^{-2}d\lambda$ and $\tilde{P}_\mu = a^2 P^\mu$ [488]. One also finds $P_\mu = \tilde{P}_\mu$. Using these relations the geodesic equation reads,

$$\frac{d\tilde{P}_0}{d\eta} = -\frac{2}{5}\tilde{P}^0\left(\frac{a}{a'}\right)'\partial_i\zeta n^i , \tag{B.8}$$

where the prime denotes a partial derivative with respect to conformal time. Using $P_0 = \tilde{P}_0$ and re-writing the above expression using the quantities defined in the original metric $g_{\mu\nu}$, one obtains at linear order in ζ,

$$\begin{aligned}\frac{dP_0}{d\eta} &= -\frac{1}{5}a^2 P^0\,\partial_i\zeta n^i \\ &= -\frac{1}{5}q\,\partial_i\zeta n^i .\end{aligned} \tag{B.9}$$

From this one can simply read off the derivative

$$\frac{dx^i}{d\eta} = \frac{P^i}{P^0} = n^i . \tag{B.10}$$

Note that we only need this term at zeroth order, since it multiplies $\partial f/\partial x^i$ which is a first order quantity. For $dq/d\eta$ we also have

$$\frac{dq}{d\eta} = \frac{1}{5}q\,\partial_i\zeta n^i . \tag{B.11}$$

Using the above results, one can finally write the Boltzman equation as

$$\frac{\partial f}{\partial \eta} + \frac{\partial f}{\partial x^i} n^i + \frac{1}{5} q \partial_i \zeta n^i \frac{\partial f}{\partial q} = 0 \,. \tag{B.12}$$

In terms of the perturbation to the distribution function

$$\delta f = -q \Gamma(\eta, \vec{x}, q, \hat{n}) \frac{\partial \bar{f}}{\partial q}, \tag{B.13}$$

one obtains,

$$\frac{\partial \Gamma}{\partial \eta} + n^i \frac{\partial \Gamma}{\partial x^i} = \frac{1}{5} \frac{\partial \zeta}{\partial x^i} n^i \,. \tag{B.14}$$

In Fourier space,

$$\frac{\partial \Gamma_k}{\partial \eta} + ik\mu\Gamma_k = \frac{ik\mu}{5} \zeta_k \,, \tag{B.15}$$

with $\mu \equiv \hat{k} \cdot \hat{n}$. This can be solved to give

$$\Gamma_k(\eta) = e^{ik\mu(\eta_{\rm in} - \eta)} \left[\Gamma_k(\eta_{\rm in}, q, \hat{n}) - \frac{1}{5} \zeta_k(\eta_{\rm in}) \right] \,, \tag{B.16}$$

Since the gauge of Eq. (B.1) is the uniform matter density gauge, it must also be the uniform GW density gauge, i.e. for adiabatic initial conditions we must have

$$\frac{\delta \rho_{\rm GW}}{\bar{\rho}_{\rm GW}} = 0 \implies \Gamma_I = 0. \tag{B.17}$$

The present day observed anisotropy then becomes,

$$\Gamma(\vec{x}_0, \eta_0, \hat{n}) = -\frac{1}{5} \zeta(\vec{x}_{\rm in}, \eta_{\rm in}) \tag{B.18}$$

with $\vec{x}_{\rm in} = \vec{x}_0 + \hat{n}(\eta_{\rm in} - \eta_0)$. In terms of $\delta^{\rm GW}$, we have

$$\delta^{\rm GW}(q, \hat{n}) = \frac{1}{5} \zeta(\eta_i, \vec{x}_i) \frac{\partial \ln \bar{f}(q)}{\partial \ln q} \tag{B.19}$$

SFSR inflation produces a power law distribution function with

$$\bar{f}(q) \propto (q_0/q)^{2(\nu+1+\epsilon)} \tag{B.20}$$

where q_0 is a reference momentum, ϵ the standard slow-roll parameter during inflation and $\nu = 2/(1+3w)$ with w being the equation of state when the GW mode q re-enters the horizon [253]. This gives

$$\delta^{\rm GW}(q, \hat{n}) = -\frac{2}{5} (\nu + 1 + \epsilon) \zeta(\eta_i, \vec{x}_i) \,. \tag{B.21}$$

which is the result of ref. [253].

This matches the Newtonian gauge results of section 4.2 if the initial conditions are set during matter domination. To see this, we make use of eqs. (4.40) and (4.42), and the fact that the Newtonian gauge potentials Φ and Ψ are constant during matter domination. From the results of section 4.4, we know that this choice of initial conditions works fine for modes re-entering the horizon during matter domination, i.e., modes with $k < k_{\rm eq}$, but not for modes with $k > k_{\rm eq}$.

Additionally, as already pointed out by the authors of [253], it does not take into account the effect of the late-time ISW arising from the transition to Λ-dominated universe which provides a relatively smaller but non-negligible contribution to the anisotropies (fig. 4.1).

B.2 Alternate derivation of the initial condition term

We present here an alternative method to derive the initial condition term (eq. (4.23)) in terms of the primordial perturbation ζ, based on the separate universe approach. We follow the derivation of ref. [489] which used this to derive the initial conditions for the CMB anisotropies.

The perturbed Newtonian gauge metric of eq. (4.1) can be can be brought to an unperturbed form

$$ds^2 = a^2(\tilde{\eta})\left[-d\tilde{\eta}^2 + \delta_{ij}d\tilde{x}^i d\tilde{x}^j\right], \tag{B.22}$$

using the coordinate transformation $x^\mu \to \tilde{x}^\mu \equiv x^\mu + \xi^\mu$ with

$$\xi^0 = \begin{cases} -\dfrac{1}{5}\zeta\eta, & \text{M.D.} \\ -\dfrac{1}{3}\zeta\eta, & \text{R.D.} \end{cases} \tag{B.23}$$

and

$$\xi^i = -\zeta x^i\,. \tag{B.24}$$

In fact, for a general equation of state w, the required time transformation is [489],

$$\xi^0 = -\frac{\zeta}{a^2}\int a^2\, d\eta. \tag{B.25}$$

Since the scale factor evolves as $a \propto \eta^{2/(1+3w)}$ for $w > -1/3$, we obtain the solution

$$\xi^0 = -\zeta\eta\frac{1+3w}{5+3w}, \tag{B.26}$$

which reduces to eq. (B.23) for $w = 0,\, 1/3$. The GW density perturbation is $\delta\tilde{\rho}_{\rm GW} = 0$ in the unperturbed coordinates. By reversing the coordinate transformation, we can obtain the required Newtonian gauge GW density perturbation as

$$\begin{aligned}\delta\rho_{\rm GW} &= \delta\tilde{\rho}_{\rm GW} + \bar{\rho}'_{\rm GW}\xi^0 \\ &= -4\mathcal{H}\bar{\rho}_{\rm GW}\xi^0\,, \end{aligned} \tag{B.27}$$

where $\bar{\rho}'_{\rm GW} = -3\mathcal{H}(1 + w_{\rm GW})\bar{\rho}_{\rm GW}$. Now, with ξ^0 given by eq. (B.26), we get the required result of eq. (4.23).

Appendix C

Noise Angular Power Spectra of GW Experiments

In this appendix we describe the calculation of the noise angular power spectra of GW detectors which is based on the analytical formalism of [403] and is used to perform the forecasts in chapters 4 and 5. We first review the basic definitions of the quantities involved in GW anisotropy detection and then list the detector networks and specifications used for the forecasts.

C.1 Formalism and definitions

We start by expanding the SGWB in plane waves,

$$h_{ij}(\vec{x},t) = \sum_{s=+,\times} \int df \int d^2\hat{n}\, h_s(f,\hat{n}) e^{i2\pi f(t-\hat{n}\cdot\boldsymbol{x})} e^s_{ij}(\hat{n})\,, \tag{C.1}$$

where s denotes the GW linear polarisation, f is the GW frequency and $\hat{n}$ the direction of propagation. The strain power spectra for unpolarised GW can be written as,

$$\langle h_s(f,\hat{n}) h_{s'}(f',\hat{n}')\rangle = \frac{1}{2}\delta(f-f')\frac{\delta^2(\hat{n}-\hat{n}')}{4\pi}\delta_{ss'} I(f,\hat{n})\,, \tag{C.2}$$

where I is the SGWB intensity. The observed detector response at a position $\boldsymbol{x}$ is the convolution of the detector response tensor a^{ij} with the GW strain plus a noise term $n(t,f)$,

$$d(f,t) = \int d^2\hat{n} \sum_s h_s(f,\hat{n}) a^{ij} e^s_{ij}(\hat{n}) e^{-i2\pi f \hat{n}\cdot\boldsymbol{x}} + n(t,f)\,. \tag{C.3}$$

The noise has its own power spectral density given by

$$\langle n(f)n(f')\rangle = \frac{1}{2}\delta(f-f')N_f\,, \tag{C.4}$$

for stationary i.e. time-independent noise. The detector response tensor, for a Michelson interferometer, can be written as

$$a^{ij} = \frac{1}{2}\left[\hat{u}^i\hat{u}^j\mathcal{T}(\hat{n}\cdot\hat{u},f) - \hat{v}^i\hat{v}^j\mathcal{T}(\hat{n}\cdot\hat{v},f)\right]\,, \tag{C.5}$$

where $\hat{u},\hat{v}$ are the unit vectors along the detector arms and the transfer function $\mathcal{T}(\hat{n}\cdot\hat{u},f)$ is [241]

$$\mathcal{T}(\hat{n}\cdot\hat{u},f) = \frac{1}{2}\Bigg[\mathrm{sinc}\left(\frac{\pi fL}{c}(1-\hat{n}\cdot\hat{u})\right)e^{-i\frac{\pi fL}{c}(3+\hat{n}\cdot\hat{u})} \tag{C.6}$$

$$+\,\mathrm{sinc}\left(\frac{\pi fL}{c}(1+\hat{n}\cdot\hat{u})\right)e^{-i\frac{\pi fL}{c}(1+\hat{n}\cdot\hat{u})}\Bigg]\,. \tag{C.7}$$

The SGWB and its anisotropies are detected by cross-correlating data across different detector pairs where the noise can safely be assumed to be uncorrelated [241]. One can then glean from this cross-correlation estimator, the statistics of the isotropic and anisotropic parts of the SGWB energy density map e.g. see [238, 241, 248, 251, 490, 491].

To define a noise angular power spectrum, we first assume that the intensity is separable into a the product of a direction dependent part and a frequency dependent part[1], $I(f,\hat{n}) = I_0(\hat{n})\xi(f)$, with $\xi(f_{\rm ref})=1$ at a reference frequency $f_{\rm ref}$. The resulting noise angular power spectrum is [403],

$$N_\ell^{-1} \equiv \frac{1}{2}\sum_{ABCD}\int df\int dt\left(\frac{2\xi(f)}{5}\right)^2(N_f^{-1})^{AB}(N_f^{-1})^{CD} \times\frac{\sum_m \mathrm{Re}(\mathcal{A}_{BC,\ell m}(t,f)\mathcal{A}^*_{DA,\ell m}(t,f))}{2\ell+1}\,, \tag{C.8}$$

where the sum is over *combinations of detector pairs* AB and CD. The N_f^{AB} denote the noise covariance matrix and $\mathcal{A}_{AB,\ell m}$ the spherical harmonic transform of the antenna pattern for the detector pair AB

$$\mathcal{A}_{AB}(\hat{n},f) = \underbrace{\frac{5}{8\pi}\left[\mathrm{Tr}(a_A^Te^+)\mathrm{Tr}(a_B^Te^+)^* + \mathrm{Tr}(a_B^Te^\times)\mathrm{Tr}(a_A^Te^\times)^*\right]}_{\text{overlap function for detector pair } AB} e^{-i2\pi f\hat{n}\cdot(\boldsymbol{x}_A-\boldsymbol{x}_B)}\,. \tag{C.9}$$

[1] Equivalently, this implies that the anisotropy $\delta^{\rm GW}$ and the monopole $\overline{\Omega}_{\rm GW}$ share the same frequency dependence.

We assume that that network of detectors under consideration behaves like a rigid body under 3D rotations so that eq. (C.8) simplifies to [403]

$$N_\ell^{-1} = \frac{T_{\rm obs}}{2} \sum_{ABCD} \int df \left(\frac{2\xi(f)}{5}\right)^2 (N_f^{-1})^{AB} (N_f^{-1})^{CD} \times \frac{\sum_m \mathrm{Re}(\mathcal{A}_{BC,\ell m}(f)\mathcal{A}^*_{DA,\ell m}(f))}{2\ell+1} \,. \tag{C.10}$$

Here, $T_{\rm obs}$ denotes the total observation time. For uncorrelated noise across detector pairs i.e. where $N_f^{AB} = \delta_{AB} N_f^A$, eq. (C.10) further simplifies to

$$N_\ell^{-1} = T_{\rm obs} \sum_{A,B\neq A} \int df \left(\frac{2\xi(f)}{5}\right)^2 \frac{\sum_m |\mathcal{A}_{AB,\ell m}(f)|^2}{N_f^A N_f^B (2\ell+1)} \,. \tag{C.11}$$

This denotes the angular power spectrum of the detector noise for the quantity I which is related to the spectral energy density parameter as [241],

$$\overline{\Omega}_{\rm GW}(f,\hat{n}) = \frac{4\pi^2 f^3}{3H_0^2} I(f,\hat{n}) \,, \tag{C.12}$$

The corresponding anisotropy and noise angular power spectra are thus related by,

$$C_\ell^{\Omega_{\rm GW}}(f) = \left(\frac{4\pi^2 f^3}{3H_0^2}\xi(f)\right)^2 C_\ell^{I_0} \,, \quad N_\ell^{\Omega_{\rm GW}}(f) = \left(\frac{4\pi^2 f^3}{3H_0^2}\xi(f)\right)^2 N_\ell \,. \tag{C.13}$$

For the forecasts in chapter 5, we work with the quantity $N_\ell^{\rm GW}$ defined as,

$$N_\ell^{\rm GW} = \frac{N_\ell^\Omega(f)}{\overline{\Omega}^2_{\rm GW}(f)} \,. \tag{C.14}$$

In section 4.3 of chapter 4 we have a situation where the frequency dependence of the monopole and anisotropy are not the same. For this, we need to define the frequency-dependent angular sensitivity of the detector network to the $\ell-$th multipole [404],

$$\Omega^\ell_{\rm GW,n}(f)^{-1} \equiv T_{\rm obs} \sum_{AB} \left(\frac{2}{5}\right)^2 \left(\frac{4\pi^2 f^3}{3H_0^2}\right)^{-2} \frac{1}{N_f^A N_f^B} \frac{\sum_m |\mathcal{A}^{\ell m}_{AB}(f)|^2}{(2\ell+1)} \,. \tag{C.15}$$

C.2 Detector Networks

The noise angular spectra for ET-CE were already calculated in ref. [403] and we adapted the corresponding code schNell to perform the same calculations for LISA-Taiji, BBO and PTAs.

ET-CE

In the case of ET-CE, we use cross-correlations among the ET vertices with noise correlation matrices $N_f^{AB} = 0.2\sqrt{N_f^A N_f^B}$ for $A \neq B$ as well as the ET-CE cross-correlations for which the noise is uncorrelated. We do not consider ET or CE self-correlations. The detector locations are assumed to be the same as the ones considered in [403] and the total time of observations is taken to be $T_{\rm obs} = 4$ years and $f_{\rm ref}^{\rm ET-CE} = 63$ Hz. The corresponding noise curves for ET[2] and CE[3] are publicly available.

LISA-Taiji

LISA and Taiji are assumed to be in earth-like orbit around the sun and separated from each other by an angle of 40° [406]. We include all LISA-Taiji cross-correlations as well as self-correlations with the noise curves taken from [371] for LISA and [406] for Taiji. The total time of observation is assumed to be $T_{\rm obs} = 4$ years and $f_{\rm ref}^{\rm LISA-Taiji} = 0.01$ Hz.

BBO

For BBO we consider the configuration consisting of four LISA-like constellations, with two of them in the form of a hexagon. The other two outer constellations will lead and lead the hexagon by 120°, all of them orbiting the sun in an earth-like orbit [118]. The BBO noise curves are obtained from [492] and for the observation and reference frequency, we take $T_{\rm obs} = 3$ years, $f_{\rm ref}^{\rm BBO} = 0.1\,{\rm Hz}$.

PTA

The PTA response function is slightly different since unlike interferometers, the Earth-pulsar system only has a one-way transmission of radiation and acts like an arm of

[2] http://www.et-gw.eu/index.php

[3] https://dcc.ligo.org/LIGO-T1500293/public

an interferometer. The corresponding detector response tensor is [241],

$$a^{ij} = \frac{1}{2}\hat{u}^i\hat{u}^j\mathcal{T}(\hat{n}\cdot\hat{u}, f)\,, \tag{C.16}$$

with

$$\mathcal{T}(\hat{n}\cdot\hat{u}, f) = \frac{L}{c}\,\mathrm{sinc}\left(\frac{\pi f L}{c}(1+\hat{n}\cdot\hat{u})\right)e^{-i\frac{\pi f L}{c}(1+\hat{n}\cdot\hat{u})}\,. \tag{C.17}$$

For the forecasts with PTA, we assume a futuristic experiment like SKA collecting data from $N_{\rm psr}$ pulsars distributed uniformly over the sky with timing noise of the form [493],

$$N_f = 2\sigma_t^2\Delta T\,. \tag{C.18}$$

Here $1/\Delta T$ is the cadence of the observations and σ_t is the rms error of the timing residuals. The following parameter set, based on the analysis of [494], is chosen for the forecasts:

ΔT	2 weeks
$N_{\rm psr}$	50
σ_t	30 ns
$T_{\rm obs}$	20 years

Table C.1: SKA parameters.

For simplicity, we have not include additional noise sources such as red timing noise or clock or solar system ephemeris errors, which are expected to be present in a more realistic case [495]. In the future, the addition of more pulsars is also expected, e.g. $N_{\rm psr} \sim 100-1000$ for SKA2 [496], which may further bring down the noise and improve angular resolution.

Appendix D

Tensor non-Gaussianity and GW anisotropies

D.1 Computation of the angular power spectra

In this section we report the intermediate steps in the calculation of the angular power spectra of the intrinsic anisotropies.

D.1.1 Auto-correlation

D.1.1.1 Monopolar TTS

We start with eq. (5.4),

$$\delta^{\rm tts}_{\rm GW}(k,\hat{n}) = \int_{q\ll k} \frac{d^3q}{(2\pi)^3}\, e^{-id\hat{n}\cdot\boldsymbol{q}} F^{\rm tts}_{\rm NL}(\boldsymbol{k},\boldsymbol{q})\zeta(\vec{q})\,. \tag{D.1}$$

In this case we have for the spherical harmonic coefficient,

$$\delta^{\rm tts}_{{\rm GW},\ell m} = \int d^2\hat{n}\, \delta^{\rm tts}_{\rm GW}(k,\hat{n}) Y^*_{\ell m}(\hat{n}) \tag{D.2}$$

Now, using

$$e^{i\boldsymbol{q}\cdot\boldsymbol{x}} = 4\pi \sum_{LM} i^L j_L(qd) Y_{LM}(\hat{q}) Y^*_{LM}(\hat{x}), \tag{D.3}$$

and the fact that there is no angular dependence in $\hat{q}\cdot\hat{k}$

$$F^{\rm tts}_{\rm NL}(\boldsymbol{k},\boldsymbol{q}) = \tilde{F}^{\rm tts}_{\rm NL}(k,q)\,, \tag{D.4}$$

we obtain

$$C_\ell^{\rm GW,tts} = \frac{2}{\pi}\int_{q\ll k} q^2 dq\, j_\ell(qd)^2 \tilde{F}_{\rm NL}^{\rm tts}(q,k)^2 P_\zeta(q)\,. \tag{D.5}$$

where we applied the definition of the auto-correlation from eq. (5.11). Finally, assuming scale invariance and applying the identity,

$$\int_0^\infty j_\ell^2(x)\frac{dx}{x} = \frac{1}{2\ell(\ell+1)}, \tag{D.6}$$

we arrive at the desired result of eq. (5.15)

$$C_\ell^{\rm GW,tts} \simeq \left(\tilde{F}_{\rm NL}^{\rm tts}\right)^2 \frac{2\pi A_S}{\ell(\ell+1)}\,. \tag{D.7}$$

D.1.1.2 Quadrupolar TTS

Here we have,

$$F_{\rm NL}^{\rm tts}(\boldsymbol{k},\boldsymbol{q}) = \tilde{F}_{\rm NL}^{\rm tts}(q,k)\left[\frac{4\pi}{5}\sum_M Y_{2M}(\hat{k})Y_{2M}^*(\hat{q})\right] = \tilde{F}_{\rm NL}^{\rm tts}\,\mathcal{P}_2(\hat{q}\cdot\hat{k})\,, \tag{D.8}$$

which gives,

$$\begin{aligned}\delta_{\ell m}^{\rm GW} = \frac{16\pi^2}{5}\sum_{LM,m'} i^L \int d^2\hat{n}\, Y_{\ell m}^*(\hat{n}) Y_{LM}^*(\hat{n}) Y_{2m'}^*(\hat{n}) \\ \times \int \frac{d^3q}{(2\pi)^3}\tilde{F}_{\rm NL}(q,k) j_L(qd) Y_{LM}(\hat{q}) Y_{2m'}(\hat{q})\zeta(\vec{q})\,.\end{aligned} \tag{D.9}$$

The resulting auto-correlation is

$$\begin{aligned}\langle \delta_{\ell_1 m_1}^{\rm GW}\delta_{\ell_2 m_2}^{*\rm GW}\rangle = \frac{32\pi}{25}\sum_{L_1M_1m_1'}\sum_{L_2M_2m_2'} i^{L_1-L_2}\mathcal{G}_{\ell_1 L_1 2}^{m_1 M_1 m_1'}\mathcal{G}_{\ell_2 L_2 2}^{m_2 M_2 m_2'}\int q^2 dq\,\tilde{F}_{\rm NL}^2(q,k) j_{L_1}(qd) j_{L_2}(qd) P_\zeta(q) \\ \times \int d^2\hat{q}\, Y_{L_1M_1}(\hat{q}) Y_{2m_1'}(\hat{q}) Y_{L_2M_2}^*(\hat{q}) Y_{2m_2'}^*(\hat{q})\,,\end{aligned} \tag{D.10}$$

where $\mathcal{G}_{\ell_1\ell_2\ell_3}^{m_1m_2m_3}$ is the Gaunt integral,

$$\begin{aligned}\mathcal{G}_{\ell_1\ell_2\ell_3}^{m_1m_2m_3} &\equiv \int d^2\hat{q}\, Y_{\ell_1 m_1}(\hat{q}) Y_{\ell_2 m_2}(\hat{q}) Y_{\ell_3 m_3}(\hat{q}) \\ &= \sqrt{\frac{(2\ell_1+1)(2\ell_2+1)(2\ell_3+1)}{4\pi}}\begin{pmatrix}\ell_1 & \ell_2 & \ell_3\\ 0 & 0 & 0\end{pmatrix}\begin{pmatrix}\ell_1 & \ell_2 & \ell_3\\ m_1 & m_2 & m_3\end{pmatrix}.\end{aligned} \tag{D.11}$$

We now apply the identity

$$\sum_{m,M}\begin{pmatrix}\ell & L & \ell_1\\ m & M & m_1\end{pmatrix}\begin{pmatrix}\ell & L & \ell_2\\ m & M & m_2\end{pmatrix} = \frac{\delta_{\ell_1,\ell_2}\delta_{m_1,m_2}}{2\ell_1+1}\,. \tag{D.12}$$

to perform the sum over the Wigner $3j$-symbols and obtain

$$\begin{aligned}\langle \delta^{\rm GW}_{\ell_1 m_1} \delta^{*\rm GW}_{\ell_2 m_2}\rangle &= 16\pi^2 \sum_{L_1,L_2}\sum_{L'M'} i^{L_1-L_2} h^2_{\ell_1 L_1 2} h^2_{\ell_2 L_2 2} \frac{\delta_{\ell_1 L'}\delta_{m_1 M'}}{2\ell_1+1}\frac{\delta_{\ell_2 L'}\delta_{m_2 M'}}{2\ell_2+1} H_{L_1 L_2} \\ &= 16\pi^2 \sum_{L_1,L_2} i^{L_1-L_2} h^2_{\ell_1 L_1 2} h^2_{\ell_2 L_2 2} \frac{\delta_{\ell_1\ell_2}\delta_{m_1 m_2}}{(2\ell_1+1)^2} H_{L_1 L_2}\,, \end{aligned} \tag{D.13}$$

where

$$h_{\ell_1\ell_2\ell_3} \equiv \sqrt{\frac{(2\ell_1+1)(2\ell_2+1)(2\ell_3+1)}{4\pi}} \begin{pmatrix} \ell_1 & \ell_2 & \ell_3 \\ 0 & 0 & 0 \end{pmatrix}, \tag{D.14}$$

and

$$H_{L_1 L_2} \equiv \frac{2}{25\pi}\int_{q\ll k} q^2 dq\, j_{L_1}(qd) j_{L_2}(qd) \tilde{F}^{\rm tts}_{\rm NL}(k,q)^2 P_\zeta(q)\,. \tag{D.15}$$

The properties of the $3j$-symbols are explained in [497].

Equivalently we can write,

$$C_\ell^{\rm GW,tts} = 16\pi^2 \sum_{L_1,L_2} i^{L_1-L_2} h^2_{\ell L_1 2} h^2_{\ell L_2 2} \frac{H_{L_1 L_2}}{(2\ell+1)^2}, \tag{D.16}$$

The final steps involve the use of the identity [498],

$$\begin{aligned}\int_0^\infty dx\, J_\nu(ax) J_\mu(ax) x^{-\lambda} =& \frac{a^\lambda\,\Gamma(\lambda)\Gamma(\frac{\mu+\nu-\lambda+1}{2})}{2^\lambda\,\Gamma(\frac{\mu-\nu+\lambda+1}{2})\Gamma(\frac{-\mu+\nu+\lambda+1}{2})\Gamma(\frac{\mu+\nu+\lambda+1}{2})}\,, \\ & [\text{for } \ {\rm Re}\{(\mu+\nu+1)\} > {\rm Re}\{\lambda\} > 0,\ a>0] \end{aligned} \tag{D.17}$$

The spherical Bessel functions j_n are related to the Bessel functions $J_{n+1/2}$ as

$$j_n(x) = \sqrt{\frac{\pi}{2x}} J_{n+1/2}(x)\,. \tag{D.18}$$

Thus, we finally get

$$C_\ell^{\rm GW,tts} \simeq \frac{2\pi}{5}\frac{(\tilde{F}^{\rm tts}_{\rm NL})^2 A_S}{(\ell-2)(\ell+3)}\,, \tag{D.19}$$

which is valid for $\ell > 2$.

D.1.1.3 TTT bispectrum

The starting point is now eq. (5.8),

$$\delta^{\rm GW}_{\rm ttt}(k,\hat{n}) = -\int_{q\ll k}\frac{d^3q}{(2\pi)^3}\, e^{-id\hat{n}\cdot\boldsymbol{q}} F^{\rm ttt}_{\rm NL}(\boldsymbol{k},\boldsymbol{q}) \sum_\lambda \gamma^\lambda(\boldsymbol{q}) \epsilon^s_{ij}(\hat{q})\hat{n}^i\hat{n}^j\,. \tag{D.20}$$

We expand the GW in the helicity basis, i.e. $\lambda = R, L$ and use the following expansion [441, 499],

$$\gamma_{ij}^{R/L}(q)\, n^i n^j\, e^{-id\hat{n}\cdot\boldsymbol{q}} = -(2\pi)\,\gamma^{R/L}(q) \sum_{LM} (-i)^L \sqrt{\frac{(L+2)!}{(L-2)!}} \frac{j_L(qd)}{(qd)^2}\, {}_{\mp 2}Y^*_{LM}(\hat{q}) Y_{LM}(\hat{n})\,. \tag{D.21}$$

where the ${}_{\mp 2}Y_{LM}$ are the spin-weighted spherical harmonics which satisfy

$$\int_{S^2} {}_sY_{\ell m}(\hat{n})\, {}_sY^*_{\ell' m'}(\hat{n})\, d^2\hat{n} = \delta_{\ell\ell'}\delta_{mm'}. \tag{D.22}$$

This allows us to write

$$\delta^{\rm GW}_{\ell m} = (2\pi)(-i)^\ell \sqrt{\frac{(\ell+2)!}{(\ell-2)!}} \sum_{s=\pm 2} \int \frac{d^3q}{(2\pi)^3}\, F^{\rm ttt}_{\rm NL}(k,q) \gamma^s_{\boldsymbol{q}} \frac{j_\ell(qd)}{(qd)^2}\, {}_{-s}Y^*_{\ell m}(\hat{q})\,. \tag{D.23}$$

The auto-correlation is thus given by

$$C_\ell^{\rm GW,ttt} = \frac{(\ell-1)\ell(\ell+1)(\ell+2)}{2\pi} \sum_{s=\pm 2} \int_{q\ll k} q^2 dq\, F^{\rm ttt}_{\rm NL}(k,q)^2 P^s_\gamma(q) \frac{j_\ell(qd)^2}{(qd)^4}\,. \tag{D.24}$$

To get to eq. (5.22) we assume scale invariance and use the following identity

$$\int_0^\infty dx\, \frac{j_\ell^2(x)}{x^5} = \frac{4}{15} \frac{(\ell-2)!}{(\ell+2)!(\ell+3)(\ell-2)}\,. \tag{D.25}$$

D.1.2 CMB-GW cross-correlation

To obtain analytic formulae for the cross-correlations we only consider the CMB SW term given by [75],

$$\delta^{\rm T}_{\ell m} = \frac{4\pi}{5} i^\ell \int \frac{d^3p}{(2\pi)^3} Y^*_{\ell m}(\hat{p}) j_\ell(p r_{\rm lss}) \zeta(\boldsymbol{p})\,, \tag{D.26}$$

The cross-correlation is defined as,

$$\langle \delta^{\rm GW}_{\ell_1 m_1} \delta^{*\rm T}_{\ell_2 m_2} \rangle \equiv C^{\rm GW\text{-}T}_{\ell_1} \delta_{\ell_1\ell_2}\delta_{m_1 m_2} \tag{D.27}$$

D.1.2.1 Monopolar TTS

In the monopolar case we obtain,

$$C_\ell^{\rm GW-T} = \frac{2}{5\pi} \int_{q\ll k} q^2 dq\, j_\ell(qd) j_\ell(q r_{\rm lss}) \tilde{F}^{\rm tts}_{\rm NL}(k,q) P_\zeta(q)\,. \tag{D.28}$$

Assuming scale invariance, this becomes

$$C_\ell^{\rm GW-T} = \frac{4\pi}{5}\tilde{F}_{\rm NL}^{\rm tts} A_S \int_{q\ll k} \frac{dq}{q}\, j_\ell(qd) j_\ell(q r_{\rm lss})\,. \tag{D.29}$$

Now, if we approximate $d = r_{\rm lss}$ and use eq. (D.6) we get

$$C_\ell^{\rm GW-T} \simeq \frac{4\pi}{5}\tilde{F}_{\rm NL}^{\rm tts} \frac{A_S}{2\ell(\ell+1)}\,. \tag{D.30}$$

However, we can obtain a better result if we use the actual values for $r_{\rm lss}$ and d. These can be calculated using,

$$\begin{aligned} r_{\rm lss} &= \int_0^{z_{\rm lss}} \frac{dz}{H(z)} \simeq \frac{1}{H_0}\int_0^{1100} \frac{dz}{\sqrt{\Omega_{\rm m}(1+z)^3+\Omega_\Lambda}} \\ &\simeq \frac{3.15}{H_0}\,, \end{aligned} \tag{D.31}$$

where we set the density parameters to their *Planck* bestfit values [15]. For d we can let $z\to\infty$ and obtain $d \simeq 3.26/H_0$.

The next step is to use the following identity [498],

$$\begin{aligned} \int_0^\infty dx\, J_\nu(ax) J_\mu(bx) x^{-\lambda} =& \frac{a^\nu\,\Gamma(\frac{\mu+\nu-\lambda+1}{2})}{2^\lambda\, b^{\nu-\lambda+1}\Gamma(\frac{\mu-\nu+\lambda+1}{2})\Gamma(\nu+1)} \\ & \times {}_2F_1\left(\frac{\mu+\nu-\lambda+1}{2}, \frac{\nu-\mu-\lambda+1}{2}; \nu+1; \frac{a^2}{b^2}\right), \\ & [\text{for } \mathrm{Re}\{(\mu+\nu-\lambda+1)\}>0,\ \mathrm{Re}\{\lambda\}>-1,\ 0<a<b] \end{aligned} \tag{D.32}$$

on eq. (D.29) to obtain

$$C_\ell^{\rm GW-T} = \frac{\pi^{3/2}}{5}\tilde{F}_{\rm NL}^{\rm tts} A_S \left(\frac{r_{\rm lss}}{d}\right)^\ell \frac{\Gamma(\ell)}{\Gamma(\ell+\frac{3}{2})}\, {}_2F_1\left(-\frac{1}{2}, \ell; \ell+\frac{3}{2}; \frac{r_{\rm lss}^2}{d^2}\right). \tag{D.33}$$

in terms of the Hypergeometric function ${}_2F_1$.

D.1.2.2 Quadrupolar TTS

The calculation for this case proceeds similarly to what was done for the quadrupolar $C_\ell^{\rm GW,tts}$. We find

$$C_\ell^{\rm GW-T,tts} = 4\pi \sum_L i^{L-\ell} h_{2L\ell}^2 \frac{G_{L\ell}}{2\ell+1}\,, \tag{D.34}$$

where

$$G_{\ell_1\ell_2} = \frac{2}{25\pi}\int_{q\ll k} q^2 dq\, j_{\ell_1}(qd) j_{\ell_2}(q r_{\rm lss}) \tilde{F}_{\rm NL}^{\rm tts}(k,q) P_\zeta(q), \tag{D.35}$$

Now we use eq. (D.32) to get

$$C_\ell^{\rm GW-T,tts} = \frac{\pi^{3/2}\tilde{F}_{\rm NL}^{\rm tts}A_S}{20}\left(\frac{r_{\rm lss}}{d}\right)^\ell\left(\frac{r_{\rm lss}}{d}-1\right)\left(\frac{r_{\rm lss}}{d}+1\right)\Delta F_\ell\,, \tag{D.36}$$

where ΔF_ℓ is given by

$$\Delta F_\ell \equiv \frac{\Gamma(\ell)}{\Gamma(\ell+3/2)}\left[(\ell+1)\,{}_2F_1\left(-\frac{1}{2},\ell;\ell+\frac{3}{2};\frac{r_{\rm lss}^2}{d^2}\right) - {}_2F_1\left(\frac{1}{2},\ell;\ell+\frac{3}{2};\frac{r_{\rm lss}^2}{d^2}\right)\right]. \tag{D.37}$$

The function ΔF_ℓ is well fit by

$$\Delta F_\ell \simeq \frac{0.2}{(\ell+2)^{0.45}}\,. \tag{D.38}$$

TTT bispectrum

We start from eqs. (5.8) and (D.23). Using eq. (D.21), the spherical harmonic coefficients for the tensor contribution to $\delta^{\rm T}$ can be written as

$$\delta^{\rm T}_{\ell m} = \pi\,(-i)^\ell\sqrt{\frac{(\ell+2)!}{(\ell-2)!}}\sum_{s=\pm2}\int_{\eta_{\rm rec}}^{\eta_0}d\eta\,\frac{d^3q}{(2\pi)^3}\frac{\partial\gamma_{\boldsymbol{q}}^s}{\partial\eta}\frac{j_\ell(q\chi(\eta))}{(q\chi(\eta))^2}\,{}_{-s}Y^*_{LM}(\hat{q})\,. \tag{D.39}$$

The resulting cross-correlation is the one given in eq. (5.33).

D.2 Statistically anisotropic case

The correlators discussed in the previous section are calculated under the assumption of statistical isotropy of the background space-time. It is also interesting to consider the correlators in a background where statistical isotropy is violated. We studied this in [1] and I provide here an overview of the main results for the correlation functions.

Such statistical anisotropy can arise in inflationary models involving vector fields, with the vev of the vector field picking out a preferred direction $\hat{v}$ in space [500–506]. The exact form of the STT (or TTT) bispectra would depend on the specifics of the inflationary model under consideration. Here, we perform a phenomenological analysis, modelling the STT bispectra in a form similar to existing examples of statistically anisotropic scalar bispectra, e.g. see [501]. The non-linearity parameter is taken to be

$$F_{\rm NL}^{\rm tts}(\boldsymbol{q},\boldsymbol{k}) = \sum_{LM}\lambda_{LM}(k,q,\hat{v})Y_{LM}(\hat{q}). \tag{D.40}$$

Additional terms involving the quantities $(\hat{v}\cdot\hat{k})$ as well as contributions such as $(\hat{v}\cdot\hat{q})(\hat{v}\cdot\hat{k})(\hat{k}\cdot\hat{q})$ may also arise, as shown for $\langle\zeta^3\rangle$ in [501, 507–510] and $\langle\gamma^3\rangle$ in [511]. The power spectra in such models may be anisotropic itself, e.g. of the form $P_\gamma(\boldsymbol{k}) = P_\gamma(k)(1+\sum_{LM} g_{LM}(k,\hat{v})Y_{LM}(\hat{k}))$ [506, 512–515]. We focus on the effects of the term in eq. (D.40), the contribution of the other terms to the correlators can be calculated similarly.

BipoSH formalism

The resulting correlations in this case are statistically anisotropic which produces non-zero off-diagonal elements of the angular power spectra $C^{\text{GW-T}}_{\ell\ell' mm'}$. Using eq. (D.40), we find

$$\begin{aligned}\langle\delta^{\rm GW}_{\ell_1 m_1}\delta^{\rm T}_{\ell_2 m_2}\rangle =& 4\pi i^{\ell_1}\int\frac{d^3q}{(2\pi)^3}Y^*_{\ell_1 m_1}(q)j_{\ell_1}(qd)\sum_{LM}\lambda_{LM}Y_{LM}(\hat{q})\\ &\times\frac{4\pi}{5}i^{\ell_2}\int\frac{d^3p}{(2\pi)^3}Y^*_{\ell_2 m_2}(\hat{p})j_{\ell_2}(pr_{\rm lss})\langle\zeta(\boldsymbol{q})\zeta(\boldsymbol{p})\rangle\\ =&\frac{2}{5\pi}i^{\ell_1-\ell_2}\sum_{LM}\Bigg[\int d^2\hat{q}\,Y^*_{\ell_1 m_1}(\hat{q})Y_{LM}(\hat{q})Y^*_{\ell_2 m_2}(\hat{q})\\ &\times\int q^2dq\,j_{\ell_1}(qd)j_{\ell_2}(qr_{\rm lss})P_\zeta(q)\lambda_{LM}\Bigg]\,.\end{aligned}\tag{D.41}$$

This becomes

$$\begin{aligned}\langle\delta^{\rm GW}_{\ell_1 m_1}\delta^{\rm T}_{\ell_2 m_2}\rangle =&\frac{2}{5\pi}i^{\ell_1-\ell_2}\sum_{LM}\left[\int q^2dq\,j_{\ell_1}(qd)j_{\ell_2}(qr_{\rm lss})P_\zeta(q)\lambda_{LM}\right]\\ &\times(-1)^M h_{\ell_1\ell_2 L}\begin{pmatrix}\ell_1 & \ell_2 & L\\ m_1 & m_2 & -M\end{pmatrix}\,,\end{aligned}\tag{D.42}$$

with $h_{\ell_1\ell_2 L}$ defined in eq. (5.18). The properties of the Wigner 3j symbols dictate that this cross-correlation is non-zero when $\ell_1+\ell_2+L=$ even and $|\ell_1-\ell_2|\leq L\leq\ell_1+\ell_2$. Thus, for $L>0$, there will be off-diagonal elements in the $C^{\rm GW-T}_{\ell_1\ell_2}$. Statistically anisotropic correlators of this form can be analysed with the BipoSH formalism [516, 517]. The bipolar harmonic coefficients, denoted as $A^{LM,f_1f_2}_{\ell_1\ell_2}$ are defined in terms of the real-space correlation function of the observables δ^{f_1}, δ^{f_2} as

$$\langle\delta^{f_1}(\hat{x}_1)\delta^{f_2}(\hat{x}_2)\rangle=\sum_{\ell_1\ell_2,LM}A^{LM,f_1f_2}_{\ell_1\ell_2}\{Y_{\ell_1}(\hat{x}_1)\otimes Y_{\ell_2}(\hat{x}_2)\}_{LM}\,,\tag{D.43}$$

where $\{Y_{\ell_1}(\hat{x}_1)\otimes Y_{\ell_2}(\hat{x}_2)\}_{LM}$ are the bipolar spherical harmonics

$$\{Y_{\ell_1}(\hat{x}_1)\otimes Y_{\ell_2}(\hat{x}_2)\}_{LM}\equiv\sum_{m_1m_2}\mathcal{C}^{LM}_{\ell_1m_1,\ell_2m_2}Y_{\ell_1m_1}(\hat{x}_1)Y_{\ell_2m_2}(\hat{x}_2)\,,\tag{D.44}$$

with

$$\mathcal{C}^{LM}_{\ell_1 m_1,\ell_2 m_2} = (-1)^{\ell_1-\ell_2+M}\sqrt{2L+1}\begin{pmatrix}\ell_1 & \ell_2 & L\\ m_1 & m_2 & -M\end{pmatrix} \tag{D.45}$$

as the Clebsch-Gordan coefficients. Inverting (D.43) and performing an angular integration over $(\hat{x}_1, \hat{x}_2)$ gives the BipoSH coefficients

$$A^{LM,f_1f_2}_{\ell_1\ell_2} = \sum_{m_1 m_2} \mathcal{C}^{LM}_{\ell_1 m_1,\ell_2 m_2}\langle \delta^{f_1}_{\ell_1 m_1}\delta^{f_2}_{\ell_2 m_2}\rangle\,. \tag{D.46}$$

As a consistency check, we see that in the statistically isotropic case, the BipoSH coefficients vanish for $L > 0$ while the $L = 0$ term reduces to the usual $C_\ell^{\mathrm{GW-T}}$. In the statistically anisotropic case, we obtain

$$A^{LM,\mathrm{GW-T}}_{\ell_1\ell_2} = i^{\ell_2-\ell_1}\frac{h_{\ell_1\ell_2 L}}{\sqrt{2L+1}}\left[\frac{2}{5\pi}\int q^2 dq\, j_{\ell_1}(qd) j_{\ell_2}(qr_{\mathrm{lss}}) P_\zeta(q)\lambda_{LM}\right]. \tag{D.47}$$

The auto-correlation of the anisotropies can be calculating in the same manner, with the result

$$A^{LM,\mathrm{GW}}_{\ell_1\ell_2} = i^{\ell_2-\ell_1}\frac{h_{\ell_1\ell_2 L}}{\sqrt{2L+1}}\left[\frac{2}{\pi}\int q^2 dq\, j_{\ell_1}(qd) j_{\ell_2}(qd) P_\zeta(q)\lambda^2_{LM}\right]. \tag{D.48}$$

Finally, working similarly to section 5.2.3, one can also obtain Fisher forecasts for the λ_{LM} parameter as also done in [1].

D.3 Spin-2 Model

D.3.1 Sound speed(s) scaling

We provide here additional details regarding the time/scale dependence of the sound speeds considered in section 5.3.1. We parameterised the weakly time dependent sound speed for the helicity mode-j as,

$$c_j(\eta) = c_j^i\left(\frac{\eta}{\eta_i}\right)^{s_j} + c_j^f\,. \tag{D.49}$$

In the limit $c_j^f \ll c_j(\eta)$, the parameter s_j reduces to the usual slow-roll parameter associated to the time-dependence of the sound speeds, defined as $s_j = \dot{c}_j/c_j H$ [153].

In section 5.3.1, we had stated that the above choice of sound speeds was equivalent to employing scale dependent sound speeds, (eq. (5.62)), in terms of calculating the relevant cosmological correlators using the *in-in* formalism. The reason behind that

can be understood as follows. It is known that the main contribution to correlators arises around the time the relevant modes cross the horizon ($c_j(\eta)k\eta \sim 1$). This is because deep inside the horizon ($c_j(\eta)k\eta \gg 1$) the mode functions, which are of the type $\mathcal{H}_\nu^{(1,2)}[-c_j(\tau)\,k\tau]$, are rapidly oscillating. In particular, for the scenarios we are interested in here we shall have

$$c_2(\eta_{\rm CMB}) \simeq c_2^i\,, \quad c_j(\eta_{\rm BBO}) \simeq c_2^f\,, \tag{D.50}$$

where $\eta_{\rm CMB/BBO}$ denote the conformal times when the CMB/BBO scales cross the horizon. This is also what one obtains in using the scale-dependent sound speeds of eq. (5.62).

One final point relevant to the calculation of the cosmological correlators is the choice of the horizon. This is obvious when the modes functions within the integral corresponding to a given vertex share the same horizon. When there are mode functions with different arguments one needs to choose the horizon corresponding to the mode which exited last (see e.g. [151, 171]). The reason behind this is the same as discussed above, at earlier times the integral is again highly oscillatory[1] due to presence of this mode.

D.3.2 Computation of the bispectra

Keeping these points in mind, we then calculate the tensor bispectra using the *in-in* formalism. The dominant contributions in $c_2 \ll 1$ limit, are given by the diagrams fig. 5.9 leading to e.g.

$$\begin{aligned}\langle\gamma^{\lambda_1}_{\boldsymbol{k}_1}(\eta)\gamma^{\lambda_2}_{\boldsymbol{k}_2}(\eta)\zeta_{\boldsymbol{k}_3}(\eta)\rangle = \int_{-\infty}^{\eta} d\eta_1 \int_{-\infty}^{\eta_1} d\eta_2 \int_{-\infty}^{\eta_2} d\eta_3 \int_{-\infty}^{\eta_3} d\eta_4 \times \\ \times \langle[H_I(\eta_4),[H_I(\eta_3),[H_I(\eta_2),[H_I(\eta_1),\gamma^{\lambda_1}_{\boldsymbol{k}_1}(\eta)\gamma^{\lambda_2}_{\boldsymbol{k}_2}(\eta)\zeta_{\boldsymbol{k}_3}(\eta)]]]]\rangle\,,\end{aligned} \tag{D.51}$$

in the *commutator* form [171, 188]. We then sum over all the terms one can form by replacing one of the H_I with $H_{(\sigma^{(2)})^2\sigma^{(0)}}$ (eq. (5.65)), another with $H_{\sigma^{(0)}\zeta}$ (eq. (5.66)), and the rest with $H_{\sigma^{(2)}\gamma}$ (eq. (5.63)). Using the mode functions of eqs. (5.56)-(5.59) and taking the squeezed limit $k_L = k_3 \ll k_1 \simeq k_2 = k_S$, we obtain (after a very lengthy calculation) the result of eqs. (5.68) and (5.72) [2].

[1] In fact, applying the $i\epsilon$ prescription in the far past to the project the interacting vacuum of the full theory on to the vacuum of the free theory turns this oscillatory behaviour into exponential decay (see e.g. [62, 91]). This suppresses the integrals in the $|c_j k\eta| \gg 1$ limit.

ν	a
0.7	0.96
1.1	2.99
1.4	506.2
1.45	7879.3
1.48	238800.

Table D.1: Values of a (eq. (5.70)) for different values of the mass in terms of the parameter $\nu = (9/4 - (m_\sigma^2/H^2))^{1/2}$. See [2] for more details.

Appendix E

ΛCDM parameter estimates

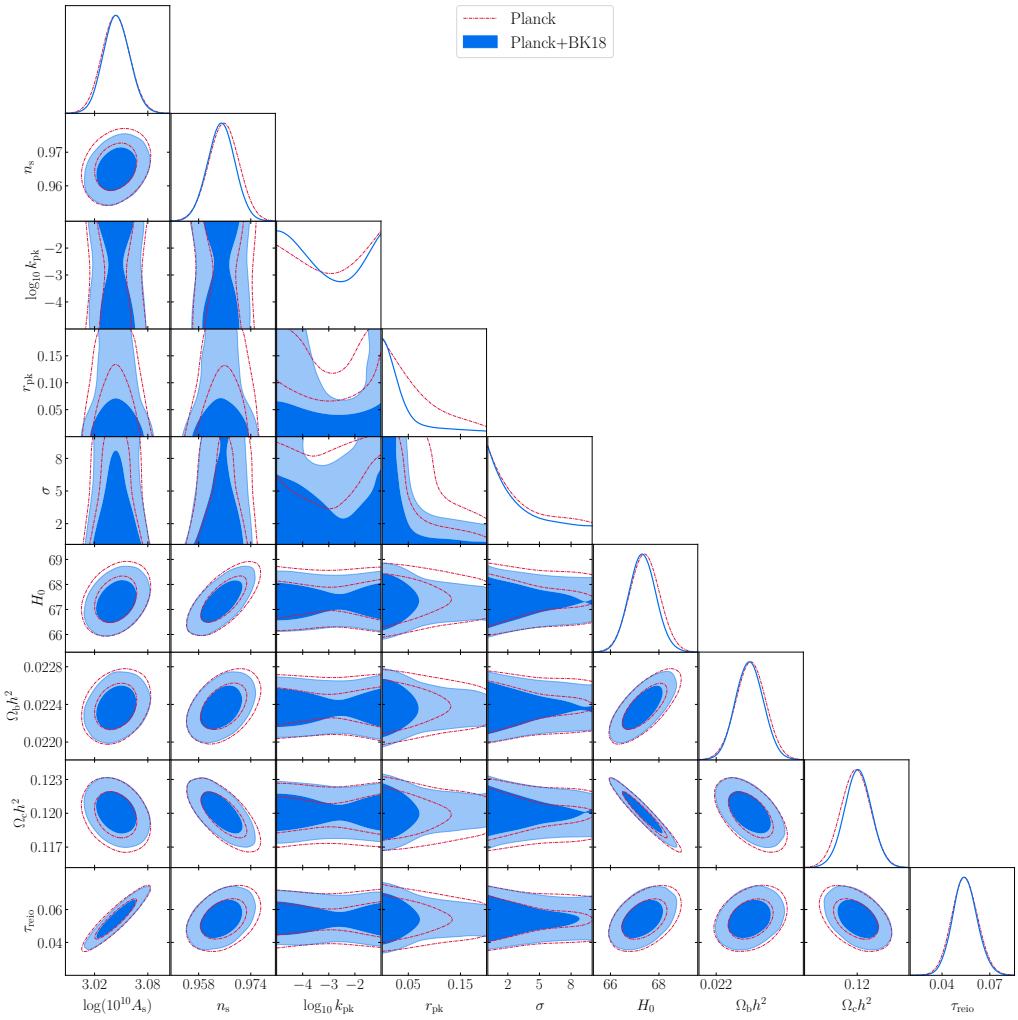

Figure E.1: Marginalised 68% and 95% contours for ΛCDM and tensor spectrum parameters.

Parameter	68% limits
$\mathbf{log(10^{10} A_s)}$	3.045 ± 0.014
$\boldsymbol{n_s}$	0.9649 ± 0.0040
$\boldsymbol{H_0}$	67.3 ± 0.53
$\boldsymbol{\Omega_b h^2}$	0.02237 ± 0.00014
$\boldsymbol{\Omega_c h^2}$	0.1201 ± 0.0012
$\boldsymbol{\tau_{reio}}$	0.054 ± 0.0073

Table E.1: ΛCDM parameter means and 68% limits for the log-normal model using *Planck*+BK18 data.

References

[1] A. Malhotra, E. Dimastrogiovanni, M. Fasiello and M. Shiraishi, *Cross-correlations as a Diagnostic Tool for Primordial Gravitational Waves*, *JCAP* **03** (2021) 088 [2012.03498].

[2] E. Dimastrogiovanni, M. Fasiello, A. Malhotra, P. D. Meerburg and G. Orlando, *Testing the early universe with anisotropies of the gravitational wave background*, *JCAP* **02** (2022) 040 [2109.03077].

[3] J. Hamann and A. Malhotra, *Constraining primordial tensor features with the anisotropies of the cosmic microwave background*, *JCAP* **12** (2022) 015 [2209.00827].

[4] E. Dimastrogiovanni, M. Fasiello, A. Malhotra and G. Tasinato, *Enhancing gravitational wave anisotropies with peaked scalar sources*, *JCAP* **01** (2023) 018 [2205.05644].

[5] A. Malhotra, E. Dimastrogiovanni, G. Domènech, M. Fasiello and G. Tasinato, *New universal property of cosmological gravitational wave anisotropies*, *Phys. Rev. D* **107** (2023) 103502 [2212.10316].

[6] Supernova Cosmology Project collaboration, *Measurements of Ω and Λ from 42 high redshift supernovae*, *Astrophys. J.* **517** (1999) 565 [astro-ph/9812133].

[7] Supernova Search Team collaboration, *Observational evidence from supernovae for an accelerating universe and a cosmological constant*, *Astron. J.* **116** (1998) 1009 [astro-ph/9805201].

[8] G. F. Smoot, C. L. Bennett, A. Kogut, E. L. Wright, J. Aymon, N. W. Boggess et al., *Structure in the COBE Differential Microwave Radiometer First-Year Maps*, ApJ **396** (1992) L1.

[9] J. C. Mather et al., *Measurement of the Cosmic Microwave Background spectrum by the COBE FIRAS instrument*, *Astrophys. J.* **420** (1994) 439.

[10] WMAP collaboration, *First year Wilkinson Microwave Anisotropy Probe (WMAP) observations: Determination of cosmological parameters*, *Astrophys. J. Suppl.* **148** (2003) 175 [astro-ph/0302209].

[11] Planck collaboration, *Planck 2018 results. I. Overview and the cosmological legacy of Planck*, *Astron. Astrophys.* **641** (2020) A1 [1807.06205].

[12] K. K. S. Wu, O. Lahav and M. J. Rees, *The large-scale smoothness of the Universe*, *Nature* **397** (1999) 225 [astro-ph/9804062].

[13] J. Yadav, S. Bharadwaj, B. Pandey and T. R. Seshadri, *Testing homogeneity on large scales in the Sloan Digital Sky Survey Data Release One*, *Mon. Not. Roy. Astron. Soc.* **364** (2005) 601 [astro-ph/0504315].

[14] Boomerang collaboration, *A Flat universe from high resolution maps of the cosmic microwave background radiation*, *Nature* **404** (2000) 955 [astro-ph/0004404].

[15] Planck collaboration, *Planck 2018 results. VI. Cosmological parameters*, *Astron. Astrophys.* **641** (2020) A6 [1807.06209].

[16] E. Di Valentino, O. Mena, S. Pan, L. Visinelli, W. Yang, A. Melchiorri et al., *In the realm of the Hubble tension—a review of solutions*, *Class. Quant. Grav.* **38** (2021) 153001 [2103.01183].

[17] E. Abdalla et al., *Cosmology intertwined: A review of the particle physics, astrophysics, and cosmology associated with the cosmological tensions and anomalies*, *JHEAp* **34** (2022) 49 [2203.06142].

[18] K. A. Olive, *Inflation*, *Phys. Rept.* **190** (1990) 307.

[19] A. D. Linde, *Inflationary Cosmology*, *Lect. Notes Phys.* **738** (2008) 1 [0705.0164].

[20] A. H. Guth, *The Inflationary Universe: A Possible Solution to the Horizon and Flatness Problems*, *Phys. Rev.* **D23** (1981) 347.

[21] V. F. Mukhanov and G. V. Chibisov, *Quantum Fluctuations and a Nonsingular Universe*, *JETP Lett.* **33** (1981) 532.

[22] A. H. Guth and S. Y. Pi, *Fluctuations in the New Inflationary Universe*, *Phys. Rev. Lett.* **49** (1982) 1110.

[23] A. A. Starobinsky, *Dynamics of Phase Transition in the New Inflationary Universe Scenario and Generation of Perturbations*, *Phys. Lett. B* **117** (1982) 175.

[24] S. Hawking, *The Development of Irregularities in a Single Bubble Inflationary Universe*, *Phys. Lett. B* **115** (1982) 295.

[25] A. H. Guth and E. J. Weinberg, *Could the Universe Have Recovered from a Slow First Order Phase Transition?*, *Nucl. Phys. B* **212** (1983) 321.

[26] A. D. Linde, *Scalar Field Fluctuations in Expanding Universe and the New Inflationary Universe Scenario*, *Phys. Lett. B* **116** (1982) 335.

[27] A. D. Linde, *Chaotic Inflation*, *Phys. Lett. B* **129** (1983) 177.

[28] J. M. Bardeen, P. J. Steinhardt and M. S. Turner, *Spontaneous Creation of Almost Scale - Free Density Perturbations in an Inflationary Universe*, *Phys. Rev. D* **28** (1983) 679.

[29] V. F. Mukhanov, *Gravitational Instability of the Universe Filled with a Scalar Field*, *JETP Lett.* **41** (1985) 493.

[30] L. P. Grishchuk, *Amplification of gravitational waves in an istropic universe*, *Zh. Eksp. Teor. Fiz.* **67** (1974) 825.

[31] A. A. Starobinskiĭ, *Spectrum of relict gravitational radiation and the early state of the universe*, *Soviet Journal of Experimental and Theoretical Physics Letters* **30** (1979) 682.

[32] V. A. Rubakov, M. V. Sazhin and A. V. Veryaskin, *Graviton Creation in the Inflationary Universe and the Grand Unification Scale*, *Phys. Lett. B* **115** (1982) 189.

[33] R. Fabbri and M. d. Pollock, *The Effect of Primordially Produced Gravitons upon the Anisotropy of the Cosmological Microwave Background Radiation*, *Phys. Lett. B* **125** (1983) 445.

[34] PLANCK collaboration, *Planck 2018 results. X. Constraints on inflation*, *Astron. Astrophys.* **641** (2020) A10 [1807.06211].

[35] BICEP, KECK collaboration, *Improved Constraints on Primordial Gravitational Waves using Planck, WMAP, and BICEP/Keck Observations through the 2018 Observing Season*, *Phys. Rev. Lett.* **127** (2021) 151301 [2110.00483].

[36] J. Martin, C. Ringeval and V. Vennin, *Encyclopædia Inflationaris*, *Phys. Dark Univ.* **5-6** (2014) 75 [1303.3787].

[37] A. A. Starobinsky, *A New Type of Isotropic Cosmological Models Without Singularity*, *Phys. Lett.* **B91** (1980) 99.

[38] A. A. Starobinsky, *The Perturbation Spectrum Evolving from a Nonsingular Initially De-Sitter Cosmology and the Microwave Background Anisotropy*, *Sov. Astron. Lett.* **9** (1983) 302.

[39] F. L. Bezrukov and M. Shaposhnikov, *The Standard Model Higgs boson as the inflaton*, *Phys. Lett. B* **659** (2008) 703 [0710.3755].

[40] K. Freese, J. A. Frieman and A. V. Olinto, *Natural inflation with pseudo - Nambu-Goldstone bosons*, *Phys. Rev. Lett.* **65** (1990) 3233.

[41] PLANCK collaboration, *Planck 2018 results. X. Constraints on inflation*, *Astron. Astrophys.* **641** (2018) A10 [1807.06211].

[42] L. Moncelsi et al., *Receiver development for BICEP Array, a next-generation CMB polarimeter at the South Pole*, *Proc. SPIE Int. Soc. Opt. Eng.* **11453** (2020) 1145314 [2012.04047].

[43] SIMONS OBSERVATORY collaboration, *The Simons Observatory: Science goals and forecasts*, *JCAP* **02** (2019) 056 [1808.07445].

[44] CMB-S4 collaboration, *CMB-S4 Science Book, First Edition*, [1610.02743].

[45] LITEBIRD collaboration, *Probing Cosmic Inflation with the LiteBIRD Cosmic Microwave Background Polarization Survey*, [2202.02773].

[46] D. Baumann and L. McAllister, *Inflation and String Theory*, Cambridge Monographs on Mathematical Physics. Cambridge University Press, 2015, 10.1017/CBO9781316105733, [1404.2601].

[47] G. Obied, H. Ooguri, L. Spodyneiko and C. Vafa, *De Sitter Space and the Swampland*, [1806.08362].

[48] M. van Beest, J. Calderón-Infante, D. Mirfendereski and I. Valenzuela, *Lectures on the Swampland Program in String Compactifications*, *Phys. Rept.* **989** (2022) 1 [2102.01111].

[49] A. Achúcarro and G. A. Palma, *The string swampland constraints require multi-field inflation*, *JCAP* **02** (2019) 041 [1807.04390].

[50] L. McAllister and E. Silverstein, *String Cosmology: A Review*, *Gen. Rel. Grav.* **40** (2008) 565 [0710.2951].

[51] E. Pajer and M. Peloso, *A review of Axion Inflation in the era of Planck*, *Class. Quant. Grav.* **30** (2013) 214002 [1305.3557].

[52] D. H. Lyth and A. Riotto, *Particle physics models of inflation and the cosmological density perturbation*, *Phys. Rept.* **314** (1999) 1 [hep-ph/9807278].

[53] D. Wands, *Multiple field inflation*, *Lect. Notes Phys.* **738** (2008) 275 [astro-ph/0702187].

[54] J.-O. Gong, *Multi-field inflation and cosmological perturbations*, *Int. J. Mod. Phys. D* **26** (2016) 1740003 [1606.06971].

[55] J. Chluba, J. Hamann and S. P. Patil, *Features and New Physical Scales in Primordial Observables: Theory and Observation*, *Int. J. Mod. Phys. D* **24** (2015) 1530023 [1505.01834].

[56] A. Slosar et al., *Scratches from the Past: Inflationary Archaeology through Features in the Power Spectrum of Primordial Fluctuations*, *Bull. Am. Astron. Soc.* **51** (2019) 98 [1903.09883].

[57] N. Bartolo et al., *Science with the space-based interferometer LISA. IV: Probing inflation with gravitational waves*, *JCAP* **12** (2016) 026 [1610.06481].

[58] M. Guzzetti, N. Bartolo, M. Liguori and S. Matarrese, *Gravitational waves from inflation*, *Riv. Nuovo Cim.* **39** (2016) 399 [1605.01615].

[59] C. Caprini and D. G. Figueroa, *Cosmological Backgrounds of Gravitational Waves*, *Class. Quant. Grav.* **35** (2018) 163001 [1801.04268].

[60] LISA Cosmology Working Group collaboration, *Cosmology with the Laser Interferometer Space Antenna*, [2204.05434].

[61] N. Bartolo, E. Komatsu, S. Matarrese and A. Riotto, *Non-Gaussianity from inflation: Theory and observations*, *Phys. Rept.* **402** (2004) 103 [astro-ph/0406398].

[62] X. Chen, *Primordial Non-Gaussianities from Inflation Models*, *Adv. Astron.* **2010** (2010) 638979 [1002.1416].

[63] M. Sasaki, T. Suyama, T. Tanaka and S. Yokoyama, *Primordial black holes—perspectives in gravitational wave astronomy*, *Class. Quant. Grav.* **35** (2018) 063001 [1801.05235].

[64] O. Özsoy and G. Tasinato, *Inflation and Primordial Black Holes*, *Universe* **9** (2023) 203 [2301.03600].

[65] P. Amaro-Seoane, H. Audley, S. Babak, J. Baker, E. Barausse, P. Bender et al., *Laser interferometer space antenna*, [1702.00786].

[66] M. Punturo et al., *The Einstein Telescope: A third-generation gravitational wave observatory*, *Class. Quant. Grav.* **27** (2010) 194002.

[67] D. Reitze et al., *Cosmic Explorer: The U.S. Contribution to Gravitational-Wave Astronomy beyond LIGO*, *Bull. Am. Astron. Soc.* **51** (2019) 035 [1907.04833].

[68] NANOGrav collaboration, *The NANOGrav 15-year Data Set: Evidence for a Gravitational-Wave Background*, [2306.16213].

[69] D. J. Reardon et al., *Search for an isotropic gravitational-wave background with the Parkes Pulsar Timing Array*, [2306.16215].

[70] H. Xu et al., *Searching for the nano-Hertz stochastic gravitational wave background with the Chinese Pulsar Timing Array Data Release I*, [2306.16216].

[71] J. Antoniadis et al., *The second data release from the European Pulsar Timing Array III. Search for gravitational wave signals*, [2306.16214].

[72] J. Antoniadis et al., *The second data release from the European Pulsar Timing Array: V. Implications for massive black holes, dark matter and the early Universe*, [2306.16227].

[73] NANOGrav collaboration, *The NANOGrav 15-year Data Set: Search for Signals from New Physics*, [2306.16219].

[74] V. Mukhanov, *Physical Foundations of Cosmology*. Cambridge University Press, Oxford, 2005.

[75] S. Dodelson and F. Schmidt, *Modern Cosmology*. Elsevier Science, 2020.

[76] D. Baumann, *Cosmology*. Cambridge University Press, 7, 2022, 10.1017/9781108937092.

[77] G. Bertone and D. Hooper, *History of dark matter*, *Rev. Mod. Phys.* **90** (2018) 045002 [1605.04909].

[78] D. J. Fixsen, *The Temperature of the Cosmic Microwave Background*, ApJ **707** (2009) 916 [0911.1955].

[79] J. J. Bennett, G. Buldgen, P. F. De Salas, M. Drewes, S. Gariazzo, S. Pastor et al., *Towards a precision calculation of $N_{\rm eff}$ in the Standard Model II: Neutrino decoupling in the presence of flavour oscillations and finite-temperature QED*, *JCAP* **04** (2021) 073 [2012.02726].

[80] L. Pagano, L. Salvati and A. Melchiorri, *New constraints on primordial gravitational waves from Planck 2015*, *Phys. Lett. B* **760** (2016) 823 [1508.02393].

[81] S. Weinberg, *The Cosmological Constant Problem*, *Rev. Mod. Phys.* **61** (1989) 1.

[82] J. Martin, *Everything You Always Wanted To Know About The Cosmological Constant Problem (But Were Afraid To Ask)*, *Comptes Rendus Physique* **13** (2012) 566 [1205.3365].

[83] E. W. Kolb and M. S. Turner, *The Early Universe*, *Front. Phys.* **69** (1990) 1.

[84] K. Sato, *First Order Phase Transition of a Vacuum and Expansion of the Universe*, *Mon. Not. Roy. Astron. Soc.* **195** (1981) 467.

[85] A. D. Linde, *A New Inflationary Universe Scenario: A Possible Solution of the Horizon, Flatness, Homogeneity, Isotropy and Primordial Monopole Problems*, *Phys. Lett.* **108B** (1982) 389.

[86] A. Albrecht and P. J. Steinhardt, *Cosmology for Grand Unified Theories with Radiatively Induced Symmetry Breaking*, *Phys. Rev. Lett.* **48** (1982) 1220.

[87] L. Kofman, A. D. Linde and A. A. Starobinsky, *Reheating after inflation*, *Phys. Rev. Lett.* **73** (1994) 3195 [hep-th/9405187].

[88] L. Kofman, A. D. Linde and A. A. Starobinsky, *Towards the theory of reheating after inflation*, *Phys. Rev. D* **56** (1997) 3258 [hep-ph/9704452].

[89] R. Allahverdi, R. Brandenberger, F.-Y. Cyr-Racine and A. Mazumdar, *Reheating in Inflationary Cosmology: Theory and Applications*, *Ann. Rev. Nucl. Part. Sci.* **60** (2010) 27 [1001.2600].

[90] K. D. Lozanov, *Lectures on Reheating after Inflation*, [1907.04402].

[91] D. Baumann, *Inflation*, in *Physics of the large and the small, TASI 09, proceedings of the Theoretical Advanced Study Institute in Elementary Particle Physics, Boulder, Colorado, USA, 1-26 June 2009*, pp. 523–686, 2011, DOI [0907.5424].

[92] A. Riotto, *Inflation and the theory of cosmological perturbations*, *ICTP Lect. Notes Ser.* **14** (2003) 317 [hep-ph/0210162].

[93] V. F. Mukhanov, H. A. Feldman and R. H. Brandenberger, *Theory of cosmological perturbations*, Phys. Rep. **215** (1992) 203.

[94] K. A. Malik and D. Wands, *Cosmological perturbations*, *Phys. Rept.* **475** (2009) 1 [0809.4944].

[95] J. M. Bardeen, *Gauge Invariant Cosmological Perturbations*, *Phys. Rev. D* **22** (1980) 1882.

[96] D. Wands, K. A. Malik, D. H. Lyth and A. R. Liddle, *A New approach to the evolution of cosmological perturbations on large scales*, *Phys. Rev. D* **62** (2000) 043527 [astro-ph/0003278].

[97] S. Weinberg, *Adiabatic modes in cosmology*, *Phys. Rev. D* **67** (2003) 123504 [astro-ph/0302326].

[98] D. Langlois, *Lectures on inflation and cosmological perturbations*, *Lect. Notes Phys.* **800** (2010) 1 [1001.5259].

[99] A. R. Liddle and D. H. Lyth, *Cosmological Inflation and Large-Scale Structure*. Cambridge University Press, 2000, 10.1017/CBO9781139175180.

[100] A. R. Liddle and D. H. Lyth, *The Cold dark matter density perturbation*, *Phys. Rept.* **231** (1993) 1 [astro-ph/9303019].

[101] D. H. Lyth, *What would we learn by detecting a gravitational wave signal in the cosmic microwave background anisotropy?*, *Phys. Rev. Lett.* **78** (1997) 1861 [hep-ph/9606387].

[102] R. Durrer, *The Cosmic Microwave Background*. Cambridge University Press, 12, 2020, 10.1017/9781316471524.

[103] Planck collaboration, *Planck 2018 results. IV. Diffuse component separation*, *Astron. Astrophys.* **641** (2020) A4 [1807.06208].

[104] M. Tegmark, A. Taylor and A. Heavens, *Karhunen-Loeve eigenvalue problems in cosmology: How should we tackle large data sets?*, *Astrophys. J.* **480** (1997) 22 [astro-ph/9603021].

[105] M. Kamionkowski, A. Kosowsky and A. Stebbins, *A Probe of primordial gravity waves and vorticity*, *Phys. Rev. Lett.* **78** (1997) 2058 [astro-ph/9609132].

[106] U. Seljak and M. Zaldarriaga, *Signature of gravity waves in polarization of the microwave background*, *Phys. Rev. Lett.* **78** (1997) 2054 [astro-ph/9609169].

[107] M. Zaldarriaga and U. Seljak, *An all sky analysis of polarization in the microwave background*, *Phys. Rev. D* **55** (1997) 1830 [astro-ph/9609170].

[108] M. Kamionkowski, A. Kosowsky and A. Stebbins, *Statistics of cosmic microwave background polarization*, *Phys. Rev. D* **55** (1997) 7368 [astro-ph/9611125].

[109] J. Lesgourgues, *The Cosmic Linear Anisotropy Solving System (CLASS) I: Overview*, [1104.2932].

[110] D. Blas, J. Lesgourgues and T. Tram, *The Cosmic Linear Anisotropy Solving System (CLASS) II: Approximation schemes*, *JCAP* **1107** (2011) 034 [1104.2933].

[111] A. Lewis, A. Challinor and A. Lasenby, *Efficient computation of CMB anisotropies in closed FRW models*, *Astrophys. J.* **538** (2000) 473 [astro-ph/9911177].

[112] S. Dodelson, *Coherent phase argument for inflation*, *AIP Conf. Proc.* **689** (2003) 184 [hep-ph/0309057].

[113] M. Zaldarriaga and U. Seljak, *Gravitational lensing effect on cosmic microwave background polarization*, *Phys. Rev. D* **58** (1998) 023003 [astro-ph/9803150].

[114] M. Tristram et al., *Improved limits on the tensor-to-scalar ratio using BICEP and Planck data*, *Phys. Rev. D* **105** (2022) 083524 [2112.07961].

[115] CMB-S4 collaboration, *CMB-S4: Forecasting Constraints on Primordial Gravitational Waves*, *Astrophys. J.* **926** (2022) 54 [2008.12619].

[116] M. Maggiore, *Gravitational wave experiments and early universe cosmology*, *Phys. Rept.* **331** (2000) 283 [gr-qc/9909001].

[117] T. Kite, J. Chluba, A. Ravenni and S. P. Patil, *Clarifying transfer function approximations for the large-scale gravitational wave background in ΛCDM*, *Mon. Not. Roy. Astron. Soc.* **509** (2021) 1366 [2107.13351].

[118] J. Crowder and N. J. Cornish, *Beyond LISA: Exploring future gravitational wave missions*, *Phys. Rev. D* **72** (2005) 083005 [gr-qc/0506015].

[119] N. Barnaby, E. Pajer and M. Peloso, *Gauge Field Production in Axion Inflation: Consequences for Monodromy, non-Gaussianity in the CMB, and Gravitational Waves at Interferometers*, *Phys. Rev. D* **85** (2012) 023525 [1110.3327].

[120] N. Barnaby, R. Namba and M. Peloso, *Phenomenology of a Pseudo-Scalar Inflaton: Naturally Large Nongaussianity*, *JCAP* **04** (2011) 009 [1102.4333].

[121] P. Adshead and M. Wyman, *Chromo-Natural Inflation: Natural inflation on a steep potential with classical non-Abelian gauge fields*, *Phys. Rev. Lett.* **108** (2012) 261302 [1202.2366].

[122] T. Fujita, J. Yokoyama and S. Yokoyama, *Can a spectator scalar field enhance inflationary tensor mode?*, *PTEP* **2015** (2015) 043E01 [1411.3658].

[123] A. Maleknejad, *Axion Inflation with an SU(2) Gauge Field: Detectable Chiral Gravity Waves*, *JHEP* **07** (2016) 104 [1604.03327].

[124] J. Garcia-Bellido, M. Peloso and C. Unal, *Gravitational waves at interferometer scales and primordial black holes in axion inflation*, *JCAP* **12** (2016) 031 [1610.03763].

[125] E. Dimastrogiovanni, M. Fasiello and T. Fujita, *Primordial Gravitational Waves from Axion-Gauge Fields Dynamics*, *JCAP* **01** (2017) 019 [1608.04216].

[126] B. Thorne, T. Fujita, M. Hazumi, N. Katayama, E. Komatsu and M. Shiraishi, *Finding the chiral gravitational wave background of an axion-SU(2) inflationary model using CMB observations and laser interferometers*, *Phys. Rev. D* **97** (2018) 043506 [1707.03240].

[127] L. Bordin, P. Creminelli, A. Khmelnitsky and L. Senatore, *Light Particles with Spin in Inflation*, *JCAP* **10** (2018) 013 [1806.10587].

[128] L. Iacconi, M. Fasiello, H. Assadullahi, E. Dimastrogiovanni and D. Wands, *Interferometer Constraints on the Inflationary Field Content*, *JCAP* **03** (2020) 031 [1910.12921].

[129] L. Iacconi, M. Fasiello, H. Assadullahi and D. Wands, *Small-scale Tests of Inflation*, *JCAP* **12** (2020) 005 [2008.00452].

[130] P. Campeti, E. Komatsu, D. Poletti and C. Baccigalupi, *Measuring the spectrum of primordial gravitational waves with CMB, PTA and Laser Interferometers*, *JCAP* **01** (2021) 012 [2007.04241].

[131] J. Fumagalli, G. A. Palma, S. Renaux-Petel, S. Sypsas, L. T. Witkowski and C. Zenteno, *Primordial gravitational waves from excited states*, *JHEP* **03** (2022) 196 [2111.14664].

[132] T. Fujita, K. Imagawa and K. Murai, *Gravitational waves detectable in laser interferometers from axion-SU(2) inflation*, *JCAP* **07** (2022) 046 [2203.15273].

[133] E. Dimastrogiovanni, M. Fasiello, M. Michelotti and L. Pinol, *Primordial Gravitational Waves in non-Minimally Coupled Chromo-Natural Inflation*, [2303.10718].

[134] J. Garcia-Bellido, A. Papageorgiou, M. Peloso and L. Sorbo, *A flashing beacon in axion inflation: recurring bursts of gravitational waves in the strong backreaction regime*, [2303.13425].

[135] S. Matarrese, S. Mollerach and M. Bruni, *Second order perturbations of the Einstein-de Sitter universe*, *Phys. Rev. D* **58** (1998) 043504 [astro-ph/9707278].

[136] K. N. Ananda, C. Clarkson and D. Wands, *The Cosmological gravitational wave background from primordial density perturbations*, *Phys. Rev. D* **75** (2007) 123518 [gr-qc/0612013].

[137] D. Baumann, P. J. Steinhardt, K. Takahashi and K. Ichiki, *Gravitational Wave Spectrum Induced by Primordial Scalar Perturbations*, *Phys. Rev. D* **76** (2007) 084019 [hep-th/0703290].

[138] G. Domènech, *Scalar Induced Gravitational Waves Review*, *Universe* **7** (2021) 398 [2109.01398].

[139] C. Cheung, P. Creminelli, A. L. Fitzpatrick, J. Kaplan and L. Senatore, *The Effective Field Theory of Inflation*, *JHEP* **03** (2008) 014 [0709.0293].

[140] S. Endlich, A. Nicolis and J. Wang, *Solid Inflation*, *JCAP* **1310** (2013) 011 [1210.0569].

[141] S. Endlich, B. Horn, A. Nicolis and J. Wang, *Squeezed limit of the solid inflation three-point function*, *Phys. Rev.* **D90** (2014) 063506 [1307.8114].

[142] N. Bartolo, D. Cannone, A. Ricciardone and G. Tasinato, *Distinctive signatures of space-time diffeomorphism breaking in EFT of inflation*, *JCAP* **03** (2016) 044 [1511.07414].

[143] A. Ricciardone and G. Tasinato, *Primordial gravitational waves in supersolid inflation*, *Phys. Rev. D* **96** (2017) 023508 [1611.04516].

[144] A. Ricciardone and G. Tasinato, *Anisotropic tensor power spectrum at interferometer scales induced by tensor squeezed non-Gaussianity*, *JCAP* **02** (2018) 011 [1711.02635].

[145] M. Celoria, D. Comelli, L. Pilo and R. Rollo, *Boosting GWs in Supersolid Inflation*, *JHEP* **01** (2021) 185 [2010.02023].

[146] M. Celoria, D. Comelli, L. Pilo and R. Rollo, *Primordial non-Gaussianity in supersolid inflation*, *JHEP* **06** (2021) 147 [2103.10402].

[147] D. Cannone, G. Tasinato and D. Wands, *Generalised tensor fluctuations and inflation*, *JCAP* **01** (2015) 029 [1409.6568].

[148] M. Mylova, O. Özsoy, S. Parameswaran, G. Tasinato and I. Zavala, *A new mechanism to enhance primordial tensor fluctuations in single field inflation*, *JCAP* **12** (2018) 024 [1808.10475].

[149] O. Ozsoy, M. Mylova, S. Parameswaran, C. Powell, G. Tasinato and I. Zavala, *Squeezed tensor non-Gaussianity in non-attractor inflation*, *JCAP* **09** (2019) 036 [1902.04976].

[150] V. Acquaviva, N. Bartolo, S. Matarrese and A. Riotto, *Second order cosmological perturbations from inflation*, *Nucl. Phys.* **B667** (2003) 119 [astro-ph/0209156].

[151] J. M. Maldacena, *Non-Gaussian features of primordial fluctuations in single field inflationary models*, *JHEP* **05** (2003) 013 [astro-ph/0210603].

[152] P. Creminelli, *On non-Gaussianities in single-field inflation*, *JCAP* **0310** (2003) 003 [astro-ph/0306122].

[153] D. Seery and J. E. Lidsey, *Primordial non-Gaussianities in single field inflation*, *JCAP* **0506** (2005) 003 [astro-ph/0503692].

[154] N. Bartolo, S. Matarrese and A. Riotto, *Nongaussianity from inflation*, *Phys. Rev.* **D65** (2002) 103505 [hep-ph/0112261].

[155] D. Babich, P. Creminelli and M. Zaldarriaga, *The Shape of non-Gaussianities*, *JCAP* **0408** (2004) 009 [astro-ph/0405356].

[156] X. Chen, R. Easther and E. A. Lim, *Large Non-Gaussianities in Single Field Inflation*, *JCAP* **0706** (2007) 023 [astro-ph/0611645].

[157] X. Chen, M.-x. Huang, S. Kachru and G. Shiu, *Observational signatures and non-Gaussianities of general single field inflation*, *JCAP* **0701** (2007) 002 [hep-th/0605045].

[158] X. Chen, R. Easther and E. A. Lim, *Generation and Characterization of Large Non-Gaussianities in Single Field Inflation*, *JCAP* **0804** (2008) 010 [0801.3295].

[159] D. Seery and J. E. Lidsey, *Non-Gaussianity from the inflationary trispectrum*, *JCAP* **01** (2007) 008 [astro-ph/0611034].

[160] D. Seery, J. E. Lidsey and M. S. Sloth, *The inflationary trispectrum*, *JCAP* **01** (2007) 027 [astro-ph/0610210].

[161] X. Chen, M.-x. Huang and G. Shiu, *The Inflationary Trispectrum for Models with Large Non-Gaussianities*, *Phys. Rev. D* **74** (2006) 121301 [hep-th/0610235].

[162] D. Seery, M. S. Sloth and F. Vernizzi, *Inflationary trispectrum from graviton exchange*, *JCAP* **0903** (2009) 018 [0811.3934].

[163] X. Chen, B. Hu, M.-x. Huang, G. Shiu and Y. Wang, *Large Primordial Trispectra in General Single Field Inflation*, *JCAP* **08** (2009) 008 [0905.3494].

[164] F. Arroja and K. Koyama, *Non-gaussianity from the trispectrum in general single field inflation*, *Phys. Rev. D* **77** (2008) 083517 [0802.1167].

[165] N. Bartolo, M. Fasiello, S. Matarrese and A. Riotto, *Large non-Gaussianities in the Effective Field Theory Approach to Single-Field Inflation: the Trispectrum*, *JCAP* **09** (2010) 035 [1006.5411].

[166] N. Bartolo, S. Matarrese and A. Riotto, *On nonGaussianity in the curvaton scenario*, *Phys. Rev. D* **69** (2004) 043503 [hep-ph/0309033].

[167] D. Seery and J. E. Lidsey, *Primordial non-Gaussianities from multiple-field inflation*, *JCAP* **0509** (2005) 011 [astro-ph/0506056].

[168] M. Alishahiha, E. Silverstein and D. Tong, *DBI in the sky*, *Phys. Rev.* **D70** (2004) 123505 [hep-th/0404084].

[169] C. Burrage, C. de Rham, D. Seery and A. J. Tolley, *Galileon inflation*, *JCAP* **01** (2011) 014 [1009.2497].

[170] A. J. Tolley and M. Wyman, *The Gelaton Scenario: Equilateral non-Gaussianity from multi-field dynamics*, *Phys. Rev. D* **81** (2010) 043502 [0910.1853].

[171] X. Chen and Y. Wang, *Quasi-Single Field Inflation and Non-Gaussianities*, *JCAP* **1004** (2010) 027 [0911.3380].

[172] X. Chen and Y. Wang, *Large non-Gaussianities with Intermediate Shapes from Quasi-Single Field Inflation*, *Phys. Rev. D* **81** (2010) 063511 [0909.0496].

[173] N. Bartolo, M. Fasiello, S. Matarrese and A. Riotto, *Large non-Gaussianities in the Effective Field Theory Approach to Single-Field Inflation: the Bispectrum*, *JCAP* **1008** (2010) 008 [1004.0893].

[174] A. Achucarro, J.-O. Gong, S. Hardeman, G. A. Palma and S. P. Patil, *Features of heavy physics in the CMB power spectrum*, *JCAP* **1101** (2011) 030 [1010.3693].

[175] A. Achucarro, V. Atal, S. Cespedes, J.-O. Gong, G. A. Palma and S. P. Patil, *Heavy fields, reduced speeds of sound and decoupling during inflation*, *Phys. Rev. D* **86** (2012) 121301 [1205.0710].

[176] J. Elliston, D. Seery and R. Tavakol, *The inflationary bispectrum with curved field-space*, *JCAP* **11** (2012) 060 [1208.6011].

[177] D. Baumann and D. Green, *Equilateral Non-Gaussianity and New Physics on the Horizon*, *JCAP* **09** (2011) 014 [1102.5343].

[178] R. Holman and A. J. Tolley, *Enhanced Non-Gaussianity from Excited Initial States*, *JCAP* **05** (2008) 001 [0710.1302].

[179] R. Flauger and E. Pajer, *Resonant Non-Gaussianity*, *JCAP* **1101** (2011) 017 [1002.0833].

[180] A. Ashoorioon and G. Shiu, *A Note on Calm Excited States of Inflation*, *JCAP* **03** (2011) 025 [1012.3392].

[181] P. D. Meerburg, J. P. van der Schaar and P. S. Corasaniti, *Signatures of Initial State Modifications on Bispectrum Statistics*, *JCAP* **05** (2009) 018 [0901.4044].

[182] R. Flauger, M. Mirbabayi, L. Senatore and E. Silverstein, *Productive Interactions: heavy particles and non-Gaussianity*, *JCAP* **1710** (2017) 058 [1606.00513].

[183] J. Schwinger, *The special canonical group*, *Proceedings of the National Academy of Sciences of the United States of America* **46** (1960) 1401.

[184] J. Schwinger, *Brownian motion of a quantum oscillator*, *Journal of Mathematical Physics* **2** (1961) 407 [https://doi.org/10.1063/1.1703727].

[185] P. M. Bakshi and K. T. Mahanthappa, *Expectation value formalism in quantum field theory. 1.*, *J. Math. Phys.* **4** (1963) 1.

[186] L. V. Keldysh, *Diagram technique for nonequilibrium processes*, *Zh. Eksp. Teor. Fiz.* **47** (1964) 1515.

[187] E. Calzetta and B. L. Hu, *Closed Time Path Functional Formalism in Curved Space-Time: Application to Cosmological Back Reaction Problems*, *Phys. Rev.* **D35** (1987) 495.

[188] S. Weinberg, *Quantum contributions to cosmological correlations*, *Phys. Rev.* **D72** (2005) 043514 [hep-th/0506236].

[189] P. Adshead, R. Easther and E. A. Lim, *The 'in-in' Formalism and Cosmological Perturbations*, *Phys. Rev. D* **80** (2009) 083521 [0904.4207].

[190] P. Creminelli and M. Zaldarriaga, *Single field consistency relation for the 3-point function*, *JCAP* **0410** (2004) 006 [astro-ph/0407059].

[191] C. Cheung, A. L. Fitzpatrick, J. Kaplan and L. Senatore, *On the consistency relation of the 3-point function in single field inflation*, *JCAP* **0802** (2008) 021 [0709.0295].

[192] P. Creminelli, G. D'Amico, M. Musso and J. Noreña, *The (not so) squeezed limit of the primordial 3-point function*, *JCAP* **1111** (2011) 038 [1106.1462].

[193] M. Li and Y. Wang, *Consistency Relations for Non-Gaussianity*, *JCAP* **09** (2008) 018 [0807.3058].

[194] L. Leblond and E. Pajer, *Resonant Trispectrum and a Dozen More Primordial N-point functions*, *JCAP* **01** (2011) 035 [1010.4565].

[195] P. Creminelli, J. Noreña and M. Simonovic, *Conformal consistency relations for single-field inflation*, *JCAP* **1207** (2012) 052 [1203.4595].

[196] K. Hinterbichler, L. Hui and J. Khoury, *An Infinite Set of Ward Identities for Adiabatic Modes in Cosmology*, *JCAP* **1401** (2014) 039 [1304.5527].

[197] W. D. Goldberger, L. Hui and A. Nicolis, *One-particle-irreducible consistency relations for cosmological perturbations*, *Phys. Rev. D* **87** (2013) 103520 [1303.1193].

[198] L. Berezhiani and J. Khoury, *Slavnov-Taylor Identities for Primordial Perturbations*, *JCAP* **02** (2014) 003 [1309.4461].

[199] P. Creminelli, A. Joyce, J. Khoury and M. Simonovic, *Consistency Relations for the Conformal Mechanism*, *JCAP* **04** (2013) 020 [1212.3329].

[200] R. Flauger, D. Green and R. A. Porto, *On squeezed limits in single-field inflation. Part I*, *JCAP* **08** (2013) 032 [1303.1430].

[201] T. Tanaka and Y. Urakawa, *Dominance of gauge artifact in the consistency relation for the primordial bispectrum*, *JCAP* **1105** (2011) 014 [1103.1251].

[202] E. Pajer, F. Schmidt and M. Zaldarriaga, *The Observed Squeezed Limit of Cosmological Three-Point Functions*, *Phys. Rev.* **D88** (2013) 083502 [1305.0824].

[203] P. Creminelli, A. Perko, L. Senatore, M. Simonović and G. Trevisan, *The Physical Squeezed Limit: Consistency Relations at Order q^2*, *JCAP* **1311** (2013) 015 [1307.0503].

[204] L. Dai, E. Pajer and F. Schmidt, *Conformal Fermi Coordinates*, *JCAP* **1511** (2015) 043 [1502.02011].

[205] G. Cabass, E. Pajer and F. Schmidt, *How Gaussian can our Universe be?*, *JCAP* **01** (2017) 003 [1612.00033].

[206] Y. Tada and V. Vennin, *Squeezed bispectrum in the δN formalism: local observer effect in field space*, *JCAP* **02** (2017) 021 [1609.08876].

[207] S. Matarrese, L. Pilo and R. Rollo, *Resilience of long modes in cosmological observables*, [2007.08877].

[208] N. Barnaby, R. Namba and M. Peloso, *Observable non-gaussianity from gauge field production in slow roll inflation, and a challenging connection with magnetogenesis*, *Phys. Rev. D* **85** (2012) 123523 [1202.1469].

[209] C. T. Byrnes, K.-Y. Choi and L. M. H. Hall, *Conditions for large non-Gaussianity in two-field slow-roll inflation*, *JCAP* **10** (2008) 008 [0807.1101].

[210] C. T. Byrnes, K.-Y. Choi and L. M. H. Hall, *Large non-Gaussianity from two-component hybrid inflation*, *JCAP* **02** (2009) 017 [0812.0807].

[211] C. T. Byrnes and K.-Y. Choi, *Review of local non-Gaussianity from multi-field inflation*, *Adv. Astron.* **2010** (2010) 724525 [1002.3110].

[212] M. Biagetti, E. Dimastrogiovanni and M. Fasiello, *Possible signatures of the inflationary particle content: spin-2 fields*, *JCAP* **1710** (2017) 038 [1708.01587].

[213] E. Dimastrogiovanni, M. Fasiello, G. Tasinato and D. Wands, *Tensor non-Gaussianities from Non-minimal Coupling to the Inflaton*, *JCAP* **02** (2019) 008 [1810.08866].

[214] I. Agullo and L. Parker, *Non-gaussianities and the Stimulated creation of quanta in the inflationary universe*, *Phys. Rev. D* **83** (2011) 063526 [1010.5766].

[215] D. Chialva, *Signatures of very high energy physics in the squeezed limit of the bispectrum (violation of Maldacena's condition)*, *JCAP* **10** (2012) 037 [1108.4203].

[216] N. Agarwal, R. Holman, A. J. Tolley and J. Lin, *Effective field theory and non-Gaussianity from general inflationary states*, *JHEP* **05** (2013) 085 [1212.1172].

[217] J.-O. Gong and M. Sasaki, *Squeezed primordial bispectrum from general vacuum state*, *Class. Quant. Grav.* **30** (2013) 095005 [1302.1271].

[218] L. Berezhiani and J. Khoury, *On the Initial State and Consistency Relations*, *JCAP* **09** (2014) 018 [1406.2689].

[219] S. Akama, S. Hirano and T. Kobayashi, *Primordial tensor non-Gaussianities from general single-field inflation with non-Bunch-Davies initial states*, *Phys. Rev. D* **102** (2020) 023513 [2003.10686].

[220] M. H. Namjoo, H. Firouzjahi and M. Sasaki, *Violation of non-Gaussianity consistency relation in a single field inflationary model*, *EPL* **101** (2013) 39001 [1210.3692].

[221] J. Martin, H. Motohashi and T. Suyama, *Ultra Slow-Roll Inflation and the non-Gaussianity Consistency Relation*, *Phys. Rev. D* **87** (2013) 023514 [1211.0083].

[222] X. Chen, H. Firouzjahi, M. H. Namjoo and M. Sasaki, *A Single Field Inflation Model with Large Local Non-Gaussianity*, *EPL* **102** (2013) 59001 [1301.5699].

[223] X. Chen, H. Firouzjahi, E. Komatsu, M. H. Namjoo and M. Sasaki, *In-in and δN calculations of the bispectrum from non-attractor single-field inflation*, *JCAP* **12** (2013) 039 [1308.5341].

[224] S. Mooij and G. A. Palma, *Consistently violating the non-Gaussian consistency relation*, *JCAP* **11** (2015) 025 [1502.03458].

[225] R. Bravo, S. Mooij, G. A. Palma and B. Pradenas, *A generalized non-Gaussian consistency relation for single field inflation*, *JCAP* **05** (2018) 024 [1711.02680].

[226] R. Bravo, S. Mooij, G. A. Palma and B. Pradenas, *Vanishing of local non-Gaussianity in canonical single field inflation*, *JCAP* **05** (2018) 025 [1711.05290].

[227] T. Noumi, M. Yamaguchi and D. Yokoyama, *Effective field theory approach to quasi-single field inflation and effects of heavy fields*, *JHEP* **06** (2013) 051 [1211.1624].

[228] V. Assassi, D. Baumann and D. Green, *On Soft Limits of Inflationary Correlation Functions*, *JCAP* **1211** (2012) 047 [1204.4207].

[229] N. Arkani-Hamed and J. Maldacena, *Cosmological Collider Physics*, [1503.08043].

[230] A. Kehagias and A. Riotto, *High Energy Physics Signatures from Inflation and Conformal Symmetry of de Sitter*, *Fortsch. Phys.* **63** (2015) 531 [1501.03515].

[231] X. Chen, Y. Wang and Z.-Z. Xianyu, *Standard Model Mass Spectrum in Inflationary Universe*, *JHEP* **04** (2017) 058 [1612.08122].

[232] X. Chen, Y. Wang and Z.-Z. Xianyu, *Standard Model Background of the Cosmological Collider*, *Phys. Rev. Lett.* **118** (2017) 261302 [1610.06597].

[233] H. Lee, D. Baumann and G. L. Pimentel, *Non-Gaussianity as a Particle Detector*, *JHEP* **12** (2016) 040 [1607.03735].

[234] P. D. Meerburg, M. Münchmeyer, J. B. Muñoz and X. Chen, *Prospects for Cosmological Collider Physics*, *JCAP* **1703** (2017) 050 [1610.06559].

[235] Planck collaboration, *Planck 2018 results. IX. Constraints on primordial non-Gaussianity*, *Astron. Astrophys.* **641** (2020) A9 [1905.05697].

[236] A. Achúcarro et al., *Inflation: Theory and Observations*, [2203.08128].

[237] W.-R. Hu and Y.-L. Wu, *The Taiji Program in Space for gravitational wave physics and the nature of gravity*, *Natl. Sci. Rev.* **4** (2017) 685.

[238] B. Allen and A. C. Ottewill, *Detection of anisotropies in the gravitational wave stochastic background*, *Phys. Rev. D* **56** (1997) 545 [gr-qc/9607068].

[239] C. Ungarelli and A. Vecchio, *Studying the anisotropy of the gravitational wave stochastic background with LISA*, *Phys. Rev. D* **64** (2001) 121501 [astro-ph/0106538].

[240] H. Kudoh and A. Taruya, *Probing anisotropies of gravitational-wave backgrounds with a space-based interferometer: Geometric properties of antenna patterns and their angular power*, *Phys. Rev. D* **71** (2005) 024025 [gr-qc/0411017].

[241] J. D. Romano and N. J. Cornish, *Detection methods for stochastic gravitational-wave backgrounds: a unified treatment*, *Living Rev. Rel.* **20** (2017) 2 [1608.06889].

[242] A. I. Renzini and C. R. Contaldi, *Mapping Incoherent Gravitational Wave Backgrounds*, *Mon. Not. Roy. Astron. Soc.* **481** (2018) 4650 [1806.11360].

[243] C. R. Contaldi, M. Pieroni, A. I. Renzini, G. Cusin, N. Karnesis, M. Peloso et al., *Maximum likelihood map-making with the Laser Interferometer Space Antenna*, *Phys. Rev. D* **102** (2020) 043502 [2006.03313].

[244] S. Banagiri, A. Criswell, T. Kuan, V. Mandic, J. D. Romano and S. R. Taylor, *Mapping the gravitational-wave sky with LISA: a Bayesian spherical harmonic approach*, *Mon. Not. Roy. Astron. Soc.* **507** (2021) 5451 [2103.00826].

[245] A. I. Renzini, J. D. Romano, C. R. Contaldi and N. J. Cornish, *Comparison of maximum-likelihood mapping methods for gravitational-wave backgrounds*, *Phys. Rev. D* **105** (2022) 023519 [2107.02292].

[246] LISA Cosmology Working Group collaboration, *Probing anisotropies of the Stochastic Gravitational Wave Background with LISA*, *JCAP* **11** (2022) 009 [2201.08782].

[247] C. M. Mingarelli, T. Sidery, I. Mandel and A. Vecchio, *Characterizing gravitational wave stochastic background anisotropy with pulsar timing arrays*, *Phys. Rev. D* **88** (2013) 062005 [1306.5394].

[248] Y. Ali-Haïmoud, T. L. Smith and C. M. F. Mingarelli, *Insights into searches for anisotropies in the nanohertz gravitational-wave background*, *Phys. Rev. D* **103** (2021) 042009 [2010.13958].

[249] Y. Ali-Haïmoud, T. L. Smith and C. M. F. Mingarelli, *Fisher formalism for anisotropic gravitational-wave background searches with pulsar timing arrays*, *Phys. Rev. D* **102** (2020) 122005 [2006.14570].

[250] N. Pol, S. R. Taylor and J. D. Romano, *Forecasting Pulsar Timing Array Sensitivity to Anisotropy in the Stochastic Gravitational Wave Background*, *Astrophys. J.* **940** (2022) 173 [2206.09936].

[251] D. Agarwal, J. Suresh, S. Mitra and A. Ain, *Angular power spectra of anisotropic stochastic gravitational wave background: developing statistical methods and analyzing data from ground-based detectors*, [2302.12516].

[252] G. Agazie, A. Anumarlapudi, A. M. Archibald, Z. Arzoumanian, P. T. Baker, B. Bécsy et al., *The NANOGrav 15-year Data Set: Search for Anisotropy in the Gravitational-Wave Background*, *arXiv e-prints* (2023) arXiv:2306.16221 [2306.16221].

[253] V. Alba and J. Maldacena, *Primordial gravity wave background anisotropies*, *JHEP* **03** (2016) 115 [1512.01531].

[254] C. R. Contaldi, *Anisotropies of Gravitational Wave Backgrounds: A Line Of Sight Approach*, *Phys. Lett. B* **771** (2017) 9 [1609.08168].

[255] N. Bartolo, D. Bertacca, S. Matarrese, M. Peloso, A. Ricciardone, A. Riotto et al., *Characterizing the cosmological gravitational wave background: Anisotropies and non-Gaussianity*, *Phys. Rev. D* **102** (2020) 023527 [1912.09433].

[256] N. Bartolo, D. Bertacca, S. Matarrese, M. Peloso, A. Ricciardone, A. Riotto et al., *Anisotropies and non-Gaussianity of the Cosmological Gravitational Wave Background*, *Phys. Rev. D* **100** (2019) 121501 [1908.00527].

[257] T. Regimbau, *The astrophysical gravitational wave stochastic background*, *Res. Astron. Astrophys.* **11** (2011) 369 [1101.2762].

[258] G. Cusin, C. Pitrou and J.-P. Uzan, *Anisotropy of the astrophysical gravitational wave background: Analytic expression of the angular power spectrum and correlation with cosmological observations*, *Phys. Rev. D* **96** (2017) 103019 [1704.06184].

[259] G. Cusin, I. Dvorkin, C. Pitrou and J.-P. Uzan, *First predictions of the angular power spectrum of the astrophysical gravitational wave background*, *Phys. Rev. Lett.* **120** (2018) 231101 [1803.03236].

[260] G. Cusin, I. Dvorkin, C. Pitrou and J.-P. Uzan, *Stochastic gravitational wave background anisotropies in the mHz band: astrophysical dependencies*, *Mon. Not. Roy. Astron. Soc.* **493** (2020) L1 [1904.07757].

[261] G. Cusin, I. Dvorkin, C. Pitrou and J.-P. Uzan, *Properties of the stochastic astrophysical gravitational wave background: astrophysical sources dependencies*, *Phys. Rev. D* **100** (2019) 063004 [1904.07797].

[262] A. C. Jenkins, M. Sakellariadou, T. Regimbau and E. Slezak, *Anisotropies in the astrophysical gravitational-wave background: Predictions for the detection of compact binaries by LIGO and Virgo*, *Phys. Rev. D* **98** (2018) 063501 [1806.01718].

[263] A. C. Jenkins, R. O'Shaughnessy, M. Sakellariadou and D. Wysocki, *Anisotropies in the astrophysical gravitational-wave background: The impact of black hole distributions*, *Phys. Rev. Lett.* **122** (2019) 111101 [1810.13435].

[264] A. C. Jenkins, J. D. Romano and M. Sakellariadou, *Estimating the angular power spectrum of the gravitational-wave background in the presence of shot noise*, *Phys. Rev. D* **100** (2019) 083501 [1907.06642].

[265] A. C. Jenkins and M. Sakellariadou, *Shot noise in the astrophysical gravitational-wave background*, *Phys. Rev. D* **100** (2019) 063508 [1902.07719].

[266] G. Cañas Herrera, O. Contigiani and V. Vardanyan, *Cross-correlation of the astrophysical gravitational-wave background with galaxy clustering*, *Phys. Rev. D* **102** (2020) 043513 [1910.08353].

[267] D. Bertacca, A. Ricciardone, N. Bellomo, A. C. Jenkins, S. Matarrese, A. Raccanelli et al., *Projection effects on the observed angular spectrum of the astrophysical stochastic gravitational wave background*, *Phys. Rev. D* **101** (2020) 103513 [1909.11627].

[268] C. Pitrou, G. Cusin and J.-P. Uzan, *Unified view of anisotropies in the astrophysical gravitational-wave background*, *Phys. Rev. D* **101** (2020) 081301 [1910.04645].

[269] D. Alonso, G. Cusin, P. G. Ferreira and C. Pitrou, *Detecting the anisotropic astrophysical gravitational wave background in the presence of shot noise through cross-correlations*, *Phys. Rev. D* **102** (2020) 023002 [2002.02888].

[270] K. Z. Yang, V. Mandic, C. Scarlata and S. Banagiri, *Searching for Cross-Correlation Between Stochastic Gravitational Wave Background and Galaxy Number Counts*, *Mon. Not. Roy. Astron. Soc.* **500** (2020) 1666 [2007.10456].

[271] G. Capurri, A. Lapi, C. Baccigalupi, L. Boco, G. Scelfo and T. Ronconi, *Intensity and anisotropies of the stochastic gravitational wave background from merging compact binaries in galaxies*, *JCAP* **11** (2021) 032 [2103.12037].

[272] N. Bellomo, D. Bertacca, A. C. Jenkins, S. Matarrese, A. Raccanelli, T. Regimbau et al., *CLASS_GWB: robust modeling of the astrophysical gravitational wave background anisotropies*, *JCAP* **06** (2022) 030 [2110.15059].

[273] G. Sato-Polito and M. Kamionkowski, *Exploring the spectrum of stochastic gravitational-wave anisotropies with pulsar timing arrays*, [2305.05690].

[274] K. Z. Yang, J. Suresh, G. Cusin, S. Banagiri, N. Feist, V. Mandic et al., *Measurement of the Cross-Correlation Angular Power Spectrum Between the Stochastic Gravitational Wave Background and Galaxy Over-Density*, [2304.07621].

[275] T. Regimbau, M. Evans, N. Christensen, E. Katsavounidis, B. Sathyaprakash and S. Vitale, *Digging deeper: Observing primordial gravitational waves below the binary black hole produced stochastic background*, *Phys. Rev. Lett.* **118** (2017) 151105 [1611.08943].

[276] Z. Pan and H. Yang, *Probing Primordial Stochastic Gravitational Wave Background with Multi-band Astrophysical Foreground Cleaning*, *Class. Quant. Grav.* **37** (2020) 195020 [1910.09637].

[277] S. Mukherjee and J. Silk, *Time-dependence of the astrophysical stochastic gravitational wave background*, *Mon. Not. Roy. Astron. Soc.* **491** (2020) 4690 [1912.07657].

[278] A. Sharma and J. Harms, *Searching for cosmological gravitational-wave backgrounds with third-generation detectors in the presence of an astrophysical foreground*, *Phys. Rev. D* **102** (2020) 063009 [2006.16116].

[279] M. Pieroni and E. Barausse, *Foreground cleaning and template-free stochastic background extraction for LISA*, *JCAP* **07** (2020) 021 [2004.01135].

[280] S. Biscoveanu, C. Talbot, E. Thrane and R. Smith, *Measuring the primordial gravitational-wave background in the presence of astrophysical foregrounds*, *Phys. Rev. Lett.* **125** (2020) 241101 [2009.04418].

[281] K. Martinovic, P. M. Meyers, M. Sakellariadou and N. Christensen, *Simultaneous estimation of astrophysical and cosmological stochastic gravitational-wave backgrounds with terrestrial detectors*, *Phys. Rev. D* **103** (2021) 043023 [2011.05697].

[282] D. Poletti, *Measuring the primordial gravitational wave background in the presence of other stochastic signals*, *JCAP* **05** (2021) 052 [2101.02713].

[283] G. Boileau, N. Christensen, R. Meyer and N. J. Cornish, *Spectral separation of the stochastic gravitational-wave background for LISA: observing both*

cosmological and astrophysical backgrounds, *Phys. Rev. D* **103** (2021) 103529 [2011.05055].

[284] G. Boileau, A. Lamberts, N. J. Cornish and R. Meyer, *Spectral separation of the stochastic gravitational-wave background for LISA in the context of a modulated Galactic foreground*, *Mon. Not. Roy. Astron. Soc.* **508** (2021) 803 [2105.04283].

[285] J. Suresh, D. Agarwal and S. Mitra, *Jointly setting upper limits on multiple components of an anisotropic stochastic gravitational-wave background*, *Phys. Rev. D* **104** (2021) 102003 [2106.09593].

[286] M. Geller, A. Hook, R. Sundrum and Y. Tsai, *Primordial Anisotropies in the Gravitational Wave Background from Cosmological Phase Transitions*, *Phys. Rev. Lett.* **121** (2018) 201303 [1803.10780].

[287] S. Kumar, R. Sundrum and Y. Tsai, *Non-Gaussian stochastic gravitational waves from phase transitions*, *JHEP* **11** (2021) 107 [2102.05665].

[288] Y. Li, F. P. Huang, X. Wang and X. Zhang, *Anisotropy of phase transition gravitational wave*, *Phys. Rev. D* **105** (2021) 083527 [2112.01409].

[289] A. Bodas and R. Sundrum, *Large primordial fluctuations in gravitational waves from phase transitions*, *JHEP* **06** (2023) 029 [2211.09301].

[290] A. Bodas and R. Sundrum, *Primordial clocks within stochastic gravitational wave anisotropies*, *JCAP* **10** (2022) 012 [2205.04482].

[291] N. Bartolo, D. Bertacca, V. De Luca, G. Franciolini, S. Matarrese, M. Peloso et al., *Gravitational wave anisotropies from primordial black holes*, *JCAP* **02** (2020) 028 [1909.12619].

[292] E. Dimastrogiovanni, M. Fasiello and G. Tasinato, *Searching for Fossil Fields in the Gravity Sector*, *Phys. Rev. Lett.* **124** (2020) 061302 [1906.07204].

[293] P. Adshead, N. Afshordi, E. Dimastrogiovanni, M. Fasiello, E. A. Lim and G. Tasinato, *Multimessenger Cosmology: correlating CMB and SGWB measurements*, *Phys. Rev. D* **103** (2021) 023532 [2004.06619].

[294] E. Dimastrogiovanni, M. Fasiello and L. Pinol, *Primordial stochastic gravitational wave background anisotropies: in-in formalization and applications*, *JCAP* **09** (2022) 031 [2203.17192].

[295] G. Orlando, *Probing parity-odd bispectra with anisotropies of GW V modes*, *JCAP* **12** (2022) 019 [2206.14173].

[296] J.-P. Li, S. Wang, Z.-C. Zhao and K. Kohri, *Primordial Non-Gaussianity and Anisotropies in Gravitational Waves induced by Scalar Perturbations*, [2305.19950].

[297] S. Olmez, V. Mandic and X. Siemens, *Anisotropies in the Gravitational-Wave Stochastic Background*, *JCAP* **07** (2012) 009 [1106.5555].

[298] S. Kuroyanagi, K. Takahashi, N. Yonemaru and H. Kumamoto, *Anisotropies in the gravitational wave background as a probe of the cosmic string network*, *Phys. Rev. D* **95** (2017) 043531 [1604.00332].

[299] A. C. Jenkins and M. Sakellariadou, *Anisotropies in the stochastic gravitational-wave background: Formalism and the cosmic string case*, *Phys. Rev. D* **98** (2018) 063509 [1802.06046].

[300] R.-G. Cai, Z.-K. Guo and J. Liu, *A New Picture of Cosmic String Evolution and Anisotropic Stochastic Gravitational-Wave Background*, [2112.10131].

[301] L. Bethke, D. G. Figueroa and A. Rajantie, *Anisotropies in the Gravitational Wave Background from Preheating*, *Phys. Rev. Lett.* **111** (2013) 011301 [1304.2657].

[302] L. Bethke, D. G. Figueroa and A. Rajantie, *On the Anisotropy of the Gravitational Wave Background from Massless Preheating*, *JCAP* **06** (2014) 047 [1309.1148].

[303] L. Valbusa Dall'Armi, A. Ricciardone, N. Bartolo, D. Bertacca and S. Matarrese, *Imprint of relativistic particles on the anisotropies of the stochastic gravitational-wave background*, *Phys. Rev. D* **103** (2021) 023522 [2007.01215].

[304] M. Braglia and S. Kuroyanagi, *Probing prerecombination physics by the cross-correlation of stochastic gravitational waves and CMB anisotropies*, *Phys. Rev. D* **104** (2021) 123547 [2106.03786].

[305] A. Ricciardone, L. V. Dall'Armi, N. Bartolo, D. Bertacca, M. Liguori and S. Matarrese, *Cross-Correlating Astrophysical and Cosmological Gravitational*

Wave Backgrounds with the Cosmic Microwave Background, Phys. Rev. Lett. **127** (2021) 271301 [2106.02591].

[306] F. Schulze, L. Valbusa Dall'Armi, J. Lesgourgues, A. Ricciardone, N. Bartolo, D. Bertacca et al., *GW_CLASS: Cosmological Gravitational Wave Background in the Cosmic Linear Anisotropy Solving System*, [2305.01602].

[307] U. Seljak and M. Zaldarriaga, *A Line of sight integration approach to cosmic microwave background anisotropies*, Astrophys. J. **469** (1996) 437 [astro-ph/9603033].

[308] B. Carr and F. Kuhnel, *Primordial Black Holes as Dark Matter: Recent Developments*, Ann. Rev. Nucl. Part. Sci. **70** (2020) 355 [2006.02838].

[309] B. Carr, S. Clesse, J. Garcia-Bellido, M. Hawkins and F. Kuhnel, *Observational Evidence for Primordial Black Holes: A Positivist Perspective*, [2306.03903].

[310] R. Allahverdi et al., *The First Three Seconds: a Review of Possible Expansion Histories of the Early Universe*, The Open Journal of Astrophysics **4** (2021) [2006.16182].

[311] M. S. Turner, *Coherent Scalar Field Oscillations in an Expanding Universe*, Phys. Rev. D **28** (1983) 1243.

[312] B. Spokoiny, *Deflationary universe scenario*, Phys. Lett. B **315** (1993) 40 [gr-qc/9306008].

[313] M. Joyce, *Electroweak Baryogenesis and the Expansion Rate of the Universe*, Phys. Rev. D **55** (1997) 1875 [hep-ph/9606223].

[314] P. G. Ferreira and M. Joyce, *Cosmology with a primordial scaling field*, Phys. Rev. D **58** (1998) 023503 [astro-ph/9711102].

[315] P. J. E. Peebles and A. Vilenkin, *Quintessential inflation*, Phys. Rev. D **59** (1999) 063505 [astro-ph/9810509].

[316] M. Joyce, *Habilitation thesis*, 2001.

[317] Y. Gouttenoire, G. Servant and P. Simakachorn, *Revealing the Primordial Irreducible Inflationary Gravitational-Wave Background with a Spinning Peccei-Quinn Axion*, [2108.10328].

[318] M. Giovannini, *Gravitational waves constraints on post-inflationary phases stiffer than radiation*, *Phys. Rev. D* **58** (1998) 083504 [hep-ph/9806329].

[319] N. Seto and J. Yokoyama, *Probing the equation of state of the early universe with a space laser interferometer*, *J. Phys. Soc. Jap.* **72** (2003) 3082 [gr-qc/0305096].

[320] H. Assadullahi and D. Wands, *Gravitational waves from an early matter era*, *Phys. Rev. D* **79** (2009) 083511 [0901.0989].

[321] D. J. H. Chung and P. Zhou, *Gravity Waves as a Probe of Hubble Expansion Rate During An Electroweak Scale Phase Transition*, *Phys. Rev. D* **82** (2010) 024027 [1003.2462].

[322] S. Kuroyanagi, K. Nakayama and S. Saito, *Prospects for determination of thermal history after inflation with future gravitational wave detectors*, *Phys. Rev. D* **84** (2011) 123513 [1110.4169].

[323] B. Li, P. R. Shapiro and T. Rindler-Daller, *Bose-Einstein-condensed scalar field dark matter and the gravitational wave background from inflation: new cosmological constraints and its detectability by LIGO*, *Phys. Rev. D* **96** (2017) 063505 [1611.07961].

[324] Y. Cui, M. Lewicki, D. E. Morrissey and J. D. Wells, *Cosmic Archaeology with Gravitational Waves from Cosmic Strings*, *Phys. Rev. D* **97** (2018) 123505 [1711.03104].

[325] B. Carr, T. Tenkanen and V. Vaskonen, *Primordial black holes from inflaton and spectator field perturbations in a matter-dominated era*, *Phys. Rev. D* **96** (2017) 063507 [1706.03746].

[326] Y. Cui, M. Lewicki, D. E. Morrissey and J. D. Wells, *Probing the pre-BBN universe with gravitational waves from cosmic strings*, *JHEP* **01** (2019) 081 [1808.08968].

[327] K. Inomata, K. Kohri, T. Nakama and T. Terada, *Enhancement of Gravitational Waves Induced by Scalar Perturbations due to a Sudden Transition from an Early Matter Era to the Radiation Era*, *Phys. Rev. D* **100** (2019) 043532 [1904.12879].

[328] K. Inomata, K. Kohri, T. Nakama and T. Terada, *Gravitational Waves Induced by Scalar Perturbations during a Gradual Transition from an Early Matter Era to the Radiation Era*, *JCAP* **10** (2019) 071 [1904.12878].

[329] F. D'Eramo and K. Schmitz, *Imprint of a scalar era on the primordial spectrum of gravitational waves*, *Phys. Rev. Research.* **1** (2019) 013010 [1904.07870].

[330] G. Domènech, *Induced gravitational waves in a general cosmological background*, *Int. J. Mod. Phys. D* **29** (2020) 2050028 [1912.05583].

[331] N. Bernal and F. Hajkarim, *Primordial Gravitational Waves in Nonstandard Cosmologies*, *Phys. Rev. D* **100** (2019) 063502 [1905.10410].

[332] D. G. Figueroa and E. H. Tanin, *Ability of LIGO and LISA to probe the equation of state of the early Universe*, *JCAP* **08** (2019) 011 [1905.11960].

[333] N. Ramberg and L. Visinelli, *Probing the Early Universe with Axion Physics and Gravitational Waves*, *Phys. Rev. D* **99** (2019) 123513 [1904.05707].

[334] C.-F. Chang and Y. Cui, *Stochastic Gravitational Wave Background from Global Cosmic Strings*, *Phys. Dark Univ.* **29** (2020) 100604 [1910.04781].

[335] G. Domènech, S. Pi and M. Sasaki, *Induced gravitational waves as a probe of thermal history of the universe*, *JCAP* **08** (2020) 017 [2005.12314].

[336] G. Domènech, C. Lin and M. Sasaki, *Gravitational wave constraints on the primordial black hole dominated early universe*, *JCAP* **04** (2021) 062 [2012.08151].

[337] Y. Gouttenoire, G. Servant and P. Simakachorn, *Kination cosmology from scalar fields and gravitational-wave signatures*, [2111.01150].

[338] R. T. Co, D. Dunsky, N. Fernandez, A. Ghalsasi, L. J. Hall, K. Harigaya et al., *Gravitational wave and CMB probes of axion kination*, *JHEP* **09** (2022) 116 [2108.09299].

[339] M. Giovannini, *Inflation, space-borne interferometers and the expansion history of the Universe*, *Eur. Phys. J. C* **82** (2022) 828 [2206.08217].

[340] D. H. Lyth and D. Wands, *Generating the curvature perturbation without an inflaton*, *Phys. Lett.* **B524** (2002) 5 [hep-ph/0110002].

[341] D. H. Lyth, C. Ungarelli and D. Wands, *The Primordial density perturbation in the curvaton scenario*, *Phys. Rev. D* **67** (2003) 023503 [astro-ph/0208055].

[342] T. Moroi and T. Takahashi, *Cosmic density perturbations from late decaying scalar condensations*, *Phys. Rev. D* **66** (2002) 063501 [hep-ph/0206026].

[343] R. A. Isaacson, *Gravitational radiation in the limit of high frequency. i. the linear approximation and geometrical optics*, *Phys. Rev.* **166** (1968) 1263.

[344] C. W. Misner, K. S. Thorne and J. A. Wheeler, *Gravitation*. W. H. Freeman, San Francisco, 1973.

[345] M. Maggiore, *Gravitational Waves. Vol. 1: Theory and Experiments*, Oxford Master Series in Physics. Oxford University Press, 2007.

[346] S. Dodelson, *Modern Cosmology*. Academic Press, Amsterdam, 2003.

[347] S. Pi and M. Sasaki, *Gravitational Waves Induced by Scalar Perturbations with a Lognormal Peak*, *JCAP* **09** (2020) 037 [2005.12306].

[348] R. Saito and J. Yokoyama, *Gravitational-Wave Constraints on the Abundance of Primordial Black Holes*, *Progress of Theoretical Physics* **123** (2010) 867 [0912.5317].

[349] S. Pi, Y.-l. Zhang, Q.-G. Huang and M. Sasaki, *Scalaron from R^2-gravity as a heavy field*, *JCAP* **05** (2018) 042 [1712.09896].

[350] M. Kawasaki, N. Sugiyama and T. Yanagida, *Primordial black hole formation in a double inflation model in supergravity*, *Phys. Rev. D* **57** (1998) 6050 [hep-ph/9710259].

[351] J. Garcia-Bellido, A. D. Linde and D. Wands, *Density perturbations and black hole formation in hybrid inflation*, *Phys. Rev. D* **54** (1996) 6040 [astro-ph/9605094].

[352] P. H. Frampton, M. Kawasaki, F. Takahashi and T. T. Yanagida, *Primordial Black Holes as All Dark Matter*, *JCAP* **04** (2010) 023 [1001.2308].

[353] G. A. Palma, S. Sypsas and C. Zenteno, *Seeding primordial black holes in multifield inflation*, *Phys. Rev. Lett.* **125** (2020) 121301 [2004.06106].

[354] J. Fumagalli, S. Renaux-Petel, J. W. Ronayne and L. T. Witkowski, *Turning in the landscape: A new mechanism for generating primordial black holes*, *Phys. Lett. B* **841** (2023) 137921 [2004.08369].

[355] M. Braglia, D. K. Hazra, F. Finelli, G. F. Smoot, L. Sriramkumar and A. A. Starobinsky, *Generating PBHs and small-scale GWs in two-field models of inflation*, *JCAP* **08** (2020) 001 [2005.02895].

[356] Y.-F. Cai, X. Tong, D.-G. Wang and S.-F. Yan, *Primordial Black Holes from Sound Speed Resonance during Inflation*, *Phys. Rev. Lett.* **121** (2018) 081306 [1805.03639].

[357] C. Chen and Y.-F. Cai, *Primordial black holes from sound speed resonance in the inflaton-curvaton mixed scenario*, *JCAP* **10** (2019) 068 [1908.03942].

[358] Y.-F. Cai, C. Chen, X. Tong, D.-G. Wang and S.-F. Yan, *When Primordial Black Holes from Sound Speed Resonance Meet a Stochastic Background of Gravitational Waves*, *Phys. Rev. D* **100** (2019) 043518 [1902.08187].

[359] R.-G. Cai, Z.-K. Guo, J. Liu, L. Liu and X.-Y. Yang, *Primordial black holes and gravitational waves from parametric amplification of curvature perturbations*, *JCAP* **06** (2020) 013 [1912.10437].

[360] C. Chen, X.-H. Ma and Y.-F. Cai, *Dirac-Born-Infeld realization of sound speed resonance mechanism for primordial black holes*, *Phys. Rev. D* **102** (2020) 063526 [2003.03821].

[361] J. Fumagalli, S. Renaux-Petel and L. T. Witkowski, *Oscillations in the stochastic gravitational wave background from sharp features and particle production during inflation*, *JCAP* **08** (2021) 030 [2012.02761].

[362] C. T. Byrnes, P. S. Cole and S. P. Patil, *Steepest growth of the power spectrum and primordial black holes*, *JCAP* **06** (2019) 028 [1811.11158].

[363] P. Carrilho, K. A. Malik and D. J. Mulryne, *Dissecting the growth of the power spectrum for primordial black holes*, *Phys. Rev. D* **100** (2019) 103529 [1907.05237].

[364] O. Özsoy and G. Tasinato, *On the slope of the curvature power spectrum in non-attractor inflation*, *JCAP* **04** (2020) 048 [1912.01061].

[365] G. Tasinato, *An analytic approach to non-slow-roll inflation*, *Phys. Rev. D* **103** (2021) 023535 [2012.02518].

[366] P. Auclair et al., *Probing the gravitational wave background from cosmic strings with LISA*, *JCAP* **04** (2020) 034 [1909.00819].

[367] A. Mazumdar and G. White, *Review of cosmic phase transitions: their significance and experimental signatures*, *Rept. Prog. Phys.* **82** (2019) 076901 [1811.01948].

[368] J. Garcia-Bellido, M. Peloso and C. Unal, *Gravitational Wave signatures of inflationary models from Primordial Black Hole Dark Matter*, *JCAP* **09** (2017) 013 [1707.02441].

[369] N. Bartolo, V. De Luca, G. Franciolini, A. Lewis, M. Peloso and A. Riotto, *Primordial Black Hole Dark Matter: LISA Serendipity*, *Phys. Rev. Lett.* **122** (2019) 211301 [1810.12218].

[370] N. Bartolo, V. De Luca, G. Franciolini, M. Peloso, D. Racco and A. Riotto, *Testing primordial black holes as dark matter with LISA*, *Phys. Rev. D* **99** (2019) 103521 [1810.12224].

[371] T. L. Smith and R. Caldwell, *LISA for Cosmologists: Calculating the Signal-to-Noise Ratio for Stochastic and Deterministic Sources*, *Phys. Rev. D* **100** (2019) 104055 [1908.00546].

[372] M. Lewicki and V. Vaskonen, *Impact of LIGO-Virgo black hole binaries on gravitational wave background searches*, *Eur. Phys. J. C* **83** (2023) 168 [2111.05847].

[373] N. Smyth, S. Profumo, S. English, T. Jeltema, K. McKinnon and P. Guhathakurta, *Updated Constraints on Asteroid-Mass Primordial Black Holes as Dark Matter*, *Phys. Rev. D* **101** (2020) 063005 [1910.01285].

[374] EROS-2 collaboration, *Limits on the Macho Content of the Galactic Halo from the EROS-2 Survey of the Magellanic Clouds*, *Astron. Astrophys.* **469** (2007) 387 [astro-ph/0607207].

[375] D. Croon, D. McKeen, N. Raj and Z. Wang, *Subaru-HSC through a different lens: Microlensing by extended dark matter structures*, *Phys. Rev. D* **102** (2020) 083021 [2007.12697].

[376] K. Griest, A. M. Cieplak and M. J. Lehner, *Experimental Limits on Primordial Black Hole Dark Matter from the First 2 yr of Kepler Data*, *Astrophys. J.* **786** (2014) 158 [1307.5798].

[377] M. Oguri, J. M. Diego, N. Kaiser, P. L. Kelly and T. Broadhurst, *Understanding caustic crossings in giant arcs: characteristic scales, event rates, and constraints on compact dark matter*, *Phys. Rev. D* **97** (2018) 023518 [1710.00148].

[378] H. Niikura, M. Takada, S. Yokoyama, T. Sumi and S. Masaki, *Constraints on Earth-mass primordial black holes from OGLE 5-year microlensing events*, *Phys. Rev. D* **99** (2019) 083503 [1901.07120].

[379] MACHO collaboration, *MACHO project limits on black hole dark matter in the 1-30 solar mass range*, *Astrophys. J. Lett.* **550** (2001) L169 [astro-ph/0011506].

[380] J. Manshanden, D. Gaggero, G. Bertone, R. M. T. Connors and M. Ricotti, *Multi-wavelength astronomical searches for primordial black holes*, *JCAP* **06** (2019) 026 [1812.07967].

[381] P. Lu, V. Takhistov, G. B. Gelmini, K. Hayashi, Y. Inoue and A. Kusenko, *Constraining Primordial Black Holes with Dwarf Galaxy Heating*, *Astrophys. J. Lett.* **908** (2021) L23 [2007.02213].

[382] P. D. Serpico, V. Poulin, D. Inman and K. Kohri, *Cosmic microwave background bounds on primordial black holes including dark matter halo accretion*, *Phys. Rev. Res.* **2** (2020) 023204 [2002.10771].

[383] A. Hektor, G. Hütsi, L. Marzola, M. Raidal, V. Vaskonen and H. Veermäe, *Constraining Primordial Black Holes with the EDGES 21-cm Absorption Signal*, *Phys. Rev. D* **98** (2018) 023503 [1803.09697].

[384] G. Hütsi, M. Raidal, V. Vaskonen and H. Veermäe, *Two populations of LIGO-Virgo black holes*, *JCAP* **03** (2021) 068 [2012.02786].

[385] B. J. Carr, K. Kohri, Y. Sendouda and J. Yokoyama, *New cosmological constraints on primordial black holes*, *Phys. Rev. D* **81** (2010) 104019 [0912.5297].

[386] S. Clark, B. Dutta, Y. Gao, L. E. Strigari and S. Watson, *Planck Constraint on Relic Primordial Black Holes*, *Phys. Rev. D* **95** (2017) 083006 [1612.07738].

[387] M. Boudaud and M. Cirelli, *Voyager 1 $e^{\pm}$ Further Constrain Primordial Black Holes as Dark Matter*, *Phys. Rev. Lett.* **122** (2019) 041104 [1807.03075].

[388] S. Clark, B. Dutta, Y. Gao, Y.-Z. Ma and L. E. Strigari, *21 cm limits on decaying dark matter and primordial black holes*, *Phys. Rev. D* **98** (2018) 043006 [1803.09390].

[389] B. Dasgupta, R. Laha and A. Ray, *Neutrino and positron constraints on spinning primordial black hole dark matter*, *Phys. Rev. Lett.* **125** (2020) 101101 [1912.01014].

[390] W. DeRocco and P. W. Graham, *Constraining Primordial Black Hole Abundance with the Galactic 511 keV Line*, *Phys. Rev. Lett.* **123** (2019) 251102 [1906.07740].

[391] R. Laha, *Primordial Black Holes as a Dark Matter Candidate Are Severely Constrained by the Galactic Center 511 keV γ -Ray Line*, *Phys. Rev. Lett.* **123** (2019) 251101 [1906.09994].

[392] R. Laha, J. B. Muñoz and T. R. Slatyer, *INTEGRAL constraints on primordial black holes and particle dark matter*, *Phys. Rev. D* **101** (2020) 123514 [2004.00627].

[393] R. Laha, P. Lu and V. Takhistov, *Gas heating from spinning and non-spinning evaporating primordial black holes*, *Phys. Lett. B* **820** (2021) 136459 [2009.11837].

[394] A. K. Saha and R. Laha, *Sensitivities on nonspinning and spinning primordial black hole dark matter with global 21-cm troughs*, *Phys. Rev. D* **105** (2022) 103026 [2112.10794].

[395] S. Mittal, A. Ray, G. Kulkarni and B. Dasgupta, *Constraining primordial black holes as dark matter using the global 21-cm signal with X-ray heating and excess radio background*, *JCAP* **03** (2022) 030 [2107.02190].

[396] M. A. Monroy-Rodríguez and C. Allen, *The end of the macho era, revisited: New limits on macho masses from halo wide binaries*, *The Astrophysical Journal* **790** (2014) 159 [1406.5169].

[397] T. D. Brandt, *Constraints on MACHO Dark Matter from Compact Stellar Systems in Ultra-Faint Dwarf Galaxies*, *Astrophys. J. Lett.* **824** (2016) L31 [1605.03665].

[398] B. Carr, M. Raidal, T. Tenkanen, V. Vaskonen and H. Veermäe, *Primordial black hole constraints for extended mass functions*, *Phys. Rev. D* **96** (2017) 023514 [1705.05567].

[399] B. J. Kavanagh, *bradkav/pbhbounds: Release version*, Nov., 2019. 10.5281/zenodo.3538999.

[400] C. T. Byrnes, M. Hindmarsh, S. Young and M. R. S. Hawkins, *Primordial black holes with an accurate QCD equation of state*, *JCAP* **08** (2018) 041 [1801.06138].

[401] A. D. Gow, C. T. Byrnes, P. S. Cole and S. Young, *The power spectrum on small scales: Robust constraints and comparing PBH methodologies*, *JCAP* **02** (2021) 002 [2008.03289].

[402] G. Cusin and G. Tasinato, *Doppler boosting the stochastic gravitational wave background*, *JCAP* **08** (2022) 036 [2201.10464].

[403] D. Alonso, C. R. Contaldi, G. Cusin, P. G. Ferreira and A. I. Renzini, *Noise angular power spectrum of gravitational wave background experiments*, *Phys. Rev. D* **101** (2020) 124048 [2005.03001].

[404] LISA Cosmology Working Group collaboration, *Probing anisotropies of the Stochastic Gravitational Wave Background with LISA*, *JCAP* **11** (2022) 009 [2201.08782].

[405] G. Mentasti, C. Contaldi and M. Peloso, *Prospects for detecting anisotropies and polarization of the stochastic gravitational wave background with ground-based detectors*, [2304.06640].

[406] W.-H. Ruan, C. Liu, Z.-K. Guo, Y.-L. Wu and R.-G. Cai, *The LISA-Taiji network*, *Nature Astron.* **4** (2020) 108 [2002.03603].

[407] M. Tegmark, *CMB mapping experiments: A Designer's guide*, *Phys. Rev. D* **56** (1997) 4514 [astro-ph/9705188].

[408] M. Tegmark, D. J. Eisenstein, W. Hu and A. de Oliveira-Costa, *Foregrounds and forecasts for the cosmic microwave background*, *Astrophys. J.* **530** (2000) 133 [astro-ph/9905257].

[409] M. Kawasaki, K. Kohri and N. Sugiyama, *Cosmological constraints on late time entropy production*, *Phys. Rev. Lett.* **82** (1999) 4168 [astro-ph/9811437].

[410] M. Kawasaki, K. Kohri and N. Sugiyama, *MeV scale reheating temperature and thermalization of neutrino background*, *Phys. Rev. D* **62** (2000) 023506 [astro-ph/0002127].

[411] T. Hasegawa, N. Hiroshima, K. Kohri, R. S. L. Hansen, T. Tram and S. Hannestad, *MeV-scale reheating temperature and thermalization of oscillating neutrinos by radiative and hadronic decays of massive particles*, *JCAP* **12** (2019) 012 [1908.10189].

[412] G. Franciolini, I. Musco, P. Pani and A. Urbano, *From inflation to black hole mergers and back again: Gravitational-wave data-driven constraints on inflationary scenarios with a first-principle model of primordial black holes across the QCD epoch*, *Phys. Rev. D* **106** (2022) 123526 [2209.05959].

[413] A. Escrivà, E. Bagui and S. Clesse, *Simulations of PBH formation at the QCD epoch and comparison with the GWTC-3 catalog*, *JCAP* **05** (2023) 004 [2209.06196].

[414] K. Saikawa and S. Shirai, *Primordial gravitational waves, precisely: The role of thermodynamics in the Standard Model*, *JCAP* **05** (2018) 035 [1803.01038].

[415] K. T. Abe, Y. Tada and I. Ueda, *Induced gravitational waves as a cosmological probe of the sound speed during the QCD phase transition*, *JCAP* **06** (2021) 048 [2010.06193].

[416] C. Caprini et al., *Detecting gravitational waves from cosmological phase transitions with LISA: an update*, *JCAP* **03** (2020) 024 [1910.13125].

[417] K. Saikawa, *A review of gravitational waves from cosmic domain walls*, *Universe* **3** (2017) 40 [1703.02576].

[418] V. Atal and G. Domènech, *Probing non-Gaussianities with the high frequency tail of induced gravitational waves*, *JCAP* **06** (2021) 001 [2103.01056].

[419] S. Balaji, G. Domenech and J. Silk, *Induced gravitational waves from slow-roll inflation after an enhancing phase*, *JCAP* **09** (2022) 016 [2205.01696].

[420] K. Enqvist and M. S. Sloth, *Adiabatic CMB perturbations in pre - big bang string cosmology*, *Nucl. Phys.* **B626** (2002) 395 [hep-ph/0109214].

[421] N. Bartolo, S. Matarrese, A. Riotto and A. Vaihkonen, *The Maximal Amount of Gravitational Waves in the Curvaton Scenario*, *Phys. Rev. D* **76** (2007) 061302 [0705.4240].

[422] S. Ghosh, S. Kumar and Y. Tsai, *Free-streaming and coupled dark radiation isocurvature perturbations: constraints and application to the Hubble tension*, *JCAP* **05** (2022) 014 [2107.09076].

[423] D. H. Lyth, K. A. Malik and M. Sasaki, *A General proof of the conservation of the curvature perturbation*, *JCAP* **05** (2005) 004 [astro-ph/0411220].

[424] M. Sasaki, J. Valiviita and D. Wands, *Non-Gaussianity of the primordial perturbation in the curvaton model*, *Phys. Rev. D* **74** (2006) 103003 [astro-ph/0607627].

[425] L. Amendola, C. Gordon, D. Wands and M. Sasaki, *Correlated perturbations from inflation and the cosmic microwave background*, *Phys. Rev. Lett.* **88** (2002) 211302 [astro-ph/0107089].

[426] N. Bartolo, S. Matarrese and A. Riotto, *Adiabatic and isocurvature perturbations from inflation: Power spectra and consistency relations*, *Phys. Rev. D* **64** (2001) 123504 [astro-ph/0107502].

[427] C. T. Byrnes and D. Wands, *Curvature and isocurvature perturbations from two-field inflation in a slow-roll expansion*, *Phys. Rev. D* **74** (2006) 043529 [astro-ph/0605679].

[428] G. Orlando, P. D. Meerburg and S. P. Patil, *Primordial tensor bispectra in μ-CMB cross-correlations*, *JCAP* **02** (2022) 004 [2109.01095].

[429] M. Shiraishi, *Tensor Non-Gaussianity Search: Current Status and Future Prospects*, *Front. Astron. Space Sci.* **6** (2019) 49 [1905.12485].

[430] D. Jeong and M. Kamionkowski, *Clustering Fossils from the Early Universe*, *Phys. Rev. Lett.* **108** (2012) 251301 [1203.0302].

[431] S. Brahma, E. Nelson and S. Shandera, *Fossilized Gravitational Wave Relic and Primordial Clocks*, *Phys. Rev. D* **89** (2014) 023507 [1310.0471].

[432] E. Dimastrogiovanni, M. Fasiello, D. Jeong and M. Kamionkowski, *Inflationary tensor fossils in large-scale structure*, *JCAP* **12** (2014) 050 [1407.8204].

[433] P. Adshead and E. A. Lim, *3-pt Statistics of Cosmological Stochastic Gravitational Waves*, *Phys. Rev. D* **82** (2010) 024023 [0912.1615].

[434] A. Margalit, C. R. Contaldi and M. Pieroni, *Phase decoherence of gravitational wave backgrounds*, *Phys. Rev. D* **102** (2020) 083506 [2004.01727].

[435] C. Powell and G. Tasinato, *Probing a stationary non-Gaussian background of stochastic gravitational waves with pulsar timing arrays*, *JCAP* **01** (2020) 017 [1910.04758].

[436] L. Dai, D. Jeong and M. Kamionkowski, *Anisotropic imprint of long-wavelength tensor perturbations on cosmic structure*, *Phys. Rev.* **D88** (2013) 043507 [1306.3985].

[437] E. Dimastrogiovanni, M. Fasiello and M. Kamionkowski, *Imprints of Massive Primordial Fields on Large-Scale Structure*, *JCAP* **02** (2016) 017 [1504.05993].

[438] A. Lue, L.-M. Wang and M. Kamionkowski, *Cosmological signature of new parity violating interactions*, *Phys. Rev. Lett.* **83** (1999) 1506 [astro-ph/9812088].

[439] N. Afshordi, Y.-S. Loh and M. A. Strauss, *Cross - correlation of the Cosmic Microwave Background with the 2MASS galaxy survey: Signatures of dark energy, hot gas, and point sources*, *Phys. Rev. D* **69** (2004) 083524 [astro-ph/0308260].

[440] G. Mentasti, C. R. Contaldi and M. Peloso, *Intrinsic limits on the detection of the anisotropies of the Stochastic Gravitational Wave Background*, [2301.08074].

[441] A. Challinor, H. Peiris, M. Novello and S. Perez, *Lecture notes on the physics of cosmic microwave background anisotropies*, *AIP Conference Proceedings* (2009) [0903.5158].

[442] Y. Watanabe and E. Komatsu, *Improved Calculation of the Primordial Gravitational Wave Spectrum in the Standard Model*, *Phys. Rev. D* **73** (2006) 123515 [astro-ph/0604176].

[443] L. Verde, *Statistical methods in cosmology*, *Lecture Notes in Physics* (2010) 147–177.

[444] A. Higuchi, *Forbidden Mass Range for Spin-2 Field Theory in De Sitter Space-time*, *Nucl. Phys.* **B282** (1987) 397.

[445] A. Achúcarro, V. Atal, P. Ortiz and J. Torrado, *Localized correlated features in the CMB power spectrum and primordial bispectrum from a transient reduction in the speed of sound*, *Phys. Rev. D* **89** (2014) 103006 [1311.2552].

[446] J. Chluba, A. L. Erickcek and I. Ben-Dayan, *Probing the inflaton: Small-scale power spectrum constraints from measurements of the CMB energy spectrum*, *Astrophys. J.* **758** (2012) 76 [1203.2681].

[447] T. Bringmann, P. Scott and Y. Akrami, *Improved constraints on the primordial power spectrum at small scales from ultracompact minihalos*, *Phys. Rev. D* **85** (2012) 125027 [1110.2484].

[448] M. Karami, N. Afshordi and J. Zavala, *Forward modelling of quasar light curves and the cosmological matter power spectrum on milliparsec scales*, [1805.06984].

[449] A. Kalaja, N. Bellomo, N. Bartolo, D. Bertacca, S. Matarrese, I. Musco et al., *From Primordial Black Holes Abundance to Primordial Curvature Power Spectrum (and back)*, *JCAP* **10** (2019) 031 [1908.03596].

[450] S. Yoshiura, M. Oguri, K. Takahashi and T. Takahashi, *Constraints on primordial power spectrum from galaxy luminosity functions*, *Phys. Rev. D* **102** (2020) 083515 [2007.14695].

[451] T. Kite, A. Ravenni, S. P. Patil and J. Chluba, *Bridging the gap: spectral distortions meet gravitational waves*, *Mon. Not. Roy. Astron. Soc.* **505** (2021) 4396 [2010.00040].

[452] S. Dubovsky, T. Gregoire, A. Nicolis and R. Rattazzi, *Null energy condition and superluminal propagation*, *JHEP* **03** (2006) 025 [hep-th/0512260].

[453] R. K. Sachs and A. M. Wolfe, *Perturbations of a Cosmological Model and Angular Variations of the Microwave Background*, ApJ **147** (1967) 73.

[454] L. Abbott and M. B. Wise, *Constraints on generalized inflationary cosmologies*, *Nuclear Physics B* **244** (1984) 541.

[455] A. A. Starobinskii, *Cosmic Background Anisotropy Induced by Isotropic Flat-Spectrum Gravitational-Wave Perturbations*, *Soviet Astronomy Letters* **11** (1985) 133.

[456] G. Galloni, N. Bartolo, S. Matarrese, M. Migliaccio, A. Ricciardone and N. Vittorio, *Updated constraints on amplitude and tilt of the tensor primordial spectrum*, *JCAP* **04** (2023) 062 [2208.00188].

[457] D. Paoletti, F. Finelli, J. Valiviita and M. Hazumi, *Planck and BICEP/Keck Array 2018 constraints on primordial gravitational waves and perspectives for future B-mode polarization measurements*, *Phys. Rev. D* **106** (2022) 083528 [2208.10482].

[458] T. Namikawa, S. Saga, D. Yamauchi and A. Taruya, *CMB Constraints on the Stochastic Gravitational-Wave Background at Mpc scales*, *Phys. Rev. D* **100** (2019) 021303 [1904.02115].

[459] T. J. Clarke, E. J. Copeland and A. Moss, *Constraints on primordial gravitational waves from the Cosmic Microwave Background*, *JCAP* **10** (2020) 002 [2004.11396].

[460] K.-W. Ng, *Redshift-space fluctuations in stochastic gravitational wave background*, *Phys. Rev. D* **106** (2022) 043505 [2106.12843].

[461] M. Maggiore et al., *Science Case for the Einstein Telescope*, *JCAP* **03** (2020) 050 [1912.02622].

[462] E. J. Copeland, E. W. Kolb, A. R. Liddle and J. E. Lidsey, *Reconstructing the inflaton potential: Perturbative reconstruction to second order*, *Phys. Rev. D* **49** (1994) 1840 [astro-ph/9308044].

[463] H. Peiris and R. Easther, *Recovering the Inflationary Potential and Primordial Power Spectrum With a Slow Roll Prior: Methodology and Application to WMAP 3 Year Data*, *JCAP* **07** (2006) 002 [astro-ph/0603587].

[464] J. Hamann, J. Lesgourgues and W. Valkenburg, *How to constrain inflationary parameter space with minimal priors*, *JCAP* **04** (2008) 016 [0802.0505].

[465] A. Kehagias, A. Moradinezhad Dizgah and A. Riotto, *Remarks on the Starobinsky model of inflation and its descendants*, *Phys. Rev. D* **89** (2014) 043527 [1312.1155].

[466] E. J. Copeland, E. W. Kolb, A. R. Liddle and J. E. Lidsey, *Observing the inflaton potential*, *Phys. Rev. Lett.* **71** (1993) 219 [hep-ph/9304228].

[467] J. L. Cook and L. Sorbo, *Particle production during inflation and gravitational waves detectable by ground-based interferometers*, *Phys. Rev. D* **85** (2012) 023534 [1109.0022].

[468] N. Barnaby, J. Moxon, R. Namba, M. Peloso, G. Shiu and P. Zhou, *Gravity waves and non-Gaussian features from particle production in a sector gravitationally coupled to the inflaton*, *Phys. Rev. D* **86** (2012) 103508 [1206.6117].

[469] S. Mukohyama, R. Namba, M. Peloso and G. Shiu, *Blue Tensor Spectrum from Particle Production during Inflation*, *JCAP* **08** (2014) 036 [1405.0346].

[470] V. Domcke and K. Mukaida, *Gauge Field and Fermion Production during Axion Inflation*, *JCAP* **11** (2018) 020 [1806.08769].

[471] P. Campeti, O. Özsoy, I. Obata and M. Shiraishi, *New constraints on axion-gauge field dynamics during inflation from Planck and BICEP/Keck data sets*, *JCAP* **07** (2022) 039 [2203.03401].

[472] M. Zaldarriaga, *Polarization of the microwave background in reionized models*, *Phys. Rev. D* **55** (1997) 1822 [astro-ph/9608050].

[473] L. Sorbo, *Parity violation in the Cosmic Microwave Background from a pseudoscalar inflaton*, *JCAP* **06** (2011) 003 [1101.1525].

[474] Planck collaboration, *Planck 2018 results. V. CMB power spectra and likelihoods*, *Astron. Astrophys.* **641** (2020) A5 [1907.12875].

[475] PLANCK collaboration, *Planck 2018 results. VIII. Gravitational lensing*, *Astron. Astrophys.* **641** (2020) A8 [1807.06210].

[476] A. Lewis and S. Bridle, *Cosmological parameters from CMB and other data: A Monte Carlo approach*, *Phys. Rev.* **D66** (2002) 103511 [astro-ph/0205436].

[477] A. Lewis, *Efficient sampling of fast and slow cosmological parameters*, *Phys. Rev.* **D87** (2013) 103529 [1304.4473].

[478] J. Torrado and A. Lewis, *Cobaya: Code for Bayesian Analysis of hierarchical physical models*, *JCAP* **05** (2021) 057 [2005.05290].

[479] A. Lewis, *GetDist: a Python package for analysing Monte Carlo samples*, [1910.13970].

[480] W. L. K. Wu, J. Errard, C. Dvorkin, C. L. Kuo, A. T. Lee, P. McDonald et al., *A Guide to Designing Future Ground-based Cosmic Microwave Background Experiments*, *Astrophys. J.* **788** (2014) 138 [1402.4108].

[481] D. K. Hazra, D. Paoletti, F. Finelli and G. F. Smoot, *Reionization in the dark and the light from Cosmic Microwave Background*, *JCAP* **09** (2018) 016 [1807.05435].

[482] C. Dickinson, *CMB foregrounds - A brief review*, in *51st Rencontres de Moriond on Cosmology*, pp. 53–62, 6, 2016, [1606.03606].

[483] M. Kesden, A. Cooray and M. Kamionkowski, *Separation of gravitational wave and cosmic shear contributions to cosmic microwave background polarization*, *Phys. Rev. Lett.* **89** (2002) 011304 [astro-ph/0202434].

[484] C. M. Hirata and U. Seljak, *Reconstruction of lensing from the cosmic microwave background polarization*, *Phys. Rev. D* **68** (2003) 083002 [astro-ph/0306354].

[485] PLANCK collaboration, *Planck 2013 results. XVIII. The gravitational lensing-infrared background correlation*, *Astron. Astrophys.* **571** (2014) A18 [1303.5078].

[486] J. Hamann and J. Wons, *Optimising inflationary features the Bayesian way*, *JCAP* **03** (2022) 036 [2112.08571].

[487] L. Boubekeur, P. Creminelli, J. Norena and F. Vernizzi, *Action approach to cosmological perturbations: the 2nd order metric in matter dominance*, *JCAP* **08** (2008) 028 [0806.1016].

[488] R. M. Wald, *General Relativity*. Chicago Univ. Pr., Chicago, USA, 1984, 10.7208/chicago/9780226870373.001.0001.

[489] P. Creminelli, C. Pitrou and F. Vernizzi, *The CMB bispectrum in the squeezed limit*, *JCAP* **11** (2011) 025 [1109.1822].

[490] LIGO Scientific, VIRGO, KAGRA collaboration, *All-sky, all-frequency directional search for persistent gravitational-waves from Advanced LIGO's and Advanced Virgo's first three observing runs*, [2110.09834].

[491] A. Renzini and C. Contaldi, *Improved limits on a stochastic gravitational-wave background and its anisotropies from Advanced LIGO O1 and O2 runs*, *Phys. Rev. D* **100** (2019) 063527 [1907.10329].

[492] T. L. Smith and R. Caldwell, *Sensitivity to a Frequency-Dependent Circular Polarization in an Isotropic Stochastic Gravitational Wave Background*, *Phys. Rev. D* **95** (2017) 044036 [1609.05901].

[493] J. S. Hazboun, J. D. Romano and T. L. Smith, *Realistic sensitivity curves for pulsar timing arrays*, *Phys. Rev. D* **100** (2019) 104028 [1907.04341].

[494] C. J. Moore, R. H. Cole and C. P. L. Berry, *Gravitational-wave sensitivity curves*, *Class. Quant. Grav.* **32** (2015) 015014 [1408.0740].

[495] NANOGrav collaboration, *The NANOGrav 12.5 yr Data Set: Search for an Isotropic Stochastic Gravitational-wave Background*, *Astrophys. J. Lett.* **905** (2020) L34 [2009.04496].

[496] A. Weltman et al., *Fundamental physics with the Square Kilometre Array*, *Publ. Astron. Soc. Austral.* **37** (2020) e002 [1810.02680].

[497] "*NIST Digital Library of Mathematical Functions*." http://dlmf.nist.gov/, Release 1.0.27 of 2020-06-15.

[498] *6–7 - definite integrals of special functions*, in *Table of Integrals, Series, and Products (Seventh Edition)*, A. Jeffrey, D. Zwillinger, I. Gradshteyn and I. Ryzhik, eds., (Boston), pp. 631–857, Academic Press, (2007), DOI.

[499] W. Hu and M. J. White, *CMB anisotropies: Total angular momentum method*, *Phys. Rev. D* **56** (1997) 596 [astro-ph/9702170].

[500] J. Soda, *Statistical Anisotropy from Anisotropic Inflation*, *Class. Quant. Grav.* **29** (2012) 083001 [1201.6434].

[501] N. Bartolo, S. Matarrese, M. Peloso and A. Ricciardone, *Anisotropic power spectrum and bispectrum in the $f(\phi)F^2$ mechanism*, *Phys. Rev. D* **87** (2013) 023504 [1210.3257].

[502] R. Emami, H. Firouzjahi and M. Zarei, *Anisotropic inflation with the nonvacuum initial state*, *Phys. Rev. D* **90** (2014) 023504 [1401.4406].

[503] T. Rostami, A. Karami and H. Firouzjahi, *Effective field theory of statistical anisotropies for primordial bispectrum and gravitational waves*, *JCAP* **06** (2017) 039 [1702.03744].

[504] N. Bartolo, S. Matarrese, M. Peloso and M. Shiraishi, *Parity-violating CMB correlators with non-decaying statistical anisotropy*, *JCAP* **07** (2015) 039 [1505.02193].

[505] A. Maleknejad, M. Sheikh-Jabbari and J. Soda, *Gauge Fields and Inflation*, *Phys. Rept.* **528** (2013) 161 [1212.2921].

[506] T. Fujita, I. Obata, T. Tanaka and S. Yokoyama, *Statistically Anisotropic Tensor Modes from Inflation*, *JCAP* **07** (2018) 023 [1801.02778].

[507] J. Ohashi, J. Soda and S. Tsujikawa, *Observational signatures of anisotropic inflationary models*, *JCAP* **12** (2013) 009 [1308.4488].

[508] J. Ohashi, J. Soda and S. Tsujikawa, *Anisotropic Non-Gaussianity from a Two-Form Field*, *Phys. Rev. D* **87** (2013) 083520 [1303.7340].

[509] G. Franciolini, A. Kehagias and A. Riotto, *Imprints of Spinning Particles on Primordial Cosmological Perturbations*, *JCAP* **1802** (2018) 023 [1712.06626].

[510] G. Franciolini, A. Kehagias, A. Riotto and M. Shiraishi, *Detecting higher spin fields through statistical anisotropy in the CMB bispectrum*, *Phys. Rev. D* **98** (2018) 043533 [1803.03814].

[511] T. Hiramatsu, K. Murai, I. Obata and S. Yokoyama, *Statistically-Anisotropic Tensor Bispectrum from Inflation*, *JCAP* **03** (2021) 047 [2008.03233].

[512] L. Ackerman, S. M. Carroll and M. B. Wise, *Imprints of a Primordial Preferred Direction on the Microwave Background*, *Phys. Rev. D* **75** (2007) 083502 [astro-ph/0701357].

[513] M. a. Watanabe, S. Kanno and J. Soda, *The Nature of Primordial Fluctuations from Anisotropic Inflation*, *Prog. Theor. Phys.* **123** (2010) 1041 [1003.0056].

[514] N. Bartolo, A. Kehagias, M. Liguori, A. Riotto, M. Shiraishi and V. Tansella, *Detecting higher spin fields through statistical anisotropy in the CMB and galaxy power spectra*, *Phys. Rev. D* **97** (2018) 023503 [1709.05695].

[515] I. Obata and T. Fujita, *Footprint of Two-Form Field: Statistical Anisotropy in Primordial Gravitational Waves*, *Phys. Rev. D* **99** (2019) 023513 [1808.00548].

[516] A. Hajian and T. Souradeep, *Measuring statistical isotropy of the CMB anisotropy*, *Astrophys. J. Lett.* **597** (2003) L5 [astro-ph/0308001].

[517] A. Hajian and T. Souradeep, *The Cosmic microwave background bipolar power spectrum: Basic formalism and applications*, [astro-ph/0501001].